



The Alliance of Laboratories in Europe for
Research and Technology

ALERT Doctoral School 2013
Soil-Structure Interaction

Editors:

Panagiotis Kotronis

Claudio Tamagnini

Stéphane Grange

Editorial

The twenty-third session of the ALERT Doctoral School = European Graduate School entitled *Soil-Structure Interaction* is organized by Panagiotis Kotronis, Claudio Tamagnini and Stephane Grange. It proceeds with the tradition established last year and offers the school book as a freely downloadable *pdf file* from the ALERT website <http://alertgeomaterials.eu>.

The new ALERT website has become an attractive blog for the news in the field of geomechanics. Conference and workshop announcements, PhD positions or research prizes are being published regularly there. In the last 12 months there were more than 21 thousand visitors counted. Many of them downloaded the book from the ALERT Doctoral School 2012. I am sure that the present book will be equally successful.

On behalf of the ALERT Board of Directors and of all the members of ALERT, I would like to thank the organizers of this School 2013 for their intensive work invested into the preparation of the published volume and the oral presentations during the event in the Paul Langevin Centre in Aussois.

Ivo Herle
Director of ALERT Geomaterials
Technische Universität Dresden, Germany

Contents

Foreword P. Kotronis, C. Tamagnini, S. Grange	1
Soil-structure interaction under earthquake loading: Theoretical framework C. G. Lai, M. Martinelli	3
Centrifuge modelling of foundations subjected to cyclic loading L. Thorel	45
Centrifuge modeling of foundations subjected to earthquake loadings S. Escoffier	177
Using strong and weak motion to identify the dynamic characteristics and the response of buildings considering soil-structure interaction P. Gueguen	109
Discontinuous Deformation R. I. Borja	137
Modeling SSI on piled foundations: The effects of kinematic interaction M. Martinelli, C. Tamagnini	147
Simplified modeling strategies for soil-structure interaction problems: The multifiber beam concept P. Kotronis	173
Simplified modeling strategies for soil-structure interaction problems: The macro- element concept S. Grange	195

Soil-Structure Interaction: Foreword

The contributions in the present volume have been prepared and collected to be used as lecture notes for students and researchers attending the 2013 ALERT Geomaterials Doctoral School devoted to “Soil-Structure Interaction”. The School has been organized and coordinated by Panagiotis Kotronis (Ecole Centrale de Nantes), Claudio Tamagnini (University of Perugia) and Stéphane Grange (Université Joseph Fourier, Grenoble). The coordinators would like to warmly acknowledge all the contributors for the work done in order to obtain papers of high quality in due time.

The volume is divided into 8 chapters: The first chapter, written by Carlo G. Lai and Mario Martinelli presents a general overview of the soil-foundation-superstructure interaction analysis and its importance when assessing the response of structures subjected to earthquake loading. Chapter 2, written by Luc Thorel, is specific to centrifuge modelling of foundations subjected to cyclic loading and chapter 3, by Sandra Escoffier, to earthquake loadings. In chapter 4 Philippe Gueguen uses strong and weak motions to study the dynamic characteristics and the response of buildings considering soil-structure interaction. In the next chapter Ronaldo I. Borja shows the capability of the extended finite element formulation to accommodate quasistatic crack propagation and spontaneous fault rupture dynamics. In chapter 6 Mario Martinelli and Claudio Tamagnini focus on the modeling of soil-structure interaction on piled foundations. The last two chapters, written respectively by Panagiotis Kotronis and Stéphane Grange, present simplified modelling strategies for soil-structure interaction problems based on the multifiber beam and the macro-element concepts.

We hope that all the papers collected herein will provide a good overview of the soil-structure interaction research field and will be a useful complement of the lectures given at the doctoral school.

Panagiotis KOTRONIS
Claudio TAMAGNINI
Stéphane GRANGE

Soil-Structure Interaction Under Earthquake Loading: Theoretical Framework

Carlo G. Lai^{1,2} and Mario Martinelli¹

¹*Department of Civil Engineering and Architecture,
University of Pavia, Italy*

²*EUCENTRE, Pavia, Italy*

This chapter presents a general overview of soil-foundation-superstructure interaction (SFSI) analysis. It focuses specifically on the importance of SFSI when assessing the response of structures subjected to earthquake loading. Both shallow and deep foundation typologies are examined. Two approaches are presented: the so-called direct method and the substructure method. Capabilities and shortcomings are highlighted for both techniques. To overcome the assumption of linearity underlying the substructure approach, the macro-element approach is also briefly introduced. This technique is particularly suitable when certain nonlinear phenomena of SFSI like sliding at the soil-foundation interface, uplift and/or pile-soil relative displacement need to be taken into account. The chapter includes an illustration of the most common procedures used to calculate the frequency-dependent, dynamic impedances matrices in the application of the substructure method. The last section shows two applications of SFSI analysis conducted using the substructure method. The first example concerns with the seismic design of the foundation of EUCENTRE (Pavia, Italy) shake table, which is the Europe most powerful. The second example concerns with the seismic demand assessment of a long-span viaduct founded on large-diameter shafts.

1. Definition of the problem and historical sketch

The vast majority of structural design is performed under the assumption that the structural elements are fixed at the foundation level against translation, settlement, and in some cases, rotation. Structures excited by earthquake ground shaking develop inertial forces that introduce base shears and bending moments at the structure-foundation interface. If the foundation system and supporting soil are not rigid, these internal forces induce displacements and rotations at the structural base. For highly flexible structural systems (e.g. slender towers), foundation displacements and rota-

4 Soil-structure interaction under earthquake loading: Theoretical framework

tions may be small compared to those in the superstructure and may be neglected. Vice versa, for stiff structural systems (e.g. buildings with shear-walls) the foundation movements may represent a significant contribution to the flexibility of the overall system. Thus, ignoring these effects may lead to gross errors in the assessment of the response under earthquake loadings.

ATC-40 (1996) [ATC96] presented an example, shown in Figure 1, that represents a shear wall connected to a flexible frame. This highlights how dramatically different are the results of the analysis if the system is considered connected to a strong and stiff supporting soil (where the SFSI can be neglected) or contrariwise to weak and flexible ground. In case of stiff supporting soil (Figure 1, *left*), the shear wall (sensible to loads) is completely cracked and the connected frame, subjected to small displacements, is perfectly intact. On the other hand, the shear wall rotation produced by the flexibility of the base, decreases the force demand inducing large displacements into the connected frame, thus, no damages will occur into the wall however significant cracks are developed into the frame (Figure 1, *right*).

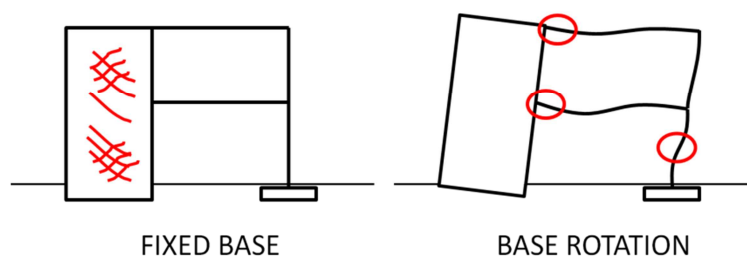


Figure 1: Comparison between the response of a structural system characterized by either a stiff/strong (*left*) or flexible/weak foundation (*right*) (*modified from* [ATC96]).

The above example highlights situations drawn from the real design practice when SFSI may be either important or negligible. However, a formal definition of what a soil-structure interaction (SSI) problem is, has yet to be given. This may not be a simple task, particularly if the definition pretends to be rigorous [Kau10]. Using an approximate description, it may be stated that the term *soil-structure interaction* (SSI) is often used to denote a particular category of *contact problems* where along the surface of a structural element (e.g. shallow/piled foundation, earth-retaining structure) in contact with the surrounding ground, the stresses acting along the interface cannot be defined without simultaneously determining the deformation and displacement fields along the very same interface.

SSI problems are thus *coupled problems* as there exist a coupling between the “action” (e.g. the contact pressure) and the “reaction” (e.g. the displacement of the soil-structure interface) along the contact surface by which the former can only be determined jointly with the latter. Mathematically, the SSI problem defined above may be formalized through an *integral equation* where the unknown function is for

instance the contact pressure. The term “interaction” is instructive of the meaning of the phenomenon since the “action” depends upon the “reaction”.

Interaction problems are numerous in physics and engineering. Some of them may be fairly involved (e.g. the well-known three bodies problem of classical mechanics). In engineering, solution of a SSI problem requires an idealization of the behaviour of two systems: “the structure” and the “soil” and also of the boundary conditions of the interface (e.g. unilateral constraint, glued/unglued, smooth interface, etc.). Linear elasticity is one natural assumption for the constitutive modeling of the structural material even though sometimes the structure is assumed rigid.

As far as soil modelling is concerned, the so-called Winkler model is one of the most common idealizations of soil response. In statics the Winkler model is composed by a continuous distribution of linear/nonlinear, non-connected, springs. Among the major shortcomings of Winkler model is its inability to account for the shear stiffness of soils a fact that is responsible of well-known paradoxes (e.g. a continuous, uniformly-loaded beam resting on a Winkler soil undergoes a uniform settlement, despite experimental evidence shows that settlement is larger at the center of the beam if compared with that at the edges).

In dynamics, the work by H. Lamb in 1904 can be considered the first attempt to study the response of an elastic, homogeneous, isotropic half-space to dynamic loadings. Lamb actually extended the solution of the classical *Boussinesq’s problem* (i.e. that of finding the stress-strain-displacement fields induced in an elastic half-space by a concentrated, vertical force applied at the boundary of the half-space) to dynamic loading. For this reason sometimes the *Lamb’s problem* is referred to as the *dynamic Boussinesq problem*. Lamb in fact calculated the displacement field induced in an elastic half-space by an oscillating vertical force applied at the free surface of the half-space.

However, only in 1936 the theory of dynamic Soil-Structure-Interaction (SSI) has been properly formulated for the first time through an article by Erich (Eric) Reissner [Rei36] in which he examined the behavior of circular disks lying over elastic half-spaces subjected to time-harmonic, vertical loads. Actually, he did not solve a true mixed boundary value problem but he only assumed a uniform stress distribution underneath a plate jointly with assumption that the displacement at the center of the load equals the displacement of the plate. Soon after, in another paper Reissner (1937) [Rei37] dealt with the problem of an elastic half-space excited at the free surface by concentrated and distributed torsional loadings. He also took into consideration the case of a finite thickness soil layer and discussed the generalization to soils whose properties vary continuously with depth. Despite the simplifications adopted in either paper concerning the distribution of contact stresses, he introduced the concepts of radiation damping and that of an equivalent mass-spring-dashpot analogue system. Therefore, as suggested by Kausel [Kau10], Reissner can be considered as the father of the dynamic SSI.

After Reissner contributions, several rigorous solutions of mixed boundary value problems have been provided, such as the Sagoci’s paper proposed in 1944 in which he examined a rigid circular plate loaded in torsion at arbitrary frequencies. A large number of papers dealing with dynamically loaded plates resting over elastic half-spaces and finite thickness layers have been studied. Some articles are remarkable

and deserve special citations. Among them the works by Quinlan (1953) [Qui53], Sung (1953) [Sun53] and Bycroft (1956) [Byc56], all listed in Kausel's recent state-of-the-art paper [Kau10].

Most of the papers mentioned above focus on the calculation of the dynamic response of a foundation where the source of vibration is located in the superstructure (e.g. wind turbines, off-shore platforms, turboalternators). However the elastic waves generated by an earthquake are transmitted to a structure from the ground through the foundations. Thus seismic excitation constitutes an alternative mechanism of dynamic loading. Once the seismic waves hit the structure, the input motion excites the superstructure and simultaneously it gets modified by the movement of the latter relative to the ground. This interaction phenomenon is called "soil-foundation-superstructure interaction" (SFSI).

The first attempt to study the phenomenon of dynamic SFSI was carried out in Japan in 1935 by Katsutada Sezawa and Kiyoshi Kanai [Sez35a, Sez35b, Sez35c]. In this work, the structure was modeled as a thin cylindrical rod with a hemispherical tip at the base completely embedded in a homogeneous half-space. The model took into account the propagation of plane, vertical P-waves through the medium. They were scattered in all directions and partly transmitted into the rod, once they hit the foundation. Despite the simplifying assumptions, the results obtained from these Japanese researchers are considered a milestone in modern earthquake engineering. Among other things, they introduced the concept of energy loss due to geometrical spreading of the waves which tend to reduce the seismic demand on the superstructure, limiting resonance effects.

Several contributions were given after the work by Katsutada Sezawa and Kiyoshi Kanai (1935). A complete account of the early-history of SSI is reported in the already cited paper by Kausel [Kau10]. One of the reasons why SSI has been studied over a period of more than eighty years is that the response of a structural system can be quite different if the supporting ground is not rigid. The actual difference will depend on the characteristics of the soil medium, the source of excitation and the particular type of foundation. Additional important factors influence the response. They include (a) non-vertically incident body waves; (b) presence of surface waves which induce coupled rotational and translational motion; (c) dissipation of strain energy through a combination of geometrical radiation and inelastic soil response; (d) relative displacements induced by a flexible foundation can cause high localized stresses; (e) in presence of a stiff embedded foundation, the free-field input motion transferred from the soil to the structure is modified by the interaction, rotational motion may arise and get transmitted to the superstructure; (f) in presence of unsymmetrical structures, coupling effects may occur such as torsional vibrations induced by horizontal excitations at the base; (g) the influence of surrounding buildings may be significant in the sense that vibration of nearby foundations can act as additional wave sources for the structure under consideration.

The objective of this work is to investigate some of the phenomena mentioned above focusing on some approaches that have been adopted to solve the SSI problem associated with earthquake loading.

2. Kinematic and inertial interaction

In accordance with the concepts introduced in the previous section, there are two phenomena that occur due to the presence of a dynamically excited structure at a soil site. These phenomena are widely known as *kinematic* and *inertial* effects.

The term “*kinematic interaction*” represents the phenomenon by which the seismic input in the absence of the structure (also denoted as *free-field* motion) is different than that with the structure sitting at the site. Kinematic interaction is essentially a *scattering* phenomenon due to a mismatch in the dynamic impedance between the foundation structure and the surrounding ground. In fact, the foundation stiffness is different from that of the adjacent soil and this causes reflection and refraction of the incoming seismic waves as these waves approach the soil-foundation interface.

Therefore, the kinematic interaction represents the difference between the structural response due to the free-field ground motion in absence of the scattering effect and the response computed using the ground motion when the presence of the structure is considered. The magnitude of the phenomenon depends on the geometry of the structure, the foundation size and embedment, the kinematics of the incident free-field motion and the angle of incidence of the seismic waves. As a special ideal case, no kinematic interaction occurs if the foundation is built at the ground surface (i.e. a shallow foundation) and is hit by a vertically propagating S wave (Figure 2).

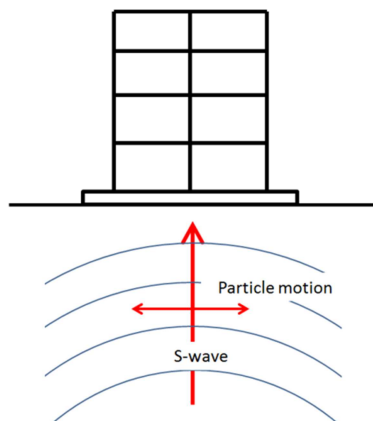


Figure 2: Building with shallow foundation subjected to vertically propagating transversal (i.e. shear) waves.

The second phenomenon occurring when a structure lying on a soil deposit is dynamically excited is the “*inertial interaction*”. This is the result of the dynamic coupling between a structure and its supporting ground. The deformability of the soil increases the kinematic degrees of freedom of the structure. In addition the ground can dissipate the vibrational energy through radiation of the seismic waves away from the structure and through inelastic deformation. In general, the inertial and dissipative properties of the soil-foundation system make the dynamic response of

the foundation frequency-dependent. Figure 3 shows the inertial forces arising from the excitation of the ground.

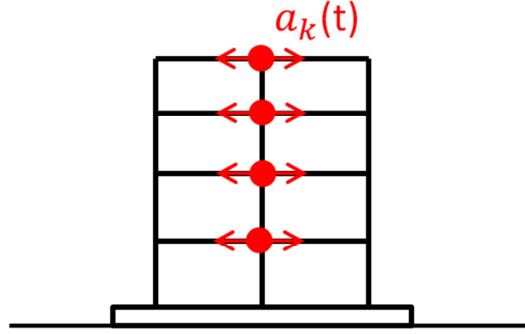


Figure 3: Inertial forces arising in a structure from ground motion.

If the deformability and energy dissipation of a supporting soil is accounted for, the response of a structure to a given ground motion would be substantially different from that of a fixed-base structure. The magnitude of this difference will depend on the mismatch between the stiffness of the superstructure-foundation system and the stiffness of the supporting ground. Thus, the inertial interaction would be negligible for structures founded on rock or very stiff soils, because in such cases the structural response would be almost identical of that of a fixed-base structure. On the other hand, the interaction effect could be quite significant for structures founded on highly-deformable, soft soils.

For example, the response of a single-degree of freedom (SDOF) system fixed at the base and composed by a mass M and a spring with flexural stiffness K (Figure 4) subjected to a horizontal displacement, is controlled by M and K . The fundamental period (T_{fix}) of the system is given by the following relation:

$$T_{fix} = 2\pi/\sqrt{K/M} \quad (1)$$

Instead, if the same SDOF system is connected at the (fixed) base through a rotational spring capturing soil compliance (Figure 4), the base can rotate and the global response of the system would then be obtained from the solution of the following pair of equations:

$$F = K_{eq}u = K_{rot}u_{rot} = Ku_{flex} \quad (2)$$

$$u = u_{rot} + u_{flex} \quad (3)$$

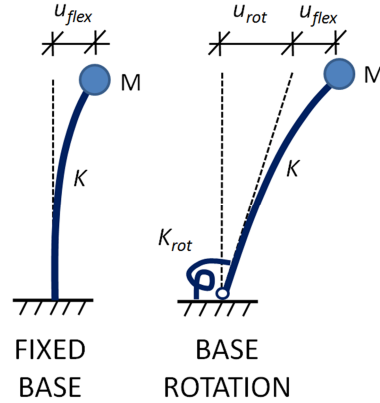


Figure 4: Single-degree-of-freedom (SDOF) fixed at the base and connected at the (fixed) base through a rotational spring.

where the equivalent stiffness (K_{eq}) and the fundamental period (T_{eq}) of the system are given by the following relations:

$$K_{eq} = 1 / \left(\frac{1}{K} + \frac{1}{K_{rot}} \right) \quad (4)$$

$$T_{eq} = 2\pi / \sqrt{K_{eq}/M} \quad (5)$$

From this simple example, it is worth noticing that accounting for the SSI effect typically amounts in lengthening the natural period of the structure. This is due to the deformability of the ground and by an increase of the damping coefficient due to geometric damping. However, it is not possible to *a-priori* determine whether inertial interaction has always a beneficial effect in the dynamic response of a structure. Gazetas and Mylonakis in 2000 [Gaz00] have in fact shown that for certain ground motions and soil types, an increase of the fundamental period due to SSI may be detrimental for it increases the displacement demand of the structure.

3. Methods of analyses

The general methods by which soil-structure interaction analyses are performed can be categorized as *direct* and *indirect* or substructure approaches. Some peculiarities of both methods will be described in the next sections. It will then follow a brief introduction of the notion of *macro-element* which is a relatively recent (in geotechnical engineering) and innovative concept to solve SSI problems that takes advantage of the individual merits of the direct and substructure approaches without however inheriting their shortcomings.

3.1. Direct approach

In the direct approach, the soil volume and the structure are both part of the same model (Figure 5) which is analyzed in a single step by using one of several numerical discretization techniques (e.g. Finite Element Method, Spectral Element Method, Finite Difference Method, etc.). For example in the Finite Element Method (FEM), the soil can be modeled with solid 3D elements and the structure as beam and/or frame elements. The equation of motion can be written as follows:

$$M_{total}\ddot{u}_{total} + Ku_{total} = -M_{total} \ddot{u}_{base} \quad (6)$$

where \ddot{u}_{base} represents the input motion applied at the base of the model, M_{total} and K are respectively the mass and stiffness matrix of the global system, \ddot{u}_{total} and u_{total} are respectively the acceleration and displacement vectors of the system.

Equation (6) can be integrated using standard explicit or implicit schemes (e.g. Newmark and Wilson- θ method) and is valid for linear as well as nonlinear analysis. The direct method allows for instance to take into account also geometrical nonlinearities like foundation uplift and gaps forming at the soil-pile shaft interface both under static and dynamic loading. With this technique soil-structure interaction and the associated phenomena are automatically taken into account.

However, the direct approach may be computationally very expensive depending on the size of the model, the constitutive laws adopted to describe the dynamic response of soils and structural elements, the type of kinematic boundary conditions at the soil-structure interfaces, in saturated soils whether the analysis is conducted under drained or undrained conditions. For the results to be meaningful, the direct method also requires a detailed geotechnical characterization of the soil deposit.

During the numerical simulation, once the structure is hit by the seismic waves, it becomes a vibrating system, so waves emitted from the soil-foundation interface will eventually propagate downward in the unbounded medium. Artificial, adsorbing boundaries are introduced at an appropriate distance from the structure to correctly simulate the radiation of energy in a deformable, unbounded continuum. Several techniques may be adopted to solve this problem including the so-called *infinite* elements that are a particular formulation of finite elements characterized by shape functions describing a displacement field which attenuate exponentially with the distance. Alternative methods include the introduction of non-reflecting boundaries (e.g. using local, consistent or integral formulation) or absorbing layers like PML (*Perfectly Matched Layer*). The adsorbing boundaries act as transmitting surfaces and reflections of the outwardly propagating waves are avoided (Figure 6).

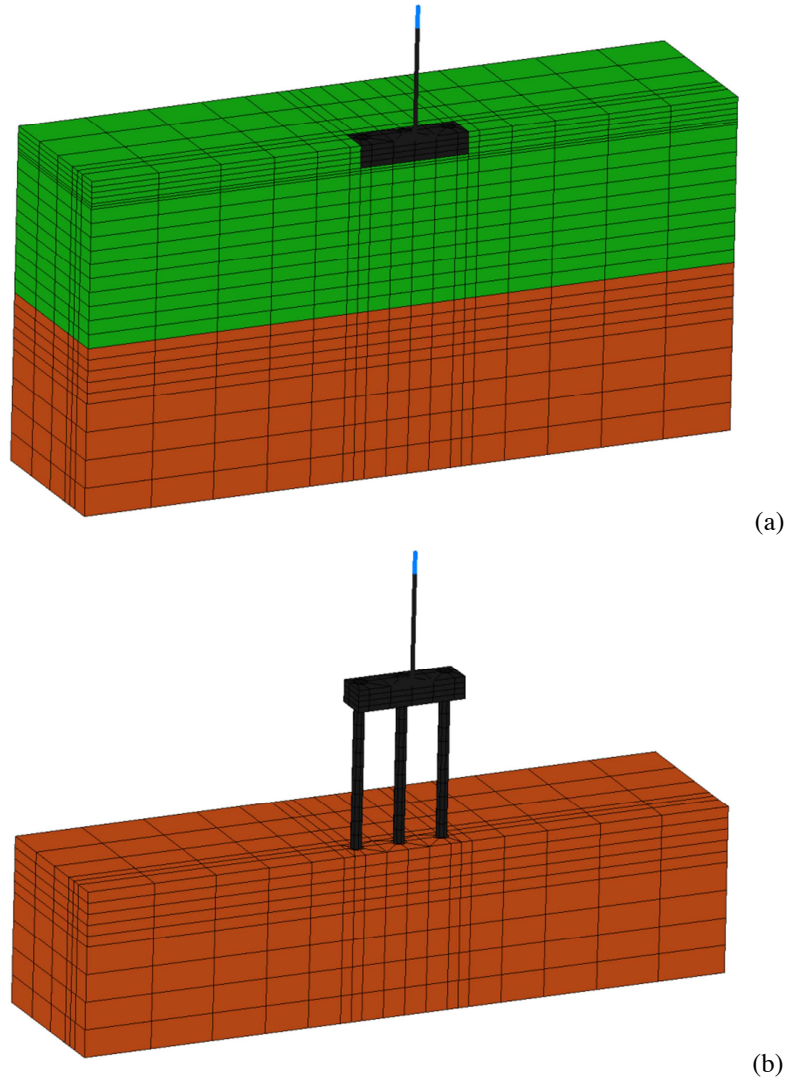


Figure 5: Example of using the direct approach to model SSI for a bridge pier on piled-raft foundation. (a) Two-layer soil deposit: soft top layer (green colour) overlying a stiff layer (brown colour). (b) Model view without top layer. (from [Mar12])

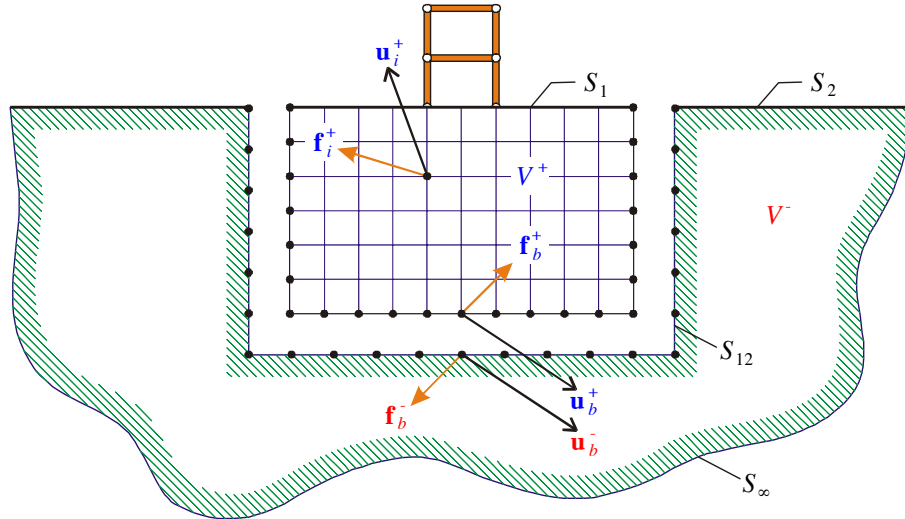


Figure 6: Boundary conditions imposed along the artificial borders of the model to simulate the radiation of energy in a deformable, unbounded continuum (from [And04])

Despite the presence of the artificial boundaries, accurate calculations require the model to have a significantly large volume of soil next to the structure. As a result, the number of degrees of freedom of the combined soil-structure system is very large. Furthermore, the need to capture the response of the soil and of the structure at relatively large frequencies, requires a very fine discretization of the system which in turn implies an extraordinary computational effort, especially for 3D non-linear analyses. For this reason, the direct approach is not routinely used in the engineering practice and when it happens only for very important projects.

3.2. Substructure approach

The substructure approach or *indirect* method of analysis is a technique by which a SSI problem is solved by decomposing the superstructure-foundation-soil system into two subsystems whose response is determined independently, separating the effects caused by kinematic interaction from those due to inertial interaction. The response of the overall system is then obtained from the application of the superposition's theorem [Kau74].

Despite a rigorous application of the substructure approach is restricted only to linear or linear-equivalent systems, data from the literature show that the superposition of the effects of kinematic and inertial interaction assessed independently, is a reasonable engineering approximation also in cases where the response of soils is expected to be moderately non-linear (for example: [Myl97] and [CLT99]).

From a design and practical standpoint, the substructure approach is routinely used for the computation of the foundation loadings due to external as well as earthquake excitation. The method is computationally affordable and quite flexible as it does not require a re-implementation of the whole steps of the procedure should the changes occur only in the superstructure. The complete seismic response of the superstructure-foundation-soil system is computed through the implementation of the following three steps (Figure 7):

1. solution of the kinematic interaction (KI) problem, that is assessing the modifications of the seismic wavefield induced by the presence of the foundation with respect to the free-field ground motion. This task allows to compute the so-called “*Foundation Input Motion*” (FIM) which is in general different from the free-field motion because the stiffness mismatch between the foundation and the surrounding soil makes the foundation unable to comply with the free-field soil deformation pattern;
2. calculation of the frequency-dependent, dynamic impedance matrix representing the dynamic response of the soil-foundation subsystem which is considered detached from the superstructure (Figure 7). The dynamic impedance matrix is complex-valued and in general fully populated because of the coupling existing between the six degrees of freedom of the foundation (three translational and three rotational). The real part of the elements of the impedance matrix reflect the compliance of the soil-foundation system and it may be represented by a spring with a frequency-dependent coefficient. The imaginary part captures the two forms of energy dissipation occurring in the soil as the foundation vibrates. They are represented by geometric or radiation damping and material attenuation due to the inelasticity of the ground when subjected to dynamic loading. A dashpot with a frequency-dependent coefficient may be used to denote the imaginary part of the dynamic impedance. Various analytical and numerical methods exist to compute all the elements of the impedance matrix. A brief account of some of these methods will be given in the next sections;
3. calculation of the dynamic response of the whole system constituted by the superstructure, the foundation and the surrounding soil subjected to the FIM computed at the step 1 above. This analysis is carried out by connecting the finite element model of the superstructure with the foundation-soil subsystem through the frequency-dependent, dynamic impedance matrix computed at the step 2 above. Inertial interaction is taken into account in this step. The dynamic analysis of the whole system may be carried out using the so-called Response Spectrum Method (RSM) or the Time-History Method (THM). Because of the frequency-dependence of the dynamic impedance matrix, the analysis is carried out iteratively.

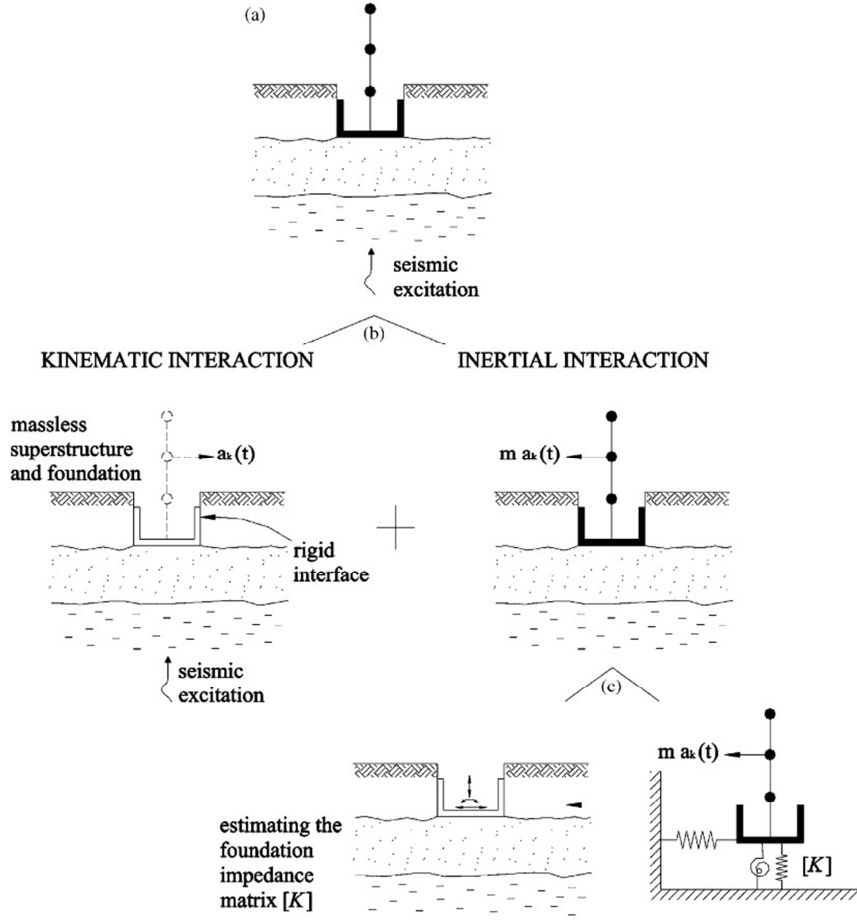


Figure 7: SSI using the substructure approach. (a) geometry of SSI problem; (b) decomposition of the problem into kinematic and inertial response; (c) two step analysis of inertial interaction (from [Myl06])

In step 1 above, it can be shown that the FIM due to kinematic interaction alone, can be computed by assuming a massless foundation and a massless superstructure (Figure 7). Thus, the equation of motion can be written as follows:

$$M_{soil}\ddot{u}_{kin} + Ku_{kin} = -M_{soil}\ddot{u}_{base} \quad (7)$$

where \ddot{u}_{base} represents the input motion applied at the base of the model, M_{soil} is the mass matrix of the global system (i.e. superstructure-foundation-soil) after having assumed equal to zero the mass of the foundation and the mass of the superstructure, K is the stiffness matrix of the global system and u_{kin} is the vector of kinemat-

ic displacements that gives the FIM (*Foundation Input Motion*). The response of the global system (accounting for inertial interaction) is computed by solving the following equation:

$$M_{total}\ddot{u}_{in} + Ku_{in} = -M_{structure}(\ddot{u}_{base} + \dot{u}_{kin}) \quad (8)$$

where $M_{structure}$ is the mass matrix of the global system assuming the soil to be massless, $(\ddot{u}_{base} + \dot{u}_{kin})$ represents the FIM and u_{in} is the vector of inertial displacements relative to the base motion.

A prove of the correctness (for linear systems) of the substructure approach is given by the following equation which combines the superposition of the effects represented by Eq. (7) and (8):

$$M_{total}\ddot{u}_{in} + M_{soil}\ddot{u}_{kin} + K[u_{kin} + u_{in}] = -[M_{soil} + M_{structure}]\ddot{u}_{base} - M_{structure}(\dot{u}_{kin}) \quad (9)$$

and, since $[u_{kin} + u_{in}] = u_{total}$ and $M_{soil} + M_{structure} = M_{total}$, the equation get converted into the original equation of motion (6), namely:

$$M_{total}\ddot{u}_{in} + M_{soil}\ddot{u}_{kin} + Ku_{total} = -M_{total}\ddot{u}_{base} - M_{structure}(\dot{u}_{kin}) \quad (10)$$

$$M_{total}\ddot{u}_{in} + [M_{soil} + M_{structure}]\ddot{u}_{kin} + Ku_{total} = -M_{total}\ddot{u}_{base} \quad (11)$$

$$M_{total}\ddot{u}_{total} + Ku_{total} = -M_{total}\ddot{u}_{base} \quad (12)$$

It's worth noticing that the FIM (Foundation Input Motion), in particular for embedded foundations, may include a non-negligible rotational part. Ignoring it, may lead to gross unconservative errors particularly in tall, slender structures [Vel75]. However, if the foundation dimensions are small compared to the characteristic wavelength (determined from the frequency range of interest), the kinematic interaction has negligible effects in the response.

As shown in Figure 7, the inertial interaction response is obtained in two steps: the first one is devoted to the computation of the dynamic impedance matrix associated with each mode of vibration. The second step consists in calculating the seismic response of the superstructure connected to the ground by means of the dynamic impedance matrix. Six are the modes of vibration: three translational (displacements along axes x, y and z) and three rotational (rotations around the same axes).

3.3. Macro-elements

The main limitation of the substructure approach is the assumption of linearity of the overall soil-structural system required for the application of Kausel's superposition theorem [Kau74]. Nonlinearities in SSI may arise in a variety of ways, from

geometrical non-linearity occurring along soil-structure interfaces, to soil non-linear hydromechanical response to nonlinear constitutive behaviour of structural materials. Non-linear effects may significantly influence the overall response of a structure sitting on the ground and they are likely to occur under both static and dynamic loadings. For instance sliding at the soil-foundation interface can occur in shallow foundations if the horizontal force exceeds the soil-foundation frictional resistance. In deep foundations, pile-soil gaps and relative displacement can also occur along the shaft. Other examples include foundation uplift which occurs if the overturning moment yields tensile stresses at the soil-foundation interface. Under strong earthquakes, foundation uplift can significantly modify the seismic response of slender structures. The bearing capacity mechanism is also characterized by non-linear effects such as permanent displacements and rotations induced in shallow foundations, particularly during earthquake loading. The capacity design principles in structural engineering (see [Pau92]) allow the development of plastic hinges in the structural elements of the superstructure to reduce the seismic demand with respect to that of the elastic response. However to prevent geotechnical failure, large, widespread nonlinearities at the soil-foundation interface are not acceptable except perhaps for a limited amount of sliding and rotation. This may be beneficial to the overall structural response as it may reduce the seismic demand and avoid over-sized foundations.

The inherent inability of the substructure approach to take into account strong nonlinear effects, poses severe restrictions upon the applicability of this technique for the solution of nonlinear SSI problems. For shallow foundations, an approach that can be adopted to overcome the above limitations and that have had a moderate success is the so-called *Beam-on-Non-linear-Winkler-Foundation* (BNWF) method. This approach is based on replacing the soil by a continuous distribution of independent, non-connected, nonlinear springs characterized by an appropriate constitutive relation (see for example Harden et al. 2005 [Har05]). Energy dissipation due to both radiation and material damping can be accounted for by introducing a continuous distribution of dashpots. The BNWF method is unable to properly take into account the coupling among the various degrees of freedom of the system. Furthermore, the spring and dashpot parameters of the non-linear constitutive relations should be frequency-dependent and their determination is non-trivial.

An alternative, innovative approach to account for non-linear effects in SSI which is having considerable success, is that associated with the notion of *macro-element*, where the whole soil-foundation system is replaced by a single element at the base of the superstructure having in general *six* and *three* degrees of freedom (DOFs) for three-dimensional and two-dimensional problems respectively. The macro-element can properly describe foundation response under horizontal, vertical and rotational loadings. The first application of the concept of macro-element in geotechnical engineering was made by Nova and Montrasio in 1991 [Nov91] who proposed a new method to compute the settlements of a strip foundation (i.e. a 2D plane strain problem) on cohesionless soils and quasi-static monotonic loading. In their work the authors represented the loading by a set of generalized forces which induced a set of generalized displacements of the foundation (Figure 8). Incremental, constitutive equations formally similar to the ones used in rate-independent plasticity theory,

were then introduced to link the generalized forces to the generalized displacements. In the formulation of the macro-element, the overall domain of the SSI problem is divided into two sub-domains: the first one is named “*far-field*” and it refers to the portion of soil that is distant from the soil-foundation-structure. In the far-field, the nonlinearities induced by the soil-foundation interaction are assumed to be negligible. The second sub-domain, called “*near-field*”, identifies the portion of the soil close to the foundation where the response is characterized by strong nonlinearities.

The notion of macro-element was first applied to seismic loadings by Paolucci in 1997 [Pao97] who adopted the same soil type and foundation configuration of Nova and Montrasio [Nov91] to study the response of a structure subjected to dynamic loading taking into account non-linear SSI. In this work the superstructure was represented by a single-degree-of-freedom mass. Cremer et al. in 2001 and 2002 [Cre01, Cre02] proposed the first application of the macro-element for purely cohesive soils with no resistance to tensile stresses. A recent review of existing macro-element models for shallow foundations is illustrated in Chatzigogos et al. in 2009 [Cha09], Figini et al 2012 [Fig12] and in Grange 2013 [Gra13].

For the strip foundation, the macro-element formulation requires the definition of a set of generalized force and displacement vectors \underline{Q} and \underline{q} respectively (Figure 8). They are usually written in dimensionless form as follows:

$$\underline{Q} = \begin{bmatrix} \xi \\ h \\ m \end{bmatrix} = \frac{1}{V_{max}} \begin{bmatrix} V \\ H \\ M/B \end{bmatrix} \quad (13)$$

$$\underline{q} = \begin{bmatrix} \eta \\ \varepsilon \\ \zeta \end{bmatrix} = \frac{1}{B} \begin{bmatrix} v \\ u \\ B\theta \end{bmatrix} \text{ displacement} \quad (14)$$

where v , u and θ represent the vertical displacement, the horizontal displacement and the rotation respectively; V_{max} is the maximum normal force applied at the foundation system under pure vertical loading; V , H and M are respectively the vertical force, the horizontal force and the moment. Finally B is the foundation width. The generalized force and displacement increments are related through a generalized non-dimensional stiffness matrix C_{ep} :

$$\underline{\dot{Q}} = C_{ep} \underline{\dot{q}} \quad (15)$$

This stiffness matrix C_{ep} is usually fully populated because of the coupling effect between forces and displacements. The standard elasto-plasticity theory (or alternative theories like hypo-plasticity) can be used to compute each element of C_{ep} . The reader can refer to the work of Salciarini and Tamagnini [Sal09] as the first macro-element for shallow foundations on sands that has been developed based on the theory of hypoplasticity.

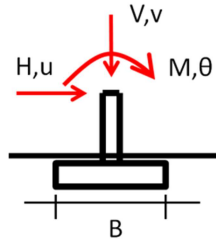


Figure 8: Macro-element formulation: generalized forces and displacements in case of a strip (shallow) foundation.

For piled foundations, macro-elements have been developed for connecting each node of the pile to the corresponding node of the soil in the far-field (free-field conditions). Taciroglu et al. (2006) [Tac06] and Rha & Taciroglu (2007) [Rha07] developed a macro-element for piles subjected to quasi-static loading conditions whereas Boulanger et al. (1999) [Bou99], Curras et al. (2001) [Cur01], Gerolymos & Gazetas (2006) [Ger06a],[Ger06b] and Varun (2010) [Var10] for dynamic loadings. Figure 9 below shows the macro-element developed by Varun (2010) for piles in liquefiable sites, which take into account the pore pressure build-up.

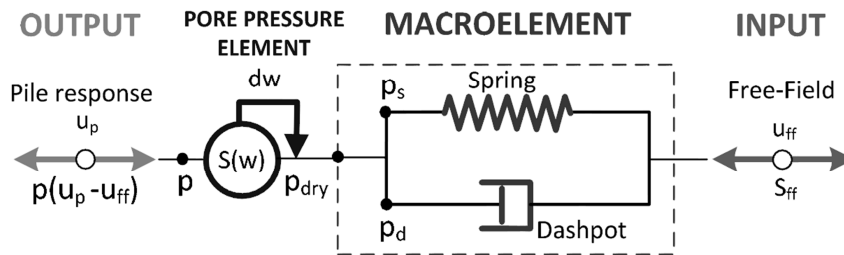


Figure 9: Macro-element formulation: sketch showing the various components for an application to pile foundations in liquefiable soils (from [Var10]).

4. Dynamic impedance functions (DIF)

4.1. Construction of DIF for shallow foundations

The key aspect of dynamic soil-structure interaction is the calculation of the force-displacement relationship at the nodes along the soil-structure interface. Under the assumption of linear soil response, rigid and mass-less foundation, the displacement of each node of the soil-structure interface, can be computed from the dynamic

response of the global foundation system. For such a system, the steady-state response to harmonic external forces and moments can be computed once the matrix of dynamic impedance functions $S(\omega)$ is determined for the frequency (ω) of interest.

For each particular frequency of excitation, the dynamic impedance is defined as the ratio between the applied force (or moment) $F(t)$ [or $M(t)$] and the resulting steady-state displacement (or rotation) $u(t)$ [or $\theta(t)$] at the centroid of the base of the mass-less foundation. For example, for the vertical mode of oscillation (Figure 10), the harmonic force $F(t)$ and the displacement $u(t)$ can be written, using the complex number formalism, as follow:

$$F_z(t) = \bar{F}_z e^{i\omega t} \quad (16)$$

$$u_z(t) = \bar{u}_z e^{i\omega t} \quad (17)$$

where \bar{u}_z and \bar{F}_z are in general complex-valued numbers. The dynamic impedance is defined as by the following relation [Gaz91a]:

$$S_z(\omega) = \frac{F_z(t)}{u_z(t)} \quad (18)$$

$$S_z(\omega) = \bar{K}_z + i\omega\bar{C}_z \quad (19)$$

where in general \bar{K}_z and \bar{C}_z are function of frequency. The term \bar{K}_z is the *dynamic stiffness* and represents the stiffness and inertia of the soil. The dashpot coefficient \bar{C}_z reflects the phenomenon of energy dissipation in the ground which is composed by two contributions. The first is the *radiation damping* generated by the spreading of the waves away from the excited foundation over increasingly large volume of soil. The second form of energy dissipation is due to the inelasticity of the soil which is called *material damping*.

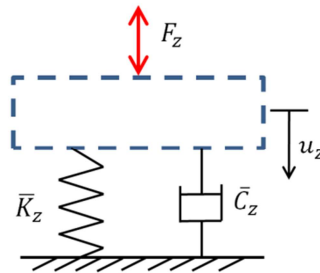


Figure 10: Dynamic impedance function for a vertically oscillating mass-less foundation (*modified from [Gaz91a]*)

The dynamic impedance functions associated to the other modes of vibration may be derived by following a similar approach, as it was shown by Gazetas [Gaz91a, Gaz91b]. Overall, in a shallow foundation there are a total of six different dynamic impedances corresponding to the six degrees of freedom (DOFs) which characterize its motion (Figure 11). The coefficients associated to the main diagonal of the dynamic impedance matrix are defined as follows:

1. S_z = vertical impedance for the motion acting in the vertical direction;
2. S_y = transversal swaying impedance for horizontal motion in the short direction;
3. S_x = longitudinal swaying impedance for horizontal motion in the long direction;
4. S_{rx} = rocking impedance for rotational motion around the x-axis;
5. S_{ry} = rocking impedance for rotational motion around the y-axis;
6. S_t = torsional impedance for rotational oscillation around the vertical axis (z)

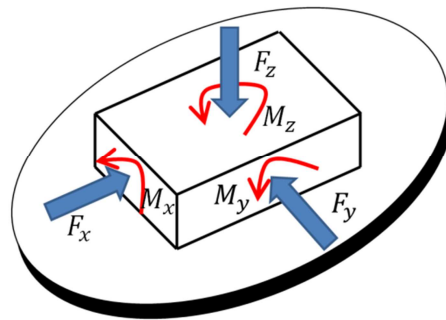


Figure 11: Modes of vibration of a shallow foundation and associated DOFs (*modified from [Gaz91a]*)

In foundations embedded into the ground the 6×6 dynamic impedance matrix is a non-diagonal matrix because some DOFs of the foundation are cross coupled, for example swaying and rocking oscillations (Figure 12). This happens because the centroid of the foundation cannot be approximated with the corresponding point at the base. Any base reaction due to the application of an horizontal force at the centroid of the foundation generates a moment that induce rotation and vice versa. Therefore, the off-diagonal terms of the dynamic impedance matrix include two more coefficients called *cross-coupled horizontal-rocking* impedances. They are usually negligible in shallow foundations but their magnitude becomes more significant at large depths of embedment.

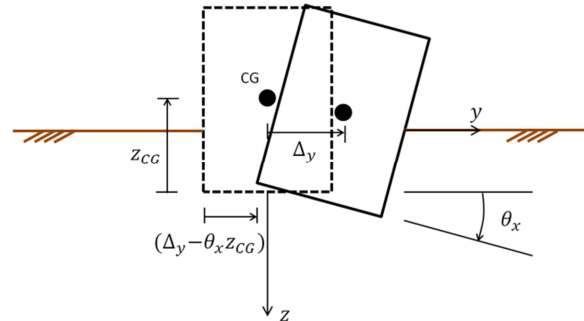


Figure 12: Cross-coupling between horizontal and rocking modes of oscillation
(modified from [Gaz91a])

The dynamic impedance matrix of a shallow or embedded foundation can be derived from *analytical solutions* which are available for simple foundation geometries and soil models (see for instance the works by Veletsos and Wei, 1971 [Vel71]; Luco, 1974 [Luc74]; Kausel and Roesset, 1975 [Kau75]; Luco, 1976 [Luc76]; Wong and Luco, 1976 [Won76]; Kausel and Ushijima, 1979 [Kau79] just to name a few of them). Alternatively, it can be calculated through advanced numerical modeling using the boundary-element method, the finite element method and hybrid methods which combine analytical and finite-element approaches. However nowadays these methods are adopted to directly solve a given SSI problem with the so-called direct approach (see Section 3.1) which makes the computation of the dynamic impedance matrix a superfluous exercise particularly in case of nonlinear analyses. A more practical approach would be that of using empirical correlations that have been developed based on rigorous and approximate analytical solutions and on the results of advanced numerical analyses (see Gazetas, 1991 [Gaz91a]). Computer programs implementing these solutions have also been made available (e.g. Novak et al., 1994 [Nvk94]). Section 4.3 will illustrate an original approach that has also been proposed to derive analytical dynamic impedance functions based on certain physical approximations that simplify the mathematical formulation of the problem.

4.2. Construction of DIF for pile foundations

The dynamic impedance functions of piled foundations are calculated from the impedance functions of a single pile which are modified through appropriate (dynamic) interaction coefficients to take into account the so-called *group effects*. The dynamic response of a head-loaded pile has been studied in the literature and the state-of-the-art paper by Novak [Nvk91] provides a comprehensive overview on the subject.

The dynamic impedances at the pile head may be derived using three different approaches: the *viscoelastic continuum* formulation, *advanced numerical techniques* and the *modified Winkler method*. In the viscoelastic continuum formulation the pile is embedded in a soil deposit idealized as a homogeneous, isotropic, elastic half-space. Radiation damping in this method is automatically taken into account in the

imaginary part of the pile impedance function. However, this approach is only applicable to viscoelastic materials and the nonlinear behavior of soils can only approximately taken into account using strain-compatible deformability parameters.

Advanced numerical techniques such as the Finite Element Method (FEM), the Boundary Element Method (BEM) or the Finite Difference Method (FDM), can be used in a manner similar to that described in the previous Section for the construction of dynamic impedance functions for shallow and embedded foundations.

The modified Winkler method is a modification of the standard Winkler model originally proposed by Winkler in 1867 [Win67] in which he considers that the deflection at any point of the soil in contact with the pile is linearly related to the corresponding contact pressure at that point (Figure 13). In the Winkler model the soil is assumed to have negligible shear stiffness and shear resistance. As a result, soil reaction along the shaft maybe considered equivalent to that of a continuous distribution of disconnected springs with constant K_h (Figure 13). In the modified Winkler model the springs may be characterized by a nonlinear, frequency dependent, constitutive relations. In addition dashpots may be added in parallel to the springs to represent energy dissipation (i.e. radiation and material damping). The method and its generalization is also known as the *Beam-on-Non-linear-Winkler-Foundation* (BNWF) technique and it was briefly mentioned in Section 3.3 when discussing the macro-element concept for shallow foundations.

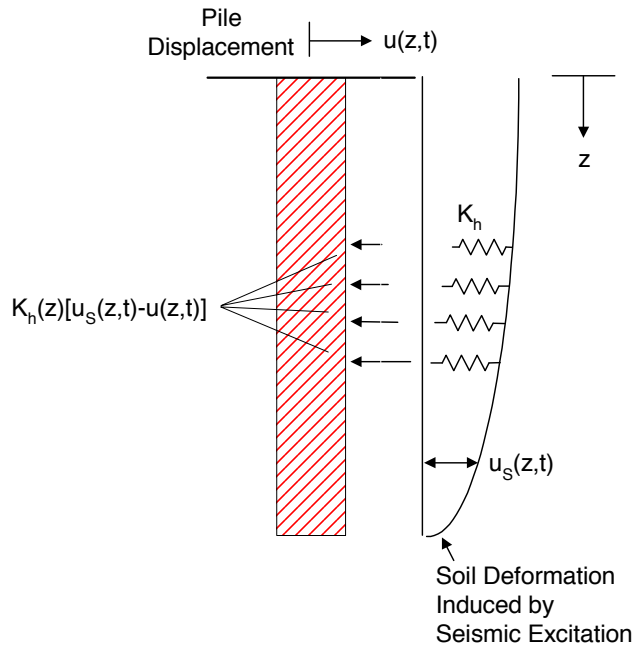


Figure 13: Dynamic pile-soil interaction using the Winkler soil model.

The main drawback of the BNWF model is the lack of connectivity within the soil mass caused by the assumption of negligible shear stiffness and strength. This implies that the soil reaction at one point is not influenced by the pressure at other points. However, the BNWF model has been widely used in the engineering practice because it is simple to implement, it is familiar to structural engineers and to a certain extent, it can take into account soil non-homogeneity and nonlinearity.

Gazetas (1991) [Gaz91a] presented very useful graphs and tables containing simple, empirical formulas for the computation of the dynamic impedance of a single pile for different soil models. The formulas are valid only for “flexible” piles, that is piles with length larger than the *active length* defined as the length along the pile in which the displacement is non-negligible.

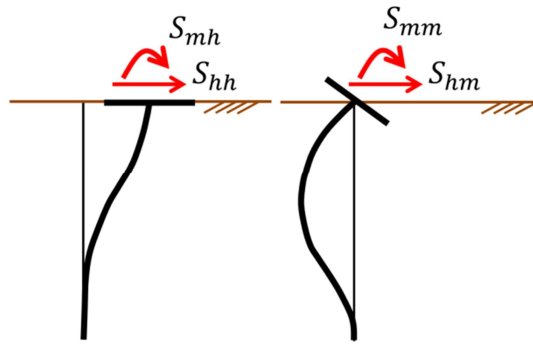


Figure 14: Pile head dynamic impedances as defined by Gazetas (*modified from* [Gaz91a])

In this formulation, the dynamic impedances for the single pile, shown in Figure 14, are assumed to have the following expression:

$$S(\omega) = \bar{K} + i\omega\bar{C} \quad (20)$$

where \bar{K} is the “dynamic” stiffness of the pile that and it is expressed as the product of the static stiffness K and a dynamic coefficient \bar{k} , assumed as a function of frequency:

$$\bar{K}(\omega) = K \cdot \bar{k}(\omega) \quad (21)$$

The global damping coefficient is composed of two parts, reflecting the contributions of radiation and material damping. It is given by the following relation:

$$\bar{C}_{total}(\omega) = \bar{C}_{radiation}(\omega) + 2\bar{K}(\omega)\xi/\omega \quad (22)$$

where ξ is the soil hysteretic damping coefficient.

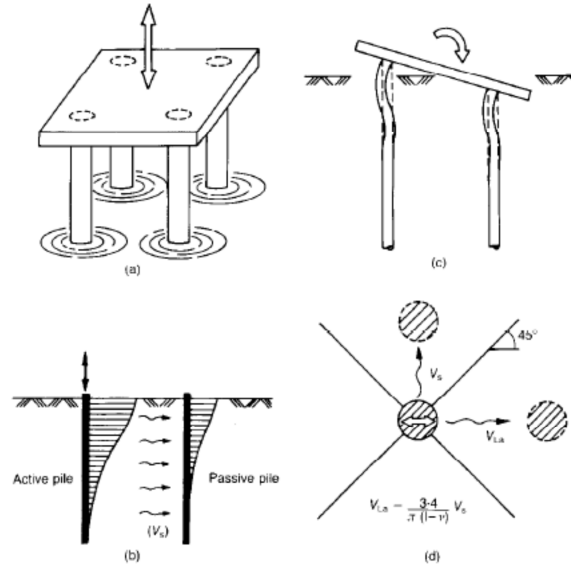


Figure 15: Simple analytical solution developed by Dobry & Gazetas (1988) to the problem of dynamic pile-soil-pile interaction in uniform soils: (a) analogy between the cylindrical wave assumption for group of piles and cylindrical water waves; (b) distribution of displacement amplitudes along the shaft of an active and a passive pile; (c) pile head deformation and reactions during rocking; (d) waves radiating from a laterally oscillating pile (*from* [Dob88]).

Gazetas (1991) remarks that the real difficulty in using the above formulas is the selection of the proper soil profile and strain-compatible shear modulus for the soil. In fact, even considering a uniform soil deposit, the shear modulus will depend on the magnitude of the induced shear strain. Moreover, phenomena of geometric non-linearity like gap formation at the soil-pile interface close to the ground surface, may also occur, and this further complicates the analysis.

Another complication to the problem is the calculation of the dynamic impedance of a group of piles from the knowledge of the impedance of a single pile to account for pile-to-pile and soil-to-pile interaction. In fact, the dynamic impedance of a group of piles in any mode of vibration cannot be computed by simply adding the impedances of the individual piles, because each pile in addition to its own loadings, is affected by the response of the neighboring piles transmitted through transversal and longitudinal waves.

The pile-to-pile and soil-to-pile interaction is frequency-dependent and the interaction coefficients can be determined by adopting the *Poulos' superposition approach* (Poulos and Davis, 1990 [Pou90]) extended to dynamic loading. By this approach the response of the pile group is obtained through the introduction of ap-

appropriate interaction coefficients derived from the study of only two piles at a time. Dynamic impedances have been computed by Kaynia and Kausel in 1982 [Kan82] through rigorous approaches (using the boundary element method). Dobry and Gazetas (1988) [Dob88] (see Figure 15) and Makris and Gazetas (1992) [Mak92] provided a very simple analytical solution by using the results obtained by Wolf [Wol94] to the problem of dynamic pile-soil-pile interaction in uniform soils for vertical and horizontal modes of deformation. Lastly, Mylonakis (1995) [Myl95] extended this work to layered soil conditions.

4.3. Construction of DIF using the cone model

An original approach to define approximate relations for the dynamic impedance functions of shallow and deep foundations has been proposed by Wolf (1994) [Wol94]. It is named the *cone model approach* because it is based on replacing the soil deposit, for each degree of freedom of the foundation, by a truncated semi-infinite elastic cone with the apex located at a height z_0 from the ground surface (Figure 16). The cone is assumed homogeneous, linear-elastic, with mass density ρ . Initially material damping is neglected. The stress-strain relationship is specified by two independent elastic constants (e.g. the shear modulus G , and the Poisson ratio ν). The foundation is idealized by a rigid, circular, mass-less disk with area A_0 and radius r_0 which imposes a displacement pattern in the material beneath.

With the cone model the complicated, exact formulation of three-dimensional elasto-dynamics is replaced by a simple, (strength of materials approach) one-dimensional description of the kinematics like assuming that plane sections remain plane. Figure 16 shows both translational and rotational cones that can be used to compute the vertical, horizontal, rocking and torsional dynamic responses of a shallow foundation.

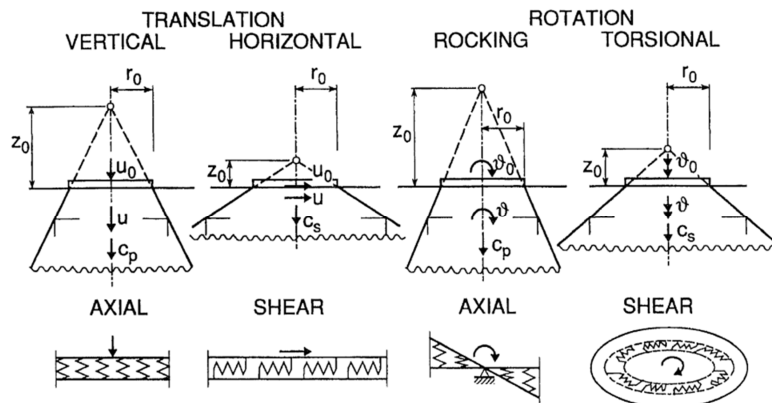


Figure 16: Representation of the cone models associated to various modes of vibration (from [Wol94]).

For each degree of freedom, only one type of body wave is postulated to exist: for horizontal and torsional motions, S-waves propagating with the shear-wave velocity whereas for vertical and rocking motions, P-waves propagating with the velocity of longitudinal P waves.

For example, the vertical response of a rigid, circular, mass-less disk with area A_0 and radius r_0 , placed on a semi-infinite, perfectly linear elastic material (no internal damping), can be obtained through the cone model represented in Figure 17. In the figure u represents the axial displacement, N the axial force, c denotes the appropriate velocity of longitudinal waves, ρ the mass density and ρc^2 is the corresponding constrained modulus. Writing the equation of motion of an infinitesimal element of cone taking into account the inertial forces, leads to:

$$-N + N + \frac{\partial N}{\partial z} dz - \rho A dz \frac{\partial^2 u}{\partial z^2} = 0 \quad (23)$$

Substituting the force-displacement relationship:

$$N = \rho c^2 A \frac{\partial u}{\partial z} \quad (24)$$

leads to the one dimensional wave equation in the zu variable:

$$\frac{\partial^2 (zu)}{\partial z^2} - \frac{\partial^2 (zu)}{\partial t^2 c^2} = 0 \quad (25)$$

For harmonic loading with frequency of excitation ω , the response is given by $u(t) = u(\omega)e^{i\omega t}$, and substituting $\ddot{u}(\omega) = \omega^2 u(\omega)$ in the previous equation, leads to:

$$\frac{\partial^2 (zu(\omega))}{\partial z^2} - \frac{\omega^2}{c^2} \frac{\partial^2 (zu(\omega))}{\partial t^2} = 0 \quad (26)$$

The interesting solution of Eq. (26) is that corresponding to outward propagating waves. In fact because of the radiation condition the inward propagating waves may be neglected. Thus the solution is:

$$u(\omega) = C_1 \frac{z_0}{z} e^{-i\frac{\omega}{c}(z-z_0)} \quad (27)$$

where C_1 is the integration constant. Enforcing the boundary conditions $u(\omega)|_{z=z_0} = u_0(\omega)$ and computing the global force $F_0(\omega)$ acting on the rigid disk, yields:

$$F_0(\omega) = -N(\omega)|_{z=z_0} = -\rho c^2 A_0 \frac{\partial u(\omega)}{\partial z} |_{z=z_0} = [\bar{K} + i\omega \bar{C}] u_0(\omega) \quad (28)$$

where $K = \frac{\rho c^2 A_0}{z_0}$ and $C = \rho c A_0$ are respectively the spring and damping coefficients. Introducing the dimensionless frequency parameter a_0 defined as:

$$a_0 = \frac{\omega r_0}{c_s} \quad (29)$$

where c_s is the shear wave velocity, the dynamic impedance can be rewritten as a function of the static stiffness K and the dimensionless parameter a_0 as follows:

$$S(a_0) = K[\bar{k}(a_0) + i a_0 \bar{c}(a_0)] \quad (30)$$

where in general $\bar{k}(a_0)$ and $\bar{c}(a_0)$ are function of a_0 however for this particular example the corresponding values are constant and equal to $\bar{k}(a_0) = 1$ and $\bar{c}(a_0) = \frac{z_0 c_s}{r_0 c}$.

It is worth noticing that the damping coefficient represents the dissipation of energy by radiation of the waves through infinity. The other source of energy dissipation is the material damping that to first approximation may be considered frequency independent because it involves frictional energy losses. It can be introduced into the solution for harmonic loading by multiplying the elastic constants by the factor $1 + 2i\xi$ where ξ is the material damping ratio.

The opening angle (z_0/r_0) of the cone is determined by equating the static-stiffness coefficient of the cone to that of a disk on a half-space determined using the three-dimensional theory of elasticity. In case of nearly-incompressible materials (i.e. materials with a Poisson's ratio larger than 1/3), the model is still applicable if the velocity of longitudinal waves is limited to twice the shear-wave velocity and a trapped mass and mass moment of inertia are introduced for the vertical and rocking degrees of freedom, respectively.

Cone models can also be used to simulate the dynamic response of foundations resting on a half-space composed of several soil layers, in which reflected waves and refracted waves are taken into account through the introduction of their own cone. Fixed and free boundary conditions as well as embedded foundations may also be represented. The interested reader is referred to the already cited work by Wolf [Wol94].

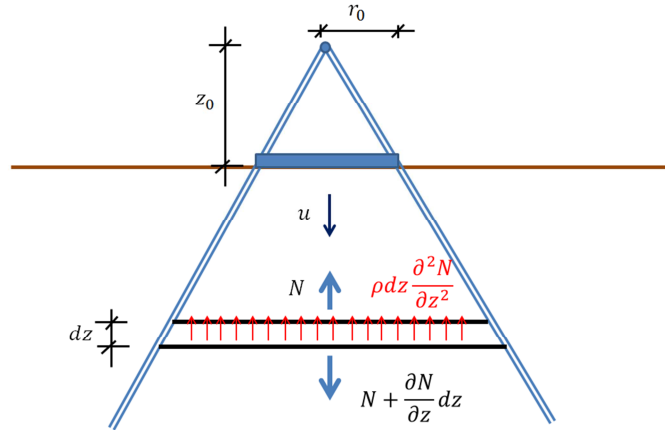


Figure 17: Vertical response of a rigid, circular, mass-less disk using the cone model (modified from [Wol94]).

5. Applications using the substructure approach

In the following Sections two applications of SSI analysis are presented. The first one involves the seismic design of the foundation of EUCENTRE shake table in Pavia, Italy, which is the Europe most powerful shake table. The second example concerns with the seismic demand assessment of a prestressed concrete viaduct whose foundations are constituted by large diameter shafts. The evaluation of seismic response of large-diameters shafts is important for the dynamic behavior of bridge piers.

5.1. Design of shake table foundation at EUCENTRE

The high-performance of the shaking table at EUCENTRE has forced the designers to face the challenging problem of having a large reaction mass to control and possibly reduce the vibrational impact of the table. Therefore detailed analyses had to be performed in order to solve a complex dynamic soil-structure interaction problem.

In the area of study, geotechnical investigation campaign was carried out to define the stratigraphy and the static and dynamic properties of the soil deposit, such as the shear wave velocity profile illustrated in Figure 18.

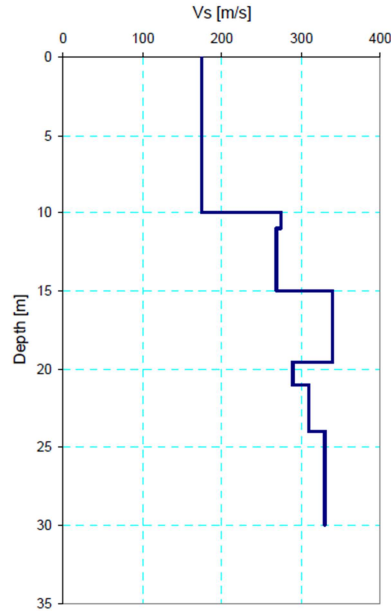


Figure 18: Shear wave velocity profile used for design. (from [Cal05])

The configuration shown in Figure 19 refers to a rigid block formed by the reaction mass and an additional mass constituted by 3.0 meters of concrete that have been added to the original precast system increasing the overall weight of the reaction mass.

The evaluation of the dynamic response of the shaking table and the foundation/soil mass has been performed through a three DOFs lumped mass model. A rigid block placed over a deformable and dissipative ground under harmonic and transient excitations was used to model the behavior of the dynamic testing facility.

Considering the uniaxial motion of the shaking table, the three DOFs shown in Figure 20 are: x-displacement (horizontal), z-displacement (vertical) and rotation in the x-z plane. These three DOFs may be defined either with reference to the centroid G or with respect to the center of the soil-structure interface O. The equation of motion is:

$$Ku = F \quad (31)$$

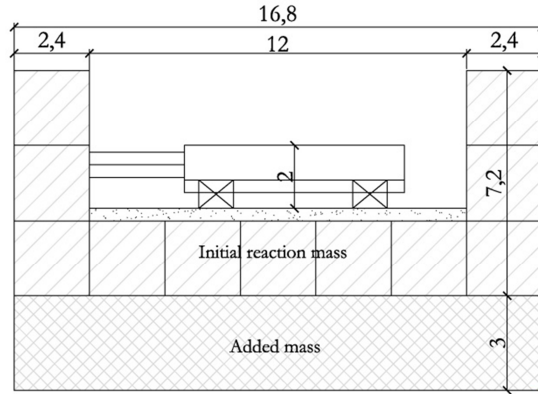


Figure 19: Competing configurations studied for the reaction mass/foundation design of the EUCENTRE shaking table. (from [Cal05])

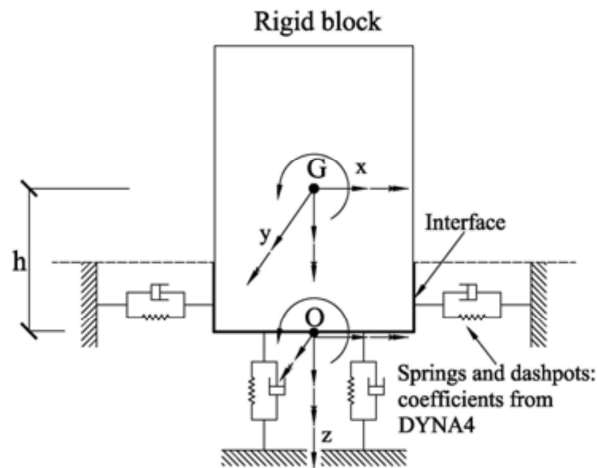


Figure 20: Lumped model of the reaction mass/foundation for the EUCENTRE dynamic facility (from [Cal05])

where K is a symmetric complex-valued matrix and it represents the dynamic impedance matrix defined as:

$$K = K_F - \omega^2 M \quad (32)$$

where K_F is the impedance matrix of the mass-less foundation and M is the mass matrix of the block:

$$K_F = \bar{K} + i\omega\bar{C} \quad (33)$$

The stiffness \bar{K} and the damping coefficient \bar{C} are frequency-dependent functions obtained using the computer code DYNA4 [Nvk94] for the frequency range 0-20Hz. They are plotted in Figure 21 and Figure 22. The impedance functions refer to the case of a rectangular footing base resting on the surface of a shallow, non-uniform layer (top shear wave velocity of 200 m/s, bottom $V_S = 300$ m/s).

Figure 21 shows the stiffness and damping coefficients for both vertical and horizontal motion whereas Figure 22 shows the contributions of the rocking around the y-axis and of the coupling between the rotation and the horizontal motion of the rigid block. Once the dynamic impedance matrix K is computed, the solution of the equation of motion is represented by the complex-valued displacement z-components, x-component and the rotation in the x-z plane of the rigid block. They are shown in Figure 23 and Figure 24.

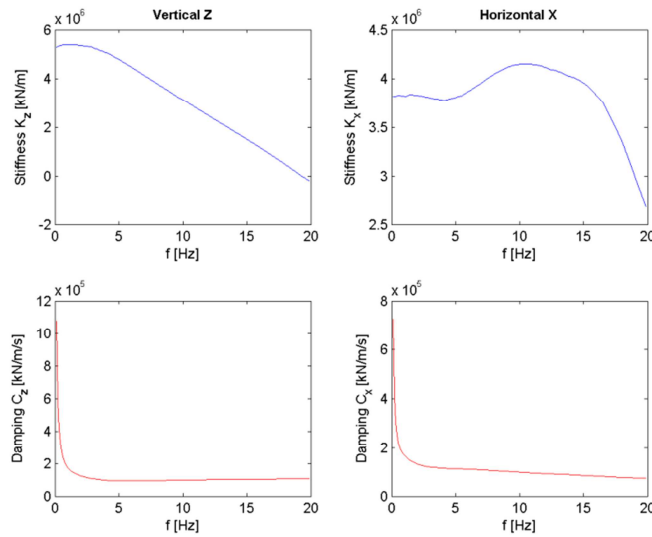


Figure 21: Dynamic Impedance Functions (DYNA4): stiffness and damping coefficient for vertical and horizontal motion (*from* [Cal05])

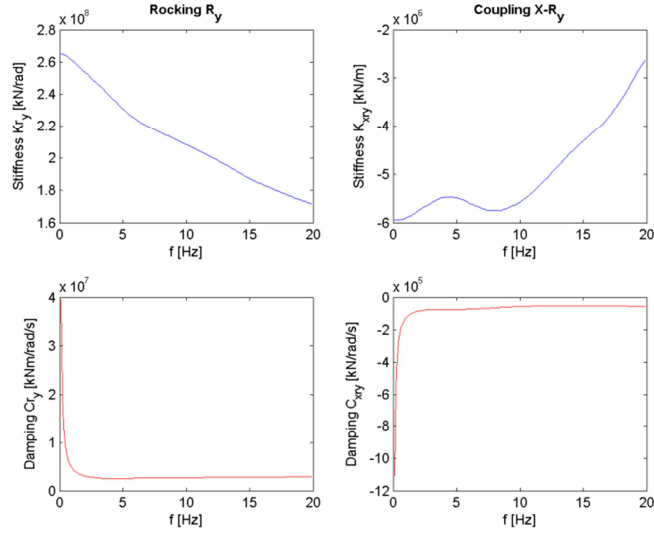


Figure 22: Dynamic Impedance Functions (DYNA4): stiffness and damping coefficient for rocking and coupled motion (*from* [Cal05])

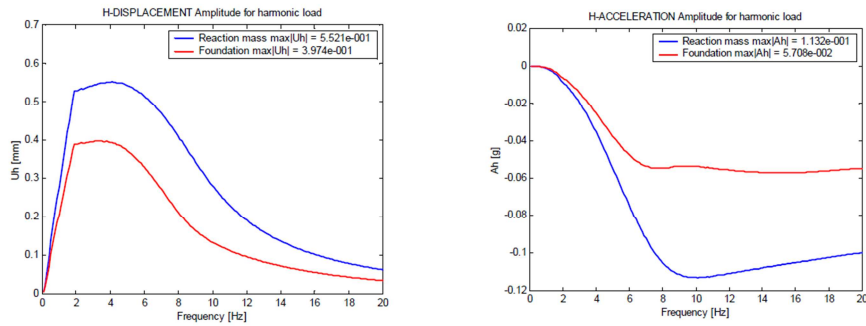


Figure 23: Response functions related to the horizontal DOF (harmonic excitations) of the 3.0 m thick rigid foundation (*from* [Cal05])

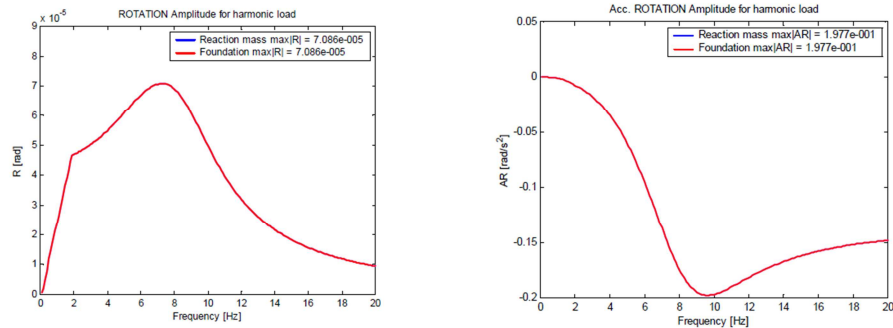


Figure 24: Response functions related to the rotational DOF (harmonic excitations) of the 3.0 m thick rigid foundation (*from* [Cal05])

The foundation response was then assessed for earthquake loading. The strong-motion records were chosen with the criterion of reproducing the excitation that would be used in carrying out the experimental tests with the shaking table on a scaled (1:3-1:2) bridge pier specimen. The reader is referred to Pavese et al. [2004] [Pav04] for the geometrical data and reinforcement details of the full-scale bridge pier. The time-histories of base shear and overturning moment from the analysis of the short bridge pier S250 specimen under the Coalinga ground motion are shown in Figure 25. The horizontal acceleration and displacement time-histories are illustrated in Figure 26 with reference to both the base and the centroid of the reaction mass.

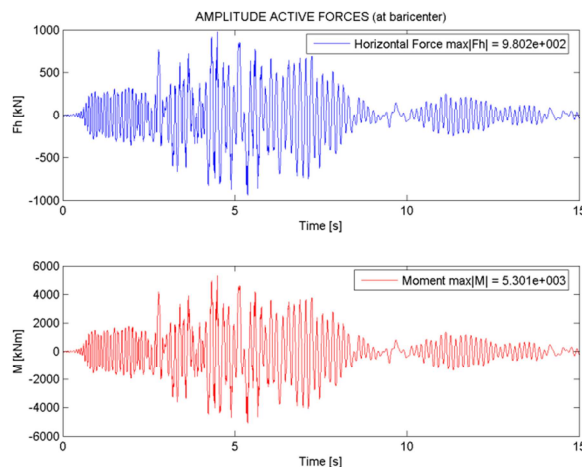
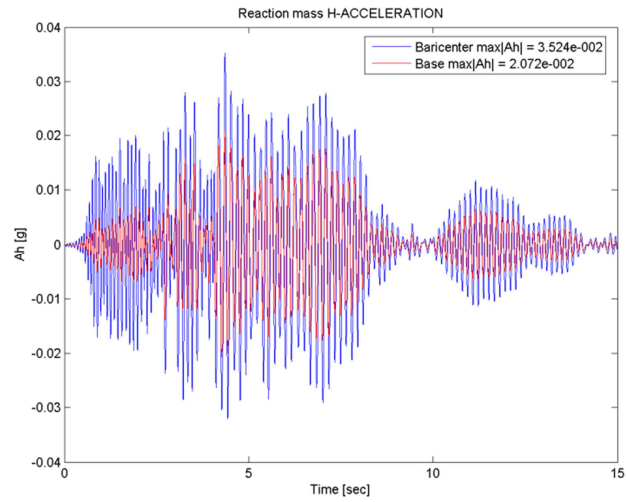
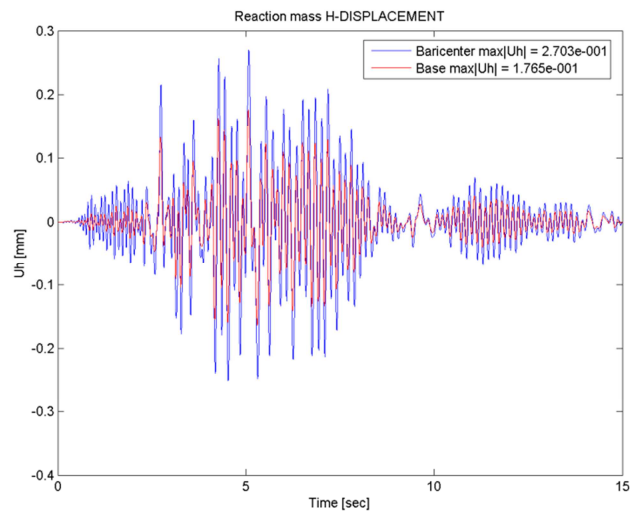


Figure 25: Excitation action time-histories (at the centroid of the reaction mass): Coalinga Earthquake, scaled 1:2 bridge pier S250 (*from* [Cal05])



(a)



(b)

Figure 26: Response functions related to the translational DOF (Coalinga earthquake): (a) horizontal acceleration, (b) horizontal displacement (*from* [Cal05])

5.2. Kinematic interaction effects of large-diameter shafts foundations

The rigorous assessment of seismic SSI of a structure founded on deep foundations is an extremely complicated problem and the difficulties are mainly represented by the evaluation of kinematic interaction and scattering effects generated by the foundation system. The study illustrated in the following, summarizes the work done by Beltrami et al. [Bel05] in trying to evaluate the kinematic interaction effects and the FIM (Foundation Input Motion) at the base of a prestressed-concrete viaduct founded on large-diameter shaft foundations. These are essentially rigid cylinders that are not expected to induce very large nonlinearities in the surrounding soil during seismic shaking; therefore, they are well suited to be studied within the framework of the superposition's theorem and the substructure approach.

The basic assumptions made in the study concerning the geometry of the foundation and soil constitutive model are as follows: (i) rigid circular cylinder of radius R embedded in a soil layer of constant thickness H and infinite extent in the horizontal plane (no topographic effects); (ii) the soil is modeled as a linear viscoelastic material with frequency-independent properties, and the damping and shear modulus are strain-compatible with the level of excitation by a preliminary equivalent-linear response analysis of the stratum; (iii) both the base of the cylinder and the layer are considered to undergo a space-invariant, uniform horizontal motion.

Furthermore the soil was assumed to deform according to the plane-stress hypothesis as it was originally proposed by Veletsos and Younan in 1995 [Vel95] for a better representation of the displacement field around a large-diameter pile. Their solution is based on the classical Baranov-Novak (BN) idealization of the medium, where the soil is represented by a series of independent thin layers with a circular hole placed at the center of the system. The shear stiffness of each thin layer is given by its dynamic impedance K . In the far-field the BN layers behave as a cantilever shear beam. The basic idea of the constrained layers is to add at each BN thin layer a system of mass-less linear springs (elastic constraints) equally directed along the two horizontal radial u and circumferential v directions (Figure 27). Finally, a rotational and horizontal displacement impedance are added at the base of the shaft to represent the effect of deformable supporting layer rather than fixed base conditions.

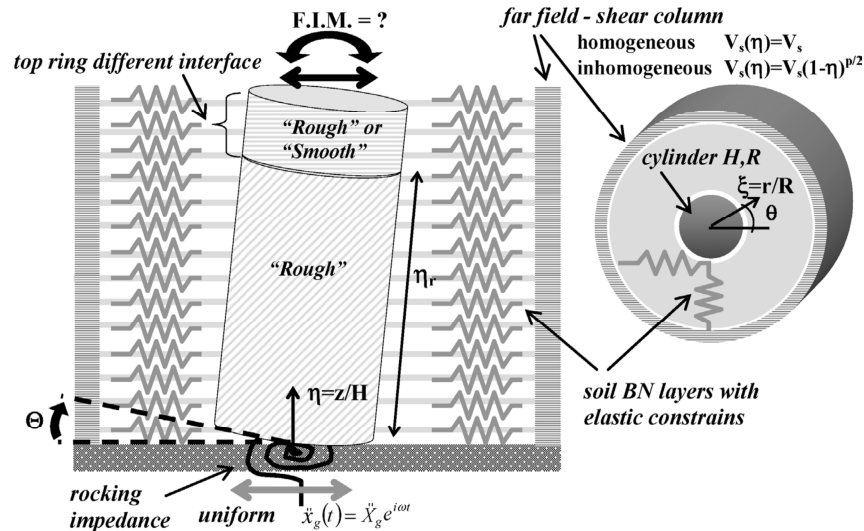


Figure 27: Schematic view of the model used to study the soil-foundation kinematic interaction problem (from [Bel05])

Afterwards, such analytical model has been validated through a benchmark test conducted with the finite element code SASSI [SAS99] and it was used to perform dynamic soil-structure-interaction analyses of the bridge foundations.

Figure 28 shows the longitudinal view of the bridge of balanced cantilever girder type forming a continuous segmental pre-stressed concrete deck of 110m spans. The bridge is symmetrical with respect to the central mid-span and crosses a wide valley characterized by the presence of a soft top soil stratum of variable thickness overlaying the bedrock. The piers have heights of 75m, 50m to 30 m, connected with large-diameter shaft foundations passing through the soil layer and founded on the top of the bedrock roof.

The dynamic response of the bridge is used to study the effects of seismic Soil-Foundation-Structure Interaction (SFSI) by means of the *substructuring approach* which assumes the validity of the Kausel's superposition theorem through the evaluation of the kinematic and inertial interaction (as discussed in Section 3.2). The effects of soil deformability and energy dissipation occurring in the soil surrounding the foundations have been evaluated through a set of complex-valued, frequency-dependent, dynamic impedance functions computed for all degrees of freedom of the nodes at the base of the piers using the computer code DYNA4 [Nvk94]. The inertial interaction has been carried out by performing linear, dynamic transient analysis of the bridge through the finite element program ADINA [ADI03] where the Foundation Input Motion (FIM) has been previously computed using the kinematic interaction model for large-diameter shafts.

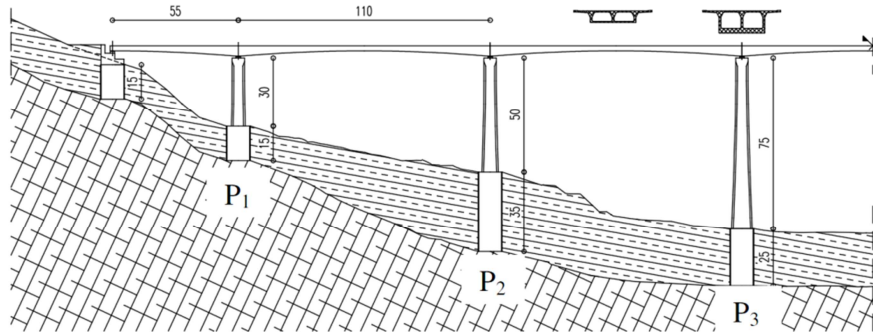


Figure 28: Longitudinal view of the viaduct used to study soil-foundation-structure interaction and longitudinal section of the foundation subsoil. (from [Bel05])

The main objective of this study was to evaluate the importance of the contribution of coupled swaying-rocking FIM excitation in the seismic demand assessment of the bridge. This was carried out through a comparison of the internal actions (i.e. axial and shear forces, bending and torsional moments) at the base of the piers computed initially considering the only translational component of motion and, afterwards, even the coupled swaying-rocking components of motion.

The first observation that came out was that the expected increase in the first natural period of the structure (T_1) resulting from the soil deformability is almost negligible ($T_1 = 2.5$ sec) with respect to the one fixed at the base of each pier ($T_1 = 2.4$ sec). This happened because the large-diameter shaft foundation with the surrounding soil forms a relatively rigid system that restrains the deformability of the structure at its base as if the bridge foundations were clamped.

Figure 29 and Figure 30 illustrate the internal actions at the base of each pier obtained from the linear, dynamic, transient analysis of the bridge. They have been computed for each of the four values of shear wave velocity V_S that have been considered for the soil layer surrounding the foundation shafts. The figures show that in all cases the effect induced by coupled swaying-rocking excitation is to increase the seismic demand of the piers in terms of both bending and torsional moments, and shear and axial forces. This effect is more pronounced for the longitudinal components which is the direction where the piers are more constrained and the structure behaves as a frame. These frame actions induce a large increase of longitudinal base moment demand that can reach up to + 40% in the tallest piers.

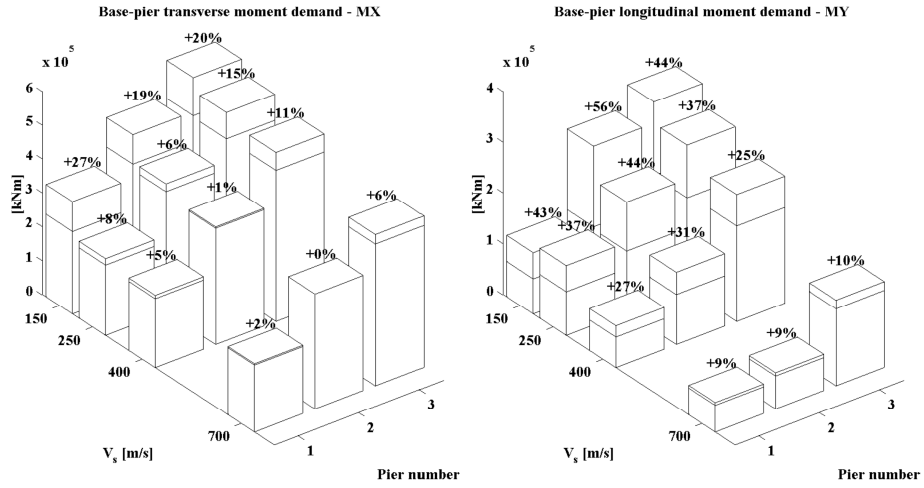


Figure 29: Transverse (MX) and longitudinal (MY) base-pier moment demand: The percentages shown indicate the increment induced by coupled swaying-rocking excitation. (from [Bel05])

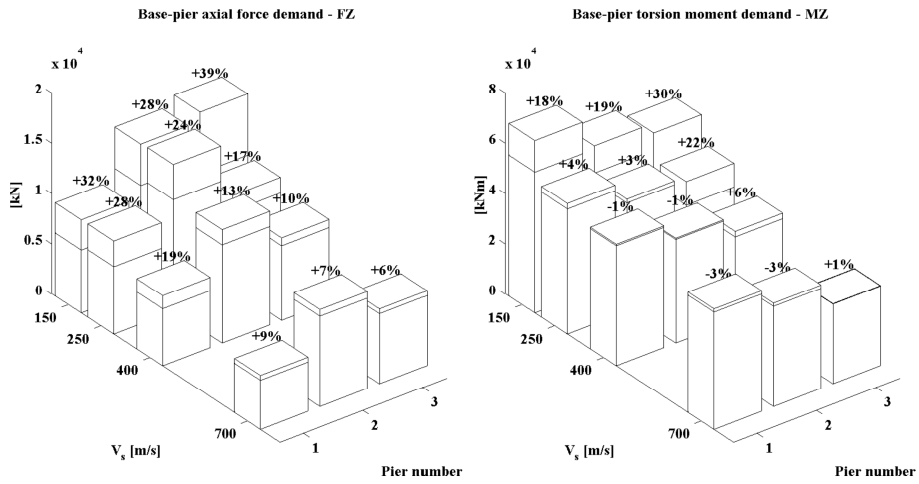


Figure 30: Axial force (FZ) and torsion (MZ) base-pier demand: The percentages shown indicate the increment induced by coupled swaying-rocking excitation. (from [Bel05])

References

- [ADI03] ADINA 900. User's Manual, Automatic Dynamic Incremental Nonlinear Analysis — Version 8.0, K.J. Bathe — ADINA R & D Inc, USA. nodes version 2003
- [And04] L. Andersen. *Elastodynamics and finite element analysis in wave propagation problems*. Course notes. Department of Civil Engineering. Aalborg University. Denmark. 2004
- [ATC96] Applied Technology Council (ATC). Seismic Evaluation and Retrofit of Concrete Buildings ATC-40. Volume 1 and 2, November 1996.
- [Bel05] C. Beltrami, C.G. Lai, A. Pecker. A kinematic interaction model for a large-diameter shaft foundation. An application to seismic demand assessment of a bridge subject to coupled swaying-rocking excitation. *Journal of Earthquake Engineering Vol. 9, Special Issue 2* 355–393. 2005
- [Bou99] R.W. Boulanger, C.J. Curras, B.L. Kutter, D.W. Wilson, A. Abghari. Seismic soilpile-structure interaction experiments and analyses, *J Geotech Geoenviron*, 125, 750-759. 1999
- [Byc56] G.N. Bycroft. Forced vibration of a rigid circular plate on a semi-infinite elastic space and on an elastic stratum. *Philosophical Transactions of the Royal Society of London, Series A*, 248, 327–368. 1956
- [Cal05] G.M. Calvi, A. Pavese, P. Ceresa, F. Dacarro, C.G. Lai and C. Beltrami. Design of a Large Scale Dynamic and Pseudo-Dynamic Testing Facilities. Research Report No. ROSE-2005/04. pp.194. 2005
- [CLT99] CALTRANS. Seismic Soil-Foundation-Structure Interaction. Final Report, Prepared by The Caltrans Seismic Advisory Board — Ad Hoc Committee on Soil-Foundation-Structure Interaction, California Department of Transportation, Sacramento (CA), USA. 1999
- [Cha09] C.T. Chatzigogos, A. Pecker, J. Salencon. Macroelement modeling of shallow foundations. *Soil Dynamics and Earthquake Engineering* 29 765–781. 2009
- [Cre01] C. Cremer, A. Pecker, L. Davenne. Cyclic macro-element for soil-structure interaction: material and geometrical nonlinearities. *Int J Num Anal Methods Geomech*;25:1257–84. 2001
- [Cre02] C. Cremer, A. Pecker, L. Davenne. Modelling of non linear dynamic behavior of a shallow strip foundation with macroelement. *J Earthquake Eng* 6(2): 175–211. 2002

- [Cur01] C.J. Curras, R.W. Boulanger, B.L. Kutter, D.W. Wilson, Dynamic experiments and analyses of a pile-group-supported structure, *J Geotech Geoenviron*, 127, 585-596. 2001
- [Dob88] R. Dobry, G. Gazetas. Simple method for dynamic stiffness and damping of floating pile groups. *Geotechnique* 38, 4, 557-574. 1988
- [Fig12] R. Figini, R. Paolucci and C. T. Chatzigogos. A macro-element model for non-linear soil–shallow foundation–structure interaction under seismic loads: theoretical development and experimental validation on large scale tests. *Earthquake Engng Struct. Dyn.* 41:475–493. 2012
- [Gaz91a] G. Gazetas. *Foundations vibrations*. Foundation engineering handbook, H. Y. Fang, ed., Chap. 15, pages 553-592, Van Nostrand Reinhold, New York. 1991
- [Gaz91b] G. Gazetas. Formulas and Charts for impedances of surface and embedded foundations. *ASCE, Journal of Geotechnical Engineering*, Vol. 117, No. 9, September, 1991
- [Gaz00] G. Mylonakis, G. Gazetas. Seismic Soil-Structure Interaction: Beneficial or Detrimental?, *Journal of Earthquake Engineering* 4 277-301. 2000
- [Ger06a] N. Gerolymos, G. Gazetas. Development of Winkler model for static and dynamic response of caisson foundations with soil and interface nonlinearities, *Soil Dyn Earthq Eng*, 26, 363-376. 2006
- [Ger06b] N. Gerolymos, G. Gazetas. Static and dynamic response of massive caisson foundations with soil and interface nonlinearities - validation and results, *Soil Dyn Earthq Eng*, 26, 377-394. 2006
- [Gra13] S. Grange. Simplified modeling strategies for soil-structure interaction problems: The macroelement concept. Lecture notes ALERT Doctoral School 2013. 3th-5th October 2013, Aussois, France. Soil-Structure Interaction. Coordination: P. Kotronis, C. Tamagnini, S. Grange.
- [Har05] C. Harden, T. Hutchinson, G. R. Martin and B. Kutter. Numerical Modeling of the Nonlinear Cyclic Response of Shallow Foundations. PEER Report. 2005
- [Kan82] A.M. Kaynia and E. Kausel. Dynamic Stiffness and seismic response of pile groups. *Research Report R82-03, Massachusetts Institute of Technology*, 1982
- [Kau74] E. Kausel and J. M. Roesset. Soil–structure interaction problems for nuclear containment structures, Electric Power and the Civil Engineering, in: *Proceedings of the ASCE Power Division Conference, Boulder, Colorado*, 1974

- [Kau75] E. Kausel and J. M. Roesset Dynamic stiffness of circular foundations. *J. Engrg. Mech. Div., ASCE*, 101(6), 771-785.1975
- [Kau79] E. Kausel and R. Ushijima. Vertical and torsional stiffness of cylindrical footings. Research Report R7-6, M.I.T., Cambridge, Mass. 1979
- [Kau10] E. Kausel. Early history of soil-structure interaction. *Soil Dynamics and Earthquake Engineering* 30,822-832. 2010
- [Luc74] J.E. Luco. Impedance functions for a rigid foundation on a layered medium. *Nuclear Engineering and Design*, 31, pp. 204-217. 1974
- [Luc76] J.E. Luco. Vibration of a rigid disk on a layered viscoelastic medium. *Nuclear Engineering and Design*, 36, pp. 325-340. 1976
- [Mak92] N. Makris and G. Gazetas. Dynamic pile-soil-pile interaction. Part II: lateral and seismic response. *Earthq. Eng. Str. Dyn.* 21, 145-162. 1992
- [Myl95] G. Mylonakis. *Contributions to static and seismic analysis of piles and pile-supported bridge piers*. PhD dissertations, State University of New York at Buffalo, 1995
- [Myl97] G. Mylonakis and A. Nikolaou. Soil-Pile-Bridge Seismic Interaction: Kinematic and Inertial Effects. Part I: Soft Soil. *Earthquake Engineering and Structural Dynamics*, Vol.26, 337-359. 1997
- [Myl06] G. Mylonakis, S. Nikolaou, G. Gazetas. Footings under seismic loading: Analysis and design issues with emphasis on bridge foundations, *Soil Dynamics and Earthquake Engineering*, 26: 824-853. 2006
- [Nov91] R. Nova and L. Montrasio. Settlements of Shallow foundations in Sand. *Geotechnique* 41 (2), 243-256. 1991
- [Nvk91] M. Novak. Piles under dynamic loads: state of art. *Proc. 2nd int. conf. on recent advances in geotech. Earthquake eng. and soil dyn. St. Louis*, vol 3, 2433-2456. 1991
- [Nvk94] M. Novak, M. Sheta, L. El-Hifnawy, H. El-Marsafawi and O. Ramadan. DYNA4 a computer program for calculation of foundation response to dynamic loads. Report No. GEOP 93-01, User Manual, Vols. I and II, Geotechnical Research Centre, The University of Western Ontario, London, Ontario, Canada. 1994
- [Pao97] R. Paolucci. Simplified evaluation of earthquake induced permanent displacements of shallow foundations. *Journal of Earthquake Engineering*, 1, Issue 3, 563-579, 1997

- [Pou90] H.G. Poulos and E.H. Davis. *Pile Foundation Analysis and Design*. Krieger Publ. 410 pp. 1990
- [Pau92] T. Paulay, M.J.N Priestley. *Seismic Design of Reinforced Concrete and Masonry Structures*. John Wiley & Sons, New York. 1992
- [Pav04] A. Pavese, C.G. Lai, G.M. Calvi, P. Ceresa and C. Beltrami. Reaction mass and foundation of the high-performance, one-degree-of-freedom EUCENTRE shaking table, in Pavia, Italy, *Proceedings of the First International Conference on Advances in Experimental Structural Engineering, Nagoya, Japan*. 2004.
- [Qui53] P.M. Quinlan. The elastic theory of soil dynamics. *In: Symposium on Dynamic Testing of Soils, Special Technical Publication 156, ASTM, pp.3–34*. 1953
- [Rei36] E. Reissner. Stationäre, axialsymmetrische, durch eine schüttelnde Masse erregte Schwingung eines homogenen elastischen Halbraum. *Ingenieur-Archiv*, VII (6), 381–396, 1936.
- [Rei37] E. Reissner. Freie und erzwungene Torsionsschwingungen des elastischen Halbraumes. *Ingenieur-Archiv*, VIII.Band,4.Heft.S229–S245, 1937.
- [Rha07] C. Rha, E. Taciroglu. Coupled macroelement model of soil-structure interaction in deep foundations, *J Eng Mech-Asce*, 133, 1326-1340. 2007
- [Sal09] D. Salciarini, C. Tamagnini. A hypoplastic macroelement model for shallow foundations under monotonic and cyclic loads. *Acta Geotechnica* 4(3), 163-176. 2009
- [SAS99] SASSI 2000. User's Manual, A System for Analysis of Soil-Structure Interaction — Revision 1. 1999
- [Sez35a] K. Sezawa and K. Kanai. Decay in the seismic vibration of a simple or tall structure by dissipation of their energy into the ground. *Bulletin of the Earthquake Research Institute, Japan*, 13, 681–696, 1935.
- [Sez35b] K. Sezawa and K. Kanai. Energy dissipation in seismic vibration of a framed structure. *Bulletin of the Earthquake Research Institute, Japan*, 13, 698-714, 1935.
- [Sez35c] K. Sezawa and K. Kanai. Energy dissipation in seismic vibration of actual buildings. *Bulletin of the Earthquake Research Institute, Japan*, 13, 925–941, 1935.
- [Sun53] T.Y. Sung. Vibration in semi-infinite solid due to periodic surface loadings. *In: Symposium on Dynamic Testing of Soils, Special Technical Publication 156, ASTM, pp.35–54*. 1953

- [Tac06] E. Taciroglu, C. Rha, J.W. Wallace, A robust macroelement model for soil-pile interaction under cyclic loads, *J Geotech Geoenviron*, 132 1304-1314. 2006
- [Var10] V. Varun. *A non linear dynamic macroelement for soil structure interaction analyses of piles in liquefiable sites*. PhD dissertations, pp 172, Georgia Tech, 2010
- [Vel71] A.S. Veletsos, Y.T. Wei. Lateral and rocking vibration of footings. *Journal of the Solid Mechanics and Foundation Division, ASCE*, 97, No SM-9, pp. 1227-1248. 1971
- [Vel75] A.S. Veletsos, V.V. Nair. Seismic interaction of structures on hysteretic foundations. *J. Struct. Eng. ASCE* 101 (1), 109-129, 1975
- [Vel95] A.S. Veletsos and A.H. Younan. Dynamic modelling and response of rigid embedded cylinders. *Journal of Engineering Mechanics ASCE* 121(9) September. 1995
- [Win67] E. Winkler. *Die Lehre von Elastizitat und Festigkeit* (On Elasticity and Fixity). Dominicus, Prague. 1867
- [Wol94] John P. Wolf. *Foundation vibration analysis using simple models*. Prentice Hall. pp.423. 1994
- [Won76] H. L. Wong and J. E. Luco. Dynamic response of rigid foundations of arbitrary shape. *Earthquake Eng. and Struct. Dynamics*, 4, 579-587. 1976

Centrifuge Modelling of foundations subjected to cyclic loading

Luc Thorel

LUNAM University, IFSTTAR, GERS Dpt., Earthworks and Centrifuge Lab., Route de Bouaye, CS4, 44344 Bouguenais Cedex, France.

Soil-structure interaction is one of the main topics that may be studied using centrifuge modeling technique. Small-scale models of instrumented foundation subjected to cyclic loading at the required g-level give data for a better understanding of several configurations of loading. An overview of centrifuge modeling and its limitations are presented in the first part, including the scaling laws and the scale effects. Then experiments performed in the IFSTTAR geo-centrifuge are presented. The case of a building founded on shallow foundation in clay and subjected to horizontal loading is a first attempt to simulate the effect of an earthquake. The last part is about deep foundations installed in sand, subjected to vertical or horizontal cyclic loading. In each example the experiment is detailed and some illustrative results are presented.

1 Introduction

Foundations subjected to a non-monotonic loading needs special attention during their design, because of a lack of design rules (only [API11] and [DNV77] take into account cyclic loading). The Eurocode 7 [NFE05, §2.4.2] mention that loads applied in a repetitive way and loads with a variable intensity must be identified in order to be considered in a specific way with regard to continuation of motion, soil liquefaction and changes of stiffness and resistance of the soils.

The French Standard devoted to deep foundation [NFP12] does not take into account the behavior of deep foundation subjected to cyclic loading, but it is suggested to refer to specialized literature and, when the intensity of the cyclic load is significant, to consider the possibility to decrease progressively the soil resistance due to fatigue phenomenon.

The wider knowledge on foundations subjected to cyclic loading has been historically developed by the off-shore industry with its specific needs. More recently, the development of wind-turbines, especially near-shore or off-shore, open a new field

of application where potentially deep foundations may be subjected to complex cyclic loading. A recent state of the art has been done for off-shore piles [Jar12].

In parallel to this new orientation, a French National Program has been launched for the study of piles subjected to cyclic loading: PN SOLCYP [Pue08, Pue12, SOL13]. This R&D project has been conducted to: 1) understand the physical phenomena conditioning the response of piles to vertical and horizontal cyclic loads; 2) develop advanced design method; 3) initiate pre-normative development of methodologies. The PN SOLCYP has included a multi tool approach with in field tests, laboratory soil characterization, small scale physical modeling at $1\times g$ and under microgravity in the geo-centrifuge, and numerical modeling.

Centrifuge modeling of foundations subjected to cyclic loading is presented here from the basics of physical modeling in geo-centrifuge to applications performed in the IFSTTAR geo-centrifuge.

2 Centrifuge modelling

The idea to test a small scale model in a centrifuge dates from 1869, when Edouard Phillips [Phi69] described the principles of the methodology and established the main scaling laws that link the small scale model to the full-scale structure. The first experiments [Gar01, Tho02, Tho08] date back to the 1930's. The development of experimental techniques for use in centrifuges has followed a scenario built by both the means available and the time required to produce instrumentation devices. As emphasized by Bachelard [Bac86], *the various ages of a science can be identified by the technique inherent in its measurement instruments*. Without necessarily ascribing the word science, advances in centrifuge-based physical modeling can be divided in four major phases: model observation before and after testing; instrumented models (correlated with the development of electronics); in-flight use of models; and lastly, in conjunction with the advent of robotics, the organization of model testing sequences without having to stop the centrifuge [Der03].

Physical modeling with a centrifuge is a widespread technique in the geotechnical field, as can be observed when consulting the proceedings from three Centrifuge symposia held periodically since 1988 [Cor88; Kim98; Ko91; Leu94; Ng06; Phi02; Spr10]. This technique makes it possible to reproduce *in situ* stresses in a small scale model, and from a practical standpoint, all types of geotechnical structures are capable of being studied on reduced-scale models. Centrifuge testing has proved its efficiency in conducting extensive series of tests, as it allows a large range of parameters to be varied while keeping associated costs relatively low, when compared to *in situ* testing [Cra88].

2.1 Scaling laws

The full-scale geotechnical model, named prototype (P) and the small scale model (M) are linked together through scaling laws [e.g. Cor89, Gar07], deduced from equilibrium equations. The main scaling factors $X^* = X^M / X^P$ used for foundations are listed in Table 1, in which N is the centrifuge acceleration or ‘g-level’.

The reproduction of both the stress and strain levels on the small scale model, similar to the one existing on the prototype, is an important advantage of this technique. Especially whatever is the nature of the material behavior (linear, non-linear, elastic, elasto-plastic...), it will be correctly reproduced on the small scale model by applying the required g-level.

The centrifugal acceleration ($\omega^2 R$) depends on both the angular rotation speed ω and radius R at which the model is positioned. It is useful to work with large-radius centrifuges ($\geq 5\text{m}$) in order to minimize acceleration gradients within the modeled soil mass. Such a set-up also make possible to work on relatively large reduced-scale models with respect to the size of instrumentation.

Table 1: Scaling factors

Parameter	Scaling Factor
Length, Displacement	$l^* = 1/N$
Density	$\rho^* = 1$
Acceleration (centrifugal and seismic)	$g^* = N$
Stress, Pressure	$\sigma^* = 1$
Force	$F^* = 1/N^2$
Mass	$m^* = 1/N^3$
Energy	$E^* = 1/N^3$
Time (dynamic)	$t^* = 1/N$
Frequency	$f^* = N$
Strain	$\varepsilon^* = 1$
Bending stiffness	$(EI)^* = 1/N^4$

2.2 Scale and size effects

The size reduction applied to a small scale model generates two types of problems that would not be encountered if the size of the tested geotechnical structures was not modified: the “size effect” and the “scale effect”.

The “size effect” is clearly linked to the size of the geotechnical work. For physical modeling in a centrifuge, it corresponds to the differences in the results obtained for several prototypes tested. In other words [Cor89], if the value of a dimensionless parameter is a function of one of the characteristic dimensions of the structure, all other things being equal (including the gravity field), there will be a “size effect”. A classic illustration [Ove79] is provided by the bearing capacity coefficient: “the larger the prototype diameter, the smaller the bearing capacity and the less tendency

to peak”. In figure 1, size effect may be observed by using models and g-levels located on a diagonal line descending to the right. The “scale effect” is observed if, for the simulation of the same prototype, the results at the prototype scale are different. This should be the case of models located on the diagonal ascending to the right on figure 1. The comparison of such models is known as the “modeling of models technique” [Sch80], which is specific to centrifuge modelling. The existence of scale effect is mainly due to the fact that it is more convenient to use the same soil in the centrifuge model than for the prototype. The ratio between the size of the model foundation and the grain size needs to be large enough in order to avoid scale effect (table 2). It is also said that there may be a “grain size effect”.

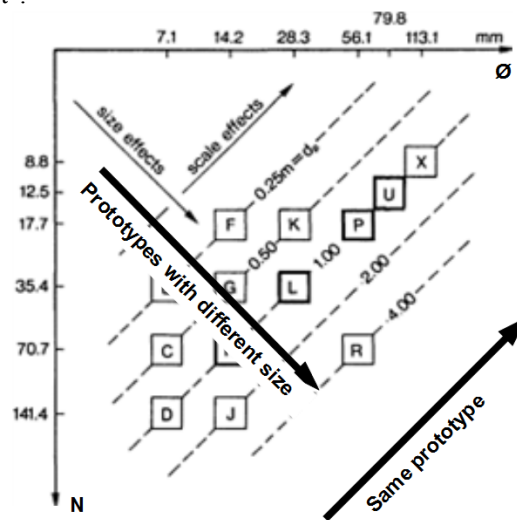


Figure 1: Chart representation for a separation of scale and size effects [Ove79].

Table 2: Conditions for scale effect for the main geotechnical works [Gar07].

B is the diameter or width of a foundation, d_{50} is the mean grain diameter.

Clay	No scale effect	
Sand	Bearing capacity of shallow footings (circular or strip) pile tip, penetrometer	$B/d_{50} > 35$
	Response of piles to lateral loads	$B/d_{50} > 45$ or 60
	Pull out load of anchor plates (circular or rectangular)	$B/d_{50} > 48$
	Stability of tunnel face (B=tunnel diameter)	$B/d_{50} > 175$
	Grain size effect on frictional interface	$B/d_{50} > 50$ or 100

The rules identified [Gar07] give a general idea of the B/d_{50} ratio that should be respected to avoid “grain size effect” and “scale effect”. The problems are quite complicated to understand for the different phenomena that occur in a soil foundation interaction; for instance there is certainly an influence of the soil density (more grains are in contact with the foundation for denser sand) which cannot be taken into account with d_{50} alone.

2.3 Geotechnical centrifuge around the world

Nowadays centrifuge modeling is developed in each continent (table 3). This method enables conducting parametric studies, ultimately taking structures to their failure and obtaining data that can be applied either for drawing comparisons with actual structures or for calibrating numerical models.

Table 3: Geotechnical centrifuge with a radius $R \geq 3\text{m}$. Bold characters indicate geo-centrifuge similar to the IFSTTAR's one, constructed by Actidyn Systèmes (formerly Acutronic France). g_{\max} = maximum g-level, m_{\max} = maximum payload.

Centre / City	Country	Year of opening	R [m]	g_{\max} [g]	m_{\max} [t]
CEA-CESTA/Le Barp	FR	1964	10,5	100	2
NIISISM/Baku	SU	1966	5,5	100	
Sandia University /Albuquerque	US	1968	7,6	200	3.5
Simon Eng. Lab. /Manchester	UK	1971	3.2	140	5.5
CUED/Cambridge	UK	1972	4,3	150	1
AZNIISM/Baku	SU	1974	5,5	500	2.5
Port & Airport Research Institute/Yokosuka	JP	1980	3,8	113	2,76
Yangtze River Scientific Research Institute/Wuhan	CN	1983	3	300	0,5
Chengdu Hydroelectric Investigation & Design Inst.	CN	1985	5,4	100	3
IFSTTAR (LCPC) / Nantes	FR	1985	5,5	200	2
Rhur Unviversität / Bochum	DE	1987	4,1	250	2
Univ. California/ Davis (California)	US	1987	9,14	300	3,64
Univ. Colorado/ Boulder	US	1987	5,49	200	2
Chuo University	JP	1988	3,05	150	0,66
Deltares / Delft	NL	1988	6	500	5.5
Rensselaer Polytechnic Institute/Troy (New York)	US	1989	3	200	1
Kajima Co. /Chofu-Tokyo	JP	1990	3	200	1
Inst. Water Conservancy & Hydroelectric Power /Beijing	CN	1991	5,03	300	1,5
Nanjing Hydraulic Research Institute	CN	1991	5,5	200	2
Shimizu Co.	JP	1991	3,35	100	0,75
Nakase Nikken Sekkei Institute/ Kawasaki	JP	1992	3	200	1
Center for Cold Ocean Resources Engineering/ St John's	CA	1993	5,5	200	2,2
Takenaka Komuten/Chiba-Tokyo	JP	1993	6,5	200	5
US Army Corps of Engineers-Waterways Experiment Station /Vicksburgh (Miss.)	US	1993	6,5	350	6
Fisheries Agency	JP	1994	3	150	0.25
National Central Univ/ Chung-li	TW	1995	3	200	0.55
Nishimatsu Construction Co. / Kanagawa	JP	1997	3,8	150	1,28
Public Works Research Institute, Ministry Constr. /Tsukuba	JP	1997	6,6	150	5
Daewoo Institue of Construction Technology/ Suwon	KR	1997	3	100	1,2
Dundee University / Dundee	UK	1999	3,5	130	0,8
Hong Kong University of Science and Technology/Kowloon	HK	2000	4,47	150	4
Technical Research Institute of Obayashi / Tokyo	JP	2000	3,5	120	7
Mansoura University / Alexandria	EG	2001	3,5	130	0,8
IIESS Téhéran	IR	2004	3,5	130	0,8
Téhéran Univ.	IR	2004	3,5	130	0,8
Tongji Univ. / Shanghai	CN	2006	3	200	1.5
Univ. Norte Fluminense / Campos	BR	2007	3.5	100	1
KAIST / Daejon	KR	2008	5	130	2.4
Zhejiang Univ. / Hangzhou	CN	2009	4.5	530	4

Most of the recent geo-centrifuges are equipped with an earthquake simulator or a robot, which is used in flight without stopping the centrifuge.

3. Cyclic loading

The non-permanent loads applied to a foundation, such as the ones induced by a storm, wind, waves, currents have no reason to be perfectly cyclic. There may be variations both in amplitude and frequency. In the sake of simplification, the laboratory cyclic loading test will consider constant stress amplitude and a constant loading frequency. This will be assumed for physical models in a centrifuge too.

A cyclic loading may be defined (Figure 2) on the basis of the mean value (Q_{mean}) of the cycle and of the half amplitude (Q_{cyclic}). It is often helpful to normalize these measures by a static capacity Q_s .

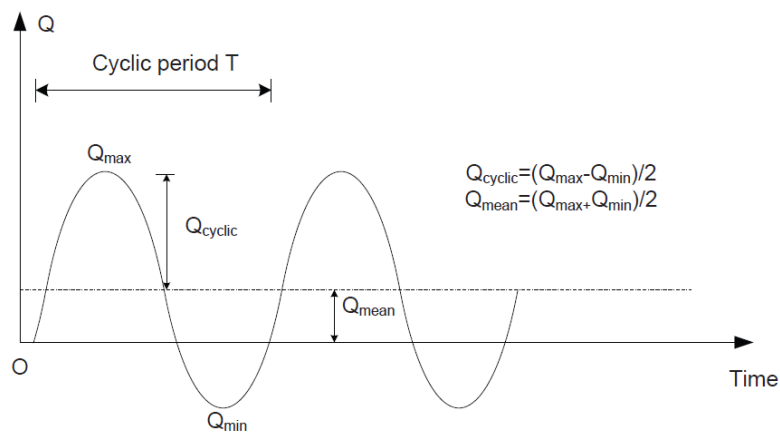


Figure 2: Cyclic loading definitions [Jar12]. Note Q_{mean} is often referred to as Q_{average} , Q_{ave} or Q_a , and Q_{cyclic} as Q_{eye} or Q_{cy} . For horizontal loading H_c and H_m are used here.

4. Shallow foundation

The effect of earthquakes on small buildings, founded on shallow foundation may be severe in terms of reuse of the building after an earthquake. Observations on several in situ cases [Gaz03] have shown that, without overturning, an important tilting may occur; even if no major failure of the building itself was observed. To understand this behavior and to try to predict the effect of cyclic and seismic loading on such structures, centrifuge tests have been performed at LCPC in the framework of the European program QUAKE [Tho06].

Foundation under combined loading has a 2D geometry but the building's is 3D. The building is placed on a saturated kaolin Speswhite clay soil model, which char-

acteristics are investigated by in-flight Cone Penetrometer Tests and shear vane tests. Two buildings have been tested in order to consider different ratio $F_v = V/V_{max} = (\text{weight}) / (\text{ultimate vertical load})$. Both undrained and drained interfaces between the building and the soil have been studied but only tests on the undrained interface are described in this paper. Centrifuge tests have been performed at $100\times g$, the centrifuge acceleration being applied at the soil surface level.

Buildings have been designed with the following features: the footing base has a square shape ($B\times B$); the slenderness ratio is 2; the center of gravity corresponds to the geometrical center of the parallelepiped building ($x=y=0, z=B$); the weight induces a vertical stress at the soil surface smaller than the bearing capacity; Instrumentation may be included on or around the model; the horizontal loading is applied on the center of gravity, whatever the settlement or rotation is.

Two buildings (Figure 3) with different weights have been designed at 1/100 scale: a light one and a heavy one (Table 4). The light one gives a vertical load (5.69 MN prototype for M2) which is about 26% of the vertical bearing capacity whereas the heavy one (13.44MN for M1 and 12.59MN for M1') gives the vertical load which is about 60% of vertical bearing capacity.

Table 4: Small scale buildings.

Model	mass [kg]	B [mm]	Vertical stress [kPa]	type of model
M'1	1.2836	100	125.9	building
M1	1.3695	100	134.4	same as M'1 with PPTs
M2	0.580	100	56.90	building with PPT's

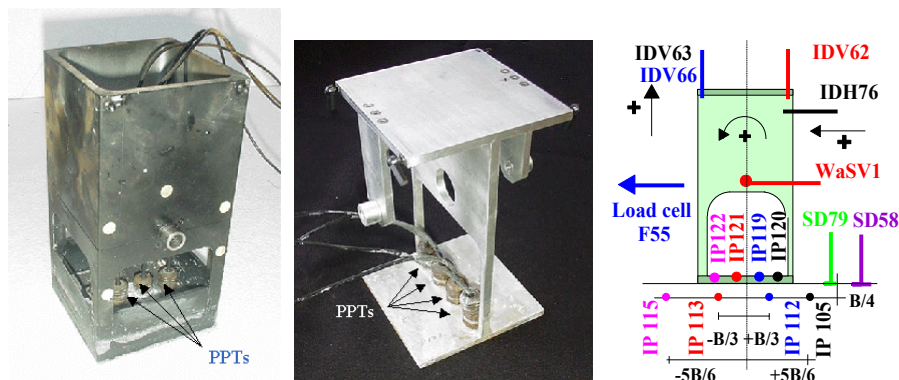


Figure 3: Models of buildings M1 (left), M2 (centre) and instrumentation (right).

The model is instrumented with (horizontal and vertical) displacement sensors placed on the building in order to identify the settlement and the rotation of the building. Pore pressure transducers (PPT) have been implemented both on the model, to measure the pore pressure distribution at the soil-foundation interface, and in the soil below the model, in order to obtain the pore pressure variation at several

depths in clay. The main parameters, deduced from measurements, used in the text are defined as follows:

Settlement: $s = (IDV63 + IDV62) / 2$; Rotation: $\theta = \arctan (IDV66-IDV62)/90$
 Horizontal displacement: $y_G = WaSV1$; Overturning moment: $M = H.B$

4.1 Soil Mass

The soil model is made of saturated kaolin Speswhite clay at a water content of about 42% and a density of about 17 kN/m^3 . Each container has been prepared by consolidation under stress in the lab, with 3 or 4 successive layers of clay, in order to obtain the expected profile of undrained cohesion S_u . Those profiles are determined using in-flight CPT and well-known correlation between the cone tip resistance q_c and the undrained shear strength S_u determined with vane test [Gar01] $q_c/S_u = 18.5$. Examples of undrained shear strength S_u profiles, obtained through in-flight CPT tests few minutes before or after the loading test, are shown on figure 4. The undrained shear strength may also be estimated [Gar01] by $S_u = 0.19\sigma'_v OCR^{0.59}$.

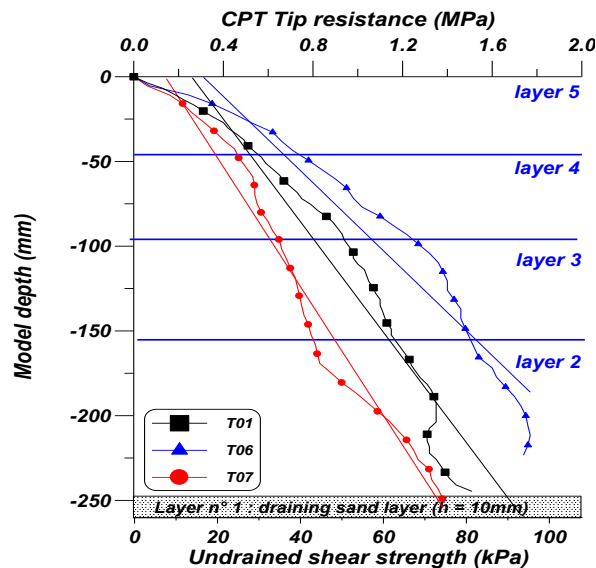


Figure 4: Examples of S_u profiles deduced from CPT tests.

For example, for clay beds in Tubs 3, 4 and 5 that were prepared in the same way and under the same consolidation stress, the theoretical undrained shear strength at a depth of 15m (prototype), derived from this equation is about 54 kPa. An agreement is found between the theoretical and experimental bearing capacities for static vertical loading.

4.2 Horizontal loading

An original loading device has been developed in order to apply horizontal cyclic loading at the building center of mass. As it may be seen in Figure 5, this device allows the building to move (horizontally and vertically) and to rotate without changing the point of application of the horizontal load to the building.

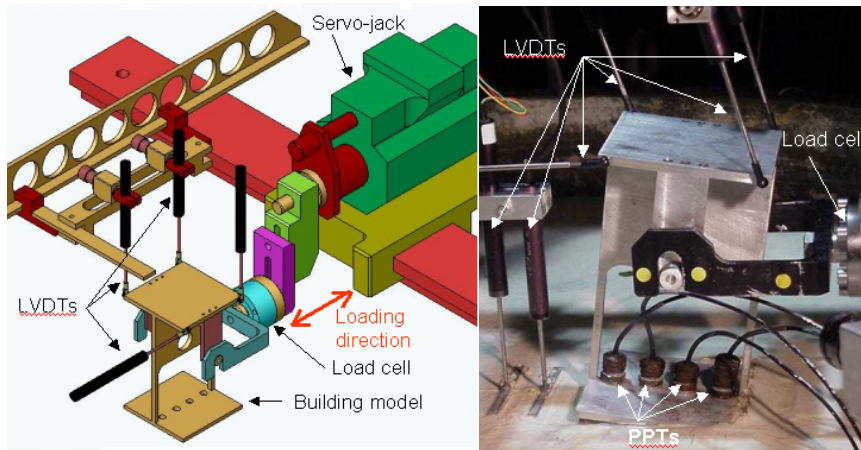


Figure 5: Horizontal cyclic loading device and instrumentation of a model.

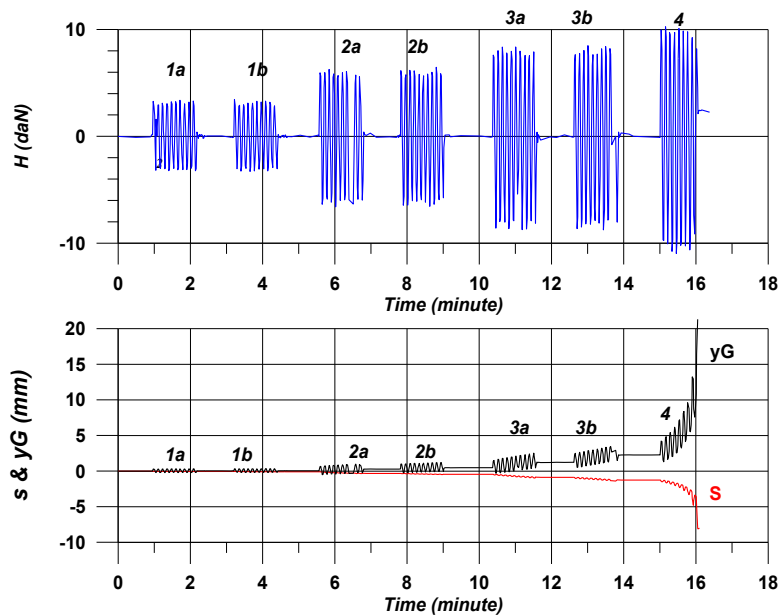


Figure 6: Typical horizontal cyclic loading (model scale).

Cyclic loading is force controlled (Figure 6). The two-ways loading is symmetrical ($H_{\text{mean}}=0$). It is applied at the altitude of the center of mass and includes doubled series of cycles of constant amplitude, varying between $H_{\text{cyclic}}=3\text{daN}$ (model scale) for the first series up to 10daN for the last one. The (model) frequency of 0.16Hz assumes that the loading is quasi-static (no inertia effect). Those loads represent few percents of the vertical load V . They simulate the effect of an earthquake that induces “two-ways” tilting of building.

Vertical settlement of the building occurs during the horizontal cyclic loading, and increases especially with the amplitude of the cycles.

The results show (Figure 7) pressure accumulation both in the soil mass, and at the soil-structure interface (which is not drained). In both cases, higher positive pressures have been observed on the side where the first loading is applied. The first amplitude of loading (3daN model) has very few influence on the pore pressure variation in comparison with the others amplitudes of load. The embedded sensors just below the building display higher variations than the others. At the interface, a “suction” effect may be observed.

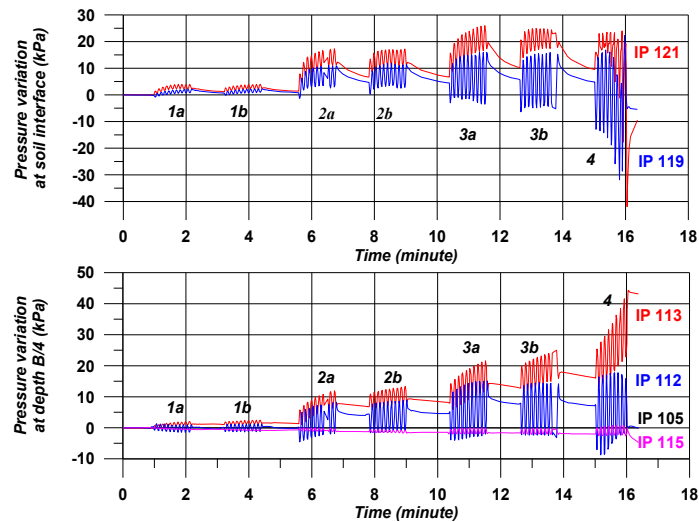


Figure 7: Pressure accumulation at the interface (top) and at depth $B/4$ (bottom) below the foundation (model scale).

When force-displacement behavior is drawn (Figure 8), it appears that the first sets of loading display a quite small irreversible behavior in comparison with the last sets of loading cycles. These results are similar to the moment-rotation curves shown in Figure 9.

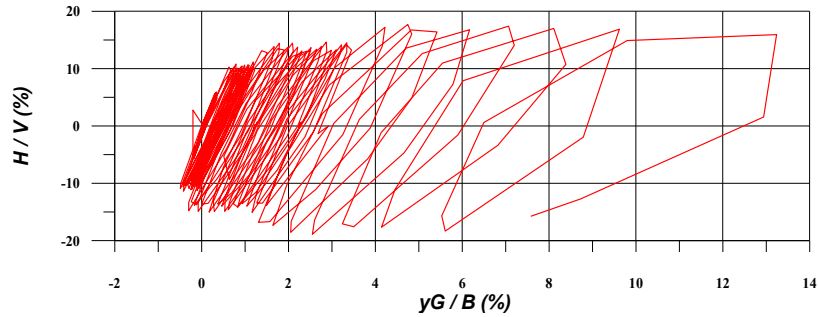


Figure 8: Dimensionless force displacement cyclic loading.

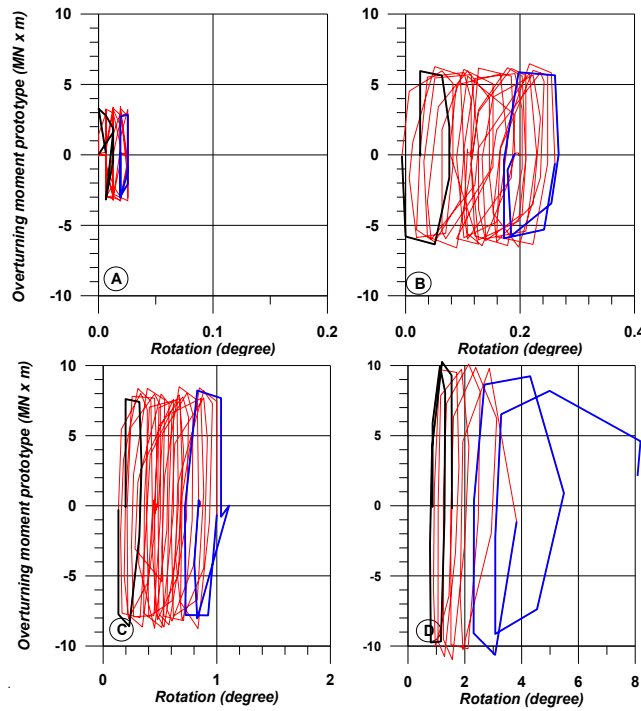


Figure 9: Moment-rotation for 4 sets of cycles (prototype scale).

Considering the kinematics at the center of the foundation, the settlement-rotation curves (Figure 10) show the similar trend in all the cases despite of differences in the amplitude cycles. But the accumulated settlement and accumulated degree of rotation changes with the change in the amplitude cycles.

From the V & H loading tests, failure loads have been measured. The failure envelope may be drawn in the V-M plane (Figure 11). Data from the two different values of the vertical loads (light and heavy building) have been plotted. The experimental data may be fitted by parabolic curves as shown in Figure 11. The data also shows

that the loading sequences have slightly enlarged the stability domain showing the necessity of additional tests to increase the definition of the failure surface.

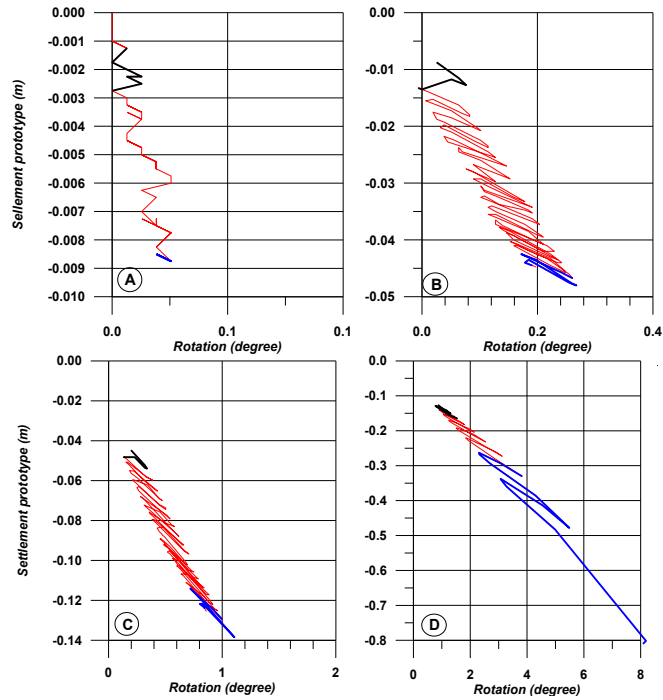


Figure 10: Settlement-rotation for four sets of cycles (prototype scale).

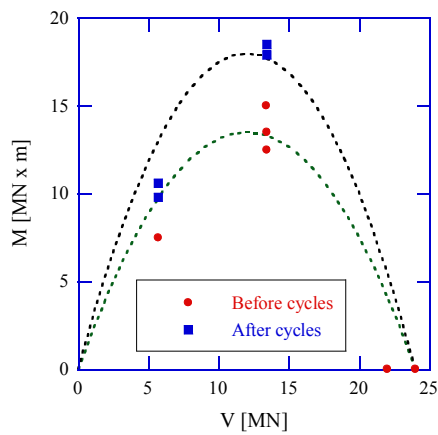


Figure 11: Failure diagram for H monotonic loading before and after cycles.

4.3 Conclusions and prospects for shallow foundations

Lateral loading applied to buildings founded on shallow foundations shows a non-linear load-displacement behavior. Strain accumulation is visible both on settlement and rotation. A large amount of work is being dissipated in the foundation. A classical parabolic failure envelope has been estimated.

Those experimental data has been used for comparison with a 2D finite element model [Apo07], giving reasonable results and opening a sensitivity study for dynamic loadings.

5 Deep foundation

If the more critical cyclic loading for shallow foundation is certainly the horizontal one, for deep foundations both vertical and horizontal cyclic loading may have an important role, depending on the type of structure considered. For instance, in off-shore engineering, a jacket founded on piles will display both vertical and horizontal loading on the foundations under the effect of wind, wave or currents. An off-shore wind turbine founded on a monopile will be subjected to a quasi-constant vertical load and to cyclic horizontal loading.

The rate of loading (or the frequency) has significant effects on time-dependent performances or inertial phenomena. Here, these two parameters are not considered because dry sand is used and the rate of loading is low enough.

5.1 Vertical cyclic loading

A pile subjected to vertical loading offers a resistance due to the tip and to the skin friction for compressive loads, and only to skin friction for tensile loads.

The results of a first series of tests [Gue12] are presented. The mode of installation of the model piles is intended to simulate soil-pile interactions relevant for cast-in-place piles. The tests, conducted in dense Fontainebleau sand, covered the full range of loading modes (monotonic versus cyclic; compressive versus tensile; and one-way versus two-way).

5.1.1 Experimental Work

The tests were carried out at the IFSTTAR geotechnical centrifuge facility under a g-level of 23. The model piles are aluminium cylinder rods 18mm in diameter and 560mm in height. These dimensions were chosen in order to simulate at $23 \times g$ a prototype pile similar to the piles used in the field [Ben12]: 0.42m in diameter and 13m embedment depth. The model pile was also designed to avoid scale effect with soil particles, following the classical scaling laws [Gar07]. The pile surface is rough, and this roughness was obtained by mechanical machining. It is characterised by a

normalised roughness R_n [Lin05], defined as the ratio between R_{max} and d_{50} (Figure 12) and is equal to 0.5 for all tested piles.

The piles were installed in Fontainebleau sand, which has a minimum density (ρ_{dmin}) of 1.417g/cm^3 and a maximum density (ρ_{dmax}) of 1.736g/cm^3 . The dry sand was filled in a strongbox using the air pluviation technique (Figure 12) to obtain a density index $I_D = 92\%$. The relative sand density was controlled by adjusting the falling height, the flow rate and the speed of the automatic hopper. The steel strongbox is rectangular with inner dimensions of 1200mm in length, 800mm in width and 720mm in depth (Figure 13).

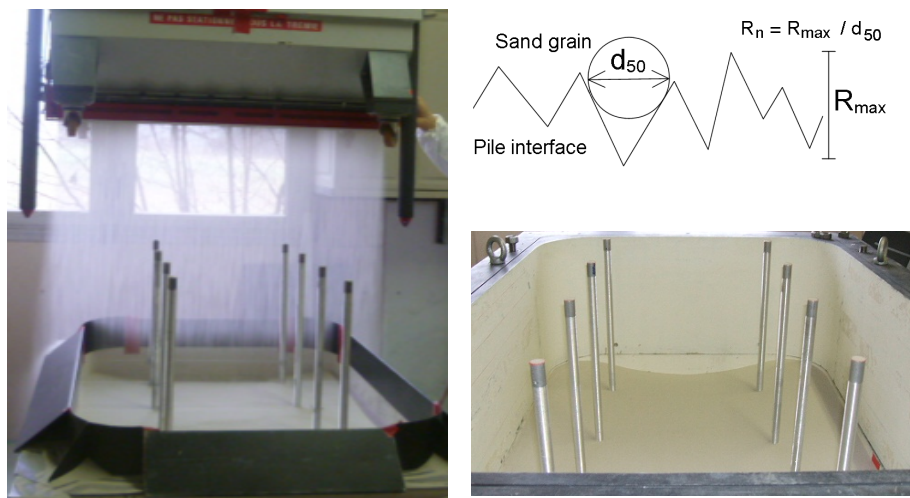


Figure 12: Pluviation above the piles pre-installed in the bottom half of the strongbox (left) ; Normalised roughness definition (top right); Piles after positioning the top half of the strongbox (bottom right)

Eight piles were pre-installed in the container before sand pluviation, with a minimum distance from the walls equal to 10 times the pile diameter. The distance between the pile tip and the bottom of the container was equal to 8.9 times the pile diameter. This installation technique was intended to simulate the behaviour of non-displacement, or cast-in-place, piles.

Figure 14 shows the complete test setup. The axial loading was applied to the pile (labelled 2 in Figure 14) using an electric actuator (1) fixed to rigid steel beams set on the container (3). A special mechanical knee-joint linked the top of the pile to the force transducer (4) directly screwed on the tie rod of the actuator. This device avoids overturning moment in the pile and provides a perfect axial link during the two-way loadings. The vertical displacement of the pile head was measured by two laser displacement transducers (5) placed symmetrically on either side of the pile top. The data was recorded in the control room using an HBM data acquisition module named Spider 8 [Tho08].

Before starting loading tests, each sand deposit was subject to an in-flight 'preconditioning phase', which consisted of raising the g-level three times between 0 and

23×g. During this sequence, unique for each container, the piles were totally free. The centrifuge was stopped to link one pile to the testing device and then restarted to reach 23×g step by step. The servo-actuator position was adjusted step by step to keep the measured force equal to zero.

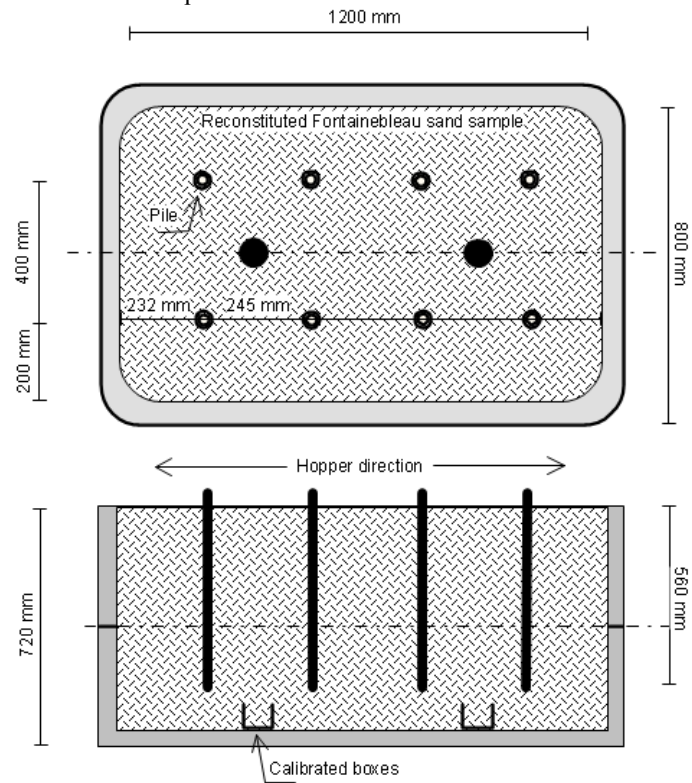


Figure 13: Rectangular strongbox with model pile positions

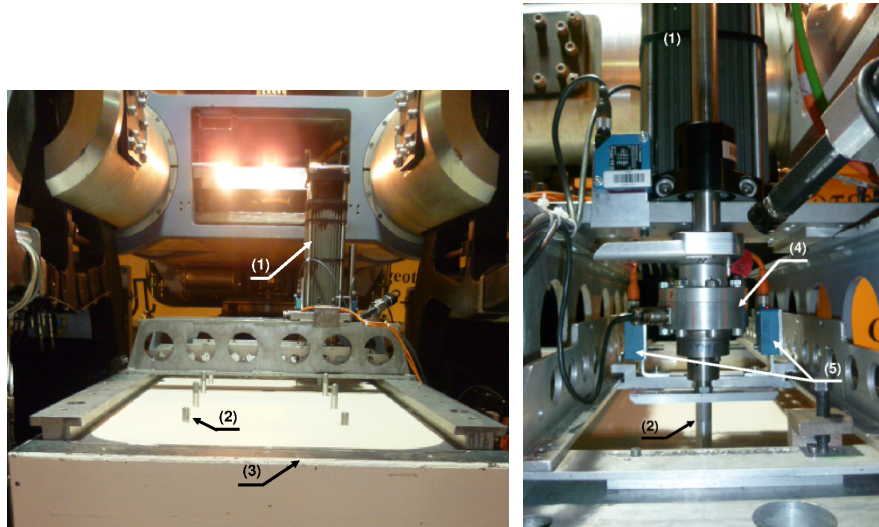


Figure 14: Test setup for centrifuge model pile

Compressive and tension static loading tests were carried out first, as reference tests, in each container to estimate the ultimate vertical load V_{rc} and V_{rt} , respectively. For these static tests, the servo-actuator was controlled in displacement at a rate of 1mm/min. V_{rt} is determined when the measured load reaches a peak value and V_{rc} is estimated at the slope breaking point of load-displacement curve. The quasi-static tests provided a control of the repeatability of the sand masses and served to define the relative amplitude of the cyclic loads.

For the cyclic tests, as soon as the g-level was reached, the force control mode was used to perform the cyclic sequences. Four parameters are needed to describe the cyclic sequence: mean load (V_m); load amplitude (V_c); period of the cycle and number of cycles.

First, the load was increased up to the mean value (V_m) at a constant rate of 4daN/s, corresponding to the similar static loading increment. Then the sinusoidal cyclic signal was applied at a frequency of 0.1Hz. The cyclic load components were expressed as a rate of the ultimate bearing capacity deduced from the static loading tests. Conventionally, positive load and displacement are selected for compressive tests (static and cyclic). Failure under cyclic loading is assumed when the measured displacement of the pile head reaches 10% of the pile diameter (1.8mm at model scale).

5.1.2. Experimental Results

Static pile behaviour

All results are presented in prototype scale. The static tests (pure compression or pure tension) are used to determine the ultimate load capacity. Figure 15 show the load

versus the normalised pile head displacement for compressive and tension loading tests, respectively, performed in different containers.

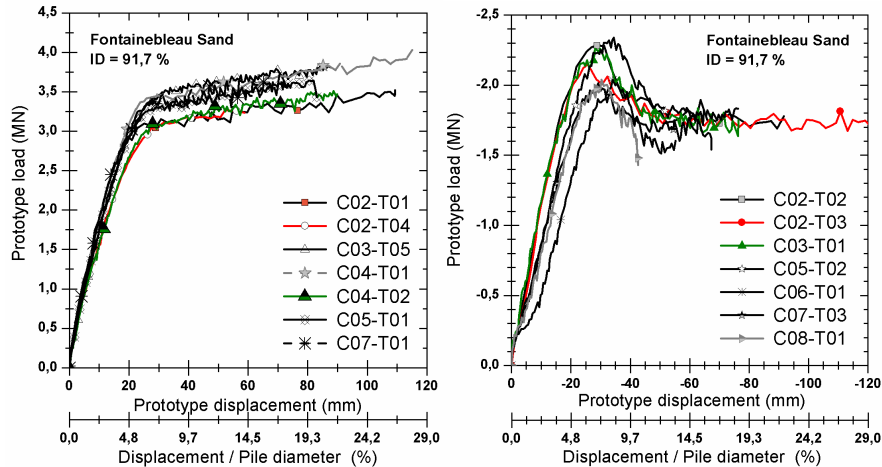


Figure 15: Load versus displacement for compressive (left) and tension (right) static tests (C: container; T: test)

The mean value outcome from seven tests for ultimate compression resistance (V_{rc}) is 3.2MN within ± 0.13 MN deviation. For tension tests, only the shaft friction is mobilised along the pile. The peak characterises the ultimate resistance of the soil; 2.2MN is the ultimate tensile bearing capacity (V_{rt}) within ± 0.12 MN deviation. The curves show a good repeatability of the pile behaviour under static loading, which results largely from the good reproducibility of the sand deposit preparation by the air pluviation technique.

Typical cyclic pile behaviour

Cyclic loading of pile is classically split in two categories: one-way or two-way tests. The latter is obtained when the cyclic magnitude (V_c) is greater than the mean load value (V_m) whatever the sign of V_m .

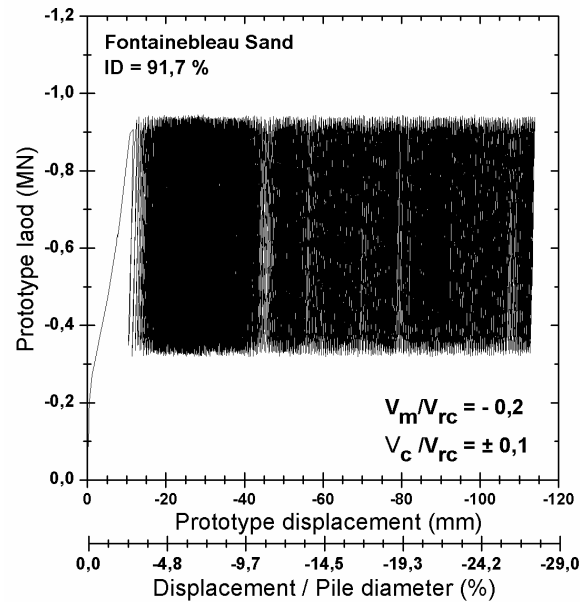


Figure 16: Load versus pile displacement for a typical one-way tension cyclic load test

Figure 16 presents the load versus pile head displacement for a typical one-way tension cyclic test. After 460 cycles the displacement reaches 10% of the pile diameter corresponding to the failure criterion; however, the test is continued up to 1000 cycles and is stopped after a displacement as large as 27% of the pile diameter.

The total load versus the pile displacement for a typical two-way test is presented in Figure 17. The curve characterises a typical behaviour of the pile with a progressive settlement as a first phase and a fast extraction in a second phase. The failure occurred at the seventh cycle, while the test was interrupted after 16 cycles with a displacement equal to 141% of the pile diameter. For other two-way tests (not presented in this paper), failure occurred after a few dozens of cycles and, in each case, at a much lower number of cycles than for one-way tests.

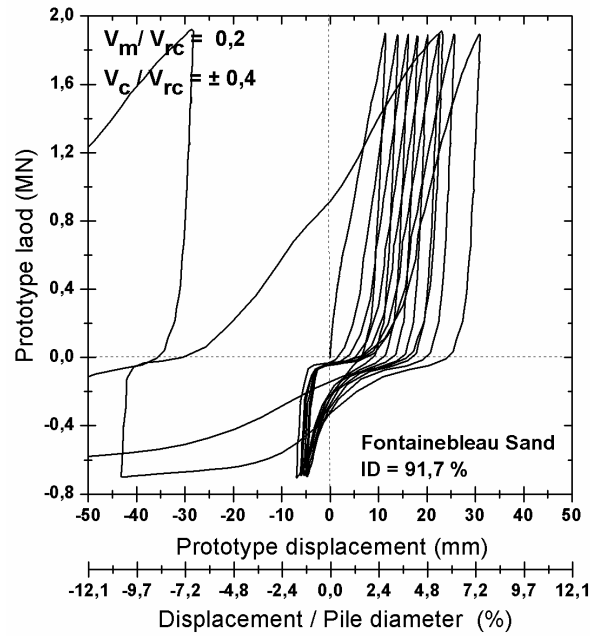


Figure 17: Load versus pile displacement for a typical two-way tension cyclic load test.

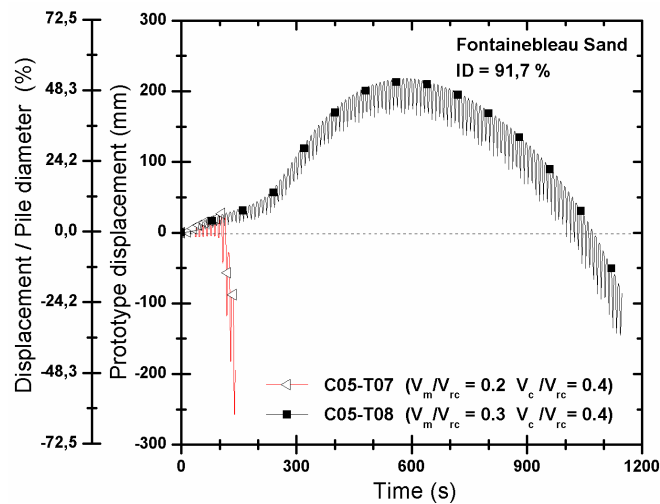


Figure 18: Trends in pile head displacements for two-way tests with compressive mean value.

The pile displacements versus time for two cyclic loading tests characterised by a positive (compressive) ratio of the mean load and the same cyclic amplitude (V_c/V_{rc})

= 0.4) are shown in Figure 18. In both cases the first cycles generate a downward movement (settlement) of the pile. Then, depending on the magnitude of the mean value, sudden or progressive reversal in the displacement direction takes place and the pile fails in pull out mode.

Effect of cyclic magnitude on pile displacement

Figure 19 compares the evolution of pile head displacements of three tests with same mean value $V_m = 0.6 V_{rc}$ and three different cyclic load amplitudes ($V_c/V_{rc} = 0.1, 0.2$ and 0.3).

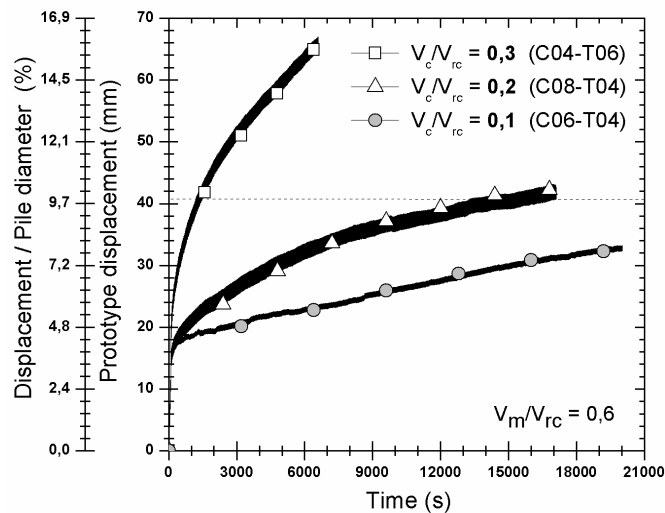


Figure 19: Pile displacement versus time for different load amplitudes.

Pile settlements increase with the number of cycles until failure. For the tests characterised by $V_c/V_{rc} = 0.3$ and 0.2 , the number of cycles to reach failure (10% of pile diameter) are 117 and 1394, respectively. The pile loaded by $V_c/V_{rc} = 0.1$ accumulates a settlement of about 8.4% of the pile diameter after 2500 cycles. The number of cycles to failure for this test can be estimated as 4190 cycles by linear extrapolation. The increase of the cyclic load magnitude accelerates the soil failure, and so reduces the number of cycles to failure.

5.1.3 Conclusions and prospects on piles loaded vertically

As expected, the number of cycles to reach failure decreases with the severity of the cyclic component. A general observation is that piles have been found to be very sensitive to cyclic loading. The most visible detrimental effects of cyclic loading on the axial response of a pile are: (a) a reduction of ultimate capacity, related to reductions in local skin friction; and (b) reductions in pile head stiffness (or increased displacements). The main final objective of these tests is the obtention of stability

diagrams as introduced by Poulos [Pou81]. A first attempt is shown on the Figure 20. This diagram illustrates the number of cycles for bored piles leading to failure as a function of the mean and cyclic load components, normalised by the pile capacity under monotonic loading [Pue12].

New series of tests are planned, including tests in medium dense sand and some tests involving different modes of installation aimed at simulating the response of displacement piles.

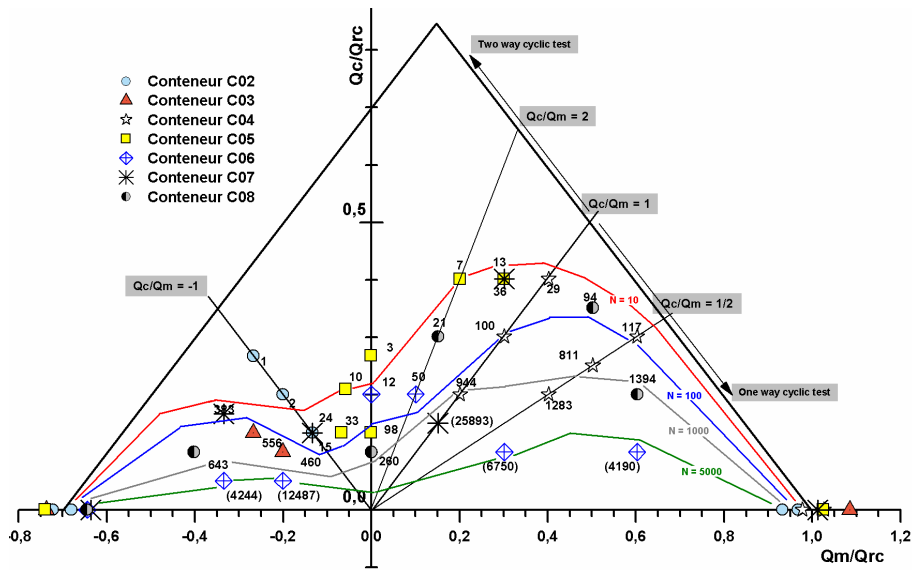


Figure 20: Stability diagram for axial cyclic tests on model piles in the centrifuge – dense Fontainebleau sand – cast in place piles (from [Pue12]).

5.2 Horizontal cyclic loading

Lateral cyclic loading on vertical piles is generally produced by waves, wind, boat accosting and mooring to quays, variable overloads or thermal dilatations. All cyclic loading sequences are characterized by four parameters (the maximum applied load F_{max} , the load variation amplitude DF , the number of cycles n , and the frequency f).

The link with the parameters defined in §4 are the following:

$$\frac{DF}{F} = \frac{2(\frac{H_c}{H_m})}{1 + \frac{H_c}{H_m}} \quad \text{and} \quad \frac{H_c}{H_m} = \frac{\frac{DF}{F}}{2 - \frac{DF}{F}} \quad (1)$$

Two-way cyclic loading can be considered as a simplified representation of dynamic loading without inertia nor damping. However, both stresses and strains are more important under the effect of one-way cyclic loads than two-way ones. Two-way lateral cyclic service loading, in dry dense sand, improves the soil characteristics.

However, although alternating loading is symmetrical, the direction of the first loading remains in the pile “memory” [Ros07].

5.2.1. Theoretical background

The consideration of cyclic effects when designing piles is generally deduced from the soil/pile interactions under applied static loads using the Winkler model [Win67]. In the case of a linear elastic response of the soil/pile system, the soil reaction $P(z)$, at a depth z , depends on the modulus of soil reaction E_s , and on the lateral displacement $Y(z)$:

$$P(z) = E_s(z) Y(z) \quad (2)$$

Based on the theory of beams, the quasi-static equilibrium of the pile is given by:

$$\frac{\partial^2 M(z)}{\partial z^2} + P(z) = 0 \quad (3)$$

Where $M(z)$ is the bending moment at a depth z . It is linked to the lateral displacement by:

$$M(z) = E_p I_p \frac{\partial^2 Y(z)}{\partial z^2} \quad (4)$$

Where E_p and I_p are respectively the Young's modulus and the Inertia of the pile. By a combination of equations (2), (3) and (4), the equilibrium equation may be written in displacements:

$$\frac{\partial^4 Y(z)}{\partial z^4} + \frac{E_s}{E_p I_p} Y(z) = 0 \quad (5)$$

There are analytical solutions (e.g. [Fra99]) if both E_s , E_p and I_p are constant with z . For a pile in soil, E_s increases generally with depth, and the method is to split the soil mass in layers with constant soil reaction.

5.2.2 Instrumentation

In the case of pure flexural bending, the displacement vector depends, in any location of the pile with coordinates (x, y, z) , on X, Y and Z (translational displacements):

$$\underline{\xi}(x, y, z) = \left(Z - x \frac{\partial X}{\partial z} - y \frac{\partial Y}{\partial z} \right) \underline{t} + X \underline{n}_x + Y \underline{n}_y \quad (6)$$

The only strain tensor component different from zero is:

$$\varepsilon_{zz} = \frac{1}{2} \left(\underline{\nabla} \underline{\xi} + {}^T \underline{\nabla} \underline{\xi} \right)_z = \frac{\partial Z}{\partial z} - x \frac{\partial^2 X}{\partial z^2} - y \frac{\partial^2 Y}{\partial z^2} \quad (7)$$

On the skin of the pile (breadth B), the strain that follows a generatrix of the cylinder pile located in the bending plane will give, depending of tension or compression:

$$\varepsilon_{zz}(x = 0, y = \pm B/2, z) = \frac{\partial Z}{\partial z} \mp \frac{B}{2} \frac{\partial^2 Y}{\partial z^2} \quad (8)$$

The half difference of strains measured respectively at the intrados and extrados gives a way to reach the pile curvature. This is possible by sticking two strain gages mounted in half-bridge. Equations (3) and (8) show that a direct relationship may be obtained between strain gages measurement and the bending moment. A calibration of the pile allows a direct identification of the bending moment from the electrical measurement of each strain gage.

The aluminium tube used for modeling the pile in the centrifuge (Figure 21) is equipped with 20 levels of strain measurement.

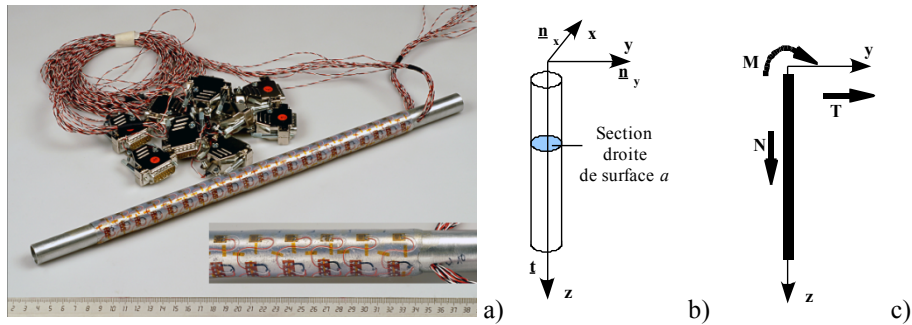


Figure 21: Model pile used in the centrifuge (a), 3D scheme (b), 1D scheme (c).

5.2.3 Model device

The pile, designed at scale 1/50, is loaded horizontally only, the vertical load being constant (pile dead weight). The load is applied at a prototype elevation of 1.6 m above the ground surface with a servo jack and transmitted to the pile through a cable (Figure 22) for a one-way cyclic load.

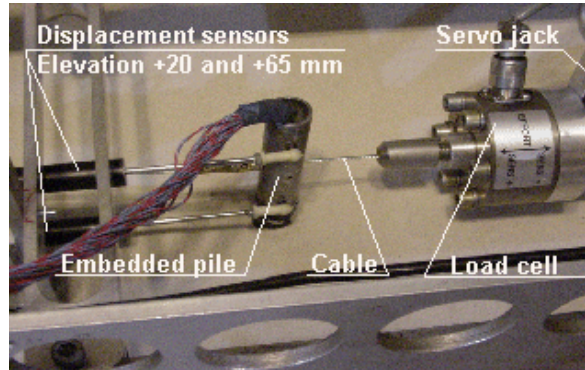


Figure 22: One way loading device [Ros07]

The boundary load conditions at the pile head are perfectly known. The pile head displacement and rotation are measured using two horizontal displacement sensors located 0.8 m and 2.6 m above the ground level in prototype values (20 and 65 mm in scale model values), respectively. On the assumption that, above the soil, there is no deflection of the pile, the displacement at the origin of load is deduced from those sensors.

Driving the pile into the dry Fontainebleau sand sample before rotating the centrifuge ensures the installation repeatability. Although the stress conditions, in which the model pile is installed, are different from those of the prototype, the differences do not affect bending moment results significantly. Similarly, the pile installation procedure does not significantly affect the comparison tests between monotonous and cyclic loading [Ros07].

5.2.4 Pile head displacement

The displacements measured in the vicinity of the load application point depends on the nature of the cyclic loading (figure 23). Those tests show that the relative displacement estimated from the displacement y_n identified for the maximum load at cycle n , may be fitted with a logarithmic law:

$$y_n/y_1 = 1 + b \ln(n) \quad (9)$$

The b parameter may be estimated from the ratio $DF/F_{max} = 2H_c/(H_m + H_c)$ with:

$$y_n = y_1 \left(1 + 0.08 \left(\frac{DF}{F_{max}} \right)^{0.35} \ln(n) \right) \quad (10)$$

The same trend is observed for high number of cycle [Rak09], up to 75000 cycles, but with a change of slope around 100 cycles (figure 24).

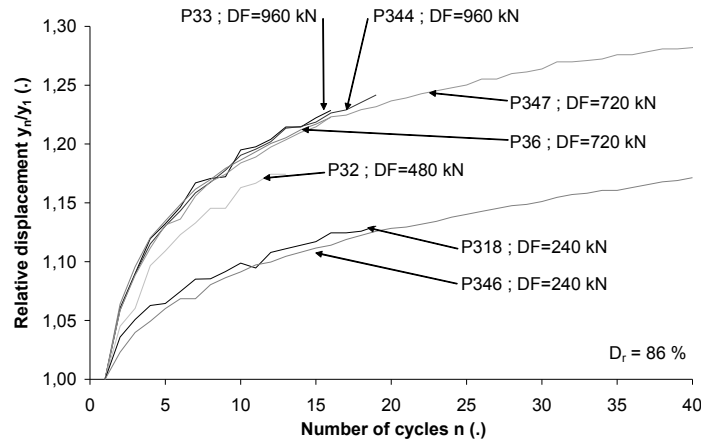


Figure 23: Relative displacement versus number of cycles for different $DF=2H_c$, and the same $H_m+H_c=F_{max} = 960 \text{ kN}$ [Ros07]

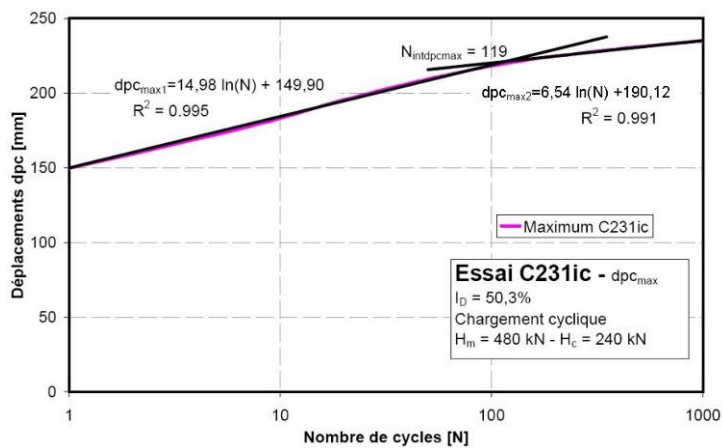


Figure 24: Example of pile head displacements for large number of cycles [Rak09].

5.2.5 Bending Moment

The influence of cyclic loading on the maximum bending moment is more important when DF/F_{max} (or $H_c/(H_m+H_c)$) is small (Figure 25). A log fitting may be done. The bending moment profile is influenced by the number of cycles, especially for the first decades of cycles. Nevertheless, as the variations of the maximum values are included in a range of 15% in the dry sand, the knowledge of the bending moment profile fixes the order of magnitude of the bending moment that the pile has to face down.

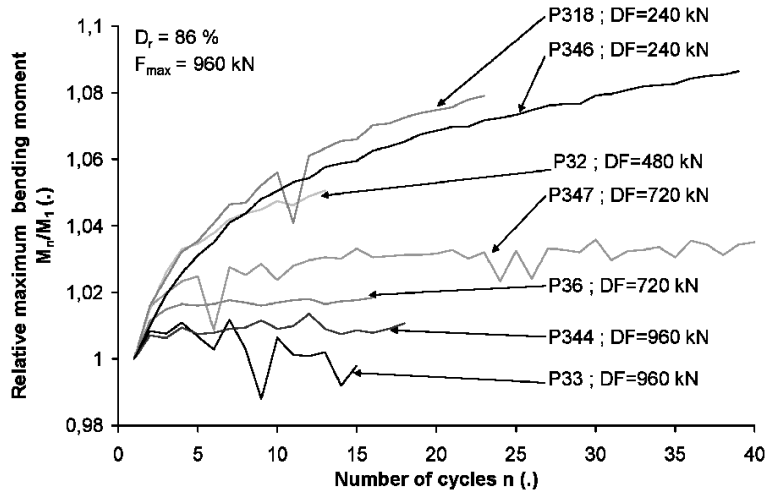


Figure 25: Relative bending moment versus the number of cycles for several load amplitudes [Ros07].

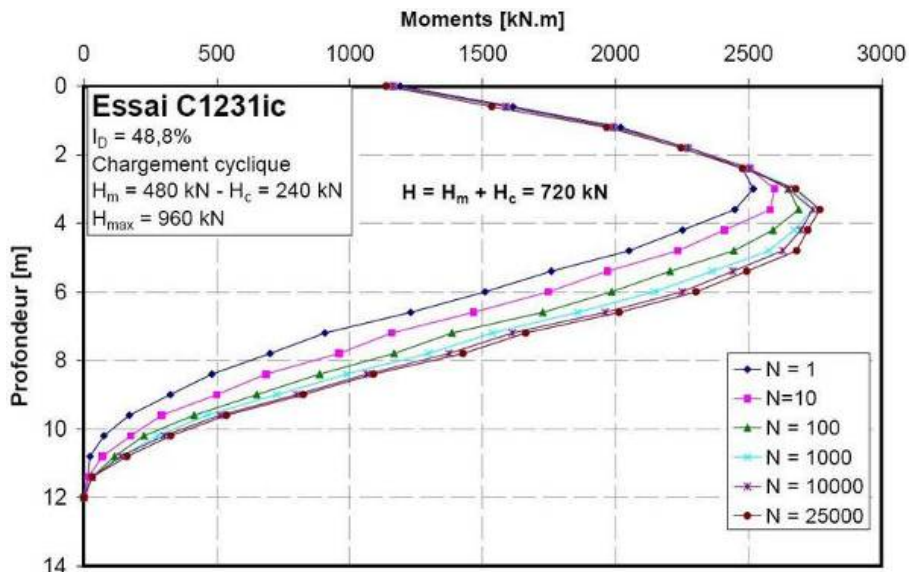


Figure 26: Evolution of bending moment profiles in a loose sand [Rak09].

5.2.6 P-Y curve

The soil-structure interaction model is classically used to design laterally loaded piles. This model, which requires the knowledge of the P-Y curves, is based on the elastic beam theory to determine the pile lateral displacements, $Y(z)$, and the bend-

ing moments. A similar method is used for the interpretation of the experimental results. Here, the bending moments are measured whereas the pile lateral displacement, $Y(z)$, and the soil reaction profile, $P(z)$, are calculated by double integration (11) and double derivation (12) of the bending moments, respectively.

$$M(z) = EI \frac{d^2 y}{dz^2} \Rightarrow y(z) = \iint \frac{M(z)}{EI} dz^2 \quad (11)$$

$$P(z) = \frac{d^2 M(z)}{dz^2} \quad (12)$$

It is then possible to reconstitute the reaction curve from experimental data (Figure 27). It can be shown that close to the surface, the dissipated energy is higher and the soil reaction is subjected to higher degradation. The same trends are observed for a test of 1000 cycles (Figure 28), where only the points corresponding to maximum load are drawn.

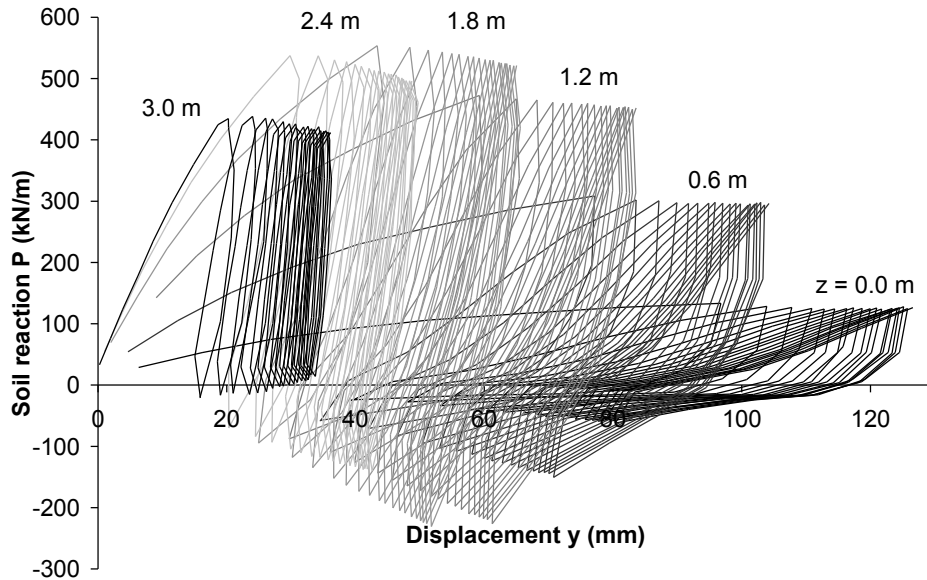


Figure 27: Detail of the cyclic P-y reaction curves at different depths (Test P344, $F_{\max} = 960$ kN, DF = 960 kN) [Ros07]

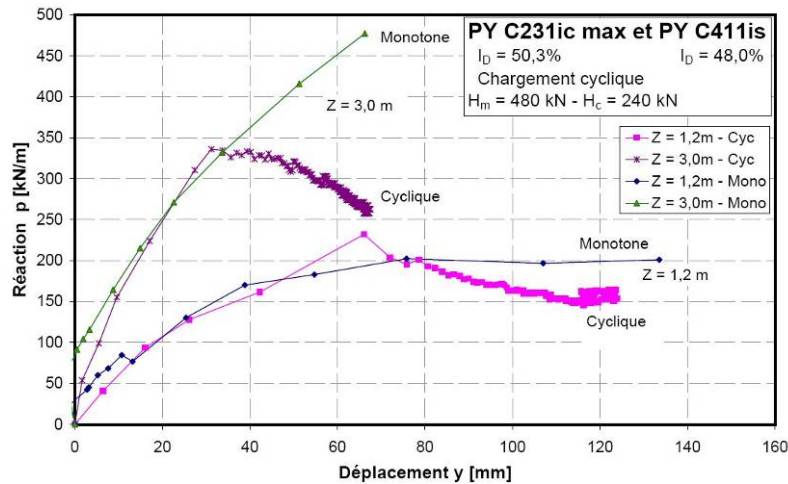


Figure 28: Example of reaction curves for static loading and for 1000 cycles [Rak09]

5.2.7 Conclusions and prospects on piles loaded horizontally

Centrifuge modelling is a powerful tool for studying pile subjected to lateral loading, as it is possible to use a highly instrumented pile in a controlled environment. Several Ph.D. theses have been performed in Nantes considering piles in sand [Ros07, Rak09] or clay [Khe12]. The interpretation of those results is being introduced in Solcyp's documents for design of piles subjected to lateral loading. The experimental data base obtained thanks to centrifuge tests should be used for comparison and validation of numerical models.

6. Conclusions

The understanding of the behaviour of foundation subjected to cyclic loading is a non-usual challenge for geotechnical engineers. The experimental approach based on centrifuge modelling technique is versatile, as it allows several types of foundations, different natures of soil and a large range of cyclic loading conditions.

For the centrifuge tests presented, it appears that most of the phenomena start during the first cycles for the shallow foundation and the pile subjected to lateral loading. For the pile axially loaded the loose of friction may be dramatic in some cases of two-ways loading, conducting to failure.

The tools for numerical modelling are still under development, and a recent benchmark [Tho12] organized within the Solcyp programme has shown that the order of magnitude were respected, but the prediction of failure is still uncertain. The coupling between physical modelling and numerical modelling is the key methodology for geotechnical problems from the 21st century.

Acknowledgments

Results presented in this paper have been obtained with the IFSTTAR geocentrifuge within the framework of the French 'Projet National SOLCYP', from the European programme Quaker and from the Region des Pays de la Loire programme R2GC. They are greatly acknowledged.

References

- [API11] A.P.I.-American Petroleum Institute. *ANSI/API Specification RP2GEO. Geotechnical and foundation design considerations for off-shore structures*. Washington DC: API. 2011.
- [Apo07] Apostolou M., Thorel L., Gazetas G., Garnier J., Rault G. Physical and numerical modelling of a building subjected to lateral cyclic loading: soil-footing interaction. *4th Int. Conf. on Earthquake Geotechnical Engineering*. CD-Rom, paper 1400.12p Thessaloniki, june 25-28 2007.
- [Bac86] Gaston Bachelard. *La formation de l'esprit scientifique*. Vrin, Paris, 1986.
- [Ben12] Omar Benzaria, Alain Puech and Alain Le Kouby. Cyclic axial load tests on driven piles in overconsolidated clay. In: *Proc. 7th Int. Conf. Off-shore Site Investigation and geotechnics*. London.307-314. 12-14 sept. 2012.
- [Bru09] M. Brun, E. Palix , A. Puech. *Prise en compte des chargements cycliques dans le dimensionnement des fondations offshore*. Rapport Solcyp R9004_a/RevA. 127p. 2009.
- [Cor88] Jean-François Corté (Ed.). *Centrifuge 88. Proceedings of the International Conference on Geotechnical Centrifuge Model*, Balkema. Paris, France, 25–27 April 1988.
- [Cor89] Jean-François Corté. *Essais sur modèles réduits en géotechnique*. Rapport général. Session 11. Essais sur modèles. *XII ICSMFE*, Rio, vol.4, 2553-2571. Aug. 1989.
- [Cra88] Craig WH. Centrifuge models in marine and coastal engineering. In: Craig WH, James RG and Schofield AN. (eds.). *Centrifuges in Soil Mechanics*. Rotterdam: Balkema, 149–168. 1988
- [Der03] François Derkx, Luc Thorel, Jacques Garnier, Gérard Rault, Patrick Gaudicheau. *Développements récents et perspectives des essais et des matériels de la modélisation physique en centrifugeuse*. *Journ. Sciences Ingénieur LCPC*. ISSN 1628-4707, VVF Dourdan, 433-438, 9-11 déc 2003.

- [DNV77] D.N.V.-Det Norske Veritas. Rules for the design construction and inspection of offshore structures, Appendix F, Foundations, 5 p, 1977.
- [Fra99] Roger Frank. *Calcul des fondations superficielles et profondes*. Editions Technique de l'Ingénieur et Presse des Ponts et Chaussées, 141p. 1999
- [Gar01] Jacques Garnier. Modèles physiques en Géotechnique: état des connaissances et développements récents. *1^{ère} conférence Coulomb*, Paris CNIT La Défense. 2001
- [Gar07] Jacques Garnier, Christophe Gaudin, Sarah M. Springman, Patricia J. Culligan, Deborah Goodings, Diethard König, Bruce Kutter, Ryan Phillips, Mark F. Randolph, Luc Thorel. Catalogue of scaling laws and similitude questions in geotechnical centrifuge modelling. *Int. J. Physical Modelling in Geotechnics* ISSN 1346-213X, vol7, n°3, pp 1-24. 2007.
- [Gaz03] Gazetas G., Apostolou M. & Anastasopoulos J. Seismic uplifting of foundations on soft soil, with example of Adapazari (Izmit 1999 earthquake). *Int. Conf. on Foundations*, Dundee37-4, Sept 2003.
- [Gue12] Guefrech A., Rault G., Chenaf N., Thorel L., Garnier J., Puech A. Stability of cast in place piles in sand under axial cyclic loading . *7th Int. Conf. Offshore Site investigation and Geotechnics*. London. 12-14 sept. 329-334. 2012.
- [Jar12] Richard Jardine, Alan Puech, Knut Andersen. Cyclic loading of offshore piles: potential effects and practical design. *Proc. 7th Int. Conf. Off-shore Site Investigation and geotechnics*. London.59-97. 12-14 sept. 2012.
- [Khe12] Meriam Khemakhem. *Etude expérimentale de la réponse aux charges laterals monotones et cycliques d'un pieu fore dans l'argile*. Ph.D. Thesis. Ecole Doctorale SPIGA. 318p. 2012.
- [Kim98] Kimura, T., Kusakabe, O., & Takemura, J. (Eds.). *Proceedings of the International Conference Centrifuge 98*. Balkema. Tokyo, Japan, 23–25 Sept. 1998.
- [Ko91] Ko, H.Y., & McLean, F. (Eds.). *Proceedings of the International Conference Centrifuge 91*. Balkema. Boulder, Colorado, USA, 13–14 June 1991.
- [Leu94] Leung, C.F.F., Lee, F.H., & Tan, E.T.S. (Eds.). *Proceedings of the International Conference Centrifuge 94*. Balkema. Singapore, 31 August–2 September 1994.
- [Lin05] Lings ML, Dietz MS. The peak strength of sand-steel interfaces and the role of dilation. *Soils and Foundations* **45**: 1–14. 2005.

- [NFE05] NF EN 1997 – 1. *Eurocode 7: geotechnical design - Part 1: general rules*. 145p. 2005.
- [NFP12] NF P 94-262 *Justification of geotechnical work. National application standards for the implementation of Eurocode 7. Deep Foundations*. 206p. 2012. (in French).
- [Ng06] Ng C.W.W., Zhang L.M., Wang Y.H. (Eds.). *Proceedings of the sixth International Conference on Physical Modelling in Geotechnics. 6th ICPMG06*. Taylor & Francis. Hong-Kong, 4–6 August 2006.
- [Ove79] N. Krebs Ovesen. The scaling law relationships, *Design parameters in geotechnical engineering, 7th ECSMFE*, Brighton, 4, 319–323. 1979.
- [Phi02] Phillips, R., Guo, P.J., & Popescu, R. *Proceedings of the International Conference on Physical Modelling in Geotechnics. ICPMG02*. Balkema. Saint John's, Newfoundland, Canada, 10-12 July 2002.
- [Phi69] Phillips, E., 1869. De l'équilibre des solides élastiques. *Comptes rendus à l'Académie des Sciences de Paris* 68 (in French).
- [Pou81] Poulos HG. Cyclic axial response of single piles. *Journal of the Geotechnical Engineering Division* **107**: 41–58. 1981
- [Pue08] Alain Puech, Jean Canou, Christian Bernardini. Solcyp: research project on the behaviour of piles submitted to cyclic loading. (in French). *Journées Nationales de Géotechnique et de Géologie de l'Ingénieur JNGG08, Nantes*. 735-742. 2008
- [Pue12] Alain Puech, Jean Canou, Christian Bernardini, Alain Pecker, Richard Jardine, Alain Holeyman. SOLCYP: a four-year joint industry project on the behaviour of piles under cyclic loading. *Proc. 7th Int. Conf. Off-shore Site Investigation and geotechnics. 12-14 sept. London*. 263-270. 2012
- [Rak09] Rakotonindriana J., Le Kouby A., Thorel L., Mestat Ph., Comportement d'un pieu isolé soumis à un chargement cyclique horizontal. *XVIIth ICSMGE Alexandrie*, 5-9 oct. Hamza, Shahhien, El-Mossallamy (eds.). Millpress. Vol.2, pp1217-1220. 2009.
- [Ros07] Rosquoët F., Thorel L., Garnier J., Canépa Y. Lateral cyclic loading of sand-installed piles. *Soils and Foundations*, october, Vol.47, No.5, 821-832. 2007.
- [Sch80] Schofield, A. N. 1980. Cambridge geotechnical centrifuge operations. *Géotechnique* 30(3): 227–268.
- [SOL13] <http://www.pnsolcyp.org/>, site visited on the 23rd April 2013.

- [SPR10] Springman, S., Laue, J., & Seward, L. *Proceedings of the 7th International Conference on Physical Modelling in Geotechnics. ICPMG10*. Taylor & Francis Group. Zurich, Switzerland, Zurich, 28 June–1 July 2010.
- [Tho02] Luc Thorel, Jacques Garnier. *High g modeling*. Video LCPC, 20mn, real. JF Ringot, 2002.
- [Tho06] Luc Thorel, Gérard Rault, Sandra Escoffier, Jacques Garnier, Céline Boura. Soil-footing interaction: building subjected to lateral cyclic loading. *6th ICPMG Int. conf. on physical modelling in geotechnics*, Hong Kong, ISBN 0415415861, Ng, Zhang & Wang (eds), pp795-800. Aug.4-6, 2006.
- [Tho08] Luc Thorel, Gérard Rault, Jacques Garnier, Carol Murillo, Patrick Gaudicheau, Alain Néel, Claude Favraud. Macro-gravity measurements on reduced-scale models of geotechnical structures. *Bulletin de liaison des Ponts et Chaussées* ISSN 1269-1496, n° 272-273 spécial Métrologie pp93-131. 2008.
- [Tho12] Luc Thorel. Benchmark numérique. Sollicitation de pieux sous charge vertical. Powerpoint document. *Solycp meeting*. 9 oct. 2012.
- [Win67] Winkler E. *Die Lehre von der Elastizität und Festigkeit*. Verlag, 182p. (in German). 1867.

Centrifuge modeling of foundations subjected to earthquake loadings

Sandra Escoffier

LUNAM Université, IFSTTAR Institut Français des Sciences et Technologies des Transports de l'Aménagement et des Réseaux, Route de Bouaye, CS4, 44344 Bouguenais cedex, France

In the framework of earthquake engineering, dynamic centrifuge modelling can be a useful tool to obtain experimental data to calibrate and validate numerical or analytical tools. Seismic centrifuge tests enable to perform parametric study to highlight the effect of several parameters, such as the design of the geotechnical structure, the input frequency, the soil layering, etc. However, centrifuge modelling has its own limitations. First some of the key features (i.e. design parameters, containers, model instrumentation, saturation) and their associated limitations are presented. In a second stage, a non-exhaustive presentation of seismic tests performed in centrifuge by several research teams is made. As the design of the experimental set-up (selection of the geotechnical structure, type and location of the instrumentation) is linked to the main objectives of a centrifuge study, examples are presented according to the aim of the study. First two types of studies on shallow foundation are presented: studies that concern the understanding of failure mechanism and studies whose objective is to provide data on the nonlinear behaviour of foundation in the framework of performance-based design approach. The third part concerns the studies of deep foundation when subjected to seismic loadings. Starting from the fact that many codes do not recommend inclined pile in seismic area, design and results of centrifuge studies devoted to the performances of inclined pile on the dynamic behaviour of pile group are presented. Finally, as liquefaction is one of the most damaging earthquake induced effects, centrifuge studies on the performances of pile in liquefiable sand are presented.

1 Introduction

In most of the case histories, information on the foundation failure is only available before and after the earthquake. There is a lack of information on the mode of failure itself during the earthquake. Even if some structures have been instrumented, there is

still insufficient database on well-documented case histories. In this framework, dynamic centrifuge tests are an alternative to provide well instrumented database that can give insights on the behaviour of foundations during an earthquake. In the last twenty years many researches have been performed on the seismic behaviour of shallow and deep foundations through centrifuge tests. A majority of these concerned foundations resting, or embedded, in sand. Among these series of tests, a significant percentage addresses the problem of the behaviour of foundation when the soil liquefies. In the following, a non exhaustive review of dynamic centrifuge tests devoted to the analysis of foundations response under earthquake loading is presented. The objective is to give some insights on the type of studies that can be performed in a centrifuge.

In this framework, some technical details related to seismic tests in a centrifuge are first presented. The second part will focus on studies performed on shallow foundations resting on dry or saturated soils. Finally the last part concerns some series of tests performed to study the behaviour of deep foundations under earthquake loadings and more especially the studies performed on two main configurations: the behaviour of inclined pile and the behaviour of piles in liquefiable soil (levelled ground).

2 Technical aspects of dynamic centrifuge tests

2.1 Design parameters

Such as for static or cyclic centrifuge tests, to obtain relevant studies it is always necessary to simplify the reality in order to put in relevance parameters that can play a significant role in the geotechnical system behaviour. As the objective is not to model an existing structure, the geometry of the system (soil column layering, distribution of soil properties, foundation and superstructure designs) are always simplified for an easier understanding of the mechanisms that take place during the base shaking. For instance, in dynamic centrifuge tests, such as for cyclic tests, to have plane strain conditions, geometry of the foundation and superstructure can be long in the direction perpendicular to the loading [ZS98].

However, in the case of the dynamic centrifuge tests, additional design parameters should be taken into account such as the dynamic properties of the fixed-base superstructure, of the soil-foundation superstructure system, of the soil column and of the input. If the bearing pressure applied by the superstructure remains a key parameter, others parameters should be considered for the design. Among these, the fixed-base frequency and the associated mode of vibration (rocking mode or shearing mode), the height of the gravity centre of the lumped mass, the footing/superstructure mass ratio and the aspect ratio (height of the centre of gravity of the superstructure to the foundation width) play also key roles in the studies.

Moreover, the selection of the base shaking signal can have a significant role on the results obtained. Its frequency content, its amplitude and its duration have to be carefully selected. Its frequency content should be compared to the *a priori* frequency response of the soil column and of the soil-foundation-superstructure system. Combi-

nation of the amplitude and the duration can have an important effect on the obtained results. Most of research teams performed several earthquakes or sinusoidal inputs on each model. In the current practice, models are subjected to input with increasing amplitude. Most of the time the input level is characterized by the peak ground acceleration (PGA) at the base of the soil column and less times by the Arias intensity which is a representation of the earthquake energy content. If most of the studies do not consider the effects of previous inputs on the response of the system, some of them take into account their effects by determining, for instance, an average evolution of the soil density through settlement measurements [DBP⁺10a] or by considering induced residual stresses in piles [Esc12].

2.2 Flexible containers

When a soil column is subjected to an earthquake at its base, it will be deformed depending on the earthquake amplitude, frequency content and the dynamic properties of the soil column (geometry and dynamic soil properties). Centrifuge tests induce a containment of a soil column in a box. The end and lateral walls of the container, such as its base, can influence the response of the soil column when it is subjected to a dynamic loading at its base. The stress and the strain states can be modified compared to the soil column behaviour in free field conditions. When shear waves propagate vertically in a soil column, the behaviour of the soil column is comparable to that of a shear beam. The use of a rigid container modifies the soil column response because of the difference of dynamic stiffness. [WL86] and [ZS96] presented the basis of the design of a container which enables to reproduce, as much as possible, the same boundary conditions as the ones of a soil column in the free field. The characteristics of an ideal container for 1D seismic tests in the centrifuge are:

- Maintain a constant horizontal cross section during shaking,
- develop complementary dynamic shear stresses on the vertical container-soil interface equal to those occurring on horizontal planes when the soil stratum is shaken,
- have zero mass to avoid undesirable inertial loadings,
- have zero stiffness to horizontal shear,
- offer no resistance to settlement of the soil during placement, spin-up of the centrifuge, or as result of shaking,
- keep the water without leakage (except at top surface) and with insignificant membrane compliance.

In practice some of these requirements are not realistic and the design of a flexible container should be a compromise between the ideal one and the feasible one. Several kinds of containers have been designed to limit the boundary effects (Figure 1).

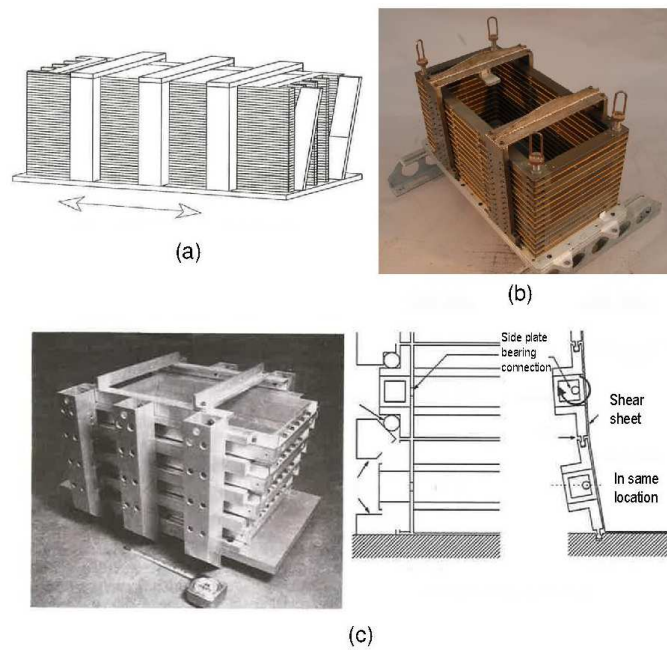


Figure 1: Different designs of flexible containers: (a) laminar container of the RPI ([VLTDE94]) (b) ESB container of the IFSTAR (c) HP container of California University ([FHI⁺94]).

The ESB (equivalent shear beam) container is made of a staking of rectangular frames separated by rubber ([BM02], [TM03], [Wil98], [ZS96], [Mad94]). The principle of the ESB design is that the dynamic stiffness of the ESB container should be almost the same as that of the soil column. Others containers, such as the HPC container (Hinged-Plate Container, [FHI⁺94]), and the laminar container ([VLTDE94]) have been designed to offer less shearing resistance with a minimum of weight compared to the soil column weight and shearing resistance. Theoretically these types of containers are more appropriated to liquefaction studies than the ESB box due to the loose of shearing stiffness of the soil column. In the case of the laminar container, rectangular frames are connected together through rollers which minimize the shearing resistance between two adjacent frames.

2.3 Tests with saturated sand layers

As liquefaction is one of the main cause of earthquake induced damage, numerous dynamic centrifuge studies are devoted to the analysis of this phenomena on different geotechnical structures (such as shallow or deep foundations). However [Kut95], starting from the scaling laws, indicated that if identical soil and pore water are used in model and prototype, the time for consolidation (a phenomenon linked to the pore pressure dissipation) at the model scale is N^2 times less than at the prototype scale while the dynamic time (linked to the pore pressure built up due to soil deformation) at the model scale is only N times less than at the prototype scale. Consequently the use of water for dynamic test results in time scale factor conflict. However, he indicated that this is only a serious problem if the time scales for diffusion and dynamics are of the same order. He added that it is known that the time required for reconsolidation of liquefied sand is similar to the duration of the shaking in typical centrifuge models involving earthquake excitation. A significant amount of dissipation often occurs during shaking in the model, while in the prototype, dissipation during shaking may be unimportant. The current method to slow down the consolidation to obtained a scaling factor of N for both, dynamic and consolidation times, is the use of a viscous fluid with a viscosity N times that of the water. If oil silicone has been previously used, the current practice is to use a mixture of HPMC powder (hydroxypropyl-methyl-cellulose) with water in order to obtain the request viscosity, keeping the density equal to the water density ([SCB98]; [DKTF99]). However [Wil98] has shown experimentally that, if it is the behaviour during the shaking that should be observed, the use of a viscous fluid with a viscosity that is lower than N times that of the water can be sufficient to catch the essential features. Another important point, when centrifuge tests concern saturated sand layer, is the efficiency of the saturation process. [TKIY06], indicated that the most suitable technique of preparing saturated model is the carbon dioxide gas and vacuum technique that is almost the same as the technique used for saturation of sample for triaxial test.

2.4 Model instrumentations for dynamic tests

Instrumentation of the models should be based on the theoretical approach of the model configuration takes into account. Instrumentation should enable all the useful parameters to be measured or calculated. Contrary to static-cyclic centrifuge tests, instrumentations should have an adapted frequency range. In most of the dynamic studies performed in centrifuge, the displacements of components that are above the soil surface (superstructure, shallow foundation, pile cap, etc.) are obtained by accelerometers or displacement transducers or by combining both. In the case of deep foundations, piles can be instrumented with strain gages to measure bending moment and axial load. The displacement of the pile and the pressure acting on the pile by unit length can be respectively obtained by double integration process and double derivation of the bending moment profile obtained ([Che07]). Concerning the soil instrumentation, accelerometers and pore pressure transducers are frequently used.

However, each type of sensors has its own limitation. For instance, most of the miniaturized accelerometers used for centrifuge experiments are unable to measure low frequency component and thus residual displacement can not be obtained. For instance, at the IFSTTAR centre, the miniaturized Brüel & Kjaer accelerometers have a frequency range from 1Hz to 20 kHz. In addition, direct double integration of the acceleration measurements causes unrealistic drift of the calculated displacement. Several methods have been proposed based on baseline correction in time domain and processing in the frequency domain ([YLL06]), based on the use of high pass filters combining with integration in the time domain or in the frequency domain ([WBB98]). To obtain low frequency components, displacement transducers, such as high frequency laser sensor or linearly variable differential transformers (LVDT), can be used. The first offers no mechanical friction or bending of the measuring system but the position of the spot varied while the second has a fixed position of the spot but friction, and in some cases, curvature of the measuring system can occur. The selection of the displacement sensor should be made to optimize the measurement and thus depends on the test configuration. In the case of the pore pressure sensor, as the measuring system is located behind a filter, phase lag between the true and the measured pore pressure, such as difference of amplitude between the measured and the true pore pressure, can exist ([Lee90]).

3 Shallow foundations

Several centrifuge studies have been devoted to the behaviour of shallow foundations under earthquake loading. However it is somewhat difficult to give an overview of these studies. Several differences exist, among which, the objectives of the series of tests that have been performed. As a consequence phenomena measured during the tests, such as the design of the tests, are much different. Among the objectives there are the characterization of the failure mechanism ([ZS98]), the investigation of the effectiveness of liquefaction remediation on the liquefaction-induced settle-

ment ([LD97]), the analysis of the energy dissipation by foundation rotation ([EC14], [UKJG07], [GK09], [GS11], [GKP⁺05]). In addition, these studies on shallow foundations can be addressed to bridge column founded on shallow foundations and shallow foundations of building. In both cases the presence of a liquefiable layer is a major feature.

3.1 Studies devoted to the understanding of failure mechanism

One of the most common modes of shallow foundation failure during earthquake is by rotation and vertical settlement due to the loss of stiffness through excess of pore pressure or large strain. However, [ZS98] indicated that the validation of the methods used in practice need experimental data to highlight the transition from linear to nonlinear behaviour and the failure onset. In this framework, they performed a series of dynamic centrifuge tests to give experimental evidence on the mechanism of failure of building on shallow foundation resting on dry or saturated sand under earthquake loading. Their study focused on the measurement of the foundation rotation and settlement and the onset of bearing failure. Five tests have been performed at the geotechnical centrifuge centre of Cambridge University ([Sch80]) on the bumpy road earthquake actuator.

In this study, the design parameters of the buildings were the bearing pressure applied on the foundation and the aspect ratio (height of the building to width of the foundation ratio). To simplify the study, rigid buildings were considered and, to have plane-strain condition, the structures were long in the direction perpendicular to the base shaking. Figure 2 presents the cross sectional view of the tests performed on saturated sand layer.

Two buildings have been considered: a heavy one and a light one that applied respectively a bearing pressure of $383kN/m^2$ and $132kN/m^2$. Their aspect ratios were respectively of 3 and 1. Notice that the height of the buildings was the same (i.e. height of the gravity centre) and the variation of aspect ratio was obtained by reducing the width of the foundation. Tests have been performed on dry and saturated sand with an ESB container. For the saturated model, the sand has been saturated with de-aired water under vacuum. The use of water was to simplify the model making due to the fact that model test did not intend to replicate a prototype structure. However pressure built up were reduced during the base shaking due to diffusion of the pore pressure as previously mentioned. The location of the instrumentation was established considering that no lateral sliding was expected. The displacement of the model structure (rotation and vertical settlement) were measured using LVDT and by integrating acceleration records. Response of the soil column was followed through acceleration and pore pressure measurements. Tests results showed that the displacements were largely influenced by the intensity of the base shaking, the bearing pressure and the presence of a water table in the ground. In the case of the lighter building, sliding mechanism in the foundation soil was not initiated. In the case of the heavier building, large residual settlement and rotation were observed. For both soil conditions, the vertical settlement

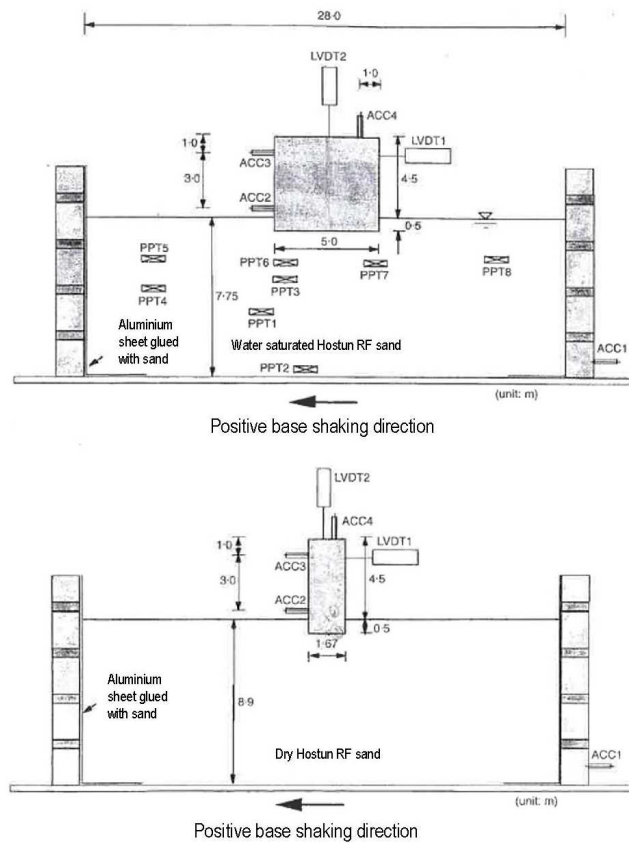


Figure 2: Cross section view of the saturated centrifuge model test performed by [ZS98].

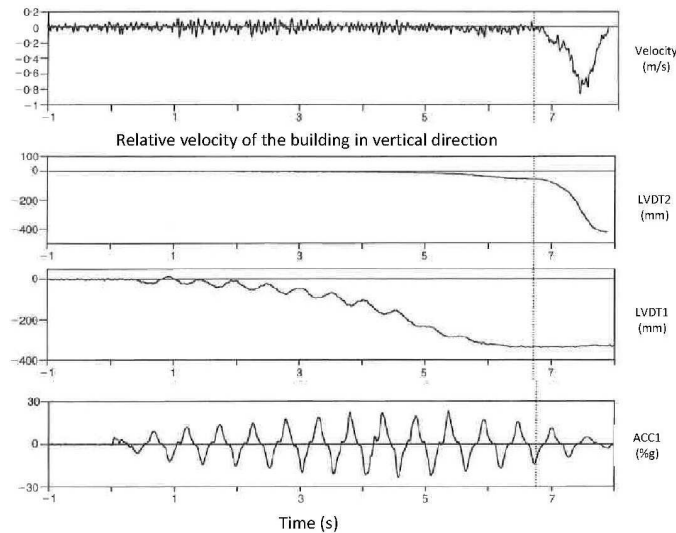


Figure 3: Time history of the vertical velocity, displacement and rotation of the building and the base shaking for the saturated test with heavy building [ZS98].

increased steadily during the base shaking leading to a pronounced increase in the rate of movement near the end of the input indicating the onset of bearing failure (Figure 3).

On the other hand, the structure rocking on each cycle induced accumulation of permanent rotation. Its amplitude was relative to the cyclic loading amplitude. The rocking mechanism was inhibited by the onset of major vertical settlement that has been highlighted by the time history of the vertical velocity obtained by derivation of the displacement measurement. The author explained the occurrence of the failure near the end of the base shaking, rather than at the peak base acceleration, by the combined effect of the permanent rotation accumulation and base shaking which both change the angle of the combined body force of the building (bearing pressure and inertial loading). A clear implication of this study was that seismic bearing capacity of a foundation cannot rely only on the PGA. The authors concluded that an earthquake with more moderate cycles which can induce permanent rotation may be more likely to cause bearing capacity failure of foundations than an earthquake with just one or two strong cycles.

In this series of tests [ZS98] did not paid much attention to the analysis of pressure built up at different location in the soil during the saturated tests contrary to the series of tests that have been made by [LD97]. They conducted two series of centrifuge model experiments to investigate the mechanism of liquefaction-induced settlement of a shallow foundation. The first series of tests focused on the effectiveness of liquefaction remediation by sand densification under the footing and the second series of

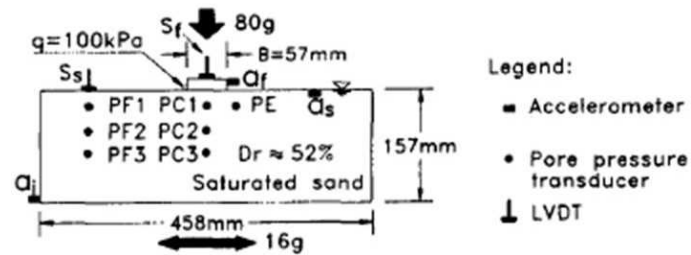


Figure 4: Cross section view of the saturated centrifuge model test performed by [LD97].

test focused on the effect of soil permeability on the pore pressure built up and footing settlement. In this study the design parameters of the building were the bearing pressure applied and the foundation shape and dimensions. Contrary to the previous study, all the mass of the building was concentrated at the foundation level, limiting the overturning moment (Figure 4).

Foundations with a circular shape, with a prototype diameter that varied from 4.56 to 5 m and a bearing pressure of 100 and 122 kPa were considered. Instrumentation did not enable the measurement of foundation rocking that was supposed to be limited due to the configuration tested. Vertical settlement of the soil surface and the building were measured with LVDT. The shaking base, soil surface and horizontal acceleration of the footing were measured with accelerometers. The pore pressure responses in the free field and below the foundation were measured with pore pressure sensors. All these tests were performed in a rectangular rigid box saturated with water. If the use of water instead of viscous fluid was mentioned, the boundary effects were ignored in this paper. In the first series of tests, the diameter of the compacted cylindrical soil mass was about 1.6 times that of the foundation and the relative density was increased from about 52% to a value of the order of 90%. In all the cases, liquefaction was achieved in the free field. Results of the tests without soil improvement showed that there was a slower pore pressure increase below the foundation, compare to that of the free field, caused mainly by dilative response of the granular soil as a substantial static driving shear stress existed due to the footing load (and thus the phase transformation line was less far than in the free field state of stress). At the end of the shaking the pore pressure a shallow depth below the foundation was of the order of that in the free field and continue to increase for a while after the shaking had stopped. This result suggested that there was an upward and a horizontal water flow but it was clear that, due to the use of water as a pore fluid, the excess of pore pressure during shaking did not take place under undrained condition. They proposed that the excess of the pore pressure was the sum of undrained pore pressure generated during the shaking, the pore pressure increase due to the water flow and the additional pore pressure due to the total stress redistribution as the soil stiffness changed. In addition, the softening induced by the rise in pore pressure significantly desimplified the base input accel-

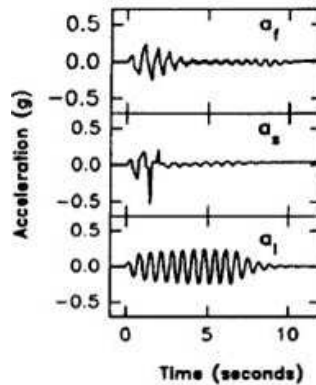


Figure 5: Time histories of the acceleration: base shaking, near the soil surface, on the footing.

eration (Figure 5). Such as for the test performed by [ZS98], the footing settlement developed more or less linearly with time. Liquefaction remediation by vibrocompaction reduced the residual settlement and most of the settlement developed during the shaking with only a small portion contributed by post shaking soil reconsolidation due to excess of pore pressure dissipation. The experimental results strongly suggested that densification by vibrocompaction of a depth $Z_c/B \geq 1.5$ (Z_c : height of the densification, B : width of the foundation) can be very effective in reducing settlement. However soil improvement will increase the efficiency of the transmission of the base shaking to the structure.

In the second series of tests, variation of soil permeability was implemented by varying the pore fluid viscosity. Tests were performed at 50g with water and with glycerol-deaire water mixtures to obtained three fluids with a viscosity of 1, 9.3 and 109 cSt. Pore pressure built up in the free field during the base shaking was almost the same for the three configurations but dissipate much slower after the shaking with the more viscous fluid. In highly pervious granular soil deposit (test with water), the pore pressure under the foundation tended to get equalized quickly, even during shaking, and tended to be controlled by the excess of pore pressure in the free field surrounding the footing. At the other extreme (test with the more viscous fluid), if the soil is very impervious, large negative excess of pore pressure may still exist under the footing at the end of the shaking. The negative pore pressure became positive some time after the shaking has ended. The authors indicated that this result with viscous fluid may help to explain the delayed foundation failure that have been observed in the free field a few minutes after the shaking.

Test with almost the same configuration has been made by [GM03]. In these tests, a 3mx3m foundation at the prototype scale applying a bearing pressure of 150 kPa and embedded in saturated medium dense sand was subjected to seismic loading. The objective was also to understand the mechanism of liquefaction -induced settlement.

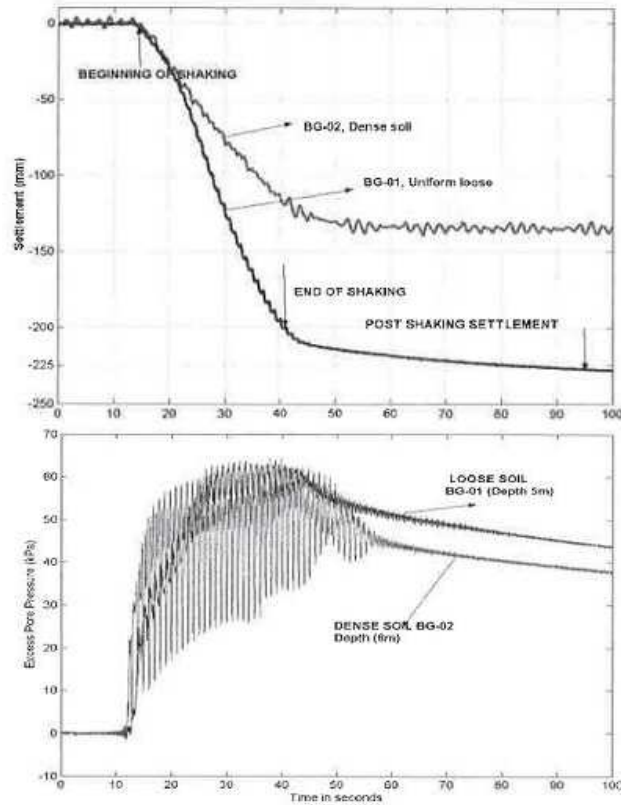


Figure 6: Founting settlement and pore pressure built up below the footing for loose and dense sand, [GM03].

They used almost the same instrumentation as for the tests previously presented. The main differences were the use of an ESB container described by [ZS96] and the soil column was saturated under vacuum using a 50 cSt silicone oil (test were performed at 50g). Consequently the pore pressure generation, such as the dissipation rate, was correctly modelled. Such as for the tests performed by [LD97] there was liquefaction in the free field. Liquefaction occurred first at shallower depth and after the end of the base shaking the excess of pore pressure propagated upward. As mentioned by [LD97], the increase of pore pressure under the raft was lower than in the free field and it appeared that it concerned a zone up to a depth of two times the foundation width. There was an increase of the pore pressure after the base shaking due to the redistribution of the excess of pore water pressure upward and toward the foundation in a 3D pattern. Such as [LD97], they studied the effectiveness of liquefaction remediation by densification of the whole soil column (the density was increased up to 85%). Figure 6 illustrates the recorded footing settlement and the pore pressure built up.

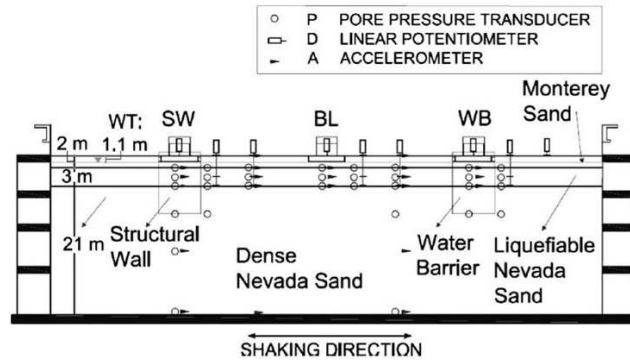


Figure 7: Experimental layout , [DBP⁺10a].

The pore pressure built up were almost the same for both soil. However, in dense sand, dilative stress strain response dominated inducing spikes in the pore pressure records. This dilative response temporally restored the effective stress and increased the shear resistance inducing less settlement than in the medium loose sand configuration. In the case of the dense sand, contrary to the medium dense sand, most of the settlement was induced during the base shaking.

A more details study have been performed by [DBP⁺10a] and [DBP⁺10b]. They have performed centrifuge tests to determined the mechanism of seismically induce settlement of building with shallow foundation on liquefiable soil but their objective was to estimate the combined effect of the deviatoric and volumetric-induced building settlement due to the cyclic soil softening/stiffening under the static and dynamic loadings of the building for which no well-calibrated procedure actually exist. Contrary to the previous studies multilayered soil column were used to focus the study on the effect of the presence of a thin liquefiable sand layer overlying, or not, by a more impervious layer. Figure 7 presents the model layout of the experiment performed.

All the tests were performed in an ESB container and the soil column was saturated with a solution of HPMC, to obtain a viscosity 22 times that of the water, (55g of centrifuge acceleration). The saturation process was the carbon dioxide gas and vacuum technique. Contrary to the previous study the structural models were single degree of freedom models (SDOF) with a lump mass supported by two side column made of steel which were placed on a rigid mat foundation. The static bearing pressures applied through the rectangular mat foundation were of 80 kPa and 130 kPa. In this configuration the additional parameter was the fixed-base natural period of the building that range between 0.2 and 0.3s. Different scale earthquakes were selected to study the dynamic response of the structure with slight and significant degrees of liquefaction in the free field. Based on the comparison of their nine tests, they proposed a list of the settlement mechanisms that were potentially active in their study. They listed five mechanisms of volumetric strain and two mechanisms induced by deviatoric strain.

Other experiments on shallow foundation resting on liquefiable layer have been made in the framework of the VELAC research program (model 12) showing the interest of such researches to give some insights for the improvement of current engineering practice.

3.2 Studies devoted to the nonlinear behaviour of geotechnical component

In the framework of the performance-based approach to seismic design, the effect of the soil-foundation-superstructure interactions on the capacity of the system is of first importance. However, in current civil engineering practice, the advantage of taking into account the soil-structure interactions, that can reduce the ductility demand on the structure, is not yet integrated. This fact is justified by the lack of well established and calibrated methods to study the post yielding behaviour of soil-foundation system under strong seismic loading ([PSY07]). Several researchers have provided experimental results on the non-linear behaviour of shallow foundations subjected to cyclic loading ([GKP⁺05, GK09]). From these previous cyclic studies two key parameters have been identified to influence the load-displacement behaviour and the damping, induced by the soil-structure interactions: the static factor of safety FS_v for a pure vertical loading and the moment-to-shear ratio applied at the base of the foundation. The first parameter is the ratio between the ultimate vertical load, V_{ult} , and the bearing pressure, V , applied by the building on the soil. The second parameter is the ratio between the moment applied on the foundation to the horizontal loading applied on the superstructure multiplied by the width of the footing in the loading direction.

In the framework of a European research program named SERIES, centrifuge tests have been performed, at the IFSTTAR centre, on dry sand to provide some experimental data on the nonlinear behaviour of soil-structure interactions. Figure 8 illustrates the experimental layout.

In this study the design parameters of the building were the bearing pressure ranging from 100 kPa to 300 kPa, the mass distribution between the lumped mass and the footing (around 2:1), the ratio of the height of the gravity centre of the lumped mass to the width of the square raft (between 1.16 and 1.3), and the fixed-base natural frequency (1Hz at the prototype scale). In a first stage, cross validation tests between with the Schofield centre of the Cambridge University ([CHH⁺12]) have been performed. Cross validation tests have ever been performed in other research programs such as the VELAC research program. Such as for laboratory tests on small sample this is a way to give confidence in the results obtained by different research centre.

In a second stage, a parametric study have been made on the effect of soil density, bearing pressure and input characteristics (amplitude and frequency content), on the dynamic moment-rotation loops. All the tests have been performed in an ESB container at 50g centrifuge. In the case of the tests performed at the IFSTTAR centre only the dynamic moment-rotation loops have been studied because the building was instrumented with accelerometers (Figure 8). The results, obtained with seismic in-

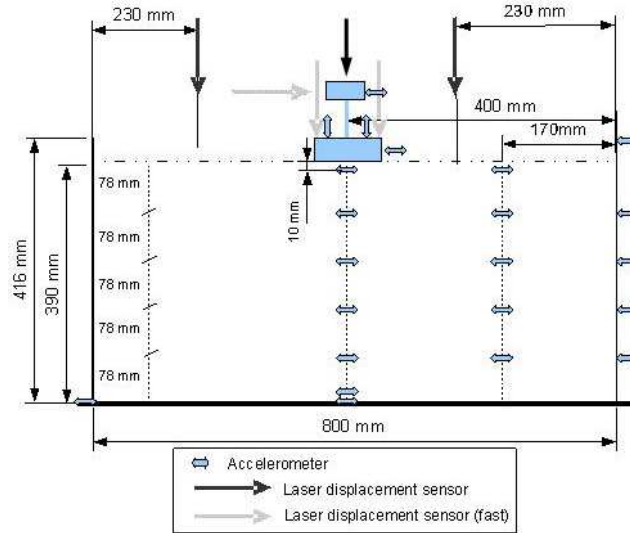


Figure 8: experimental layout of test on shallow foundation [EC14].

put, highlight that the response frequency of the soil-foundation-superstructure system and of the soil column were respectively around 0.85-0.95 Hz and 2.75 Hz. The settlement was highly influenced by the relation between the frequency range of the input and the frequency response of the soil-foundation-superstructure system. Concerning the analysis of the moment-rotation loops the main features were a limited effect of the soil density, the noticeable effects of the input amplitude, especially for the lighter building, and of the bearing pressure. In addition, the effect of the frequency content of the input was highlighted by subjected the different configurations of building/soil column density to two different inputs. Such as other earthquake simulators, the one of the IFSTTAR centre offers the advantage of reproducing real and synthetic earthquake such as sinusoidal inputs ([CEG⁺08]). In this study one of the inputs, T1F1E2, obtained by the SAM actuator of the Cambridge University, was reproduced by the IFSTTAR actuator and its effect on the building response was compared to that of a pure sine. Inputs had the same Arias Intensity, the sinusoidal input had the same frequency as the principal component of the T1F1E2 input and the amplitude of this component was the same. Thus Figure 9 illustrates the effect of the presence of a harmonic which frequency was around three times that of the soil-building system. For all the configurations the presence of the third energetic harmonic did not change the maximum moment applied to the building foundation, indicating that the acceleration of the superstructure was not influenced by the third harmonic. However the rotational stiffness of the soil-building system decreased. For both buildings, the presence of this higher order harmonic induced a noticeable increase of the soil-structure interaction damping. This phenomenon was particularly none negligible in the case of the

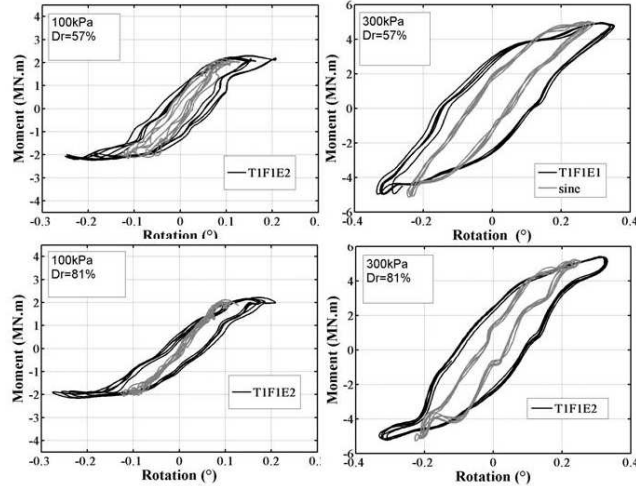


Figure 9: Effect of frequency content of the input on the moment-rotation loops for different building/soil density configurations. [EC14].

heavier building resting on the dense sand. Thus the presence of energetic frequency components that correspond to higher order harmonics of the soil-building system can have an influence on the soil-structure interaction in terms of rotational stiffness and damping. This phenomenon can have been enhanced for these selected inputs due to the fact the frequency of the third harmonic is not far from the response frequency of the soil column.

4 Deep foundations

4.1 Effect of inclined piles on the seismic behaviour of pile groups

In many codes the behaviour of inclined pile is considered as detrimental [af9]. For the engineering point of view the main drawbacks are the reduction of the bending capacity due to large tensile forces, the bending moments being induced by the possible settlement, the larger forces at the pile cap interface and the undesirable permanent rotation of the cap when the inclination of the pile is not symmetric. Dynamic centrifuge tests have ever been performed on battered micropile group [JBDH98] and on inclined pile group ([ECG08]; [OKKZ02]). Figure 10 illustrates the kind of inclined pile group configurations that can be used in centrifuge experiments.

In all the cases, there was a rigid connection at the pile head due to the difficulties to control the properties of other pile head connections in dynamic centrifuge

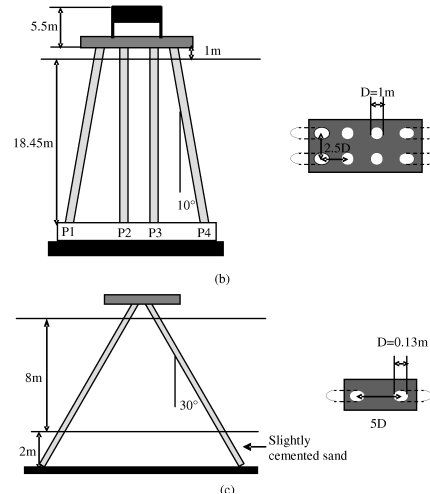


Figure 10: Dynamic studies on the effect of inclined pile, pile group configurations, (a)[OKKZ02], (b)[JBDH98].

tests. Floating and end-bearing pile group configuration can be studied with symmetric and non-symmetric configurations. If these studies highlighted that inclined pile increased the lateral stiffness of the pile group, results of some key points, such as the bending moment near the pile head connection, were contradictory. In this framework a series of dynamic centrifuge tests was performed at the IFSTTAR centre ([Esc12]). The selected experimental approach to highlight the effects of inclined pile was based on the comparison of the response of two simple pile groups. The first one, the reference one was a 2x1 vertical pile group. The second pile group was an asymmetric inclined pile group with a pile inclined at 25° to the vertical and a vertical pile (Figure 11).

In practice the angle of rake is commonly in the $10^\circ - 1^\circ$ range. Centrifuge test offers the possibility to play with the parameter values in order to highlight their effects. Such as for lot of centrifuge tests model piles were aluminium tubular pile. In this series of tests they represented prototype flexible piles with an external diameter of $0.72m$ and a bending stiffness of $505MN.m^2$. Several strain gage levels enabled the bending moment and the axial load to be measured all along the pile length. Kinematic response of the pile cap was followed through accelerometers and high frequency laser sensors. In addition, the soil response was analysed based on acceleration measurements. Two series of tests were performed. One of the objectives of the first series of tests was the determination of the frequency responses of the soil column and of the pile-cap-soil systems. As previously mentioned, the analysis of the frequency response of the different components of a dynamic centrifuge tests is a key point as it can largely influenced the response of the geotechnical structures. The second series

of tests was a parametric study of the input frequency on the performances of inclined pile in pile group.

Theoretically, the use of transfer function should be used in the framework of linear behaviour of a system. However, in practice, determination of the frequency response of different components in dynamic centrifuge tests is performed by using the transfer function approach even if the elastic domain of the soil behaviour is limited. The frequency response of the soil column was determined from the transfer function between the acceleration measured at the base of the container and near the soil surface (Figure 11) and was about 3.7 Hz. In the case of the pile groups, inclined pile increased the frequency response (7.5 Hz and 9.5 Hz instead of 6Hz) and induced a more complicated behaviour (two frequency responses observed instead of one, based on the horizontal acceleration of the pile cap). Based on the determined frequency responses, the parametric study has been performed by considering three sinusoidal inputs 3, 4 and 5Hz at the prototype scale. The lower selected frequency was smaller than all the frequency responses, the second frequency was closed to the response frequency of the soil column and, the third, was about 1Hz larger and 1Hz smaller than respectively the response frequency of the soil column and of the vertical pile group. However it was noticed that the 4 and 5 Hz sinusoidal inputs were in the frequency range amplified by the vertical pile group.

The analysis of the horizontal acceleration, displacement and rotation at the pile cap highlighted that the input frequency largely influenced the performances of the inclined pile. Figure 12 illustrates the horizontal, H1, and the vertical, V2 and V1, acceleration measured on the pile cap. Comparing the results obtained for the 3Hz and the 4Hz sinusoidal inputs, the inclined pile induced a decrease of respectively 20% and 60% for the maximum horizontal acceleration and of 35% and 65% for the horizontal displacement. In addition, double integration of the vertical acceleration of the pile cap enabled the determination of the dynamic rotation of the pile cap. The inclined pile increased the dynamic rotation of the cap of 330% for the 3Hz sine input and of 66% for the 4Hz sine input. However, such as for other kind of tests, confidence in the results depends on the amplitude level of the measured phenomena. In this case, as the rotation angles remained lower than 0.1° , additional tests were recommended by the author to confirm this point.

Finally, one key point of this study was that, in the case of the inclined pile, it was of first importance to take into account the residual bending moment induced by previous events and, the input frequency largely influenced the performances of the inclined pile concerning the maximum bending moment profile (Figure 13).

4.2 Pile and pile group behaviour in liquefiable levelled ground

A lot of series of tests have been performed by different centrifuge teams on the behaviour of pile in liquefiable sand layer. Some of them are reported below to illustrate the experimental researches performed on pile in liquefiable sands. In the follow-

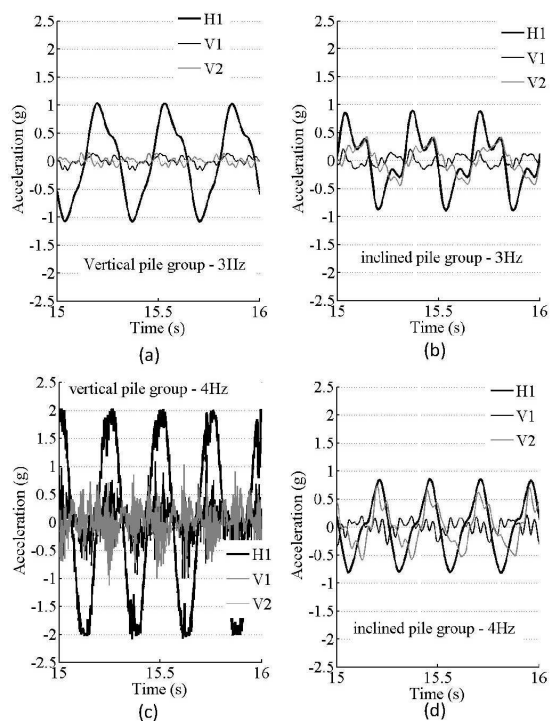


Figure 12: Kinematic reponse of the pile cap : effect of frequency input on the performances of inclined pile, [Esc12].

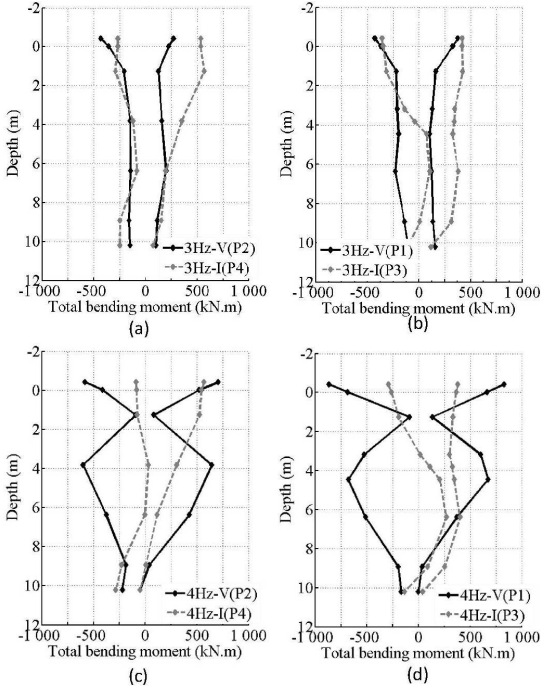


Figure 13: Sinusoidal tests performed at 3 and 4Hz envelop curves of the total bending moment for the pile of the vertical (P1 and P2) and the inclined (P3 and P4) pile group [Esc12].

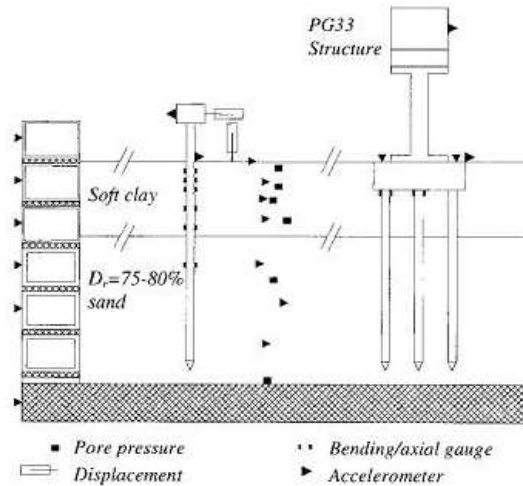


Figure 14: Schematic layout and instrumentation, [CKD01].

ing only studies that concern levelled ground are presented, some example of studies performed in sloping ground can be find in [Dob01].

A series of tests have been performed at Davis University by [Wil98] on single pile, 2x2 and 3x3 pile groups in two layers soil profile of fine Nevada sand (Figure 14).

One of the main purpose of this series of dynamic centrifuge tests was to evaluate the degradation of the p-y curves as the pore pressure built up and the soil liquefied (comparison with the calculated p-y curves using the API codes ([ap993])for a drained response under monotonic loading). All the tests have been performed in an ESB container at a centrifuge gravity of 30g. A 10 cSt viscous fluid has been used as the authors considering that only the response of the pile during the base shaking was of interest. Structural components were selected to be representative of selected bridge structures: prototype piles were steel pipes with a diameter of 0.67 m supporting a superstructure load of 480 kN located 3.81 m above the soil surface. Instrumentation included accelerometers in the soil and on the pile superstructure, pore pressure sensors, LVDT to measure the soil settlement and the superstructure displacement, instrumented piles to obtain the bending moment. Each container has been subjected to several inputs starting from a low level shaking and progressing through strong motions with prototype peak acceleration of up to 0.6g. Full liquefaction appears in the upper layer ($Dr = 35\%$ or 55%) for the higher events.

To obtain the experimental p-y loops, the load p, at a given time during the shaking, was back calculated by double differentiation with respect to depth of the recorded bending moments along the pile, while the displacement of the pile, y_{pile}, was obtained by double integration of the same bending moment. The simultaneous dis-

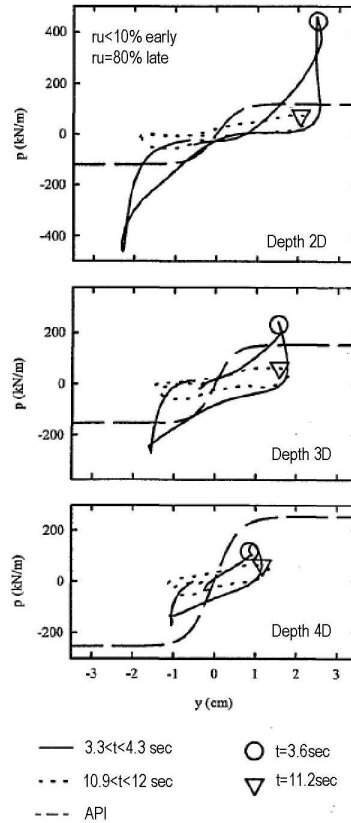


Figure 15: Observed experimental p-y curves in the upper layer $Dr = 55 - 60\%$, [WBB98].

placement of the soil, y_{soil} , in the free field at the same depth was obtained by double integration of the acceleration measured in the soil and $y = y_{pile} - y_{soil}$. Once calculated, the experimental loops on single piles highlighted both, the degradation of the p-y curves with pore pressure built up, and their stiffening when value of y exceed a certain value due to the undrained dilative response of the sand in shear (Figure 15).

The results clearly illustrated that p-y curves, coming from the API code, did not catch the essential features of the dynamic p-y curves in saturated sand.

In another study, [LD95] conducted tests on end-bearing single pile in liquefiable sand (Figure 16).

The main objective was the same as the previous study (obtain a correlation between the p-y curves degradation and the pore pressure built up). However the approach was slightly different: the degradation of the p-y curve was based on results of static

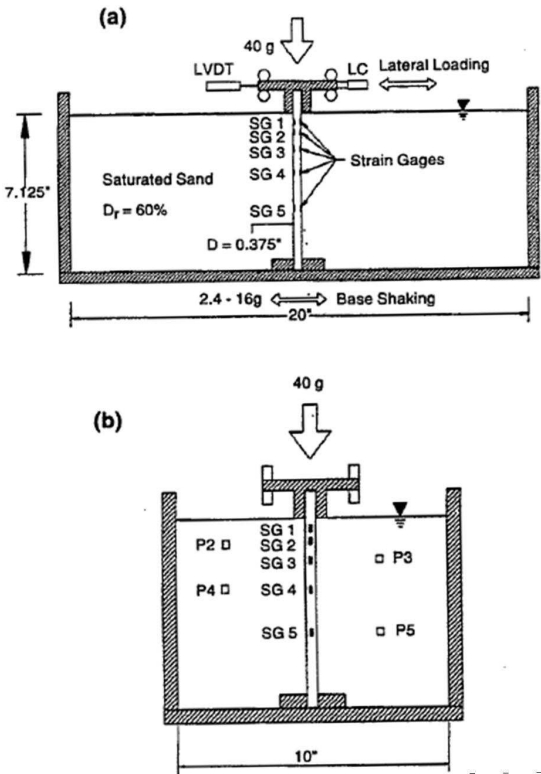


Figure 16: Setup of the experimental model of single pile in liquefiable sand,[LD95].

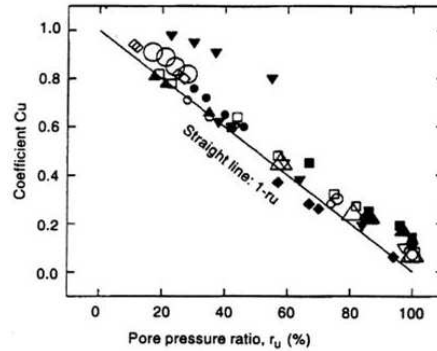


Figure 17: Pore pressure ratio, r_u , versus degradation parameter, [LD95].

cyclic lateral load testing of the pile in flight performed immediately after the shaking. During the seismic event the pile head was fixed and move as the rigid container. Just after the shaking, it was released and a horizontal cyclic loading was applied at the pile head. All the tests were performed at 40g with a 10cSt viscous fluid. The authors indicate that this viscous fluid avoids too rapid dissipation of the excess of pore pressure. The soil response was only follow through pore pressure measurement. The prototype piles were representative of many highway bridge foundations. Contrary to the previous tests the pile tips were rigidly fixed to the bottom of the container and the obtained results did not involve structural inertial forces. Figure 17 below illustrates the results of the analysis that have been performed. A parameter, the dimensionless degradation coefficient C_u , that represents the degradation of the lateral resistance compare to that of the pile before any pressure built up is represented versus the pore pressure built up ratio, r_u . When r_u increased the C_u decreased indicating a degradation of the lateral resistance compare to that of the pile before any pressure built up.

[TIR04] performed a series of tests which main objective was to highlight, or not, if the pile group effects and a p-y curve of a coefficient of subgrade reaction for seismic design can be evaluated based on the data from static tests. Among the series of tests, experiment were made on a single pile and on a 3x3 pile group embedded in saturated sand and subjected to dynamic loadings (Figure 18).

Tests were performed at 40g, using a rigid container and viscous fluid (metolose). Brass tubes were used for the model piles which represented prototype piles of 10 m in length 0.3 m to 0.28 m in diameter with a bending stiffness of $1.7410^7 MN.mm^2$ to $2.1110^7 MN.mm^2$. End bearing configuration was obtained by rigidly fixed the pile tip to the bottom of the container through a stainless plate. Contrary to the previous tests presented the fixity conditions at the pile head was so intended as to be rotation free, but the author indicated that there might be limitations in achieving the perfect rotation free condition because of the friction at the edge contact. In the case of the

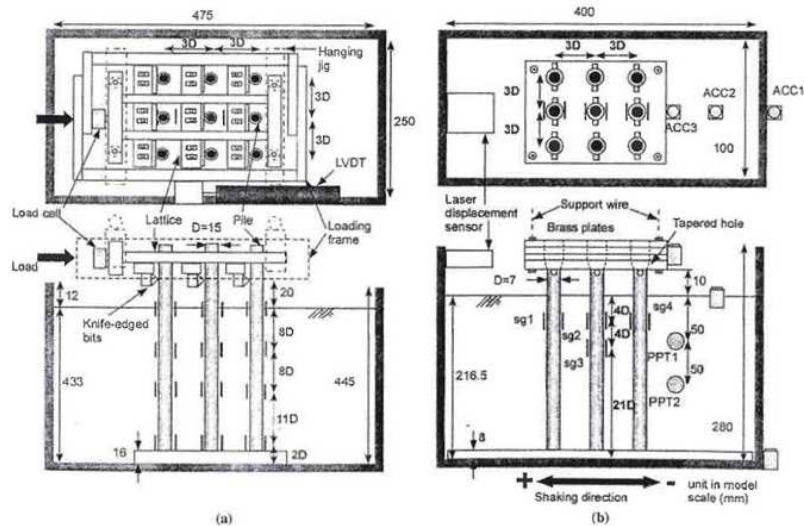


Figure 18: Illustration of the model setup for (a) static test and (b) seismic tests,[TIR04].

saturated sand, the sand water pluviation method was used. This technique is largely less used than the air pluviation following by a saturation step. The dynamic input consisted 20 cyclic loadings at a frequency of 1Hz and amplitude of 0.25g at the prototype scale. Instrumentation enabled acceleration and pore pressure measurements in the soil, measurements of the horizontal acceleration and displacement of the top mass (laser sensors and accelerometers) and bending moment measurement on the piles.

As shown on Figure 19, which illustrates the pile head load-displacement loops, when the soil was liquefied the slope of the load-displacement curve of the pile group was smaller than that of a single pile. Even in a liquefied soil the pile group effect can have been detected. In addition, the analysis clearly highlighted the degradation of the p-y loops due to the liquefaction. However the authors indicated that due to difference that existed between the tests performed on dry and saturated sand, definite conclusion couldn't be derived from this test program.

The main objective of the dynamic centrifuge tests performed by [KM09] was completely different from the previous studies. [KM09] started from the observation that if it is commonly accepted that the lateral displacement can be severely damaging, little attention has been paid to the vertical settlement which can similarly lead to structure damage especially in liquefiable sand. Consequently they performed a series of tests to determine the seismic bearing capacity of 2x2 pile group in saturated two layers

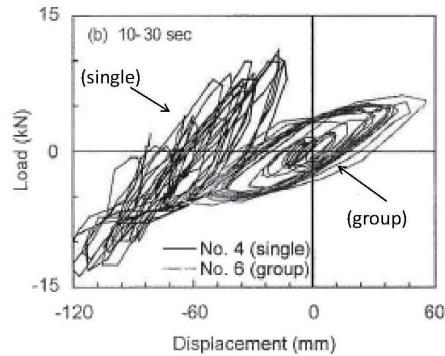


Figure 19: A changer, [TIR04].

soil profiles. More precisely they wanted to develop more deterministic methods for predicting the onset of damaging pile settlement.

In this framework centrifuge tests were performed at 80 g in an ESB box on floating pile groups (Figure 20).

Model pile used corresponded to prototype closed end steel pipe of 0.5m in diameter, a bending stiffness of $164MN.m$ and axial compressive stiffness of $0.96MNm^{-1}$. A top mass was rigidly fixed at the pile head. The pile cap was clear of the surface or in contact with the sand surface (more common condition for pile foundation). Two methods have been used for the pile installation: at 1g or under increasing self weight during the spin up of the centrifuge. Piles were instrumented to measure the loads carried by pile both at the pile base and along the shaft when the soil around liquefied. The A PRIORI assumption was that as dense sand located at the pile tip could experience large increase of pore pressure their stiffness could experience a large decrease during cyclic mobility phenomena and it could have a none negligible influence on the total settlement of the pile. Viscous fluid was used to avoid scaling conflicts. Instrumentation enables the free field response analysis through acceleration and pore pressure measurements. Such as for the previous configurations presented the top mass was rigidly fixed to the pile heads.

Authors highlighted that the settlement has been controlled by the bearing layer settlement higher than 1 diameter and up to 5 diameters and the co-seismic settlement was largely higher than the post-earthquake settlement. The authors concluded that settlement occurring during the shaking were found in all the cases to be damagingly large (in excess of one pile diameter) which was correlated with an increase in excess pore pressure to full liquefaction conditions in what is conventionally considered to be non-liquefiable soil. Additionally, non-zero pile shaft loads were observed in fully liquefied soil in all tests contrary to commonly accepted design assumption. Based on these findings, an analytical solution was presented which allows for the determination of a suitable static safety factor in pile design to avoid bearing capacity failure for given liquefaction conditions.

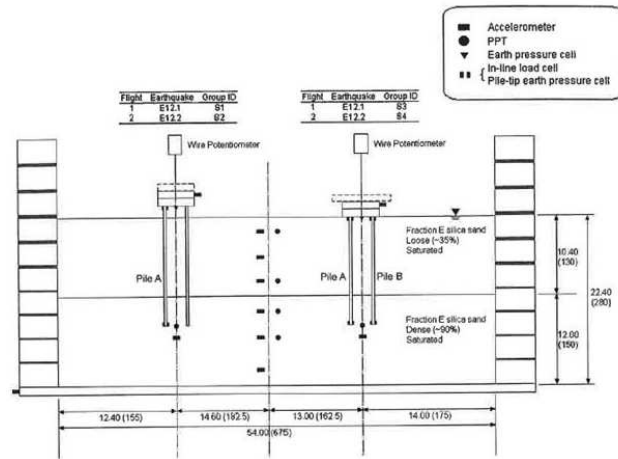


Figure 20: Experimental layout - dimensions at the model scale in mm, [KM09].

5 Conclusion

The different studies that have been presented illustrate that the objective of dynamic centrifuge studies is not to replicate a prototype structure. Compared to real geotechnical structures, centrifuge models are more simpler in order to put in relevance the effect of some parameters. The experimental studies are based on a parametric approach, or on a comparative or on a combination of both. Use of centrifuge modelling offers this advantage of performing analysis on the effect of the input frequency that can largely influence the response of the soil-structure interaction. Moreover to enhance the effect of a parameter it is possible to increase its value out of the practice range, such as for pile inclination. The case of studies on shallow foundations that have been reported illustrate that some simplifications can be made, depending on the objective (design of the structure : rigid building, heavy foundation, SDOF building). However in all the cases they enabled to highlight the seismic behaviour. In the cases of deep foundations, such as for the shallow foundations, limitation still exist such as the connectivity at the pile head for pile group, limitation in terms of the size of the pile group. However the key feature can be put in relevance. Nevertheless, even if dynamic centrifuge modelling can provide some data for the calibration and validation of numerical or analytical model, it is important to take into account the limitation of the studies that come from the experimental possibilities (use of a rigid box, use of a non viscous fluid, limitations of the sensors properties etc).

References

- [af9] Eurocod 8: Calcul des structures pour leur recentsistances auxreeismes parie 5: Fondations, ouvrages de soutenements et aspects geotechniques nf en 1998-5.
- [ap993] Recommended practice for planning, desdesign and constructing fixed offshore platforms, 1993.
- [BM02] A.J. Brennan and S.P.G. Madabhushi. Design and performances of a new deep model container for dynamic centrifuge testing. In Philips, Guo, and Popescu, editors, *Physical Modelling in Geotechnics: ICPMG'02*, pages 183–188, 2002.
- [CEG⁺08] J.L. Chazelas, S. Escoffier, J. Garnier, L. Thorel, and G. Rault. Original technologies for proven performances for the new lcpc earthquake simulator. *Bulletin of earthquake engineering*, 6:723–728, 2008.
- [Che07] N. Chenaf. *Interaction inertielle et interaction cinematique sol-pieu*. PhD thesis, Universite de Nantes, 2007.
- [CHH⁺12] U. Cilingir, S. Haigs, C. Heron, G. Madabushi, J.L. Chazelas, and S. Escoffier. *Cross-Facility Validation of Dynamic Centrifuge Testing*, chapter 5, pages 83–98. Springer Netherlands, 2012.
- [CKD01] C.J. and Boulanger R.W. Curras, B.L. Kutter, and Wilson D.W. Dynamic experiments and analysis of a pil-group-supported structure. *Journal of geotechnical*, 127:585–596, 2001.
- [DBP⁺10a] S. Dashti, J.D. Bray, J.M. Pestana, M. Riemer, and D. Wilson. Centrifuge testing to evaluate and mitigate liquefaction-induced building settlement mechanism. *Journal of Geotechnical and Geoenvironmental Engineering*, 136(7):918–929, 2010.
- [DBP⁺10b] S. Dashti, J.D. Bray, J.M. Pestana, M. Riemer, and D. Wislon. Mechanisms of seismically induced settlement of buildings with shallow foundations on liquefiable soil. *Journal of Geotechnical and Geoenvironmental Engineering*, 136:151–164, 2010.
- [DKTF99] M. M. Dewoolkar, H.-Y. Ko, Stadler A. T., and Astaneh S. M. F. A substitute pore fluid for seismic centrifuge modelling. *Geotechnical Testing Journal*, 22:196–210, 1999.
- [Dob01] T. Dobry, R. and Abdoun. Recent studies on ceismic centrifuge modelling of liquefaction and its effect on deep foundations. In *Fourth International Conference on Recent Advances in Geotechnical Earthquake Engineergin and Soil Dynamics and Symposium in Honnod of Professor W.D. Liam Finn*, San Diego, California, 2001.

- [EC14] S. Escoffier and J.L. Chazelas. Seismic soil structure interaction: a parametric study on shallow foundations. In *Physical Modelling in geotechnics*, 2014. to be published.
- [ECG08] S. Escoffier, J.L. Chazelas, and J. Garnier. Centrifuge modelling of racked piles. *Bulletin of Earthquake Engineering*, 6:689–704, 2008.
- [Esc12] S. Escoffier. Experimental study if the effect of inclined pile on the seismic behavior of pile group. *Soil Dyn. and Earthq. Engrg.*, 42:275–291, 2012.
- [FHI+94] G.L. Fiegel, M. Hudson, I.M. Idriss, B.L. Kutter, and X. Zeng. Effect of model containers on dynamic soil response. In Leung, Lee, and Tan, editors, *Centrifuge 94*, pages 145–150, 1994.
- [GK09] S. Gajan and B.L. Kutter. Effects of moment-to-shear ratio on combined cyclic load-dispalcement behavior of shallow foundations in centrifuge experiments. *J. of geotech. and geoenv. Engrg.*, 135:1044–1055, 2009.
- [GKP+05] S. Gajan, B.L. Kutter, J.D. Phalen, Hutchinson T.C., and Martin G.R. Centrifuge modeling of load-deformation behavior of rocking shallow foundations. *Soil Dyn. and Earthq. Engrg.*, 25:773–783, 2005.
- [GM03] B. Ghosh and S.P.G. Madabhushi. Physical modelling of faillure of raft foundation during earthquake liquefaction. In Magnan and Droniuc, editors, *Fondations superficielles*, pages 287–294, 2003.
- [GS11] S. Gajan and D.S. Saravanathiiban. Modeling of energy dissipation in structural devices and foundation soil during seismic loading. *Soil Dynamics and Earthquake Engineering*, 31:1106–1122, 2011.
- [JBDH98] I. Juran, A. Benslimane, S. Drabkin, and S. Hanna. Centrifuge model test on single, group and network of micropile. preliminary report, seismic behaviour of micropile systems. Technical report, Polytec. Univ. Dept. of Civil and Environ. Eng., 1998.
- [KM09] J.A. Knappett and S.P.G. Madabhushi. Seismic bearing capacity of piles in liquefiable soils. *Soils and Foundations*, 49:525–535, 2009.
- [Kut95] B.L. Kutter. Recent advances in centrifuge modeling of seismic shaking. In *Third International Conference on recent advances in geotechnical earthquake Engineering and soil Dynamics*, volume 2, St Louis Missouri, April 1995.
- [LD95] L. Liu and R. Dobry. Effect of liquefaction on lateral response of piles by centrifuge model tests. *NCEER Bulletin*, pages 7–11, 1995.
- [LD97] L. Liu and R. Dobry. Seismic response of shallow foundation on liquefiable sand. *Journal of geotechnical and geoenvironmental engineering*, 123:557–567, 1997.

- [Lee90] F.-H. Lee. Frequency response of diaphragm pore pressure transducer in dynamic centrifuge model tests. *Geotechnical Testing Journal*, 13:201–207, 1990.
- [Mad94] S.P.G. Madabhushi. Dynamic response of the equivalent shear beam (esb) container. Technical Report CUED/D-SOILS/TR270, Cambridge university Schofield center, 1994.
- [OKKZ02] K. Okawa, H. Kamei, M. Kimura, and F. Zhang. Dynamic behaviour of a group-pile foundation with inclined piles in loose sand. In G. Philips and Popescu, editors, *International Conference of Physical modelling in Geotechnics ICPMG'02*, 2002.
- [PSY07] R. Paolucci, M. Shirato, and T. Yilmaz. Seismic behaviour of shallow foundations: shaking table experiments vs numerical modelling. *Earthquake Engineering and structural dynamics*, 37:577–595, 2007.
- [SCB98] D.P. Stewart, Y.R. Chen, and B.L. Butter. Experience with the use of methylcellulose as a viscous pore fluid in centrifuge models. *Geotechnical Testing Journal*, 21:365–369, 1998.
- [Sch80] A.N. Schofield. Cambridge geotechnical centrifuge operation. *Geotechnique*, 30:227–268, 1980.
- [TIR04] T. Tobita, S. Iai, and K.M. Rollins. Group pile behaviour under lateral loading in centrifuge model tests. *International Journal of Physical Modelling in Geotechnics*, 4:1–11, 2004.
- [TKIY06] H. Takahashi, M. Kitazume, S. Ishibashi, and S. Yamawaki. Evaluating the saturation of model ground by p-wave velocity and modelling of models for liquefaction study. *International Journal of Physical Modelling in Geotechnics*, 6:13–25, 2006.
- [TM03] B. Teymur and S.P.G. Madabhushi. Experimental study of boundary effect in dynamic centrifuge modelling. *Geotechnique*, 53:655–663, 2003.
- [UKJG07] J.A. Ugalde, B.L. Kutter, B. Jeremic, and S. Gajan. Centrifuge modelling of rocking behaviour of bridge on shallow foundations. In *4th international conference on Earthquake Geotechnical Engineering*, 2007.
- [VLTDE94] P.A. Van Laak, V.M. Taboada, R. Dobry, and A.-W. Elgamal. Earthquake centrifuge modelling using a laminar box. In *Dynamic Geotechnical Testing II*, pages 370–384. ASTM american society for testing and material, 1994.
- [WBB98] D. W. Wilson, R. W. Boulanger, and B. L. Bruce. Signal processing for and analyses of dynamic soil-pile interaction. In Kimura, Kusakabe, and Takemura, editors, *Centrifuge 98*, pages 135–140, 1998.
- [Wil98] D. Wilson. Soil-pile-structure interaction in liquefying sand and soft clay. Technical Report UDC/CGM698/04, Center for Geotechnical

- Modelling , department of Civil Engineering, University of California, 1998.
- [WL86] R.V. Whitman and P.C. Lambe. Effect of boundary conditions upon centrifuge modelling using ground motion simulation. *Geotechnical testing Journal*, 9:61–71, 1986.
- [YLL06] J. Yang, J.B. Li, and G. Lin. A simple approach to integration of acceleration data for soil structure interaction analysis. *Soil Dyn. and Earthq. Engrg.*, 26:725–734, 2006.
- [ZS96] X. Zeng and A.N. Schofield. Design and performance of an equivalent-shear-beam container fo earthquake centrifuge modelling. *Geotechnique*, 46:83–102, 1996.
- [ZS98] X. Zeng and R.S. Steedman. Bearing capacity failure of shallow foundations in earthquakes. *Geotechnique*, 48:235–256, 1998.

Using strong and weak motion to identify the dynamic characteristics and the response of buildings considering soil-structure interaction

Philippe GUEGUEN

ISTerre, Université Joseph Fourier Grenoble 1/CNRS/IFSTTAR

Experimental assessment of existing buildings is of increasing interest for applications in mechanical engineering, civil engineering and earthquake engineering. For example, elastic fundamental frequency and damping ratio are two key-parameters of simplified seismic design and vulnerability assessment methods. Empirical relationships exist in codes to estimate this frequency and damping but experimental data could be used for improving them, accounting for national feature of building design and, above all, corresponding uncertainties. With advances in data acquisition systems (number of measurement points, continuous recording, low-noise instrument) and advances in signal processing algorithms, further and better studies can be conducted on civil engineering structures for evaluating their modal parameters and their physical properties, with a high level of confidence. Moreover, permanent instrumentations provide also earthquake data helping in the improvement of the building response in case of severe event. The aim of this course is to show how the experimental data, providing from temporary or permanent instrumentation, can be used for adjusting behavior models for each class of structure for vulnerability assessment, for monitoring the wandering effect of the elastic parameters on the fragility curves and their uncertainties and for analyzing the soil-structure interaction.

1 Introduction

Dynamic building response assessment under moderate-to-strong shaking is a multi-disciplinary activity, involving structural engineering, signal processing and earthquake engineering applications. Most of these activities result in searching physical parameters that provide information on the building characteristics, and therefore its seismic behavior and resistance in case of earthquakes. Since the design forces

in structures are frequency and damping dependent (based on the seismic coefficient $C(T, \xi)$ where T is the period of the building and ξ is the damping ratio), these two parameters are the subject of special attention and focus of many research activities. This is all the more important that the evaluation of existing structures requires knowledge of the design and quality of materials which is often difficult to obtain.

In response to the growing complexity in building design and construction, new instruments and signal processing techniques are being developed, using earthquake recordings or ambient vibrations. Most surveys consist in installing accelerometers or velocimeters in the target building and recording vibrations using digital and handheld acquisition systems. After the first experiences in 1930's, in the middle of 80's numerical modeling gained more and more interest and the activities related to field testing decreased. Nevertheless, while the first application were focused on the understanding of the data, some recent applications have emerged again, taking advantages on recent developments of signal processing theory and more than anything by the accessibility of the new extensive data and the performance of modern acquisition systems.

Over the last two decades, efforts have been made in moderate seismic regions to update Eurocode 8 [EC898], by improving the seismic hazard evaluation using probabilistic seismic hazard assessment (PSHA) methods, and by including recent knowledge on structural dynamics theory. Nevertheless, most losses produced by earthquakes throughout the world are due to deficient seismic behavior in existing buildings in spite of improvements made to seismic codes [CS02]. A critical step in seismic risk assessment is therefore to be able to predict the expected damage for a given earthquake in existing structures. In the literature (see [CMB⁺06] for a complete review), the first vulnerability methods were developed in strong seismic regions, based on post-seismic inventories used to adjust continuous (Vulnerability Functions VF) or discrete (Damage Probability Matrices DPM) functions of seismic damage. DPM give the conditional probability of obtaining a specific damage level for a given level of hazard severity while VF provide average damage for a given level of ground motion. Since the publication of these methods, they have been widely applied in-extenso especially in regions without recent destructive earthquakes that allowed to calibrate the vulnerability curves including the regional specific design. In this way, the vulnerability analysis can be biased and introducing some epistemic uncertainties. Spence et al. [SBDR⁺03] supported that the adjustment of structural models should assume a large set of unknown parameters influencing the response of existing buildings and introducing a large range of errors and epistemic uncertainties for the establishment of fragility curves, generally due to the lack of structural plans, aging and structural design. One solution to reduce these epistemic uncertainties is to perform field testing in buildings, providing an estimate of the elastic modal parameters of structures (resonance frequencies, damping ratios and modal shapes). Weak and strong excitations can be used, their characteristics and recording devices deployed in the structure having influences on the data processing (output only or input-output methods), the interpretation (linear or nonlinear behavior, including soil-structure interaction or not), and their applicability (building specific analysis or by typologies).

The main goal of this course is to show how field testings can be implemented for earthquake engineering, vulnerability assessment and structural health monitoring ac-

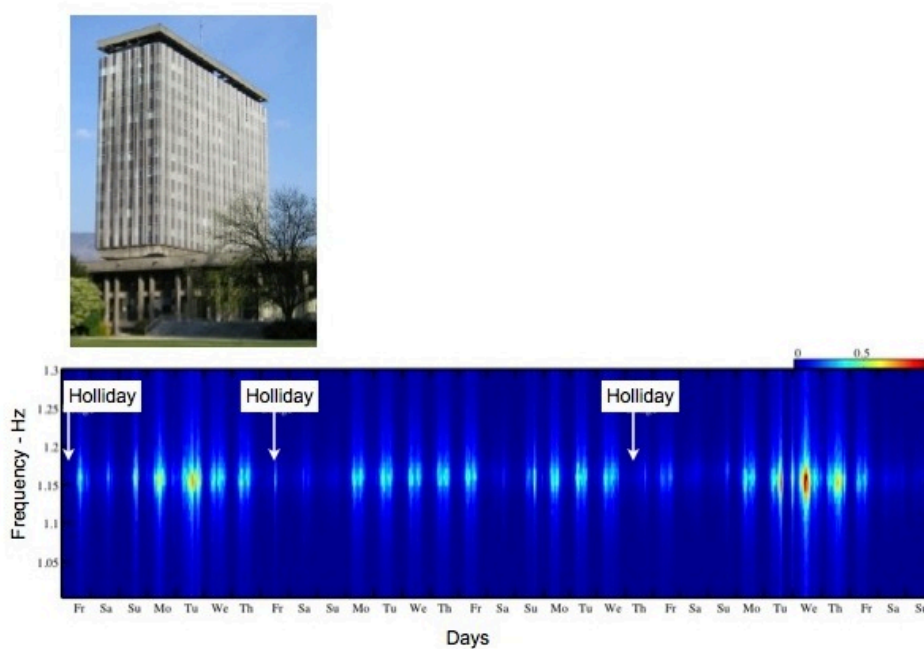


Figure 1: Fourier transform of the ambient vibrations recording at the top of the City-Hall building of Grenoble during May 2009 (after [Mik11]).

tivities, by contributing to the improvement of the dynamic response of existing buildings. After a brief remain of the first application for earthquake engineering, the stability and accuracy of the experimental modal parameters are discussed.

2 Experimental assessment of building characteristics for earthquake engineering

2.1 First testings in buildings using ambient vibrations

We very probably owe the first building recordings to the Japanese seismologist F. Omori at the start of the 20th century whose works are described by Davison [Dav24]. Part of his work consisted in the evaluation of resonance frequency in structures under weak stress before and after an earthquake and linked the observed variations to damage [Omo22]. We can also note the work of Ishimoto and Takashi [IT29] who published in French on the recording of ambient vibrations in buildings. Ambient

vibrations are produced by the wind (low frequencies $< 1Hz$), internal sources (machinery, lift at high frequencies) and seismic noise (broadband) (Figure 1). The use of AV methods provides relevant information on the elastic characteristics of the building at reducing cost. In the United States also, as early as the 1930s, with the beginning of the construction of skyscrapers, researchers focus on the recording of ambient vibrations in high buildings to understand their dynamics, particularly during a seismic event [BHM31]. A measurement campaign therefore takes place between 1934 and 1935 by the US Coast and Geodetic Survey [Car36], especially in California. This campaign is a follow-up of the 1933 Long Beach earthquake. The collected data is at the origin of the first empirical expressions giving the vibration period according to the height [Spa35]. This study has been carried out in 336 Californian buildings, which was at the time, considering the available means of recording, storing and processing data, a considerable achievement. Indeed, if the engineering seismologists are interested in high buildings, it is because of the fact that, to be sensitive, the seismometers require large masses. As a result the *portable* apparatus can only record the large amplitudes that we find at the top of buildings. To further increase these amplitudes, Blume [Blu35] proposes for the first time a rotating device allowing to force buildings into vibration. Tests under forced vibrations are further developed in Japan (e.g. [KTS49]) and in the United States (e.g. [HH54]) keeping the objective of characterizing the structures for seismic analysis.

2.2 Permanent instrumentation for earthquake engineering

From the 1960s, the empirical expression giving the period, obtained in the 1930s and included in the American earthquake engineering regulations, are discussed [KY61] [HB63]. They are put in question particularly because the recording devices and tools of signal processing were very approximate, but also because the recordings were made in buildings of which the build had changed since then. More modern recording techniques of ambient vibrations are described by Crawford and Ward in 1964 [CW64] who also revoke the expressions obtained in the 1930s. Trifunac [Tri72] shows that the obtained results under ambient and forced vibrations are identical, but the former remain hardly used. In Europe, the IZIIS institute (Macedonia) appears as a precursor with a program of ambient vibration recordings in structures following the Skopje earthquake in 1963 [KT05]. It appears however with the experiment that the only indisputable validation of engineering calculations can only come from the recording of strong motions in buildings. After the Japanese [TYOM69], California launches in 1972 a vast program of instrumentation of buildings, dams and bridges (CSMIP) [Hou57] [JK68] [Blu72] [LTW87]. Several researchers (e.g., [GC98]) directly use these recordings to propose empirical expressions giving the period but until the 2000s, the number of available recordings remains statistically insufficient. Research then focuses on a very small number of instrumented buildings, including the Millikan Library [CBHF06]. Consequently, the variations in resonance frequencies due to the amplitude of the applied stress, to climatic conditions, to seismic damage

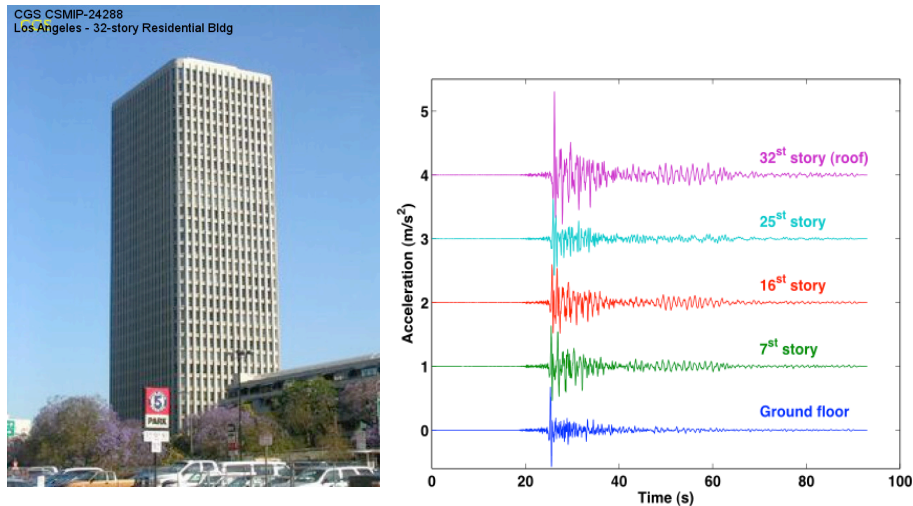


Figure 2: Examples of seismic data recorded in one building of the CSMIP database in California.

and the soil-structure interactions can be studied. Today the CSMIP has 170 buildings, 20 dams and 60 bridges (Figure 2). In Japan, the Building Research Institute (BRI) in Tsukuba manages a network of accelerometers in place in 74 buildings, the main objective being the analysis of the dynamical behavior of buildings representative of Japan (e.g., [Sat96]). Most instrumentation consists in one device at the base and one device at the top of the building with an additional sensor in the middle according to the dimensions of the edifice. Finally, a free-field sensor is sometimes installed for the analysis of the soil-structure interactions. In New-Zealand, the GeoNet Building Instrumentation Program [UKCG11], coordinated by the GNS Geological Neo-Zealand Service focused on the analysis of buildings and bridges. Several 3 component sensors are installed, on the different floors, to analyze the seismic response of the structures and the soil-structure interactions. Deformation sensors (LVDT: linearly variable differential transducers) complete the instrumentation so as to observe the differential displacements between different points. In Taiwan, the project Taiwan Strong Motion Instrumentation Program (TSMIP) began in 1992 with the objective of building a network of free field and building accelerometric stations. Currently, around 60 networks in buildings have been deployed, with configurations of several stations distributed on different floors or below ground level. The scientific objectives of these instrumentations are the dynamical response of typical edifices in Taiwan and the soil-structure interaction phenomena. The data is not available and it is difficult to know the importance of these instrumentations, whereas the seismic level of Taiwan suggests a rich database. In Europe, several punctual operations also exist, for which the available information is rare and the data non-public.

In France, the permanent accelerometric network (RAP) launched in 2004 a national instrumentation of buildings program (RAP-NBAP: National Building Array Program) of which the data is public and available on the web. In France mainland, three buildings are instrumented in Grenoble, Lourdes and Nice. In the Antilles, with the participation of the regional council of Martinique, it is two additional buildings that provide data of strong motion [PGHL08]. After a pilot phase on the Grenoble city hall, a schematic of standard instrumentation has been proposed, gathering 24 sensors, tri-axial or mono-axial, distributed in the building for the analysis of mode shapes [MGEA⁺10], of the dynamical response [MG10], of the soil-structure interaction [MGEA⁺10] and serves as pilot site to test numerical models using data from earthquakes [MGEA⁺10] [MGD11]. The data acquisition is perfectly synchronized, with a temperature sensor added to the top of the structure. One can also note the instrumentation of structures in moderate-to-weak seismic prone regions, as for example in Romania [ASEK07]. Actually, the UCLA Factor Building is certainly the best instrumented building in the world with 72 components continuously recording the vibrations [KDS05], [KDS05].

2.3 Improving the instrumentation for a better assessment

At the same time as permanent instrumentation programs are being developed, new technologies appear, allowing to make the mobile recording devices more compact and able to record simultaneously in different studied parts of the structure. Digital acquisition system, light and of high resolution (with is to say with dynamic range of 24 bits), allow to record several synchronized channels onto Flash memory drives, to visualize the signals, or even to directly make preliminary calculations. The synchronization is done by cable, by GPS or even by remote triggering. For the works presented here, the choice of robustness has been made with a CitysharkTM 2 station [CGG⁺00] [CGG⁺12] allowing the recording of 18 simultaneous (cables) channels (either six 3 component sensors) but without the possibility of visualization. Clinton et al. [CH02] demonstrated also the evolution of the accelerometric sensors coupled to modern 24-bit digitizers, increasing the resolution and the range of amplitude of signal and having also an absolute time reference for each recording.

These 3 characteristics make the quality of a seismological sensor that can be used in a structure. Amongst them, the 5s Lennartz seismometers are well adapted to the measurements of ambient vibrations in structures. Relatively heavy, they guarantee a good coupling with the support and are therefore almost insensitive to close movements (movement of the cable, wind etc.). They have a response flat in velocity between 0.2 and 50 Hz and are more sensitive than the best accelerometers. However, the evolutions are rapid, whether it is for the permanent or temporary instrumentations. For example, the permanent networks develop wireless communication systems [CFP⁺06] [Lyn07], with continuous real time transmissions, allowing to permanently follow the

evolution of the characteristics of the structures and therefore of their structural integrity (Structural Health Monitoring), that we imagine with ease, could integrate an warning device. We can also cite the apparition of tri-axial micro accelerometric sensors. These sensors are made with the MEMS technology (micro-electro-mechanical system) coupled to numerical control. The sensor is called numerical as the information out of the sensor is directly numerical. This technology offers the advantage of having a much reduced size, a very reliable consumption, a very good mechanical resistance and a very good immunity to electric/electromagnetic noises (steps of analogic signals). Their sensitivity, not as good as that of classic digital sensors, is compensated by the possible deployment of large numbers of sensors. For temporary experiments, new means for vibration recordings appear, based on the Lidar terrestrial technology [GJMS10], recordings of vibrations by radar [GB10], or by correlation of images taken by rapid and high resolution cameras [CRSP85] [MR11]. In all cases, the objective is to facilitate the acquisition of information without deploying the instruments in the buildings, or by increasing the quantity of information or recording points, that when we wish to work at the scale of a city, contribute in the selection of the most efficient and profitable solutions. Moreover, it may be more worthwhile and safer to record the resonance frequencies of buildings using a remote system. Worthwhile because of the repeatability of measurements without entering the buildings, making this approach suitable for the analysis of large sets of buildings, and safer for the post-earthquake assessment of building integrity when aftershocks are able to cause total collapse of damaged buildings.

3 Signal processing and analysis

The experimental modal analysis has for objective the use of vibration recordings in structures to determine their modal parameters (frequencies, damping, mode shapes, or even the participation coefficient). The recordings in structure are processed in a different manner if the studied signal is transitory (earthquake, shock...) or stationary (ambient vibrations, forced vibrations...). If we assume that a structure behaves in a linear manner with viscous damping, its dynamical behavior can be described with the help of its normal modes: the modal analysis [CP93]. Each mode is characterized by its normal frequency (or resonance), its damping coefficient, its modal deformation and its participation coefficient. In structure dynamics, 1D models of *beam* type are often used to demonstrate the behavior of regular buildings and allow to estimate the seismic behavior. And so, with the help of such models, we can show that the three first modes are generally enough to describe the dynamical behavior, as it mobilizes more than 90% of the modal mass in most cases. Most of the time, only the first mode is considered. For the analysis of transitory signals, we use the so-called *input-output* analysis methods. They consist in the determination of filter models, linear most of the time, allowing from the recorded input signal (at the base of the building for the seismic case) to recreate the output signal (response), also recorded (at different floors of the building, for example). The characteristics of the filter, that is to say the transfer

function of the system, yield estimations of the resonance frequencies, of their damping or eventually of their deformation according to the position of the recordings. The most simple technique consists in the estimation of the input and output spectrums and to make a ratio. The determination of the characteristics can then be made by manual peak picking or by adjustment of a linear filter, for example auto-regressive (AR), or more generally ARMAX [Saf89]. These techniques do not allow however to indicate the temporal variation of the modal parameters as the one that, for example, occurs during an earthquake. Another family of techniques used to study the variations in resonance frequency with time is the time-frequency analysis (e.g., [MG10]). They consist in the application of an input-output technique, either successive temporal windows (with limitation on precision), or direct estimation of the energy repartition in the time/frequency plan with the help of mathematical distributions [AFGL95].

For the analysis of long lasting signals that describe a stationary motion (ambient vibrations), we resort to *output only* techniques. The hypothesis behind these methods is that the input shaking is white noise and the measured response of the structure, average over a sufficiently long period of time, is directly its transfer function. This hypothesis is valid considering the strong signal-to-noise ratio and the low damping of the civil engineering structures. Many time or frequency methods exist [PDR01]. For the frequency related methods, the first step consists in the estimation of the spectral power densities. Several signal processing techniques allow this calculation. The most common [Wel67] consists in making the average of the Fourier transformation on apodized windows that cover each other. When simultaneous recording are available, the already made correlation of each recording with a reference, for example at the top a building, allows to remove the non-correlated noise. This technique is sometimes called manual *peak picking* (Figure 3). Or even better, the *Frequency Domain Decomposition* (FDD) [BZA01] performs the decomposition into singular values the spectrum density matrices (correlation between all recordings). This method, relatively simple, yields significantly better results for civil engineering structures. The FDD allows to decompose the modes, even at close proximity, under the following hypotheses that we find in buildings in urban environments: white noise input signal, weak damping and orthogonal close modes. Finally, the methods of adjustments of linear filters in described frequencies for the analysis of transitory signals are also applicable to the ambient vibrations.

The time related methods have as objective to recover the impulse responses of each mode. These responses characterize the mode by their frequency of oscillation (number of crossings to zero) and their damping (logarithmic decrement to find the damping coefficient). Here again, different strategies exist. With just one recording, the random decrement technique consists in the averaging of filtered temporal windows in the interval of frequency sought with the same initial conditions [VDCC82] [ABI99] [MGB⁺13]. This allows to delete the non-correlated noise and therefore to recover the impulse response. Other methods allow to adjust the variables of dynamic system state models considered (Stochastic Subspace Identification) [RDR08].

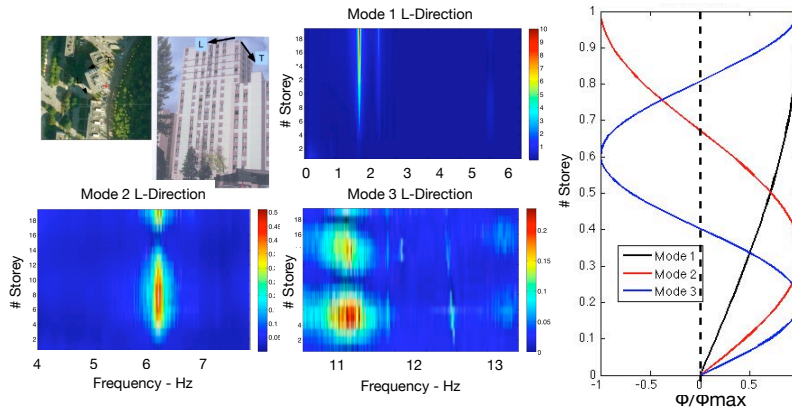


Figure 3: Peak-picking method applied to the Ophite tower (Lourdes - France) part of the National Building Array Program of the French Accelerometric Network. The variation of the amplitude of the Fourier spectra at each floor gives the position of the nodes and anti-nodes of the mode shapes of the building.

Finally, another family of methods, the seismic interferometry, has recently been applied with success to the experimental modal analysis of buildings [SS06]. The idea of this technique is not to directly study the modal parameters but the functions of Green between different points of a structure, functions that describe the way in which the wave field is transformed between one point and another. To obtain these functions, Snieder and Safak [SS06] propose to deconvolute the recorded signals by one of them, a good option being of doing this with the signal at the top of the building to obtain the simplest functions as possible (Figure 4). These authors have shown that we can observe in this manner the energy traveling in the structure from bottom to top and from top to bottom. Like this we can easily calculate the velocity of energy propagation in the structure. Assuming that the structure is equivalent to a shear beam model, the authors have shown that this velocity is linked to the normal mode of the structure, with a fundamental frequency proportionate to the quarter of the wavelength τ , $f_0 = 1/4\tau$. The damping, assumed to be viscous, is deducted from the decay of the amplitude of the Green functions. Prieto et al. [PLCK10] have extended the method to the analysis of ambient vibrations. The practical interest of this method has been shown in particular by Todorovska [Tod09] who affirms that in the case of a building experiencing a rocking of its foundations, this method is the only one capable of giving modal parameters of the structure at fixed base, independently from the ground-structure interactions. Indeed, when rocking occurs, the movement of the foundations and the building are intimately linked and no processing of signals can distinguish one from another. The recordings therefore allow, at best, to estimate the modal parameters of the soil-structure system. On the other hand, seismic interferometry gives in a general manner the way in which the waves propagate between two points, so also between

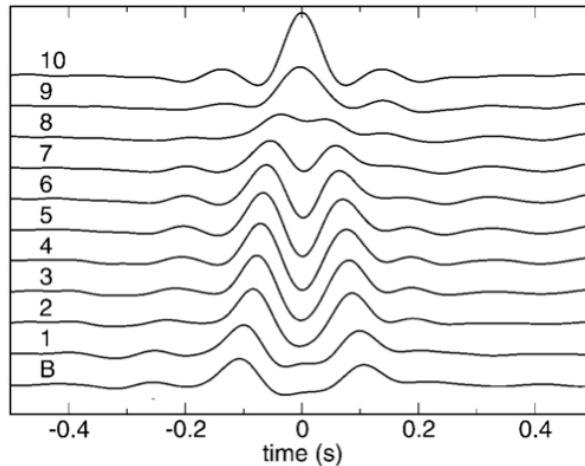


Figure 4: Seismic interferometry of the building computed at the Milikan Library by Snieder and Safak [SS06]

the base and top of the structure, which corresponds to its characteristics at fixed base.

However, this method requires a model to go from Green's functions to resonance frequencies (not for the damping). In other words, the way of finding the modal shapes has not yet been proposed. The fundamental limitation comes from the hypothesis of a pure shear beam. Michel et al. [MGL11] have shown that resulting from it would be a systematic shift of several tens of percents in the estimation of the frequency for shear-wall buildings. This allows to use this method in a relative but not absolute manner.

4 Updating model using field testings

4.1 Improving the empirical relationship found in the seismic code

Michel et al. [MGLB10] have regrouped available data of ambient vibrations in France to study the relationship between the first resonance frequency and building characteristics, as was done in the 1930s by the pioneers in the discipline. These expressions are used in the earthquake design rules of different countries to allow the engineer to estimate the frequency of the structure that he dimensions in the calculation of seismic forces (or of the displacements) to be taken into account, if no model is yet available. More recently, such expressions have been used in the analysis of vulnerability at a large scale [LG06] [CP10].

There is an ongoing debate on the definition of the *elastic frequency*, or of its oppo-

site the elastic period T that therefore need to be used [GMC11]. If in an force-based approach, recommended in the earthquake codes until the 2000s, it is best to overestimate the frequency to stay conservative, which is the opposite of an displacement-based approach that is now encouraged for the seismic design of new structures. Also, for an estimation of the vulnerability of the existing building, it is a non-biased value that must be sought for.

In the US codes, the simplified expressions for buildings with these walls have firstly taken the form of:

$$T = \frac{C_t H}{\sqrt{L}} \quad (1)$$

with H the height of the structure, L the length of the building in the considered direction and C_t a constant depending on the construction materials. This expression originated from a hypothesis of behavior in bending [CP10]. The values of the constant have been obtained experimentally with the help of data with ambient vibrations by Carder [Car36] and Japanese data [HB63]. We also find this kind of expression in numerous codes over the world (Korea, Algeria). We note in code PS92, effective in France until recently, the presence of similar original expressions, but of which the source is unknown by the authors. Today, the very large majority of the simplified expressions that we can find in the literature are under the following form:

$$T = C_t H^\beta \quad (2)$$

The origin of this expression is a simplified calculation available in the ATC3-06 [ATC78] [CP10] for frames in reinforced concrete (RC) or steel. This calculation therefore gives $\beta = 0.75$ for this type of structure, but this value is used again in Eurocode 8 [EC898] for all types of structures. The values of C_t have been generally obtained empirically, for example with the help of several recordings of strong motion in structures [CP10]. For this walls in reinforced concrete, Eurocode gives $C_t = 0.05$. Michel et al. [MGLB10] defined the relationships in common conception French buildings, using recordings made in reinforced concrete buildings in Grenoble (66 structures) and in Nice (28 structures) have been gathered together and studied. Coefficient β is found to be equal to 0.98 and 0.92 for parameters H and N , respectively, and they approximated the relationship for reinforced concrete structures in France by:

$$T = 0.013H = \frac{N}{25} \quad (3)$$

with a standard deviation estimated around 0.08 and 0.09 s, respectively of the expression using H or N .

120 Using strong and weak motion to identify the dynamic characteristics and the response of buildings considering soil-structure interaction

4.2 Updating numerical modelling

We have seen that the experimental modal analysis made from recordings with ambient vibrations allowed to access the real dynamical parameters of a structure under weak motion. From this data it is possible to model the structure response using a modal model, that is to say by representing the structure solely with the help of these modal characteristics, and the analytical formulation of the Duhamel's integral [MGB08] [MGEA⁺10]. The hypotheses allowing this calculation are: linear behavior, the concentration of the mass at the level of the floors, these supposed to be rigid (lumped models). This model has been validated with the recordings in a building in Grenoble following the planned destruction of a bridge close by [MIC 08]. In this case, the fall of the bridge deck onto the ground has generated a seismic wave, recorded at several levels of a nearby building. The solicitation was sufficiently weak to consider the response of the structure as elastic. The recordings at the base of the construction and the experimental modes previously obtained with ambient vibrations (FDD method) have allowed to reproduce the displacements at the top of the building that were also recorded. The comparison of the modal modeling and observation confirm that at the first order this modal model is satisfying.

The city hall of Grenoble has also been tested with ambient vibrations in 35 measuring points [MGEA⁺10]. The results of the experimental modal analysis by FDD are presented in figure 5. They show that the motion under ambient vibrations is dominated by the motion according to the fundamental mode of the 3 degrees of freedom of a building, respectively the longitudinal bending (1.16 Hz), the transverse bending (1.21 Hz) and the torsion (1.46 Hz). The damping coefficient for these three modes is of the order of 1%. These degrees of freedom are weakly coupled for this building thanks to the symmetry of its bracing against the wind and have frequencies, and therefore stiffness, that are very similar. In elevation, on the other hand, we note an important discontinuity at the level of the pre-stressed concrete slab of the third floor. The stiffness of the structure under this slab is much stronger, as if the foundation began at this level. The part above behaves like a bending beam because of the thin reinforced concrete walls that make the stair cases that control the behavior of the structure. The information extracted from ambient vibrations allowed to valid a numerical modeling done by Desprez et al. [KDG13] and the comparison of the numerical model with the simplified modal model shows a very good fit between both approaches.

5 Instrumentation and Structural health monitoring

Structures becoming more and more complex, systems of acquisition more and more efficient and numerous, and dealing with the aging of infrastructure, the two last decades have seen the development of many activities around the non-destructive evaluation of entire structures (NDE). Most of them consist in the following of eventual

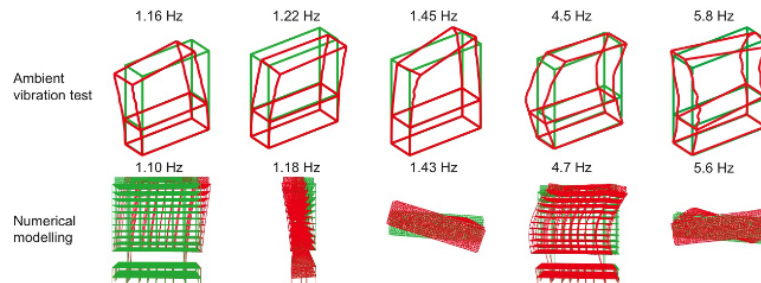


Figure 5: Comparaision between the modal frequencies and shapes obtained using ambient vibrations and FEM methods (after Michel et al. [MGEA⁺10]).

changes of the modal dynamical response of a structure. The main idea is that the modification of the characteristics of the rigidity, the mass or the energy of a system, produces with its aging, its voluntary transformation or its accidental damage, is seen in its response, the latter being defined at the first order by its frequencies, is damping and its modal forms [DFPS96] [FW07]. The variation of these modal parameters can be produced by changes of conditions at the limits (for example, due to the ground-structure interaction [TAR06]), to changes in conception (for example, the reinforcing [Dun05]) or at the degradation of the elastic properties of the material (for example the Young module). Dunand et al. [DAMG⁺04] have for example linked the degradation of resonance frequency of a structure to its level of damage, following the Boumerdes earthquake (Algeria). The measures between before and after the event have allowed quantifying the loss of integrity of many structures with the help of ambient vibrations. A second level of analysis consists in localizing and quantifying damage. The existing experimental methods rely in general on the variation of modal forms, these being linked to the stiffness matrix of the structure. We can cite in particular the mode flexibility method [PB94], the curvature flexibility method [ZA95], the mode shape curvature method [PBS91] or even a combination of these methods. Nevertheless, the experimental assessment of mode shape is not generally enough to detect and locate slight variations, compared with the sensitivity of modal frequencies having led to the development of methods using only frequency variation [RT99] [BILW96] [XZE07] [BGR13]. The third level detects whether changes have occurred, determines the location and estimates the severity of damage. Few applications are available in practice, in spite of the fact that the estimation of damage severity makes a significant contribution to the action of decision-makers in emergency situations after extreme events [DAMG⁺04].

Certain variations slow and of weak amplitude, have also been observed over long time series of ambient vibrations (Figure 6). Recently, Clinton et al. [CBHF06], Todorovska and Al Rjoub [TAR06] and Mikael et al. [MGB⁺13] have observed variations of resonance frequency values of buildings. These variations have been studied, attributed to variations in air temperature to do exposition to the sun, along with changes in the condition of the ground following precipitation. There is no

122 Using strong and weak motion to identify the dynamic characteristics and the response of buildings considering soil-structure interaction

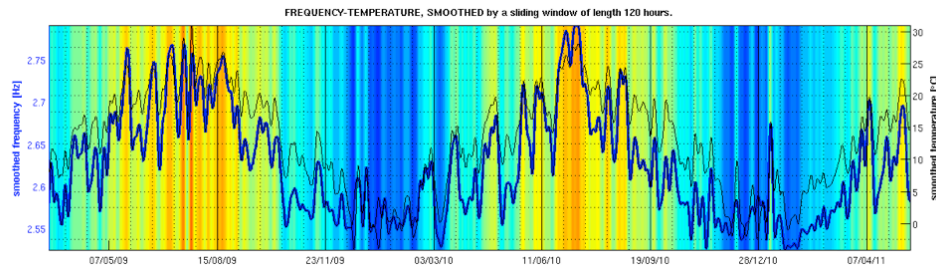


Figure 6: Variations of the fundamental frequency for one single stand-alone building located in Grenoble. The color scale corresponds to the air temperature variations.

doubt that the air temperature is the exterior forcing explaining a large part of the response oscillations around the fundamental frequency of the edifice (e.g., [CBHF06] [DRDRK08] [HNKW07] [NMGNO8] [MGB⁺13]). There remain uncertainties however on the physical origins of these variations, particularly as have shown Mikael et al. [MGB⁺13] on four tested buildings presenting different tendencies according to temperature. However, these variations remain reliable, inferior to 0.1% in frequency and 1% in damping, which allows us to confirm the large stability of these measurements, and consequently their importance for the dynamical analysis of existing buildings.

6 Nonlinear response and soil-structure interaction of structures

6.1 Observation of nonlinear behavior under strong seismic motion.

Although the dynamical characteristics obtained with ambient vibrations are valuable over a very large range of amplitudes, an apparent non-negligible decrease in stiffness takes place when the intensity of the solicitation increases but before the yield limit is reached [DGB⁺06]. We will not discuss at this point the decrease in apparent frequency due to damage after this yield limit has been reached, necessarily more important. The part of this decrease that is attributable to the damage to non-structural elements is negligible as their stiffness is itself negligible compared to the global stiffness of the structure.

The drop in apparent frequency is observed in masonry structures [MZL⁺11], with reinforced concrete [BRJ03] and even with steel [DGB⁺06], even despite the fact that

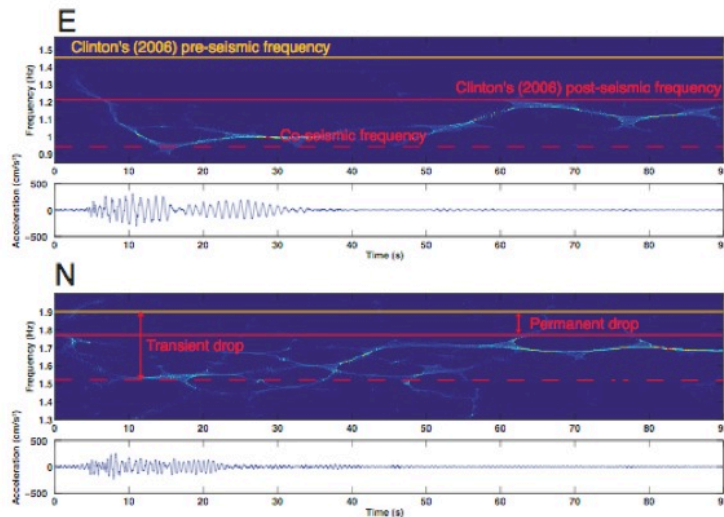


Figure 7: Time-Frequency distribution (smoothed reassigned pseudo-Wigner-Ville) of 1971/02/09 $M_L = 6.6$ San Fernando Earthquake recordings at the roof of the Millikan Library on CalTech campus (California) in E (top) and N (bottom) directions.

steel is a material that behaves in a very linear fashion all the way to its yield limit. We can show such a drop in frequency with real data using time-frequency techniques on structure recordings [MG10]. We also observe wandering in frequency, either around the resonance frequency but confined to the inside of the mode's envelope [MG10] (Figure 7) or linked to jumps in behavior from one mode to another, which, when close, can make us think of a decrease in stiffness [Gue12]. The knowledge of the modal model then becomes critical to avoid false interpretations. It must be noted that close to all the numerical models are not capable of reproducing this drop in apparent stiffness, dependent on the amplitude of the solicitation. If a part probably comes from the material, that is to say the operation of pre-existent fissures, particularly for concrete, a part of this drop only appears when we look at the structure's scale: it would therefore occur in the connection between elements. To overcome this, the modeler uses an elastic module (concrete for example) said to be *fissured* that is a determined fraction of the module of the intact material. It is then necessary with tests in laboratories and numerical models to better understand the evolution of the apparent stiffness with dynamical solicitation to better model the response of the structures and allow to predict the behavior under strong motion from recordings under weak amplitudes.

Brun et al. [BLBC11] and Michel et al. [MZL⁺11] have quantified this drop in frequency respectively for reinforced concrete and masonry from laboratory tests and experimental data, and they proposed simplified laws of behavior, based on the evo-

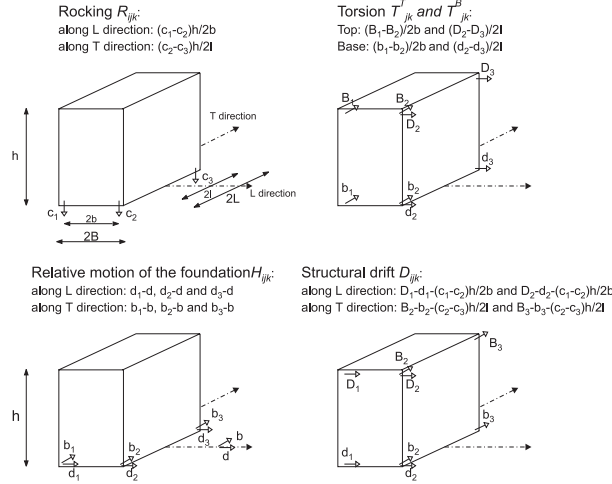


Figure 8: Schematic view of the process used for obtaining the structural drift D_{ijk} , the rocking acceleration (R_{jk}^T), the torsion (T_{jk}^T and T_{jk}^B) and the horizontal acceleration of the foundation (H_{ijk}). k means the number of event considered

lution of frequency. For non-reinforced modern masonry structures, Michel et al. [MZL⁺11] suggest the use of a value of 2/3 of the frequency under ambient vibrations to perform a classic seismic calculation.

Other phenomena appear, certainly linked to an exterior forcing of the structure or to variations in conditions at the limits. For example, the analysis of long temporal series of ambient vibrations in buildings shows weak and reversible fluctuations of the resonance frequency and at a smaller scale that of damping [MGB⁺13]. These fluctuations are highly correlated to fluctuations in air temperature and certain authors [TAR06] also suggest the effects of the condition of the ground, particularly linked to the variation of the soil-structure interaction with precipitation.

6.2 Soil-structure interaction.

The contribution of each mode of deformation to the total building acceleration is summarized in Figure 8 in the time domain for transverse and longitudinal directions.

- *Torsion.* Torsion at the top (T_j^T) and at the base (T_j^B) are derived from the difference between horizontal components recorded at each corner, for stations installed on the same edge of the system, where $2l < 2L$ and $2b < 2B$ are the distances between sensors in the T- and L-directions, respectively. At the base level, T_{Lk}^B and T_{Tk}^B must show roughly similar wave shapes, except when

small inhomogeneities of soil beneath the foundation exist, producing variations of soil-footing system stiffness in parts of the foundation. This phenomenon was already experimentally observed for foundation systems consisting of friction piles [TT99], that produced an eccentricity in the center of stiffness of the foundation system and then variations of rigidity, also expected in case of large footings.

- *Rocking.* As mentioned in Bard [Bar88], rocking acceleration R_{jk} is computed as being the difference between the vertical components of stations spreading along the same foundation edge ($j = L$ or T), normalized by the distance between the two vertical sensors (i.e., $2b$ or $2l$) and multiplied by the height of the building. In reality, this formulation of the rocking represents the horizontal acceleration that the building would experience at its top in case of rigid assumption. Moreover, this rocking corresponds to the total rocking of the basement, including the rocking of the soil, which is generally considered as negligible. As reported in various papers (e.g. [Bar88], [Pao93], [MFMV⁺98]), buildings founded on soft soils usually exhibit significant rocking owing to soil-structure interactions, even for structures founded on piles.
- *Structural drift.* The structural drift D_{ijk} , which corresponds to the fixed-base structure behavior, is computed by subtracting the total acceleration of the foundation (i.e. rocking plus horizontal acceleration including the input acceleration) from the building top acceleration. The coherence C_{rd} between rocking and structural drift is computed as follows:

$$C_{rd} = \frac{|S_{xy}^2|}{S_{xx} * S_{yy}} \quad (4)$$

where S_{xx} and S_{yy} are the power spectral density of signal x and y , respectively and S_{xy} is the cross spectral density of x and y . For events giving high coherences observed at the frequencies of the structure, the coherency gives information on the strong *SSI* effects [Bar88].

- *Relative motion of the foundation.* Horizontal foundation acceleration H_{ijk} relative to the ground is described by subtracting the free-field motion from the total building base acceleration. Non null H_{ijk} 's values confirm the suspected effect of the foundation, which may modify the free-field acceleration through scattering and/or radiating processes.

The frequency \tilde{f} of the fundamental mode of the soil-structure system is usually obtained from the transfer function between the top of the building and the free-field motion [Pao93], [MFMV⁺98]. Nevertheless, more relevant transfer functions FT_{ijk} are obtained by removing the foundation input motion (*FIM*) effects from the building's top motion, where i refers to the set of stations, j to the direction and k to the event, as follows:

$$FT_{ijk} = \frac{\dot{J}_{TS_i^T} - \dot{J}_{TS_i^B}}{\dot{J}_{TS_s}} \quad (5)$$

Todorovska [Tod09] has shown with data that this soil-structure system is perfectly coupled if the rocking of the foundations intervenes. It currently is not simple to separate the properties of the structure from the properties of the SSI by simply processing the signal. And so, all the recordings in the structures (ambient vibrations and earthquakes) are those of the soil-structure system. We can argue that if the SSI is not negligible in the measurements, it should be taken into account in the analysis of vulnerability. However, this is difficult in calculations that often ignore it. A model without the SSI cannot then be compared to measurements including this SSI. It is therefore a challenge to successfully extract the properties of the *fixed base* structure from recordings so as to obtain parameters comparable to the models used in practice. Todorovska [Tod09], Snieder and Safak [SS06] and Prieto et al. [PLCK10] have proposed such a method, using the apparent propagation velocity in the structure to obtain the frequency using a simple model. Michel et al. [MZL⁺11] have used this method and shown that the non linear aspects in the elastic domain could be more powerful in the SSI than in the structure.

7 Conclusions

The scientific interests of large-scale instrumentation and monitoring of existing buildings are then the monitoring of the structure in time, the assessment in changing the physical properties of structures between before and after earthquake for seismic damage assessment and the understanding of the building response to external shaking. Improving the knowledge of the building characteristics reduces the uncertainties of the fragility curves. Ambient vibrations help to improve seismic vulnerability assessment by reducing the epistemic uncertainties due to the lack of knowledge in building models. Ambient vibration-based methods help to adjust the building model to realities in the field. The modal model derived therefore allows some design specificities to be taken into account and is adapted to the recent definition of seismic hazard: full waveform or response spectra may be employed to estimate whether or not the building may suffer from damage by the end of shaking.

The quality and relevancy of the modal parameters extracted by this approach are good. Moreover, recent initiatives started, taking advantages of the reducing cost of news instruments (such as MEMS sensor, Micro-Electro- Mechanical Systems) for improving the building monitoring. The Quake Catcher Network (QCN) employs existing laptops to form a dense and distributed computing seismic network installed in buildings, schools etc... [CLCJ09]. The QCN capitalizes on the main advantage of distributed computing - achieving large numbers of processors with low infrastructure costs - to provide a dense, large-scale seismic network. While MEMS accelerometers are less sensitive than typical broadband or short-period sensors, a larger number of

stations is advantageous for both the study of earthquakes, structural health monitoring and, potentially, earthquake crisis managing.

The ability of Lidar to measure the modal frequencies of existing buildings has been shown in [GJMS10]. By comparing the vibration spectra obtained by sensitive velocimeter sensor and coherent Lidar sensor, they observed a good fit of the values of modal frequencies detected by both approaches. Even if the level of noise is higher for Laser remote sensing (10^{-6} m/s) than velocimeter (10^{-7} m/s), most of the existing buildings could be checked by this method for whole urban area covering.

References

- [ABI99] J.C. Asmussen, R. Brincker, and S.R. Ibrahim. Statistical theory of the vector random decrement technique. *Journal of Sound and Vibration*, 226(2):329–344, 1999.
- [AFGL95] F. Auger, P. Flandrin, P. Goncalvès, and O. Lemoine. *Time-Frequency Toolbox for use with Matlab - Reference guide*. CNRS GdR Information, Image, Signal Vision (ISIS), 1995.
- [ASEK07] A. Aldea, Demetriu S., Albotă E., and T. Kashima. Instrumental response of buildings. Studies within JICA project in Romania. In *International Symposium on Seismic Risk Reduction (ISSRR)*, number 6, pages 157–170, Bucharest, Romania, 2007.
- [ATC78] ATC. Tentative provisions for the development of seismic regulations for buildings. Technical Report Report No. ATC3-06, Applied Technology Council, Palo Alto, CA, 1978.
- [Bar88] P.-Y. Bard. The importance of rocking in building motion: an experimental evidence. In *Proceedings of the Ninth World Conference on Earthquake Engineering*, volume VIII, pages 333–338, August 2-9, 1988.
- [BGR13] L. Baillet, P. Gueguen, and P. Roux. Structural damage localization and monitoring through perturbation theory. *Structural Control and Health monitoring*, in press, 2013.
- [BHM31] P. Byerly, J. Hester, and K. Marshall. The natural periods of vibration of some tall buildings in San Francisco. *Bulletin of the Seismological Society of America*, 21(4):268–276, 1931.
- [BILW96] H.T. Banks, D.J. Inman, D.J. Leo, and Y. Wang. An experimentally validated damage detection theory in smart structures. *Journal of Sound and Vibration*, 191(5):859–880, 1996.

- [BLBC11] M. Brun, P. Labbe, D. Bertrand, and A. Courtois. Pseudo-dynamic tests on low-rise shear walls and simplified model based on the structural frequency drift. *Engineering Structures*, 33(3):796–812, 2011.
- [Blu35] J. A. Blume. A machine for setting structures and ground into forced vibrations. *Bulletin of the Seismological Society of America*, 25(4):361–379, 1935.
- [Blu72] J. A. Blume. Highrise building characteristics and responses determined from nuclear seismology. *Bulletin of the Seismological Society of America*, 62(2):519–540, 1972.
- [BRJ03] M. Brun, J. Reynouard, and L. Jezequel. A simple shear wall model taking into account stiffness degradation. *Engineering Structures*, 25:1–9, 2003.
- [BZA01] R. Brincker, L. Zhang, and P. Andersen. Modal identification of output only systems using Frequency Domain Decomposition. *Smart Materials and Structures*, 10:441–445, 2001.
- [Car36] D. S. Carder. Observed vibrations of buildings. *Bulletin of the Seismological Society of America*, 26(3):245–277, 1936.
- [CBHF06] J. F. Clinton, S. C. Bradford, T. H. Heaton, and J. Favela. The observed wander of the natural frequencies in a structure. *Bulletin of the Seismological Society of America*, 96(1):237–257, 2006.
- [CFP⁺06] K. Chintalapudi, T. Fu, J. Paek, N. Kothari, S. Rangwala, J. Caffrey, R. Govindan, E. Johnson, and S. Masri. Monitoring civil structures with a wireless sensor network. *Internet Computing IEEE*, 10(2):26–34, 2006.
- [CGG⁺00] J.-L. Chatelain, P. Guéguen, B. Guillier, J. Fréchet, F. Bondoux, J. Sarrault, P. Sulpice, and J.M. Neuville. Cityshark: A user-friendly instrument dedicated to ambient noise (microtremor) recording for site and building response studies. *Seismological Research Letters*, 71(6):698–703, 2000.
- [CGG⁺12] J.-L. Chatelain, B. Guillier, P. Guéguen, J. Fréchet, and J. Sarrault. Ambient vibration recording for single-station, array and building studies made simple: CityShark II. *International Journal of Geosciences*, 03(6A):1168–1175, 2012.
- [CH02] J.F. Clinton and T.H. Heaton. Potential advantages of a strong-motion velocity meter over a strong-motion accelerometer. *Seismological Research Letters*, 73(3):332–342, 2002.
- [CLCJ09] E.S. Cochran, J.F. Lawrence, C. Christensen, and R.S. Jakka. The Quake-Catcher Network: Citizen science expanding seismic horizons. *Seismological Research Letters*, 80(1):26–30, 2009.

- [CMB⁺06] G.M. Calvi, G. Magenes, J.J. Bommer, R. Pinho, H. Crowley, and L.F. Restrepo-Vélez. Displacement-based methods for seismic vulnerability assessment at variable geographical scale. *ISET J. Earthquake Technology*, 43(3):75–104, 2006.
- [CP93] R.W. Clough and J. Penzien. *Dynamics of Structures*. Mc Graw-Hill, New-York, 2nd edition, 738, ISBN 0-07-011394-7, 1993.
- [CP10] H. Crowley and R. Pinho. Revisiting Eurocode 8 formulae for periods of vibration and their employment in linear seismic analysis. *Earthquake Engineering and Structural Dynamics*, 39(2):223–235, 2010.
- [CRSP85] T.C. Chu, W.F. Ranson, M.A. Sutton, and W.H. Peters. Application of digital image correlation techniques to experimental mechanics. *Experimental Mechanics*, 25:232–244, 1985.
- [CS02] A. Coburn and R. Spence. *Earthquake protection*. John Wiley and Sons, Ltd, 2nd edition, 420 pages, 2002.
- [CW64] R. Crawford and H. S. Ward. Determination of the natural periods of buildings. *Bulletin of the Seismological Society of America*, 54(6):1743–1756, 1964.
- [DAMG⁺04] F. Dunand, Y. Ait Meziane, P. Guéguen, J.-L. Chatelain, B. Guillier, R. Ben Salem, M. Hadid, M. Hellel, A. Kiboua, N. Laouami, D. Machane, N. Mezouer, A. Nour, E.H. Oubaiche, and A. Remas. Utilisation du bruit de fond pour l’analyse des dommages des bâtiments de Boumerdes suite au séisme du 21 mai 2003. *Mém. Serv. Géol. Alg.*, 12(177-191), 2004.
- [Dav24] C. Davison. Fusakichi Omori and his work on earthquakes. *Bulletin of the Seismological Society of America*, 14(4):240–255, 1924.
- [DFPS96] S. W. Doebling, C. R. Farrar, M. B. Prime, and D.W. Shevitz. Damage identification and health monitoring of structural and mechanical systems from changes in their vibration characteristics: a literature review. Technical Report LA-13070-MS., Los Alamos National Laboratory, USA, 1996.
- [DGB⁺06] F. Dunand, P. Guéguen, P.Y. Bard, J. Rodgers, and M. Celebi. Comparison of the dynamic parameters extracted from weak, moderate and strong building motion. In *1st European Conference of Earthquake Engineering and Seismology*, number 1021, Geneva, Switzerland, 6-8 September 2006.
- [DRDRK08] A. Deraemaker, E. Reynders, G.R De Roeck, and J. Kulla. Vibration-based structural health monitoring using output-only measurements under changing environment. *Mechanical Systems and Signal Processing*, 22(1):34–56, 2008.

- [Dun05] F. Dunand. *Pertinence du bruit de fond sismique pour la caractérisation dynamique et l'aide au diagnostic sismique*. Phd thesis, Université Joseph Fourier, Grenoble (France), 2005.
- [EC898] EC8. *Design provisions for earthquake resistance of structures*. European commission, Bruxelles, 1998.
- [FW07] C. R. Farrar and K. Worden. An introduction to structural health monitoring. *Philosophical transactions of the Royal Society*, 365(1851):303–315, 2007.
- [GB10] C. Gentile and G. Bernadini. An interferometric radar for non-contact measurement of deflections on civil engineering structures: laboratory and full-scale tests. *Structure and Infrastructure Engineering*, 6(5):521–534, 2010.
- [GC98] R. K. Goel and A. K. Chopra. Period formulas for concrete shear wall buildings. *Journal of Structural Engineering*, pages 426–433, 1998.
- [GJMS10] P. Guéguen, V. Jolivet, C. Michel, and A.-S. Schweitzer. Comparison of velocimeter and coherent Lidar measurements for building frequency assesment. *Bulletin of Earthquake Engineering*, 8(2):327–338, 2010.
- [GMC11] D. Gilles, G. McClure, and L. Chouinard. Uncertainty in fundamental period estimates leads to inaccurate design seismic loads. *Canadian Journal of Civil Engineering*, 38(8):870–880, 2011.
- [Gue12] P. Gueguen. Experimental analysis of the seismic response of an isolating building according to different levels of shaking: example of the Martinique earthquake (2007/11/29) Mw 7.3. *Bulletin of Earthquake Engineering*, 10(4):1285–1298, 2012.
- [HB63] G.W. Housner and A. G. Brady. Natural periods of vibration of buildings. *Journal of the Engineering Mechanics Division*, 89:31–65, 1963.
- [HH54] D. E. Hudson and G.W. Housner. Vibration tests of a steel-frame building. Technical report, Earthquake Engineering Research Laboratory, California Institute of Technology, Pasadena (California), 1954.
- [HNKW07] X.G. Hua, Y.Q. Ni, J.M. Ko, and K. Y. Wong. Modeling of temperature–frequency correlation using combined principal component analysis and support vector regression technique. *Journal of Computing in Civil Engineering*, 21(2):122–135, 2007.
- [Hou57] G.W. Housner. Interaction of buildings and ground during an earthquake. *Bulletin of the Seismological Society of America*, 47:179–186, 1957.
- [IT29] M. Ishimoto and R. Takahasi. Mesures des mouvements d’un bâtiment dans des conditions tranquilles. *Bulletin of the Earthquake Research Institute, Tokyo*, 7(1):175–184, 1929.

- [JK68] P. C. Jennings and J.H. Kuroiwa. Vibration and soil-structure interaction tests of a nine-story reinforced concrete building. *Bulletin of the Seismological Society of America*, 58(3):891–916, 1968.
- [KDG13] P. Kotronis, C. Desprez, and S. Grange. *Seismic vulnerability of structures*, chapter 5: Stratégies de modélisation simplifiées pour l'évaluation de la vulnérabilité sismique des structures existantes, page 368. Civil Engineering and geomechanics series. John Wiley and Son (Hoboken USA) and ISTE (London, UK) editor, 2013.
- [KDS05] M. D. Kohler, P. M. Davis, and E. Safak. Earthquake and ambient vibration monitoring of the steel-frame UCLA Factor Building. *Earthquake Spectra*, 21(3):715–736, 2005.
- [KT05] L. Krstevska and L. Taskov. In Situ testing of building structures: methodology and practical applications - IZIIS experience. In *1st International Operational Modal Analysis Conference (IOMAC)*, pages 329–336, Copenhagen, Denmark, April 2005.
- [KTS49] K. Kanai, T. Tanaka, and T. Suzuki. Vibration experiments with the actual buildings. *Bulletin of the Earthquake Research Institute, Tokyo*, 27(1-4):91–95, 1949.
- [KY61] K. Kanai and S. Yoshizawa. On the period and the damping of vibration in actual buildings. *Bulletin of the Earthquake Research Institute, Tokyo*, 39(3):477–489, 1961.
- [LG06] S. Lagomarsino and S. Giovinazzi. Macroseismic and mechanical models for the vulnerability and damage assessment of current buildings. *Bulletin of Earthquake Engineering*, 4:415–443, 2006.
- [LTW87] J. E. Luco, M.D. Trifunac, and H. L. Wong. On the apparent change in dynamic behavior of a nine-story reinforced concrete building. *Bulletin of the Seismological Society of America*, 77(6):1961–1983, 1987.
- [Lyn07] J.P. Lynch. An overview of wireless structural health monitoring for civil structures. *Philosophical transactions of the Royal Society*, 365(1851):345–372, 2007.
- [MFMV⁺98] R. Meli, E. Faccioli, D. Murià-Vila, R. Quaas, and R. Paolucci. A study of site effects and seismic response of an instrumented building in Mexico City. *Journal of Earthquake Engineering*, 2(1):89–111, 1998.
- [MG10] C. Michel and P. Guéguen. Time-frequency analysis of small frequency variations in civil engineering structures under weak and strong motion. *Structural health monitoring*, 9(2):159–171, 2010.
- [MGB08] C. Michel, P. Guéguen, and P.-Y. Bard. Dynamic parameters of structures extracted from ambient vibration measurements: An aid for the

- seismic vulnerability assessment of existing buildings in moderate seismic hazard regions. *Soil Dynamics and Earthquake Engineering*, 28(8):593–604, 2008.
- [MGB⁺13] A. Mikael, P. Gueguen, P.-Y. Bard, P. Roux, and M. Langlais. Long-term frequency and damping wandering in buildings analysed using the Random Decrement Technique (RDT). *Bulletin of the Seismological Society of America*, 103(1):236–246, 2013.
- [MGD11] J. Mazars, S. Grange, and C. Desprez. Seismic risk : structural response of constructions. *European Journal of Civil and Environmental Engineering*, 15(1):223–246, 2011.
- [MGEA⁺10] C. Michel, P. Gueguen, S. El Aram, Mazars J., and P. Kotronis. Full scale dynamic response of a RC building under weak seismic motions using earthquake loadings, ambient vibrations and modelling. *Earthquake Engineering and Structural Dynamics*, 39(4):419–441, 2010.
- [MGL11] C. Michel, P. Gueguen, and P. Lestuzzi. Observed non-linear soil-structure interaction from low amplitude earthquakes and forced-vibration recordings. In G. De Roeck, G. Degrande, G. Lombaert, and G. Muller, editors, *Proceedings of the 8th International Conference on Structural Dynamics, EURODYN 2011*, volume ISBN 978-90-760-1931-4, pages 601–606, Leuven, Belgium, 4-6 july 2011.
- [MGLB10] C. Michel, P. Guéguen, P. Lestuzzi, and P.-Y. Bard. Comparison between seismic vulnerability models and experimental dynamic properties of French buildings. *Bulletin of Earthquake Engineering*, 8(6):1295–1307, 2010.
- [Mik11] A. Mikael. *Evaluation des paramètres physiques des bâtiments : amortissement, fréquence et modes de comportement des structures de génie civil : approche expérimentale*. PhD thesis, Université Joseph Fourier - Grenoble 1, 2011.
- [MR11] M. Moretti and G.L. Rossi. Structural integrity detection of historical structures by dynamic digital image correlation. In *Proceedings of the conference on Experimental Vibration Analysis for Civil Engineering Structures (EVACES)*, Varenna - Italy, 3-5 October 2011.
- [MZL⁺11] C. Michel, B. Zapico, P. Lestuzzi, F. J. molina, and J. Weber. Quantification of fundamental frequency drop for unreinforced masonry buildings from dynamic tests. *Earthquake Engineering and Structural Dynamics*, 40(11):1283–1296, 2011.
- [NMG08] R.D. Nayeri, S.F. Masri, R.G. Ghanem, and R.L. Nigbor. A novel approach for the structural identification and monitoring of a full-scale 17-story building based on ambient vibration measurements. *Smart Materials and Structures*, 17(2):1–19, 2008.

- [Omo22] F. Omori. The semi-destructive earthquake of April 26, 1922. *Seismological Notes (Imperial Earthquake Investigation Committee)*, 3:1–30, 1922.
- [Pao93] R. Paolucci. Soil-structure interaction effects on an instrumented building in Mexico City. *European earthquake Engineering*, 3:33–44, 1993.
- [PB94] A.K. Pandey and M. Biswas. Damage detection in structures using changes in flexibility. *Journal of Sound and Vibration*, 169(1):3–7, 1994.
- [PBS91] A.K. Pandey, M. Biswas, and N.M. Samman. Damage detection from changes in curvature mode shapes. *Journal of Sound and Vibration*, 145(2):321–332, 1991.
- [PDR01] B. Peeters and G. De Roeck. Stochastic system identification for operational modal analysis: a review. *Journal of Dynamic Systems, Measurement and Control*, 123:659–667, 2001.
- [PGHL08] C. Péquegnat, P. Guéguen, D. Hatzfeld, and M. Langlais. The french accelerometric network (RAP) and national data centre (RAP-NDC). *Seismological Research Letters*, 79(1):79–89, 2008.
- [PLCK10] G.A. Prieto, J.F. Lawrence, A.I. Chung, and M. D. Kohler. Impulse response of civil structures from ambient noise analysis. *Bulletin of the Seismological Society of America*, 100(5A):2322–2328, 2010.
- [RDR08] E. Reynders and G. De Roeck. Reference-based combined deterministic-stochastic subspace identification for experimental and operational modal analysis. *Mechanical Systems and Signal Processing*, 22(3):617–637, 2008.
- [RT99] L.R. Ray and L. Tian. Damage detection in smart structures through sensitivity enhancing feedback control. *Journal of Sound and Vibration*, 227(5):987–1002, 1999.
- [Saf89] E. Safak. Optimal-adaptive filters for modelling spectral shape, site amplification, and source scaling. *Soil Dynamics and Earthquake Engineering*, 8(2):75–95, 1989.
- [Sat96] H. Satake, N. and Yokota. Evaluation of vibration properties of high-rise steel buildings using data of vibration tests and earthquake observations. *Journal of Wind Engineering and Industrial Aerodynamics*, 59:265–282, 1996.
- [SBDR⁺03] R. Spence, J. Bommer, D. Del Re, J. Bird, N. Aydinoglu, and S. Tabuchi. Comparing loss estimation with observed damage: a study of the 1999 Kocaeli earthquake in Turkey. *Bulletin of Earthquake Engineering*, 1:83–113, 2003.

- [Spa35] N. R. Sparks. Building vibrations. *Bulletin of the Seismological Society of America*, 25:381–386, 1935.
- [SS06] R. Snieder and E. Safak. Extracting the building response using seismic interferometry: theory and application to the Millikan Library in Pasadena, California. *Bulletin of the Seismological Society of America*, 96(2):586–598, 2006.
- [TAR06] M.I. Todorovska and Y. Al Rjoub. Effects of rainfall on soil-structure system frequency: example based on poroelasticity and a comparison with full-scale measurements. *Earthquake Engineering and Structural Dynamics*, 26(7-8):708–717, 2006.
- [Tod09] M.I. Todorovska. Soil-structure system identification of Millikan Library north-south response during four earthquakes (1970–2002): What caused the observed wandering of the system frequencies? *Bulletin of the Seismological Society of America*, 99(2A):626–635, 2009.
- [Tri72] M.D. Trifunac. Comparison between ambient and forced vibration experiments. *Earthquake Engineering and Structural Dynamics*, 1:133–150, 1972.
- [TT99] M.D. Trifunac and M.I. Todorovska. Recording and interpreting earthquake response of full scale structure. In *NATO Advanced Research Workshop on Strong-Motion Instrumentation for Civil Engineering Structures*, Istanbul, Turkey, June 1999. Kluwer.
- [TYOM69] T. Tanaka, S. Yoshizawa, Y. Osawa, and T. Morishita. Period and damping of vibration in actual buildings during earthquakes. *Bulletin of the Earthquake Research Institute, Tokyo*, 47(6):1073–1092, 1969.
- [UKCG11] S.R Uma, A. King, J. Cousins, and K. Gledhill. The Geonet building instrumentation programme. *New Zealand Society for Earthquake Engineering*, 44(1):53–63, 2011.
- [VDCC82] J. K. Vandiver, A. B. Dunwoody, R. B. Campbell, and M. F. Cook. A mathematical basis for the random decrement vibration signature analysis technique. *Journal of Mechanical Design*, 104:307–313, 1982.
- [Wel67] P.D. Welch. The use of Fast Fourier Transform for the estimation of Power Spectra: A method based on time averaging over short, modified periodograms. *I.E.E.E Transactions on Audio and Electroacoustics*, 15(2):70–73, 1967.
- [XZE07] G.Y. Xu, W.D. Zhu, and B.H. Emory. Experimental and numerical investigation of structural damage detection using changes in natural frequencies. *Journal of Vibration and Acoustics*, 129(6):686–700, 2007.

- [ZA95] Z. Zhang and A.E. Aktan. The damage indices for constructed facilities. In *Proceedings of the IMAC Conference*, pages 1520–1529, Nashville, 1995.

Discontinuous Deformation

Ronaldo I. Borja

Stanford University

Material failure and damage typically result in discontinuous deformation. Discontinuities can be in the form of fractures, cracks, faults, or deformation bands. Discontinuous deformations propagate in a random manner and cannot be recovered even if the applied loads are removed. To numerically simulate randomly propagating discontinuities, the conventional finite element interpolation must be enhanced. In this work, we discuss the extended finite element method as a numerical technique for resolving the discontinuities passing through the interior of finite elements. The technique entails introducing additional degrees of freedom into existing nodes that serve to interpolate the slip degree of freedom within a finite element crossed by a discontinuity. With this approach, discontinuities are interpolated continuously across element boundaries.

1 Introduction

Over the last three decades there has been a steady stream of publications in the computational mechanics literature dealing with the topics of material failure and damage [1]. A class of problems that has attracted enormous attention involves discontinuous deformation occurring over a narrow zone. Deformation bands are narrow zones of intense shear, compaction, and/or dilation. On a macroscopic scale the displacement field is continuous but the strain field inside the band is intense. Faults are highly damaged gouge zones where granulated particles roll and slide past each other even as the material outside this zone remains relatively undamaged. Fractures or cracks are much narrower zones of intense deformation where two surfaces either separate or slide past each other. Because of nearly overlapping definitions, qualitative descriptions of failure modes are quite artificial. Actual mechanism of deformation could involve combinations of several far more complex processes.

Regardless of the type of discontinuity, the main problem concerns the ability of a numerical technique to capture the high deformation gradient arising from the discontinuous deformation field, including the random propagation of this discontinuous field.

In the context of the finite element method, the discontinuity could pass randomly through the interior of finite elements, which the method should be able to accommodate. In this work, we discuss the extended finite element technique for capturing randomly propagating discontinuities. First, we formulate the governing equations in the presence of a discontinuous deformation. Then, we present numerical examples involving crack propagation in quasistatic and dynamic loading conditions.

2 Governing equations

Assuming infinitesimal deformation, the balance of linear momentum with inertia load in domain Ω takes the form

$$\nabla \cdot \boldsymbol{\sigma} + \mathbf{b} = \rho \ddot{\mathbf{u}}, \quad (1)$$

where $\boldsymbol{\sigma}$ is the Cauchy stress tensor, \mathbf{b} is the body force vector, $\ddot{\mathbf{u}}$ is the acceleration vector, ρ is the mass density of the body, and ∇ is the gradient operator. The boundary of Ω is denoted by Γ , which is partitioned into Dirichlet and Neumann boundaries Γ_u and Γ_t , where the displacement and traction are prescribed, respectively. The boundary conditions are as follows

$$\mathbf{u} = \hat{\mathbf{u}} \quad \text{on } \Gamma_u, \quad (2)$$

$$\boldsymbol{\sigma} \cdot \boldsymbol{\nu} = \hat{\mathbf{t}} \quad \text{on } \Gamma_t, \quad (3)$$

where $\boldsymbol{\nu}$ is the unit normal vector to Γ_t , and $\hat{\mathbf{u}}$ and $\hat{\mathbf{t}}$ are the specified displacement and traction boundary conditions, respectively. We assume that the initial displacement and velocity of any point $\mathbf{x} \in \Omega$ are given as

$$\mathbf{u}(\mathbf{x}, 0) = \mathbf{u}_0(\mathbf{x}), \quad (4)$$

$$\dot{\mathbf{u}}(\mathbf{x}, 0) = \dot{\mathbf{u}}_0(\mathbf{x}). \quad (5)$$

Let S denote a fault contained in Ω , with faces S_- and S_+ . Following the formulation presented in [5], the natural boundary conditions on these faces are

$$\boldsymbol{\sigma} \cdot \mathbf{n} = \mathbf{t}_{S_-} \quad \text{on } S_-, \quad (6)$$

$$\boldsymbol{\sigma} \cdot (-\mathbf{n}) = \mathbf{t}_{S_+} \quad \text{on } S_+, \quad (7)$$

where \mathbf{n} is the unit normal vector to S_- , which is assumed to be in direct contact with S_+ . The variational form of dynamic equilibrium may be written as follows. Given $\mathbf{b} : \Omega \rightarrow \mathbb{R}^{n_{\text{dim}}}$, $\hat{\mathbf{t}} : \Gamma_t \rightarrow \mathbb{R}^{n_{\text{dim}}}$, and $\hat{\mathbf{u}} : \Gamma_u \rightarrow \mathbb{R}^{n_{\text{dim}}}$, find $\mathbf{u} \in \mathcal{U}$ such that for all $\boldsymbol{\eta} \in \mathcal{V}$,

$$\int_{\Omega} \nabla^s \boldsymbol{\eta} : \boldsymbol{\sigma} \, d\Omega = \int_{\Omega} \boldsymbol{\eta} \cdot (\mathbf{b} - \rho \ddot{\mathbf{u}}) \, d\Omega + \int_{\Gamma_t} \boldsymbol{\eta} \cdot \hat{\mathbf{t}} \, d\Gamma, \quad (8)$$

where $\boldsymbol{\eta}$ is the first variation of \boldsymbol{u} , and ∇^s denotes the symmetric component of the gradient operator. The space of trial functions is defined as

$$\mathcal{U} := \{\boldsymbol{u} : \Omega \rightarrow \mathbb{R}^{n_{\text{dim}}} \mid u_i \in H^1, u_i = \hat{u}_i \text{ on } \Gamma_{u_i}\}, \quad (9)$$

while the space of variations is defined as

$$\mathcal{V} := \{\boldsymbol{\eta} : \Omega \rightarrow \mathbb{R}^{n_{\text{dim}}} \mid \eta_i \in H^1, \eta_i = 0 \text{ on } \Gamma_{u_i}\}, \quad (10)$$

where H^1 is the first Sobolev space and n_{dim} is the number of spatial dimensions.

To allow a discontinuous displacement field on the fault, we enrich the displacement field with the Heaviside function $H_S(\boldsymbol{x})$ and write

$$\boldsymbol{u} = \bar{\boldsymbol{u}} + H_S(\boldsymbol{x})\tilde{\boldsymbol{u}}, \quad (11)$$

where $\bar{\boldsymbol{u}}$ is the continuous part of displacement and $\tilde{\boldsymbol{u}}$ is the jump in the displacement field. The weighting function is written in a similar form as

$$\boldsymbol{\eta} = \bar{\boldsymbol{\eta}} + H_S(\boldsymbol{x})\tilde{\boldsymbol{\eta}}. \quad (12)$$

We require that $\bar{\boldsymbol{u}}$, $\tilde{\boldsymbol{u}}$, $\bar{\boldsymbol{\eta}}$, and $\tilde{\boldsymbol{\eta}}$ be regular functions (i.e., single-valued and analytic). Although these functions are not required to satisfy any specific boundary condition on their own, they must combine so that $\boldsymbol{u} \in \mathcal{U}$ and $\boldsymbol{\eta} \in \mathcal{V}$.

Substituting (11) and (12) into (8) results in two independent variational equations,

$$\int_{\Omega} \nabla^s \bar{\boldsymbol{\eta}} : \boldsymbol{\sigma} \, d\Omega = \int_{\Omega} \bar{\boldsymbol{\eta}} \cdot (\boldsymbol{b} - \rho \ddot{\boldsymbol{u}}) \, d\Omega + \int_{\Gamma_t} \bar{\boldsymbol{\eta}} \cdot \hat{\boldsymbol{t}} \, d\Gamma \quad (13)$$

for the continuous part, and

$$\begin{aligned} \int_{\Omega} [H_S(\boldsymbol{x}) \nabla^s \tilde{\boldsymbol{\eta}}] : \boldsymbol{\sigma} \, d\Omega + \mathcal{G}_c(\tilde{\boldsymbol{\eta}}, \boldsymbol{t}_S) &= \int_{\Omega} H_S(\boldsymbol{x}) \tilde{\boldsymbol{\eta}} \cdot (\boldsymbol{b} - \rho \ddot{\boldsymbol{u}}) \, d\Omega \\ &+ \int_{\Gamma_t} H_S(\boldsymbol{x}) \tilde{\boldsymbol{\eta}} \cdot \hat{\boldsymbol{t}} \, d\Gamma \end{aligned} \quad (14)$$

for the discontinuous part, where $\mathcal{G}_c(\tilde{\boldsymbol{\eta}}, \boldsymbol{t}_S)$ is the so-called contact surface integral representing the virtual work done by the traction field on the fault \mathcal{S} ; see Chapter 7 of [1], and also Reference [5], for step-by-step derivations of this contact integral.

In the extended FE approach, the elements intersected by a discontinuity are enhanced with additional displacement degrees of freedom at the nodes to interpolate the discontinuous displacement field, which is then superimposed to the conforming displacement field. The standard FE approximation for the continuous displacement field $\bar{\boldsymbol{u}}(\boldsymbol{x})$ is given by

$$\bar{\boldsymbol{u}}^h(\boldsymbol{x}) = \boldsymbol{N}(\boldsymbol{x})\boldsymbol{d}, \quad \forall \boldsymbol{x} \in \Omega^h, \quad (15)$$

while the FE approximation for the discontinuous displacement field $\tilde{\boldsymbol{u}}(\boldsymbol{x})$ is given by

$$\tilde{\boldsymbol{u}}^h(\boldsymbol{x}) = \boldsymbol{N}(\boldsymbol{x})H_S(\boldsymbol{x})\boldsymbol{e} = \tilde{\boldsymbol{N}}(\boldsymbol{x})\boldsymbol{e}, \quad \forall \boldsymbol{x} \in \Omega_S^h, \quad (16)$$

where Ω_S^h is the local support of the surface of discontinuity \mathcal{S} , while \mathbf{d} and \mathbf{e} are the nodal displacement vectors interpolating $\bar{\mathbf{u}}$ and $\tilde{\mathbf{u}}$, respectively. The matrix form consistent with variational equation (13) is given by

$$\bar{\mathbf{M}}(\ddot{\mathbf{d}}, \ddot{\mathbf{e}}) + \bar{\mathbf{F}}_{\text{INT}}(\mathbf{d}, \mathbf{e}) = \bar{\mathbf{F}}_{\text{EXT}}, \quad (17)$$

where

$$\bar{\mathbf{M}}(\ddot{\mathbf{d}}, \ddot{\mathbf{e}}) = \left(\int_{\Omega^h} \rho \mathbf{N}^T \mathbf{N} \, d\Omega \right) \ddot{\mathbf{d}} + \left(\int_{\Omega^h} \rho \mathbf{N}^T \tilde{\mathbf{N}} \, d\Omega \right) \ddot{\mathbf{e}}, \quad (18)$$

$$\bar{\mathbf{F}}_{\text{INT}}(\mathbf{d}, \mathbf{e}) = \int_{\Omega^h} \mathbf{B}^T \boldsymbol{\sigma}(\mathbf{d}, \mathbf{e}) \, d\Omega, \quad (19)$$

and

$$\bar{\mathbf{F}}_{\text{EXT}} = \int_{\Omega^h} \mathbf{N}^T \mathbf{b} \, d\Omega + \int_{\Gamma_t^h} \mathbf{N}^T \mathbf{t} \, d\Gamma. \quad (20)$$

In the above notations, we have used the same symbol $\boldsymbol{\sigma}$ for the Cauchy stress tensor and for the vector form of this tensor. The matrix equation consistent with variational equation (14) is given by

$$\tilde{\mathbf{M}}(\ddot{\mathbf{d}}, \ddot{\mathbf{e}}) + \tilde{\mathbf{F}}_{\text{INT}}(\mathbf{d}, \mathbf{e}) + \mathcal{G}_c(\mathbf{e}) = \tilde{\mathbf{F}}_{\text{EXT}}, \quad (21)$$

where

$$\tilde{\mathbf{M}}(\ddot{\mathbf{d}}, \ddot{\mathbf{e}}) = \left(\int_{\Omega_S^h} \rho \tilde{\mathbf{N}}^T \mathbf{N} \, d\Omega \right) \ddot{\mathbf{d}} + \left(\int_{\Omega_S^h} \rho \tilde{\mathbf{N}}^T \tilde{\mathbf{N}} \, d\Omega \right) \ddot{\mathbf{e}}, \quad (22)$$

$$\tilde{\mathbf{F}}_{\text{INT}}(\mathbf{d}, \mathbf{e}) = \int_{\Omega_S^h} \tilde{\mathbf{B}}^T \boldsymbol{\sigma}(\mathbf{d}, \mathbf{e}) \, d\Omega, \quad (23)$$

$$\mathcal{G}_c(\mathbf{e}) = \int_{\mathcal{S}} \mathbf{N}^T \mathbf{t}_S \, d\mathcal{S}, \quad (24)$$

and

$$\tilde{\mathbf{F}}_{\text{EXT}} = \int_{\Omega_S^h} \tilde{\mathbf{N}}^T \mathbf{b} \, d\Omega + \int_{\Gamma_t^h} \tilde{\mathbf{N}}^T \mathbf{t} \, d\Gamma. \quad (25)$$

We construct augmented nodal acceleration, velocity, and displacement vectors as

$$\mathbf{A} = \begin{Bmatrix} \ddot{\mathbf{d}} \\ \ddot{\mathbf{e}} \end{Bmatrix}, \quad \mathbf{V} = \begin{Bmatrix} \dot{\mathbf{d}} \\ \dot{\mathbf{e}} \end{Bmatrix}, \quad \mathbf{D} = \begin{Bmatrix} \mathbf{d} \\ \mathbf{e} \end{Bmatrix}. \quad (26)$$

The above vectors contain the standard nodal degrees of freedom \mathbf{d} , $\dot{\mathbf{d}}$ and $\ddot{\mathbf{d}}$, plus additional global degrees of freedom \mathbf{e} , $\dot{\mathbf{e}}$ and $\ddot{\mathbf{e}}$ at the enriched nodes. We remark that these vectors will normally have variable dimensions as the discontinuity continues to propagate and intersect more finite elements. Next, we combine the FE equations (17) and (21) as follows:

$$\mathbf{M}\mathbf{A} + \begin{Bmatrix} \bar{\mathbf{F}}_{\text{INT}} \\ \tilde{\mathbf{F}}_{\text{INT}} + \mathcal{G}_c \end{Bmatrix} = \begin{Bmatrix} \bar{\mathbf{F}}_{\text{EXT}} \\ \tilde{\mathbf{F}}_{\text{EXT}} \end{Bmatrix}, \quad (27)$$

where M is the consistent mass matrix given by

$$M = \begin{bmatrix} M_{11} & M_{12} \\ M_{21} & M_{22} \end{bmatrix}, \quad (28)$$

in which

$$M_{11} = \int_{\Omega^h} \rho \mathbf{N}^T \mathbf{N} \, d\Omega, \quad M_{12} = \int_{\Omega_s^h} \rho \mathbf{N}^T \tilde{\mathbf{N}} \, d\Omega, \quad (29)$$

$$M_{21} = M_{12}^T, \quad M_{22} = \int_{\Omega_s^h} \rho \tilde{\mathbf{N}}^T \tilde{\mathbf{N}} \, d\Omega. \quad (30)$$

Given the displacement vector D_n at time t_n , the acceleration vector A_n at the same time instant can be calculated as

$$\mathbf{A}_n = M^{-1} \begin{Bmatrix} \bar{\mathbf{F}}_{\text{EXT}} \\ \tilde{\mathbf{F}}_{\text{EXT}} \end{Bmatrix}_n - M^{-1} \begin{Bmatrix} \bar{\mathbf{F}}_{\text{INT}} \\ \tilde{\mathbf{F}}_{\text{INT}} + \mathcal{G}_c \end{Bmatrix}_n, \quad (31)$$

In an explicit time marching scheme, the augmented velocity and displacement nodal vectors at time t_{n+1} are updated from the formulas

$$\mathbf{V}_{n+1/2} = \mathbf{V}_{n-1/2} + \Delta t \mathbf{A}_n, \quad (32)$$

$$\mathbf{D}_{n+1} = \mathbf{D}_n + \Delta t \mathbf{V}_{n+1/2}, \quad (33)$$

where $\Delta t = t_{n+1} - t_n$ is the time increment. Clearly, the only computational burden in the above algorithm is the inversion of the consistent mass matrix M . Mass lumping procedures are typically employed to form a diagonal mass matrix, and thus, render the simultaneous equation solving trivial [2, 3, 4].

3 Numerical example

We consider two examples dealing with crack propagation where the geometry of the crack is not known a priori. The first example is static crack propagation; the second includes inertia loads.

3.1 Static crack propagation

This problem is presented in [5] and includes a square elastic domain with advancing crack tips. The finite element mesh is shown in Fig. 1(a) and consists of 20,000 constant strain triangular elements defined by 10,201 nodes and arranged in cross-diagonal pattern. The domain has in-plane dimensions of 1×1 m (square) and contains a 0.566 m center crack oriented at $\theta = \pi/4$ relative to the horizontal. In order for the crack to not intersect the nodes, the tips were specified coordinates (0.29999, 0.29998)

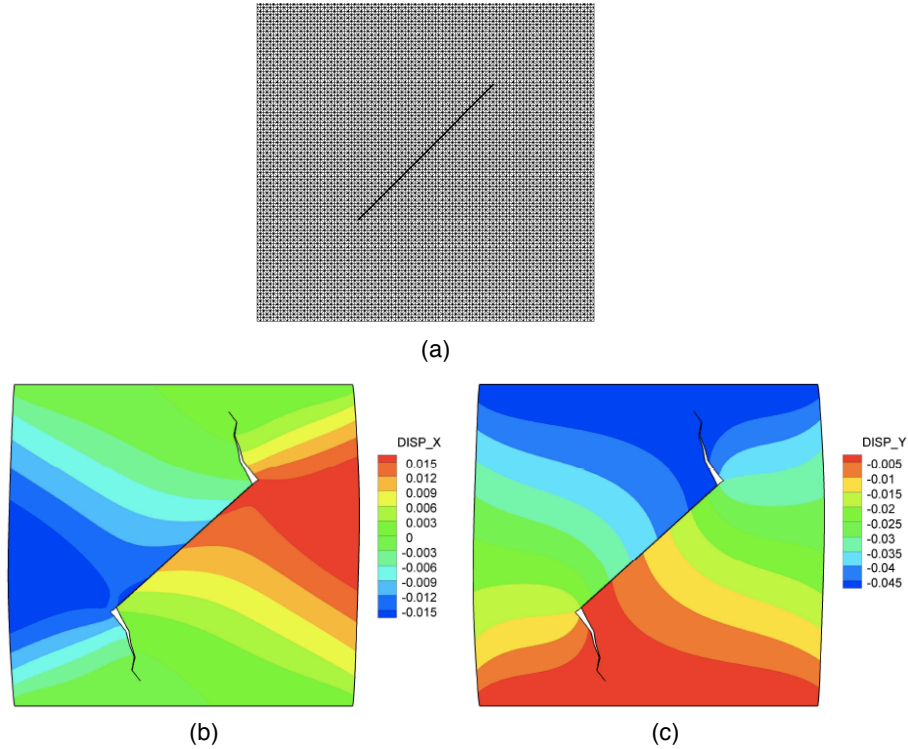


Figure 1: Quasistatic crack propagation in plane strain: (a) finite element mesh; (b) horizontal displacement contour; (c) vertical displacement contour. Color bar in meters. After Reference [5].

and $(0.70002, 0.70001)$ m. The material is linearly elastic with Young's modulus $E = 10,000$ MPa and Poisson's ratio $\nu = 0.30$. The crack is fully frictional with a coefficient of friction $\mu = 0.10$. We use the penalty regularization for the crack, with normal and tangential penalty parameters equal to 10^7 MN/m³. The body was deformed by applying a uniform vertical displacement at the top nodes while constraining the top and bottom surfaces from moving horizontally. For this example, we assumed that the crack could undergo frictional sliding while allowing the crack tips to advance.

We employed linear elastic fracture mechanics (LEFM) and compared the equivalent stress intensity factor K_I^{eq} to the critical stress intensity factor K_c (also called the fracture toughness), and activated crack growth when $K_I^{\text{eq}} \geq K_c$. For convenience, we assumed an unstable crack growth and propagated the crack according to a predefined length of 0.04 m at each step. We propagated the crack in the direction of the maximum hoop, or circumferential, stress, which is determined by using the stress intensity factors K_I and K_{II} in LEFM. As a brief background of these stress intensity factors,

K_I and K_{II} may be viewed as finite measures of the singular crack-tip normal and shear stresses, respectively. Therefore, the direction of the maximum hoop stress can be determined from these stress intensity factors by treating them as the stresses acting at the crack tip themselves. The propagation direction in terms of the stress intensity factors is given by

$$\theta_c = 2 \arctan \frac{1}{4} \left(\frac{K_I}{K_{II}} \pm \sqrt{\frac{K_I}{K_{II}} + 8} \right). \quad (34)$$

For purposes of calculating the mixed-mode stress intensity factors, we assumed a radius of $r_d = 0.025$ m for the interaction integral. Also, we set $K_c = 30$ so that the crack stops growing at the end of step #6.

Table 1 shows the stress intensity factors calculated by the method. Figure 1(b) and 1(c) show the horizontal and vertical displacements calculated by the extended finite element solution after applying a uniform vertical displacement of -0.10 m at the top surface. For the penalty method with full Newton iteration, we used an error tolerance of $\|\mathbf{r}\|/\|\mathbf{r}_0\| = 10^{-10}$ based on the L_2 norm of the residual, and convergence to machine precision was achieved after only three iterations.

Table 1. Stress intensity factors for modes I and II fracture calculated by the penalty method. LCT = left crack tip; RCT = right crack tip.

		Mode I	Mode II
Step 1	LCT	-42.82	-265.36
	RCT	-48.99	-249.79
Step 2	LCT	170.72	-3.94
	RCT	171.40	-0.65
Step 3	LCT	119.58	23.59
	RCT	122.56	21.97
Step 4	LCT	84.67	-6.01
	RCT	85.46	-6.04
Step 5	LCT	51.01	15.29
	RCT	50.54	15.71
Step 6	LCT	20.08	-14.59
	RCT	21.02	-15.05

3.2 Fault rupture dynamics

This example is also concerned with fault growth in an elastic medium where the direction of fault propagation is not a priori known; however, this time the fault propagates dynamically. The dimensions of the computational domain are $60 \text{ km} \times 20 \text{ km}$, with the lower left-hand corner of the domain located at the origin of a Cartesian reference frame. An initially horizontal fault 8 km long was centered in the domain at coordinates $(30 \text{ km}, 10 \text{ km})$. Fault rupture was triggered by reducing the frictional coefficient to a dynamic value over a nucleation length defined by the range $L_n := \{x | 28.5 \text{ km} \leq x \leq 31.5 \text{ km}\}$. The initial stresses inside the computational domain are set to $\sigma_{11} = \sigma_{22} = -120 \text{ MPa}$ and $\sigma_{12} = 70 \text{ MPa}$. In this paper, we use an explicit perfectly matched layer (PML) on the boundaries to absorb outgoing waves [3].

In order to predict the growth path of a newly-generated fault, certain fracture and propagation criteria must be prescribed. In this example, we used the Coulomb criterion for failure in shear (see the textbook by Pollard and Fletcher [6], pp. 357–364). The angle γ_c between the critical slip plane and the direction of the maximum compressive stress is given as

$$\gamma_c = \frac{1}{2} \arctan \left(\frac{1}{\mu_s} \right), \quad (35)$$

where μ_s is the static frictional coefficient of the fault surface. The Coulomb stress is defined as

$$\sigma_{CC} = \frac{1}{2}(\sigma_1 - \sigma_3)(1 + \mu_s^2)^{1/2} + \frac{1}{2}(\sigma_1 + \sigma_3)\mu_s, \quad (36)$$

where σ_1 and σ_3 are the maximum and minimum principal stresses, respectively (i.e., minimum and maximum compressive stresses, respectively). If the Coulomb stress σ_{CC} is greater than an inherent shear cohesion c_0 , new slip planes are generated. In general, the Coulomb criterion predicts two sets of slip planes with an equal likelihood of mobilization. For purposes of analysis, we selected the slip plane that is closer to the horizontal plane, since the initial fault is defined by a horizontal plane. The shear cohesion is assumed to be $c_0 = 3.5 \text{ MPa}$. Every 0.5 s , we evaluate the Coulomb stresses for each fault tip, and propagate the fault once the Coulomb fracture criterion is reached. We prescribe a propagation length of $\Delta L = 0.30 \text{ km}$ for newly generated fault segments, and set the initial traction on newly generated fault faces to be equal to the bulk stress projected on the fault face.

The computational domain has dimensions 2 km by 20 km . The half-space is discretized into uniform right-angle CST elements with a side length of $h = 10 \text{ m}$, resulting in the creation of $40,2201$ nodes and $800,000$ CST elements. We use the PML for all the boundaries except at the top free surface, and the width of the PML is taken as $\delta = 6h$. No viscous damping is used in the interior domain.

Figure 2 shows the predicted fault nucleation and random propagation processes considering both the shear rupture propagation along the given initial fault and the random

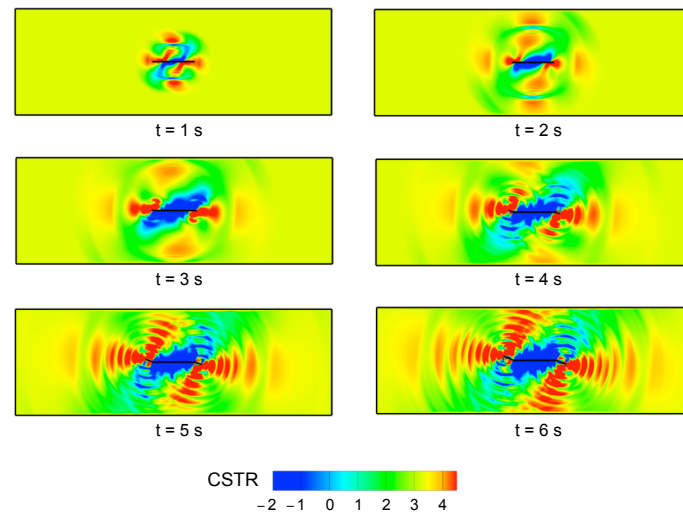


Figure 2: Fault rupture dynamics and random propagation of new fault faces. CSTR = Coulomb stress in MPa. After Reference [3].

generation of new fault faces. The calculated Coulomb stresses are also shown as they radiate away from the nucleating fault segments. Because of the uniform initial stress distribution assumed in the simulation, the stress waves show an anti-symmetric pattern where depth effects are not present. More realistic simulations may involve the effect of non-uniform stress distribution accounting for depth effects, which would make the stress wave pattern less anti-symmetric. We remark that it would be difficult to use the classical split-node technique for this problem since it cannot readily accommodate the creation of new fault faces and the random advance of fault tips.

4 Conclusions

An extended finite element technique was used to capture propagating discontinuities under quasistatic and dynamic loading conditions. This technique does not require a priori information about the location and geometry of the discontinuities, and does not suffer from the inaccuracies of adaptive mesh refinement techniques. The two examples discussed in this paper highlighted the capability of the formulation to accommodate quasistatic crack propagation and spontaneous fault rupture dynamics. It must be pointed out, however, that the extended finite element technique does not provide a theory for crack propagation. This is a common misconception, that the

technique by itself is self-sufficient to propagate a discontinuity. The extended finite element technique is only a means of enhancing the interpolation capability of a finite element to accommodate the kinematics of a discontinuity passing through its interior, but the technique still needs a crack propagation theory to enable the discontinuity to propagate through the solid.

Acknowledgment

The author acknowledges support from the US Department of Energy under Grant No. DE-FG02-03ER15454 to Stanford University.

References

- [1] Borja RI (2013). *Plasticity Modeling and Computation*. Springer-Verlag, Berlin Heidelberg.
- [2] Coon, ET, Shaw BE, Spiegelman M (2011). A Nitsche-extended finite element method for earthquake rupture on complex fault systems, *Computer Methods in Applied Mechanics and Engineering* 200, 2859–2870.
- [3] Liu F, Borja RI (2013). Extended finite element framework for fault rupture dynamics including bulk plasticity. *International Journal for Numerical and Analytical Methods in Geomechanics*. DOI: 10.1002/nag.2179.
- [4] Liu F, Borja RI (2011). Dynamic fault rupture and propagation through a fixed finite element grid, In: R.I. Borja (Ed.) *Multiscale and Multiphysics Processes in Geomechanics*, Springer-Verlag, Berlin Heidelberg, pp. 161–164.
- [5] Liu F, Borja RI (2008). A contact algorithm for frictional crack propagation with the extended finite element method, *International Journal for Numerical Methods in Engineering* 76, 1489–1512.
- [6] Pollard DD, Fletcher RC (2005). *Fundamentals of Structural Geology*. Cambridge University Press.

Modeling SSI on piled foundations: the effects of kinematic interaction

Mario Martinelli* and Claudio Tamagnini†

* *University of Pavia, Pavia, Italy*

† *University of Perugia, Perugia, Italy*

In this paper, a series of 3-d, fully coupled dynamic consolidation analyses are used to investigate the kinematic interaction effects in the classical problem of a single end-bearing pile immersed in a two-layer soil profile with a significant stiffness discontinuity at the interface between the two layers. The objectives of this work is threefold. First, to investigate the influence that the use of advanced constitutive models, capable of reproducing the main features of the observed cyclic behavior of granular soils, may have on the numerical predictions of the SSI effects, and, in particular, to the values of the bending moments along the pile axis. Second, to investigate the impact of the development and dissipation of excess pore pressures during the earthquake event on soil deformations and pile loads. Third, to use the results of advanced numerical simulations as benchmarks to evaluate the predictive capabilities of the simplified analysis methods available in current design practice. The results of the numerical simulations clearly show that significant pore pressure build-up can occur under seismic conditions even in soils with relatively high permeability, and that the associated changes in the effective stress field can have an important effect in determining the response of the soil-pile system, both in terms of pile loads and ground surface accelerations. As far as kinematic bending moments are concerned, the comparison of the FE predictions with the results obtained with a number of simplified design methods indicates that, although the predictive capabilities of such methods appears relatively satisfactory when no excess pore pressures are expected to develop within the soil, some care must be taken in applying them in undrained or partially undrained conditions, due to the limitations inherent in the non-linear elastic soil models used to perform the 1-d site response analysis, employed by the simplified methods to characterize the effects of the seismic shaking.

1 Introduction

Pile–soil kinematic interaction has been investigated by many researchers in the last decades and emphasis has been placed on kinematic bending effects. Observations in the field, laboratory, and computer simulations have demonstrated that kinematic pile bending may be severe in the case of piled foundations constructed in weak soil conditions, mostly near interfaces separating soil layers of sharply different stiffness and on the pile head in presence of a stiff restraining cap.

Only recently technical regulations have given indication on pile design including kinematic interaction effects. In particular, Eurocode 8 prescribes to compute bending moments due to kinematic interaction “when all of the following conditions occur simultaneously”:

- i) the ground profile is of type D, S1 or S2, and contains consecutive layers of sharply differing stiffness;
- ii) the zone is of moderate or high seismicity, *i.e.*, the maximum expected acceleration at ground surface, $a_{\max} = a_g S$, exceeds $0.10 g$;
- iii) the structure is of importance class III or IV.

The approaches suggested in the technical literature for the quantitative evaluation of kinematic interaction effects in the pile–soil system can be grouped in three different categories, in order of increasing model accuracy and complexity:

1. Approaches based on the results of free–field, 1d wave propagation analyses. In these approaches, the bending moment distribution along the pile axis is computed by assuming that the pile follows exactly the soil displacements, without considering SSI (*i.e.*, the stiffening effects of the piles is not taken into account) [MH77, NEH97]. These methods cannot be used in layered soils, as the horizontal displacement gradient at the interfaces between layers of different stiffness is discontinuous, while the curvature of the pile axis is always finite.
2. Approaches based on simplified numerical methods which consider the pile as a beam on a dynamic Winkler foundation (BDWF), characterized by a given distribution of stiffness and damping coefficients with depth. These approaches allows to account for soil–pile interaction, stiffness discontinuities along the pile axis (*i.e.*, layered soils), and different boundary conditions at the pile ends [My101, NMGT01].
3. Approaches based on numerical methods which consider the pile as a beam immersed in a (possibly inhomogeneous and inelastic) continuous medium (the foundation soils), and use the finite element (FE) or boundary element (BE) approximations to integrate the dynamic equations of motion [CD07, DCL09, MdSAM09, DL09, Mar12].

All the aforementioned approaches have been used to derive a number of practical design methods which are used to estimate the kinematic interaction effects in terms

of maximum bending moments either at the pile head (in the case of constrained rotations) or at the interface between a rigid and a more deformable layer. However, all these methods are based, in most cases, on relatively simple linear or non-linear elastic soil models, and completely neglect the possible effects of the solid skeleton-pore water interaction in saturated soils.

The objectives of this work is threefold. First, to investigate the influence that the use of advanced constitutive models, capable of reproducing the main features of the observed cyclic behavior of granular soils, may have on the numerical predictions of the SSI effects, and, in particular, to the values of the bending moments along the pile axis. Second, to investigate the impact of the development and dissipation of excess pore pressures during the earthquake event on soil deformations and pile loads. Third, to use the results of advanced numerical simulations as benchmarks to evaluate the predictive capabilities of the simplified analysis methods available in current design practice.

The paper is organized as follows. Sect. 2 presents a brief review of some of the most common simplified design methods developed from approaches (2) and (3). Sect. 3 provides the details of the specific benchmark problem considered, summarizes the main characteristics of the advanced soil model adopted in the FE simulations, and illustrates some of the main results obtained. The assessment of the predictive capabilities of a number of simplified methods is presented in Sect. 4, while Sect. 5 summarizes the main conclusions of this work.

2 Review of simplified design methods

A simple model to analyze the kinematic pile-soil interaction problem in a two-layer soil and to determine the kinematic bending moment at the interface between two layers has been proposed by Dobry & O'Rourke [DO83]. This model is based on the following assumptions:

- 1) the soil in each layer is homogeneous, isotropic and linear elastic;
- 2) both layers are thick enough so that boundary effects do not influence the response at the interface between the two soils;
- 3) the pile is linear elastic and its axis is vertical;
- 4) perfect adhesion is assumed at the pile-soil interface;
- 5) the soil is subjected to a uniform static shear stress, τ , which generates a constant shear strain within each layer;
- 6) the displacements are small.

Modeling the pile as a beam on a Winkler foundation (BDWF) with Winkler subgrade reaction moduli assumed proportional to the shear moduli of the two layers:

$$k_1 = 3 G_1 \qquad k_2 = 3 G_2$$

Dobry & O'Rourke provided the following explicit solution for the pile bending moment at the interface between the two layers:

$$M = 1.86 (E_p J_p)^{3/4} (G_1)^{1/4} \gamma_1 F(G_1, G_2) \quad (1)$$

where: E_p is the Young's modulus of the pile; G_1 and G_2 are the shear moduli of the upper (layer 1) and lower (layer 2) soil layers, respectively; F is a non-dimensional function of the shear moduli G_1 and G_2 in the two layers, given by:

$$F(G_1, G_2) = \frac{1}{c^3} (c - 1) (c^2 - c + 1) \qquad c = \sqrt[4]{\frac{G_1}{G_2}} \quad (2)$$

and $\gamma_1 = \tau_{\max}/G_1$ is the (uniform) shear strain in the upper soil layer, computed from the maximum shear stress in the soil layer obtained in a 1-d free-field site response analysis, or, as an alternative, computed from the following simplified expression, proposed by Dente et al. [Den05]:

$$\gamma_1 = \frac{\rho_1 h_1}{G_1} a_{\max} \quad (3)$$

The function F in eq. (2) assumes values between 0 and 1 and increases with increasing stiffness contrast between the layers. In the case of a homogenous soil ($c = 1$ and $F = 0$) eq. (1) yields an unrealistic solution ($M = 0$), since kinematic bending moments are generated even in homogeneous soil.

An alternative method has been developed by Nikolaou et al. [NMGT01] based on the results of a parametric study conducted with the BDWF approach. In their work, Nikolaou et al. considered a pile embedded in a two-layer soil deposit subjected to vertically propagating harmonic shear waves, and evaluated the maximum bending moments at the interface between the two layers based on the steady-state solution of the dynamic problem, according to the following expression:

$$M_{\max}(\omega) = 0.042 \tau_c d^3 \left(\frac{L}{d}\right)^{0.3} \left(\frac{E_p}{E_1}\right)^{0.65} \left(\frac{V_{s2}}{V_{s1}}\right)^{0.5} \quad (4)$$

In the above expression, d is the pile diameter; L is the pile length; E_1 is the Young's modulus of the upper soil layer; V_{s1} and V_{s2} are the shear wave velocities of the upper and the lower soil layers, respectively, and τ_c is "characteristic" shear stress, proportional to the maximum free-field surface acceleration (a_{\max}):

$$\tau_c = a_{\max} \rho_s h_1 \quad (5)$$

where ρ_s is the soil density, and h_1 the thickness of the upper soil layer. According to eq. (4), the bending moment increases with increasing pile diameter, pile-soil 1

stiffness ratio and layer stiffness ratio. However, a weakness of this model is that the bending moment tends to infinity for very large slenderness ratios.

Under a seismic excitation, the above equations are still valid but the peak values of the transient bending moments are smaller than the steady-state amplitudes. Therefore, Nikolaou et al. proposed to apply a correction factor η to the value of $M_{\max}(\omega)$ provided by eq. (4) to obtain the actual maximum value of M in the time domain:

$$M_{\max}(t) = \eta M_{\max}(\omega) \quad \eta := \begin{cases} 0.04 N_c + 0.23 & \text{for } T \simeq T_1 \\ 0.015 N_c + 0.17 & \text{for } T \neq T_1 \end{cases} \quad (6)$$

where T_1 is the fundamental period of the upper layer; T is the predominant period of the seismic input, and N_c the number of equivalent cycles of the seismic excitation. For preliminary design purposes, η can be assumed in the range between 0.2 and 0.3. Recently, Dente et al. [DCSS11] proposed two alternative expressions for the correction factor η derived from the results of an extensive parametric study. In the first of them, considered in Sect. 4, η is given by the following function of the ratio T/T_1 :

$$\eta = \begin{cases} 0.624 \left(\frac{T}{T_1} \right)^{-1.378} & \text{for } T > T_1 \\ 0.205 + 0.42 \left(\frac{T}{T_1} \right) & \text{for } T \leq T_1 \end{cases} \quad (7)$$

Maiorano et al. [MdSAM09] re-arranged the original model of Nikolaou et al., by replacing eq. (4) with the following expression:

$$M_{\max}(t) = \beta G_1 \gamma_{\text{ff}} d^3 \left(\frac{L}{d} \right)^{0.3} \left(\frac{E_p}{E_1} \right)^{0.65} \left(\frac{V_{s2}}{V_{s1}} \right)^{0.5} \quad (8)$$

where γ_{ff} stands for the peak shear strain acting at the interface between the two soil layers calculated from a 1d, free-field wave propagation analysis. The coefficient β in eq. (8), linking the maximum transient bending moment to the peak soil shear strain at the interface, has been set to 0.07 by Maiorano et al., based on the results of an extensive parametric study conducted with the FE code VERSAT-P3D. More recently, Sica et al. [SMS11], based on the results of a different parametric study using the BDWF approach, proposed to use a slightly lower value for β , setting it equal to 0.053.

Instead of considering the bending moment, Mylonakis [Myl01] suggested to use the maximum pile bending strain:

$$\epsilon_p = \frac{M_{\max} d}{E_p J_p 2}$$

as the representative quantity to describe the effects of dynamic interaction. In his work, carried out using the BDWF approach, Mylonakis introduced some significant improvements with respect to the method proposed by Dobry & O'Rourke [DO83], namely:

- a) the seismic excitation imposed at the base of the soil profile is an harmonic displacement with frequency ω ;
- b) both radiation and material damping are taken into account by considering a viscoelastic Winkler model for the soil reaction to the horizontal pile displacements;
- c) the two layers in the soil profile are of finite thickness.

For the maximum bending strains at the interface separating the two soil layers, Mylonakis provides the following “strain transmissibility” function, valid for quasi-static conditions ($\omega \rightarrow 0$):

$$\left(\frac{\epsilon_p}{\gamma_1}\right)_{\omega=0} = \frac{1}{2c^4} (c^2 - c + 1) \left(\frac{d}{h_1}\right) \times \left\{ \left[3 \left(\frac{k_1}{E_p}\right)^{1/4} \left(\frac{h_1}{d}\right) - 1 \right] c(c-1) - 1 \right\} \quad (9)$$

where γ_1 is the free-field soil shear strain at the interface; k_1 is the Winkler modulus of the upper layer, and c is the layer stiffness contrast, provided by eq. (2)₂. To take into account for the transient nature of the seismic excitation, the strain transmissibility function of eq. (9) has to be corrected as follows:

$$\left(\frac{\epsilon_p}{\gamma_1}\right)_{\text{dyn}} = \left(\frac{\epsilon_p}{\gamma_1}\right)_{\omega=0} \Phi \left(\frac{T}{T_1}, \frac{E_p}{E_1}, \frac{G_2}{G_1}, \frac{h_1}{d} \right) \quad (10)$$

taking into account the effects of: the predominant period of the seismic excitation; the relative stiffness of the pile; the stiffness contrast between the two layers and of the upper layer thickness. For relatively deformable piles and low frequency input ($\omega d/V_{s1} < 0.1$) Mylonakis observes that the correction factor Φ varies in the range 1.0–1.25.

As a last example of simplified analysis methods, it is worth mentioning the recent work of Di Laora et al. [DLMM12], who derived the following simplified relation for the maximum pile deformation at the interface between the soil layers:

$$\epsilon_p = \alpha \gamma_1 \left\{ -\frac{d}{2h_1} + \left(\frac{E_p}{E_1}\right)^{-0.25} (c-1)^{0.5} \right\} \quad (11)$$

with $\alpha = 0.93 \simeq 1$.

3 The problem examined: piled raft on a two-layer soil

As already mentioned in the introduction, all the simplified analysis methods discussed in the previous section are based on the results of parametric studies conducted

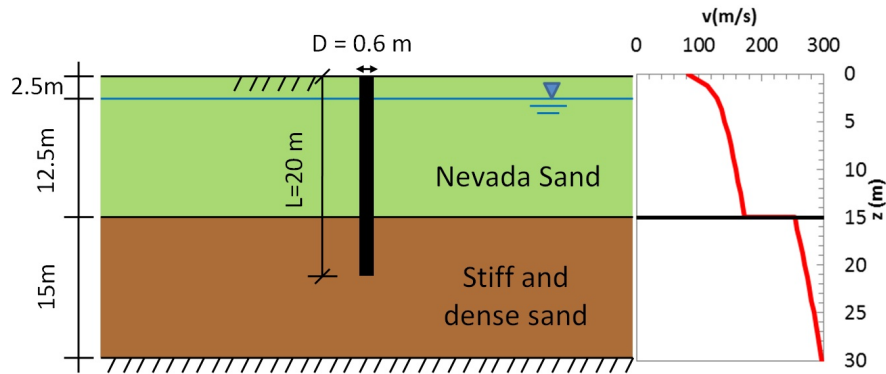


Figure 1: The problem examined: pile geometry and soil profile.

using relatively simple linear (or non-linear) elastic soil models, and neglecting the effects of the development of excess pore pressures in saturated soils due to the rapid cyclic deformations imposed by the earthquake excitation.

In order to assess the influence of the constitutive assumptions made on the soil, and of the development and dissipation of excess pore pressures, the classical problem of a end-bearing pile immersed in a two-layer soil profile with a significant stiffness discontinuity at the interface between the two layers has been reconsidered, performing a series of 3d dynamic coupled consolidation analyses with an advanced constitutive model capable of representing the most relevant features of soil behavior under cyclic/dynamic conditions.

3.1 Problem geometry and seismic input

The problem geometry and the assumed soil profile are detailed in Fig. 1. The cast in place r.c. pile has a diameter $d = 0.6$ m and a length $L = 20$ m. In the FE simulations, the pile is considered as linear elastic, with a Young's modulus $E_p = 24$ GPa, corresponding to a cracked concrete with $R_{ck} = 25$ MPa.

The soil profile is composed, from the ground surface, by a first layer of silty sand, with a thickness of 15 m, underlain by a second layer of stiffer coarse sand, also 15 m thick. The contact with the bedrock is located at the bottom of the second layer.

Fig. 1 shows also the shear wave velocity profile with depth resulting from the assumed soil properties and initial state for each sand layer (discussed in the following Sect. 3.2). At the stratigraphic contact, the small-strain shear stiffness of the top layer is more than two times smaller than that of the lower layer. Based on EN 1998-1 (EC8) soil profile classification for the simplified evaluation of local seismic amplification, the subsoil belongs to class D.

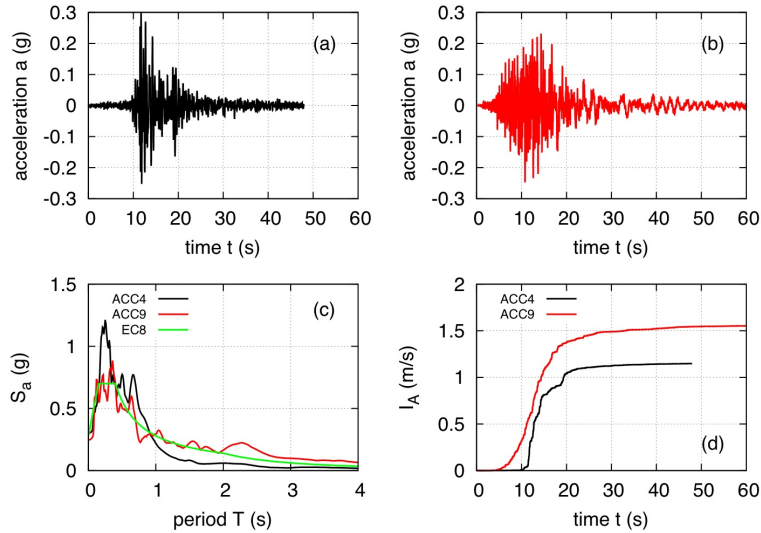


Figure 2: Seismic input at the bedrock: a) time history of horizontal acceleration for accelerometer ACC4; b) time history of horizontal acceleration for accelerometer ACC9; c) response spectra of the two accelerograms; d) time history of Arias intensity for the two accelerograms.

The assumed seismic input is defined in terms of the time history of the horizontal acceleration at the bedrock. A number of recordings of real accelerograms have been considered and scaled in order to obtain a series of (on average) spectrum-compatible accelerograms with the response spectrum provided by EC8 for soil type A. Two of them (accelerograms ACC4 and ACC9) have been used in the simulations reported in this work.

The time histories of the horizontal acceleration, the response spectra and the evolution with time of Arias intensity I_A for the two accelerograms are shown in Fig. 2. Their main characteristics are summarized in Tab. 1. In the table, T_d is the significant duration of the event; T_p its predominant period, and T_m its mean period, as defined by Rathje et al. [RAB98]. The two seismic signals are not significantly different in their main characteristics. However, the peak acceleration in ACC4 is about 21% higher than in ACC9, while the duration of this last one is almost double. For this reason, the Arias intensity in ACC9 is larger than in ACC4.

Table 1: Main characteristics of accelerograms ACC4 and ACC9.

Property		ACC4	ACC9
I_A	(m/s)	1.148	1.553
a_{\max}	(g)	0.301	0.248
T_d	(s)	10.99	19.96
T_p	(s)	0.26	0.36
T_m	(s)	0.42	0.56

3.2 Constitutive model adopted and soil properties

As the response of the pile–soil system under earthquake loading conditions can be significantly affected by such aspects of soil behavior as non–linearity, irreversibility, pressure dependence and contractancy/dilatancy under shear deformations, in the FE simulations the mechanical behavior of the two soil layers has been described using an advanced anisotropic hardening elastoplastic model for sand recently proposed by Dafalias & Manzari [DM04]. The most significant features of this model are briefly recalled in this section; the reader is referred to [DM04] for further details.

3.2.1 Summary of the constitutive equations

The constitutive equations in rate form for the Dafalias & Manzari model can be summarized as follows. Let $(\boldsymbol{\sigma}, \boldsymbol{\alpha}, \boldsymbol{z}, e)$ define the set of state variables for the material, where $\boldsymbol{\alpha}$ (with $\boldsymbol{\alpha} \cdot \mathbf{1} = 0$) is a tensorial internal state variable (deviatoric back–stress) accounting for stress–induced anisotropy, \boldsymbol{z} is a fabric tensor accounting for the effects of previous stress history on material dilatancy, and e is the void ratio of the material, accounting for the effects of soil density. The evolution equations for the state variables read:

$$\dot{\boldsymbol{\sigma}} = \mathbb{D}^{ep}(\boldsymbol{\sigma}, \boldsymbol{\alpha}, \boldsymbol{z}, e) \dot{\boldsymbol{\epsilon}} \quad \dot{\boldsymbol{\alpha}} = \mathbb{H}_{\alpha}(\boldsymbol{\sigma}, \boldsymbol{\alpha}, \boldsymbol{z}, e) \dot{\boldsymbol{\epsilon}} \quad \dot{\boldsymbol{z}} = \mathbb{H}_z(\boldsymbol{\sigma}, \boldsymbol{\alpha}, \boldsymbol{z}, e) \dot{\boldsymbol{\epsilon}} \quad (12)$$

where:

$$\mathbb{D}^{ep} = \mathbb{D}^e - \frac{\mathcal{H}}{K_p} (\mathbb{D}^e \boldsymbol{R}) \otimes (\boldsymbol{L}^T \mathbb{D}^e) \quad (13)$$

$$\mathbb{H}_{\alpha} = \frac{\mathcal{H}}{K_p} \boldsymbol{h}_{\alpha} \otimes (\boldsymbol{L}^T \mathbb{D}^e) \quad \mathbb{H}_z = \frac{\mathcal{H}}{K_p} \boldsymbol{h}_z \otimes (\boldsymbol{L}^T \mathbb{D}^e) \quad (14)$$

are the elastoplastic tangent stiffness tensor and the hardening tensors for the deviatoric back stress and the fabric tensor; \mathbb{D}^e is the elastic tangent stiffness tensor; \boldsymbol{L} is the loading direction tensor; \boldsymbol{R} is the plastic flow direction tensor; $K_p := \boldsymbol{L} \cdot \mathbb{D}^e \boldsymbol{R} + H_p$ is the (strictly positive) hardening modulus, and H_p is the plastic modulus, depending on the hardening functions \boldsymbol{h}_{α} and \boldsymbol{h}_z . In eqs. (13)–(14), the scalar \mathcal{H} is zero for elastic processes ($\boldsymbol{L}^T \mathbb{D}^e \dot{\boldsymbol{\epsilon}} \leq 0$), and 1 for plastic processes ($\boldsymbol{L}^T \mathbb{D}^e \dot{\boldsymbol{\epsilon}} > 0$).

The (hypo)elastic behavior of the material is defined in by the following elastic tangent stiffness tensor:

$$\mathbb{D}^e = K \mathbf{1} \otimes \mathbf{1} + 2G \left(\mathbb{I} - \frac{1}{3} \mathbf{1} \otimes \mathbf{1} \right) \quad (15)$$

where:

$$G = G_{\text{ref}} p_a \frac{(2.97 - e)^2}{1 + e} \left(\frac{p}{p_a} \right)^{0.5} \quad K = \frac{2(1 + \nu)}{3(1 - 2\nu)} G \quad (16)$$

are the tangent shear and bulk moduli, respectively; $p = \text{tr}(\boldsymbol{\sigma})/3$ is the mean stress; p_a the atmospheric pressure; G_{ref} is a reference value for the shear modulus, and ν is the Poisson's ratio.

The elastic domain is limited in stress space by a conical yield surface (YS) with vertex on the origin (see Fig. 3), of equation:

$$f(\boldsymbol{\sigma}, \boldsymbol{\alpha}) = (\mathbf{s} - p\boldsymbol{\alpha}) \cdot (\mathbf{s} - p\boldsymbol{\alpha}) - \frac{2}{3}(mp)^2 = 0 \quad (17)$$

where $\mathbf{s} = \text{dev}(\boldsymbol{\sigma})$, and m is a model constant defining the opening angle of the cone. Fig. 3b shows that the deviatoric tensor $\boldsymbol{\alpha}$ defines the position of the center of the (circular) YS in the deviatoric plane.

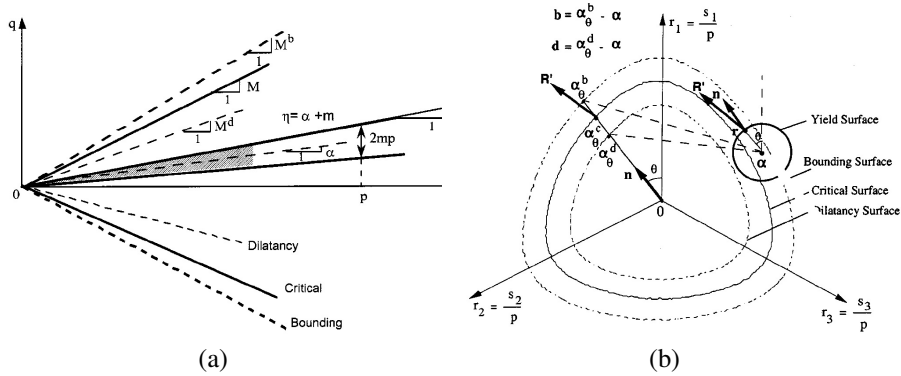


Figure 3: Dafalias & Manzari model: sections of yield, critical, bounding and dilatancy surfaces in $q:p$ plane (a) and normalized deviatoric plane (b), from [DM04].

Plastic deformations induce changes to $\boldsymbol{\alpha}$ according to eq. (12)₂, which correspond to a rotation of the YS around the origin. For extreme plastic deformations, the material attains a *critical state* (CS) in which it deforms at constant stress and constant volume. At CS, the void ratio is a unique function of the mean stress p :

$$e_c = e_{c0} - \lambda \left(\frac{p}{p_a} \right)^\xi \quad (18)$$

with λ and ξ material constants. In the stress space, the CS locus is provided by the envelope of the YF corresponding to the following limiting values of α :

$$\alpha^c = \sqrt{\frac{2}{3}} \alpha^c \mathbf{n} = \sqrt{\frac{2}{3}} g(\theta) \alpha_c^c \mathbf{n} \quad \mathbf{n} = \frac{\mathbf{s}}{\|\mathbf{s}\|} \quad \cos(3\theta) = \sqrt{6} \operatorname{tr}(\mathbf{n}^3) \quad (19)$$

In eq. (19), α_c^c is a material constant (value of α^c for axisymmetric compression), and $g(\theta)$ is a function of the Lode angle θ of $\boldsymbol{\sigma}$. In the original formulation of the model, the Argyris et al. [AFS⁺74] function was used. In this work, the function $g(\theta)$ proposed by van Eekelen [VE80] has been used instead, as it is more accurate for high values of the stress ratio at CS.

As in classical plasticity, the loading direction \mathbf{L} is provided by the gradient of the YS; on the contrary, the plastic flow direction is not obtained from a scalar plastic potential, but rather defined a priori, based on an assumed *dilatancy function* D :

$$\mathbf{L} = \frac{\partial f}{\partial \boldsymbol{\sigma}} \quad \mathbf{R} = \bar{\mathbf{R}} + \frac{1}{3} D \mathbf{1} \quad \bar{\mathbf{R}} := B \mathbf{n} + C \left(\mathbf{n}^2 - \frac{1}{3} \mathbf{1} \right) \quad (20)$$

where:

$$B = 1 + \frac{3(1-c)}{2c} g(\theta) \cos(3\theta) \quad C = 3\sqrt{\frac{3}{2}} \frac{1-c}{c} g(\theta) \quad (21)$$

$$D := A_d (\boldsymbol{\alpha}^d - \boldsymbol{\alpha}) \cdot \mathbf{n} \quad \boldsymbol{\alpha}^d = \sqrt{\frac{2}{3}} \alpha^d \mathbf{n} \quad (22)$$

$$\alpha^d = g(\theta) \alpha_c^c \exp(n^d \psi) \quad A_d = A_0 (1 + \langle \mathbf{z} \cdot \mathbf{n} \rangle) \quad (23)$$

and: $\psi := e - e_c(p)$ is the state parameter defined in [BJS⁺86]. In the above equations, c , n^d and A_0 are material constants. For a given value of the void ratio, the set of tensors $\boldsymbol{\alpha}^d$ define a conical surface in stress space (*dilatancy surface*). For states with $(\boldsymbol{\alpha}^d - \boldsymbol{\alpha}) \cdot \mathbf{n} > 0$, D is positive and the material is contractant; otherwise the material dilates. According to eq. (23)₁, $\alpha^d < \alpha^c$ if $\psi < 0$, and $\alpha^d > \alpha^c$ otherwise. In the first case, the material dilates as soon as the stress-path crosses the dilatancy surface, before reaching the critical state at a larger void ratio. In the second, the material contracts continuously until it reaches the critical state. At critical state, $\psi = 0$ and $\alpha^d = \alpha^c$.

The formulation of the constitutive equation is completed by the following hardening laws for the two internal variables $\boldsymbol{\alpha}$ and \mathbf{z} :

$$\dot{\boldsymbol{\alpha}} = \dot{\gamma} \mathbf{h}_\alpha \quad \dot{\mathbf{z}} = \dot{\gamma} \mathbf{h}_z \quad \dot{\gamma} = \frac{1}{K_p} \mathbf{L}^T \mathbb{D}^e \dot{\boldsymbol{\epsilon}} > 0 \quad (24)$$

where $\dot{\gamma}$ is the plastic multiplier, and the hardening functions \mathbf{h}_α and \mathbf{h}_z are given by:

$$\mathbf{h}_\alpha = \frac{2}{3} h (\boldsymbol{\alpha}^b - \boldsymbol{\alpha}) \quad \mathbf{h}_z = -c_z \langle -\mathbf{R} \cdot \mathbf{1} \rangle (z_{\max} \mathbf{n} + \mathbf{z}) \quad (25)$$

where:

$$\alpha^b = \sqrt{\frac{2}{3}} \alpha^b \mathbf{n} \quad \alpha^b = g(\theta) \alpha_c^c \exp(-n^b \psi) \quad (26)$$

$$h = \frac{b_0}{(\alpha - \alpha_{\text{in}}) \cdot \mathbf{n}} \quad b_0 = G_{\text{ref}} h_0 (1 - c_h e) \sqrt{\frac{p_a}{p}} \quad (27)$$

and n^b , h_0 and c_h are material constants, and α_{in} is the value of α at the beginning of a new loading process, updated when the scalar $(\alpha - \alpha_{\text{in}}) \cdot \mathbf{n}$ becomes negative.

According to eq. (25)₁, $\dot{\alpha} = \mathbf{0}$ for $\alpha = \alpha^b$. For a dense material, with $\psi < 0$, the set of α^b provided by eq. (27) define a conical surface in stress space – called “bounding surface” – which limits the rotation of the YS and thus controls the maximum attainable value of the stress ratio (*i.e.*, the peak shear strength). As (negative) plastic volumetric strain accumulate after reaching a peak stress ratio, $\psi \rightarrow 0$, and the final stress state converges to critical state, with $\alpha^b = \alpha^d = \alpha^c$.

3.2.2 Soil properties and initial state

The set of material constants used for the two soils in Fig. 1 is reported in Tab. 2. The constants adopted for the top layer (soil 1) are those determined by Dafalias & Manzari for Nevada sand. The constants of Toyoura sand provided by the same Authors have been adopted for the bottom layer, with the only exception of the values of G_{ref} and α_c^c . The reader is referred to [DM04] for the details of the calibration procedure.

A relatively large value has been assumed for the soil permeability k of soil 2 (coarse sand), so that pore pressure gradients are very small during the seismic excitation. On the contrary, different values of permeability have been adopted for soil 1 (silty sand), to investigate the effects of excess pore pressure generation and dissipation.

The initial stress state has been defined by assuming geostatic conditions, with a constant $K_0 = 1 - \sin \phi_c$. The initial stress state has been assumed as centered with

Table 2: Summary of material constants adopted in the FE simulations.

Property	Soil 1	Soil 2	Property	Soil 1	Soil 2
G_{ref}	125	350	h_0	9.70	7.05
ν	0.05	0.05	c_h	1.300	0.968
α_c^c	1.13	1.32	n^b	2.56	1.1
c	0.780	0.693	A_0	0.81	0.704
λ	0.027	0.019	n^d	1.05	3.5
e_{c0}	0.83	0.934	z_{max}	5.0	4.0
ξ	0.45	0.70	c_z	800	600
m	0.01	0.01	k (m/s)	variable	1.0e-2

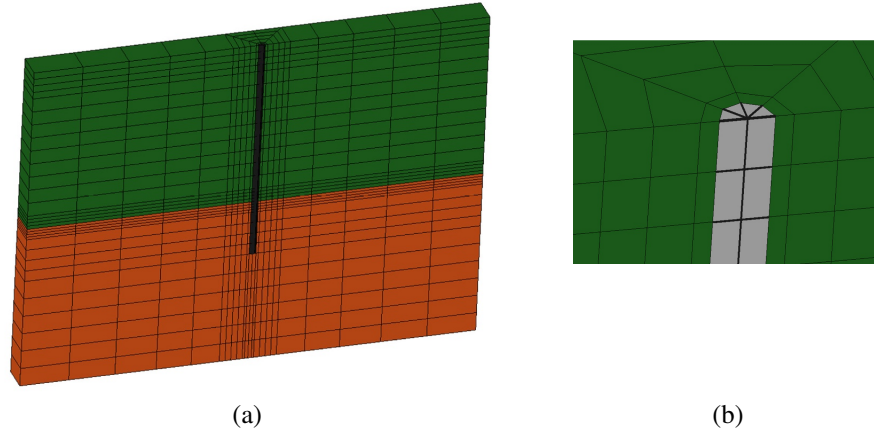


Figure 4: Finite element discretization adopted in the simulations: a) general view; b) detail of the pile–soil contact.

respect to the YS ($\alpha = s/p$). The void ratio in the two layers is such that $\psi = -0.22$ in soil 1, and $\psi = -0.3$ in soil 2. The fabric tensor has been set to $\mathbf{z} = \mathbf{0}$

3.3 Finite element model and analysis program

The simulations reported in this study have been carried out using the FE code Tochnog professional v.14 [Rod13]. The Fe discretization adopted for the study of kinematic interaction effects is shown in Fig. 4. The model is $25 \times 2.5 \text{ m}^2$ in plan and has a vertical size of 30 m. Due to symmetry in both geometry and applied loads (seismic accelerations at the base acting in direction x only), only half of the pile has been included in the model. The dimension of the model in direction y , orthogonal to the direction of polarization of the seismic excitation at the base, has been kept relatively small to reduce the computational cost of each simulation, and has been selected from the results of a preliminary study which indicate that the influence of the model size in y direction on the computed structural loads is small.

The soil is discretized with 264 8-noded isoparametric hexahedral elements for coupled consolidation, implementing the UP approximation to the balance equations of momentum and mass conservation [ZCP⁺90]. Two-noded, linear elastic beam elements have been used to simulate the pile. The pile–soil connection has been modeled using short orthogonal beam elements, as shown in Fig. 4b.

As for the boundary conditions, the base has been considered as a perfectly rough, impervious boundary. The seismic input has been applied by imposing at the base of the model the horizontal displacement history $v_x(t)$ consistent with the two accelerograms considered. Horizontal displacements in the normal direction are fixed along

Table 3: Program of FE simulations.

Analysis no.	Seismic input	k (soil 1) (m/s)	Analysis no.	Seismic input	k (soil 1) (m/s)
r01	ACC4	1.0e-2	r04	ACC9	1.0e-2
r02	ACC4	2.3e-5	r05	ACC9	2.3e-5
r03	ACC4	2.3e-7	r06	ACC9	2.3e-7

the two vertical planes of symmetry (normal to the y direction), while periodic boundary conditions have been assumed for the displacements on the two planes orthogonal to the x direction. Natural boundary conditions (no flow) have been imposed to the pore pressure field on all vertical boundaries. Atmospheric pore water pressure have been imposed at the ground water table level, located 2.5 m below the ground surface.

The program of FE simulations performed in this study is detailed in Tab. 3. Two different sets of simulations have been performed with different seismic input. In each series, the permeability k of soil 1 has been changed from 1.0e-2 to 2.3e-7. In the first case, the permeability is sufficiently large that almost no pore pressure gradients develop in the soil (drained conditions, DC). In the last case, on the contrary, the permeability is so low that the upper layer deforms in almost undrained conditions (UC) during the seismic shaking. Between these two extremes, in analyses r02 and r05, excess pore pressure generation and dissipation occur during the event (coupled consolidation, CC).

3.4 Selected results

The results of the numerical simulations can be used to assess the effects of soil-pile kinematic interaction on pile bending moments and to quantify the modifications induced in the seismic ground motion at ground surface by the presence of the pile.

Bending moment distributions along the pile axis computed with varying seismic input motions and with different soil drainage conditions (from fully drained to almost undrained) are shown in Fig. 5. The envelopes of minimum and maximum bending moments along the pile length computed in analyses r02 (ACC4) and r05 (ACC9) under fully coupled consolidation conditions are plotted in Fig. 5a, together with the bending moment distributions at the two time stations at which the minimum/maximum moment is attained ($t = 19.3$ s for r02 and $t = 16.93$ s for r05; curves plotted with dotted lines). As the pile head is free to rotate, the moment at the pile head is zero and the maximum bending moments (in absolute terms) occur at the interface between the two layers.

As expected, the largest values of the bending moments are found at the interface between the two soil layers, in correspondence with a strong discontinuity in shear stiffness. While accelerogram ACC4 is characterized by the largest peak and spectral

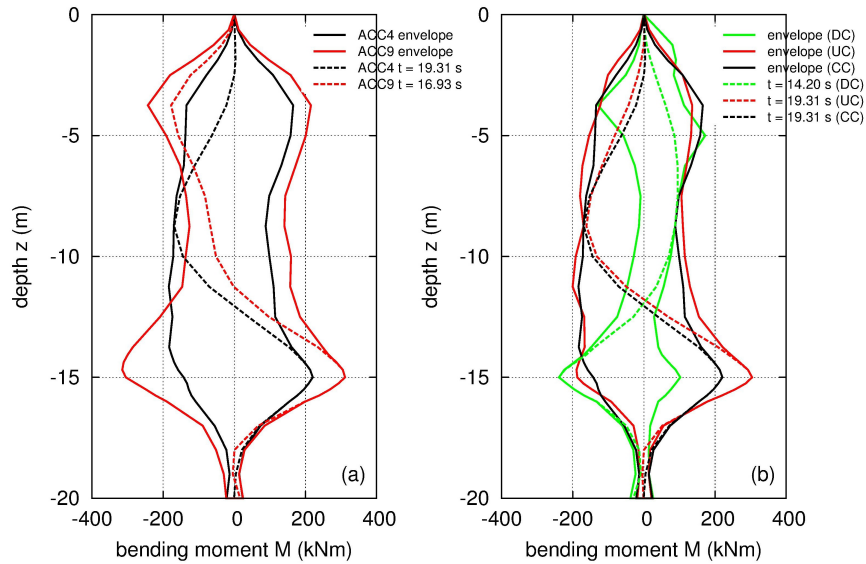


Figure 5: Envelopes of min/max bending moments: a) comparison of coupled consolidation analyses r02 (ACC4) and r05 (ACC9); b) comparison of analyses r01 (DC), r02 (CC) and r02 (UC), with ACC4 seismic input.

accelerations, the largest kinematic bending moments are associated to ACC9 seismic input, which is characterized by the largest Arias intensity. Therefore caution should be exerted in using simplified models to estimate maximum bending moments which characterize the seismic input in terms of peak acceleration at ground surface only.

The effects of pore water pressure build-up in the saturated soil layers on pile bending moments can be assessed by comparing the results obtained in analyses r01 (DC), r02 (CC) and r03 (UC) for the same seismic input (ACC4). Fig. 5b shows the envelopes of minimum and maximum bending moments along the pile length computed in these three cases, together with the moment distributions along the pile at the different time stations at which the minimum/maximum moment is attained (curves plotted with dotted lines). From the figure it is immediately apparent that the same seismic input can give rise to significantly different bending moment distributions if excess pore pressure develop as a result of partial or no drainage of pore water during the seismic shaking. In the particular case examined, the differences between the fully undrained case (r03) and the coupled consolidation case (r02) are less important from a qualitative point of view, but relevant in terms of maximum computed bending moment at the stratigraphic contact between the two layers (which is also a drainage boundary). It is

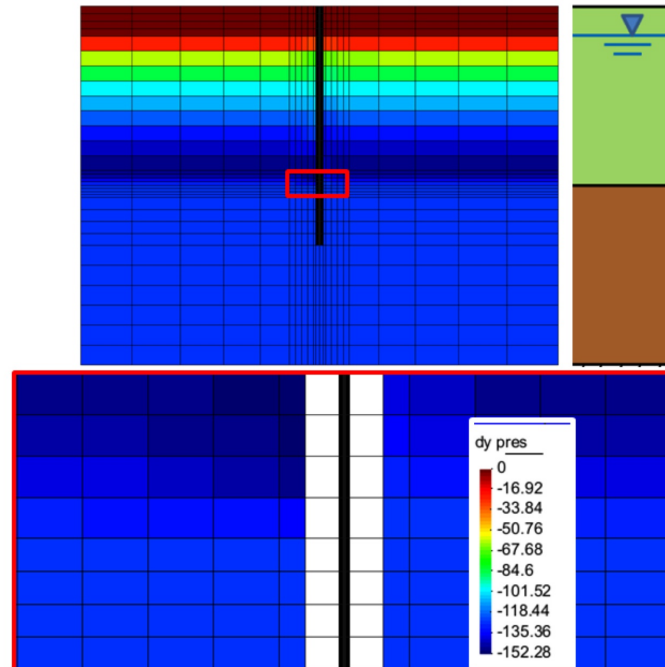


Figure 6: Excess pore water pressure field at $t = 19.3$ s, for r02 (CC) with ACC4 seismic input. The bottom part of the figure is a close-up of the region marked with a red rectangle.

also worth noting that, while in the drained case the peak bending moment is attained at $t = 14.2$ s, in the CC and UC cases the peak bending moment on the pile is attained more than 5 s later, at $t \in [19.31, 19.51]$ s.

A complete picture of the pore pressure field computed in analysis r02 at $t = 19.31$ s is given in Fig. 6 in terms of contour lines of excess pore water pressure Δu over the initial hydrostatic conditions.

Even if both soil layers are relatively dense, positive excess pore water pressures are generated in the upper layer due to the high contractancy of Nevada sand. The largest positive excess pore pressures are found close to the stratigraphic contact. The values of Δu decrease upwards, as the distance to the upper draining boundary is reduced. On the contrary, Δu remains quite large close to the bottom drainage boundary, at the contact with the soil layer 2, in spite of its high permeability. This is due to the fact that the bottom and lateral boundaries of soil 2 are impervious: the pore water flowing downwards from the upper layer cannot be drained from the other boundaries and thus the pore pressure in the bottom layer are forced to increase to reduce the downward hydraulic gradient and maintain the global mass balance. Due to the high

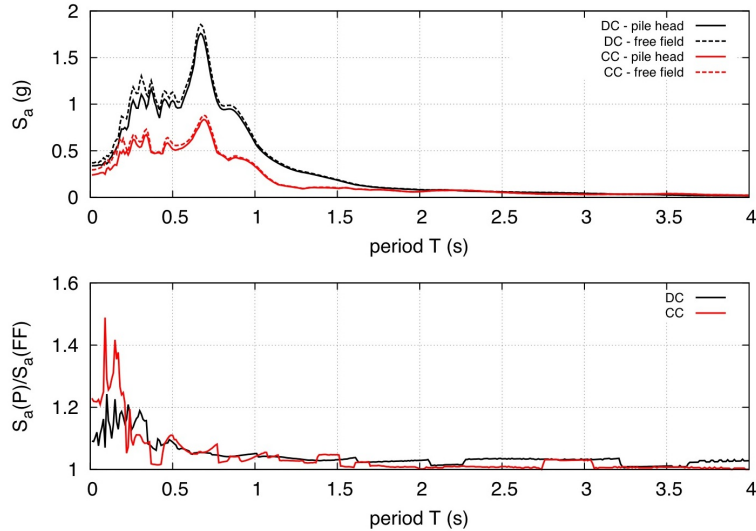


Figure 7: Pile head and free surface accelerations for analyses r01 (DC) and r02 (CC): a) response spectra; b) spectral acceleration ratio $S_a(P)/S_a(FF)$.

permeability of soil 2, the excess pore pressure in this layer are constant, to keep the hydraulic gradient nil. The contour lines of the excess pore pressure are almost horizontal, as the presence of the pile has only a limited effect on the deformation pattern of the solid skeleton and thus on excess pore pressure build-up.

The influence of excess pore pressure build-up on the soil-pile system response under the seismic shaking is clearly visible on the accelerations computed at the pile head and far from the pile, in (almost) free-field conditions. Fig. 7a shows the acceleration response spectra computed at the pile head and in free-field conditions in analyses r01 (ACC4, DC) and r02 (ACC4, CC), respectively; for the same simulations, Fig. 7b provides the ratio between the spectral ordinates $S_a(P)$ for the pile head and $S_a(FF)$ in free-field conditions.

From the data it is quite clear that a significant amplification of the spectral ordinates occurs in drained conditions as compared to the fully coupled consolidation case. The observed differences can be due partly to the changes in soil stiffness associated to the variation of mean effective stress with depth, but also on the additional dissipation occurring as a consequence of the pore water transient seepage. In this respect, it is interesting to note that the shape of the spectra and the dominant frequencies are quite similar between fully drained and consolidation cases. On the contrary, no significant differences are found between the pile head and the free-field spectra in both the cases considered. Differently from what is typically observed in piles with fixed rotation at the head, the spectral ratio $S_a(P)/S_a(FF)$ is slightly larger than 1, although the

maximum difference does not exceed 20% for DC, and about 40% for CC in a period range from 0.05 to 0.2 s.

4 Performance of simplified methods

The results of the FE simulations have been used as a benchmark to test the predictive capabilities of some of the simplified methods for evaluating the maximum kinematic bending moment, discussed in previous Sect. 2. In particular, the methods considered are reported in Tab. 4, together with the input data required by each of them.

As the pile considered in Sect. 3 is embedded in the bottom layer for a length sufficient to consider it as infinitely long, and the distance of the stratigraphic contact from the head is such that any interaction between the loads originating from kinematic interaction at the pile head and at the stratigraphic contact can be excluded, the fundamental assumptions on which the methods listed in Tab. 4 are based can be considered applicable.

The input data for each method is obtained from a linear equivalent site response analysis performed with the FE code EERA [BIL00]. The stiffness degradation and damping curves required for such an analysis have been obtained by simulating a series of cyclic simple shear tests with the Dafalias & Manzari model [DM04], as detailed in Appendix. As far as the stiffness degradation is concerned, different assumptions have been made for the different drainage condition assumed in the simulated simple shear tests (Fig. 8). For drained conditions, a single curve interpolating the simulation data has been chosen (curve D in Fig. 8a). For undrained conditions, the simulated test result display a tendency of shear stiffness to increase for γ values larger than 10^{-3} (0.1%). Therefore, two different modulus decay curves have been considered (indicated as curves U(a) and U(b) in Fig. 8a), to achieve the best fit with the shear test results in the medium and large strain ranges, respectively.

Since the results of the 1-d site response analyses are used to characterize the effect of the seismic excitation in the simplified methods, before analyzing the performance of such methods in terms of maximum pile loads, it is interesting to compare the

Table 4: Simplified methods considered and relevant input data.

Method	Input data
Dobry & O'Rourke (1983)	$G_1, G_1/G_2, \gamma_1$
Mylonakis (2001)	$G_1, G_1/G_2, \gamma_1, h_1, \omega$
Di Laora et al. (2012)	$G_1, G_1/G_2, \gamma_1, h_1$
Nikolaou et al. (2001)	$G_1, G_1/G_2, a_{\max}, N_c$
Dente et al. (2011)	$G_1, G_1/G_2, a_{\max}, T_1$
Sica et al. (2011)	$G_1, G_1/G_2, a_{\max}, \gamma_{ff}$

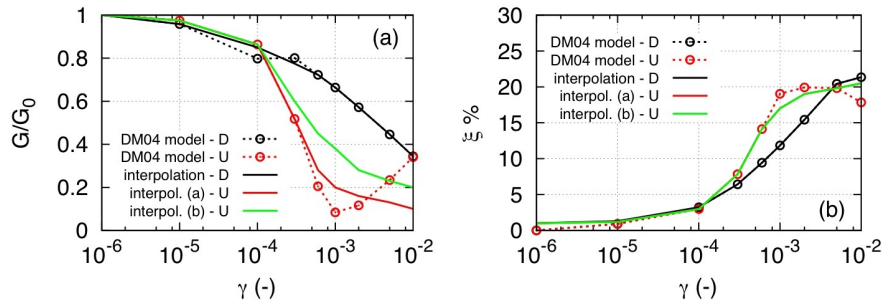


Figure 8: Simulation of cyclic simple shear tests in Soil 1: a) stiffness degradation vs. shear strain amplitude; b) damping ratio vs. shear strain amplitude.

results of the linear equivalent FE simulations with the free field response provided by the fully coupled 3-d simulations with the advanced elastoplastic model of Dafalias & Manzari. Such a comparison is presented in Fig. 9 in terms of response spectra computed at ground surface for fully drained conditions, coupled consolidation (full 3-d FE model) and undrained conditions (EERA).

The data reported in Fig. 9 show that, even if carefully calibrated, the linear equivalent approach implemented in the code EERA provides site response predictions in terms of ground surface accelerations which are largely different (in this case, in excess) from those obtained in the more accurate 3-d FE analyses performed with an advanced soil model. In particular, the comparison seems to indicate that the real material response is more dissipative than that provided by the simple non-linear model implemented in EERA, regardless of the effort taken for the proper calibration of the constitutive curves. This effect is apparent not only in coupled consolidation analyses but also in drained conditions.

The maximum shear strain profiles with depth computed in simplified 1-d site response analysis and in the 3-d simulations in free-field conditions are plotted in Fig. 10, for the two seismic inputs considered. Although the values of γ calculated with the two approaches in the bottom layer appear in substantial agreement, this is not the case for the upper layer, where the simplified EERA simulations tend to underestimate significantly the maximum shear deformations in this layer. The largest differences are observed between the results of undrained 1-d site response analyses and the 3-d fully coupled consolidation analysis performed with the ACC9 seismic input, at depths between 5 and 10 m. The observed differences are smaller, but still significant, at the stratigraphic contact. It is also interesting to note that the results of the undrained EERA simulations appear quite sensitive to the adopted shear modulus decay curve, as large differences can be observed in the shear strain profiles obtained with the decay curves U(a) and U(b) of Fig. 8a.

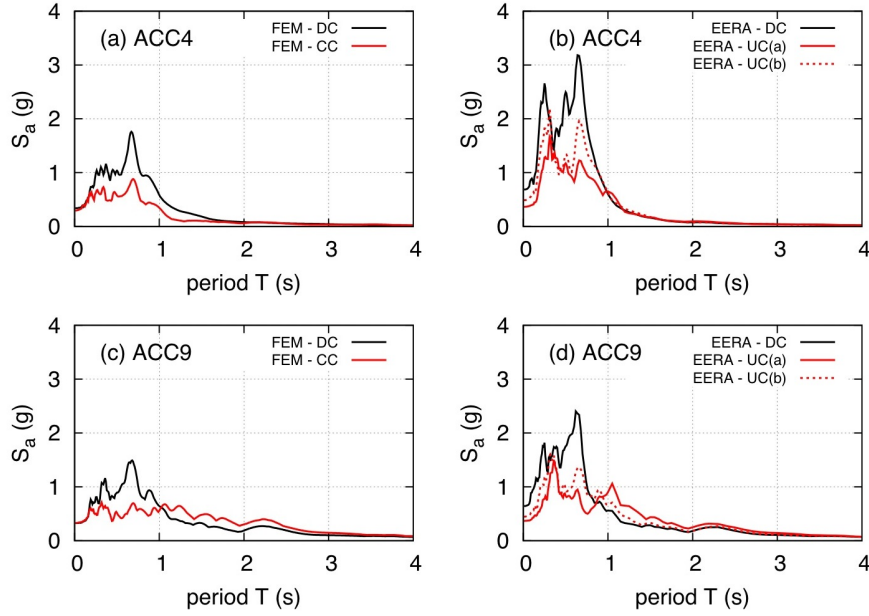


Figure 9: Free-field response spectra at ground surface: a) ACC4, FEM predictions for DC and CC simulations; b) ACC4, EERA predictions for DC and UC simulations; a) ACC9, FEM predictions for DC and CC simulations; b) ACC9, EERA predictions for DC and UC simulations.

Some of the methods in Tab. 4 [NMGT01, DCSS11] evaluate the maximum bending moment at the stratigraphic contact using the maximum acceleration at ground surface, a_{\max} as an indicator of the earthquake intensity, while the others [DO83, Myl01, SMS11, DLMM12] use a measure of the shear strain in the top layer for the same purpose. In both cases, these quantities are determined from simplified 1-d site response analyses like the ones considered in this study. The significant differences observed in the predictions of both quantities from EERA simulations and full 3-d drained or coupled consolidation FE analyses performed with an advanced constitutive model for the soil should be taken into account in the evaluation of the predictive capabilities of the simplified methods.

A quantitative measure of the performance of the different simplified methods in the prediction of the maximum bending moment at the stratigraphic contact is provided by the following relative error measure:

$$\text{ERR} = \frac{|M_{\max}| - |M_{\max}^{\text{FEM}}|}{|M_{\max}^{\text{FEM}}|} \times 100 \quad (28)$$

where M_{\max} is the maximum bending moment predicted by each simplified method

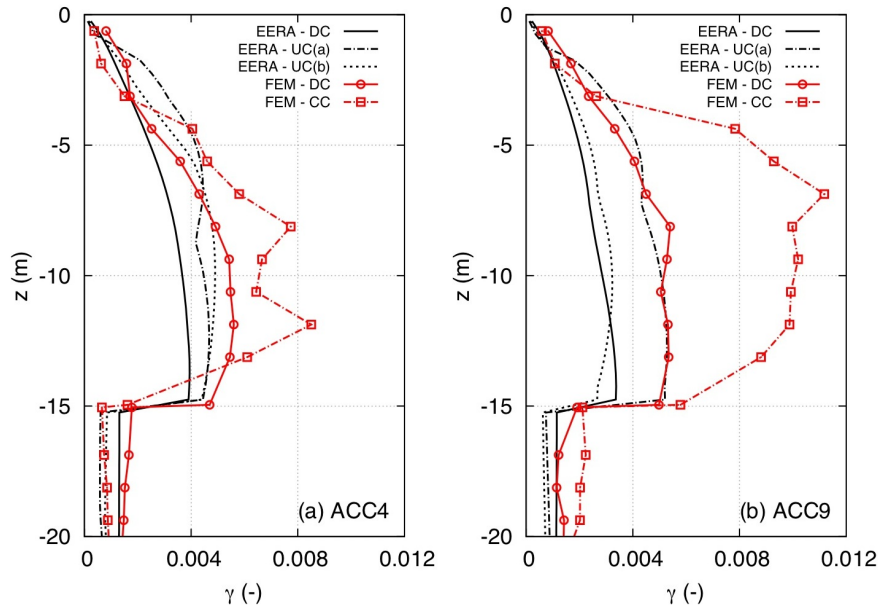


Figure 10: Maximum shear strain γ vs. depth profiles obtained from FEM and EERA simulations: a) ACC4 seismic input; b) ACC9 seismic input.

and M_{\max}^{FEM} is the corresponding maximum bending moment obtained from the 3-d FE simulations with the Dafalias & Manzari model, assumed as a reference for the actual response of the pile. The results of the 3-d coupled consolidation simulations have been compared with the prediction of the simplified methods under undrained conditions, considering the two different stiffness decay curves, U(a) and U(b), of Fig. 8a.

The relative error values obtained for the two seismic inputs considered are plotted in Fig. 11. In drained conditions, the simplified approaches differ from the reference value of M_{\max} by a maximum of about 35% (Dobry & O'Rourke method), and the relative errors are generally smaller than 20%. All the simplified methods tend to underestimate M_{\max} , except Sica et al., which significantly overestimates it. The method of Nikolaou et al. provide the best performance for this case. No substantial differences are observed in the performance of the different methods for the two seismic inputs considered.

For the coupled consolidation case, the simplified models predictions are generally much less accurate, with differences ranging from -70% (Dobry & O'Rourke, case U(b)) to +60% (Nikolaou et al., case U(a)). It is interesting to note that, in this case, the predictions of the simplified models are quite sensitive to both the adopted soil

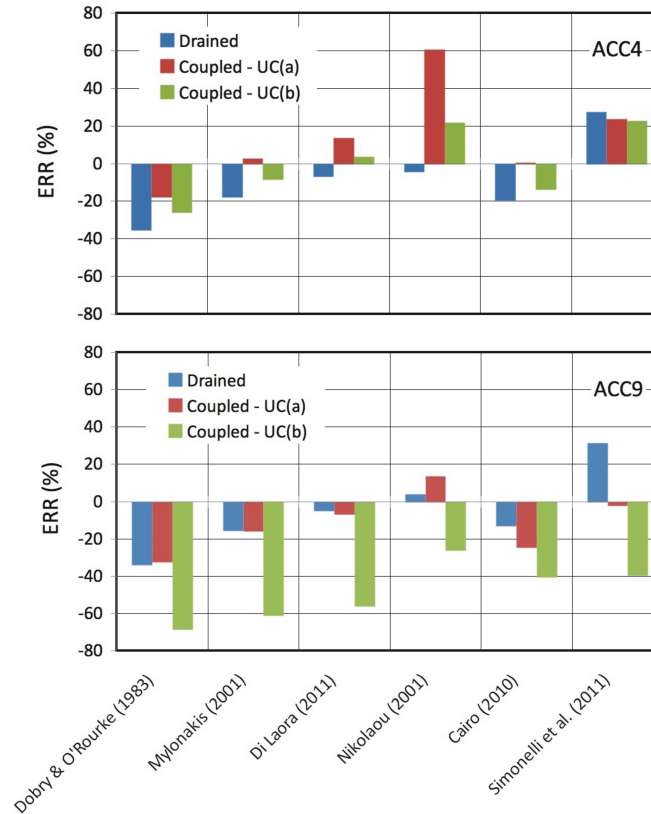


Figure 11: Relative error associated to simplified methods: a) ACC4 seismic input; b) ACC9 seismic input.

model and the seismic input considered. In fact, for ACC9 seismic input, the relative errors computed assuming undrained behavior are much larger (in absolute values) for the case U(b) than for the case U(a), for all the methods considered. On the contrary, for ACC4 seismic input the two undrained predictions are much closer each other and more accurate, with the only notable exception of Nikolaou et al. and Sica et al. methods.

5 Concluding remarks

In this work, a series of 3-d, fully coupled dynamic consolidation analyses have been used to investigate the kinematic interaction effects in the classical problem of a single end-bearing pile immersed in a two-layer soil profile with a significant stiffness

discontinuity at the interface between the two layers,

In the simulations, an advanced constitutive model, capable of representing the most relevant features of soil behavior under cyclic/dynamic conditions, has been used with the specific aim of investigating: i) the influence of the constitutive assumptions on the predicted system response; and, ii) the effects of the development and dissipation of excess pore pressures within the soil mass on pile loads and ground deformations.

The results of the numerical simulations clearly show that significant pore pressure build-up can occur under seismic conditions even in soils with relatively high permeability, and that the associated changes in the effective stress field can have an important effect in determining the response of the soil-pile system, both in terms of pile loads and ground surface accelerations.

The results of the numerical simulations have also been used to assess the predictive capabilities of a number of simplified methods recently proposed for the evaluation of the maximum kinematic bending moment at the stratigraphic contact between the two layers. Generally speaking, the best performance overall seems to be associated to such methods as the one proposed by Di Laora et al., which rely heavily on the informations provided by a detailed site response analysis. However, while the predictive capabilities of currently available design procedures for the evaluation of kinematic interaction effects appears relatively satisfactory when no excess pore pressures are expected to develop within the soil, some care must be taken in applying the same procedures in undrained or partially undrained conditions, due to the limitations inherent in the non-linear elastic soil models used to perform the 1-d site response analysis, employed by the simplified methods to characterize the effects of the seismic shaking.

References

- [AFS⁺74] J. H. Argyris, G. Faust, J. Szimmat, E. P. Warnke, and K. J. Willam. Recent developments in the finite element analysis of prestressed concrete reactor vessels. *Nuclear Engineering and Design*, 28(1):42–75, 1974.
- [BIL00] J. P. Bardet, K. Ichii, and C. H. Lin. *EERA: a computer program for equivalent-linear earthquake site response analyses of layered soil deposits*. University of Southern California, Department of Civil Engineering, 2000.
- [BJS⁺86] K Been, MG Jefferies, JA Sladen, J Krahn, and RD Hollander. A state parameter for sands. *Géotechnique*, 36(1), 1986.
- [CD07] R. Cairo and G. Dente. Kinematic interaction analysis of piles in layered soils. In *ISSMGE ERTC 12 Workshop, Geotechnical Aspects of EC8*, 2007.

- [DCL09] F. Dezi, S. Carbonari, and G. Leoni. A model for the 3d kinematic interaction analysis of pile groups in layered soils. *Earthquake Engineering & Structural Dynamics*, 38(11):1281–1305, 2009.
- [DCSS11] G. R. Dente, R. Cairo, A. L. Simonelli, and S. Sica. Multi-variable relations for simplified evaluation of soil–pile kinematic effects. *Rivista Italiana di Geotecnica*, 11(1):33–46, 2011.
- [Den05] G. Dente. *Fondazioni su pali. Linee guida sugli aspetti geotecnici della progettazione in zona sismica (in Italian)*, pages 147–160. Patron ed., 2005.
- [DL09] R. Di Laora. *Seismic soil–structure interaction for pile supported system*. PhD thesis, Università degli Studi di Napoli Federico II, 2009.
- [DLMM12] R. Di Laora, A. Mandolini, and G. Mylonakis. Insight on kinematic bending of flexible piles in layered soil. *Soil Dyn. and Earthquake Engng.*, 43:309–322, 2012.
- [DM04] Y. F. Dafalias and M. T. Manzari. Simple plasticity sand model accounting for fabric change effects. *J. of Engng. Mechanics, ASCE*, 130(6):622–634, 2004.
- [DO83] R. Dobry and M. J. O’Rourke. Discussion on “Seismic response of end-bearing piles” by Raul Flores-Berrones and Robert V. Whitman (april, 1982). *J. of Geotech. Engng., ASCE*, 109(5):778–781, 1983.
- [Mar12] M. Martinelli. *Comportamento dinamico di fondazioni su pali in sabbia (in Italian)*. PhD thesis, Sapienza Università di Roma, 2012.
- [MdSAM09] R. M. S. Maiorano, L. de Sanctis, S. Aversa, and A. Mandolini. Kinematic response analysis of piled foundations under seismic excitation. *Canadian Geotechnical Journal*, 46(5):571–584, 2009.
- [MH77] E. Margason and M. Holloway. Pile bending during earthquakes. In *6th World Conference on Earthquake Engineering*, volume 4, pages 231–238, 1977.
- [My101] G. Mylonakis. Simplified model for seismic pile bending at soil layer interfaces. *Soils and foundations*, 41(4):47–58, 2001.
- [NEH97] NEHRP. *National Earthquake Hazards Reduction Program: guidelines for the seismic rehabilitation of buildings*. Federal Emergency Management Agency, 1997.
- [NMGT01] S. Nikolaou, G. Mylonakis, G. Gazetas, and T. Tazoh. Kinematic pile bending during earthquakes: analysis and field measurements. *Geotechnique*, 51(5):425–440, 2001.

- [RAB98] E. M. Rathje, N. A. Abrahamson, and J. D. Bray. Simplified frequency content estimates of earthquake ground motions. *J. of Geotech. and Geoenv. Engng., ASCE*, 124(2):150–159, 1998.
- [Rod13] D. Roddeman. *TOCHNOG PROFESSIONAL User's manual – Version 14*. FEAT – Finite Element Application Technology, 2013.
- [SMS11] S. Sica, G. Mylonakis, and A. L. Simonelli. Transient kinematic pile bending in two-layer soil. *Soil Dynamics and Earthquake Engineering*, 31(7):891–905, 2011.
- [SS08] A. L. Simonelli and S. Sica. Fondazioni profonde sotto azioni sismiche. In *Opere geotecniche in condizioni sismiche. XII Ciclo di Conferenze in Meccanica ed Ingegneria delle Rocce*. Pàtron Bologna, 2008.
- [VE80] H. A. M. Van Eekelen. Isotropic yield surfaces in three dimensions for use in soil mechanics. *Int. J. Num. Anal. Meth. Geomech.*, 4(1):89–101, 1980.
- [ZCP+90] O. C. Zienkiewicz, A. H. C. Chan, M. Pastor, D. K. Paul, and T. Shiomi. Static and dynamic behaviour of soils: a rational approach to quantitative solutions. i. fully saturated problems. *Proceedings of the Royal Society of London. A. Mathematical and Physical Sciences*, 429(1877):285–309, 1990.

Simplified modeling strategies for soil-structure interaction problems: The multifiber beam concept

Panagiotis Kotronis

LUNAM Université, Ecole Centrale de Nantes, Université de Nantes, CNRS UMR 6183, GeM (Institut de Recherche en Génie Civil et Mécanique), 1 rue de la Noë, BP 92101, 44321, Nantes, cedex 3, France

Starting with the study of different Euler Bernoulli and Timoshenko beam finite element formulations, a displacement based multifiber Timoshenko beam is presented. The element is free of shear locking problems and it is able to reproduce the non linear behaviour of composite structures. It is validated using the experimental results of a reinforced concrete viaduct subjected to earthquake loadings. Despite the small number of degrees of freedom of the finite element model, the non linear behaviour of the viaduct is predicted satisfactorily. Not only the peaks in both directions are well reproduced but the frequency content of the response is correctly matched. Multifiber beams combined with macro-elements [Gra13] can take into account in a efficient, fast and robust way soil-structure interaction phenomena. This is shown in the last section of the article where the influence of the soil-structure interaction on the behaviour of the reinforced viaduct is highlighted.

1 Introduction

The objective of this course is to introduce the differences between the Euler Bernoulli and Timoshenko theories, to present various finite element beam formulations and to show the equations of displacement based Timoshenko multifiber beam elements. The paper follows mainly the work and ideas exposed in [Peg94], [GPP94], [KM05], [MKRC06], [Bit13], [CKCed]. The important subject of force based beam finite elements is not discussed hereafter. The reader can find information on this subject in the following references [SFT96a], [SFT96b].

2 Classical beam theories

2.1 Kinematics

We consider hereafter a beam of length L and section $S(x)$ (figure 1). $G(x, y, z)$ is the center of gravity of the section $S(x)$ and $P(x, y, z)$ a point in the section. We define as neutral axis the line that links the center of gravities of all the sections. We also suppose that G_x, G_y, G_z are principal axes. For the 2D case studied hereafter (loadings are in the $x - y$ plane), the displacements $\underline{u}^T = \{u_x, u_y\}$ of the point $P(x, y, z)$ can be expressed as a function of the displacements $U_x(x), U_y(x)$ and the rotation $\Theta_z(x)$ of the section $S(x)$ (often defined in the literature as *generalised* displacements, see also equations (8) and (16)) considering the following two kinematic hypotheses:

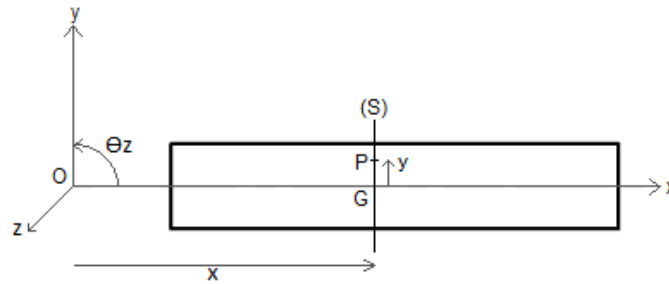


Figure 1: Beam [Bit13]

- Euler Bernoulli theory: In this theory, the section remains plane and perpendicular to the neutral axis (figure 2).

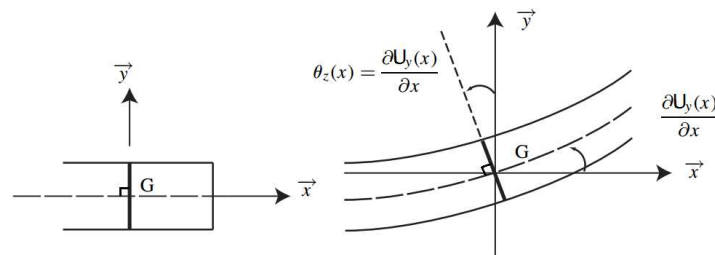


Figure 2: Euler Bernoulli theory [Bit13]

A consequence of the previous kinematic assumption is that the rotation of the section $\Theta_z(x)$ equals $U'_y(x)$ (the symbol $'$ defines hereafter the first derivative with respect to x and the symbol $''$ the second derivative with respect to x)

(figure 2). The displacements of the point $P(x, y, z)$ take thus the following form [GPP94]:

$$\begin{aligned} u_x(x, y) &= U_x(x) - y\Theta_z(x) = U_x(x) - yU_y'(x) \\ u_y(x, y) &= U_y(x) \end{aligned} \quad (1)$$

and the strains are calculated as (infinitesimal strain theory assumption):

$$\begin{aligned} \varepsilon_x &= \frac{\partial u_x}{\partial x} = U_x'(x) - y\Theta_z'(x) = U_x'(x) - yU_y''(x) \\ \gamma_{xy} &= \frac{\partial u_x}{\partial y} + \frac{\partial u_y}{\partial x} = U_y'(x) - \Theta_z(x) = 0 \end{aligned} \quad (2)$$

One can notice that due to the adopted kinematic hypothesis shear strains are found equal to zero.

- Timoshenko theory: In this theory, the kinematic assumption is that the section remains plane but not necessarily perpendicular to the neutral axis. In other words, $\Theta_z \neq U_y'(x)$, see figure 3. Displacements and strains (infinitesimal strain theory assumption) are now calculated as [GPP94]:

$$\begin{aligned} u_x(x, y) &= U_x(x) - y\Theta_z(x) \\ u_y(x, y) &= U_y(x) \end{aligned} \quad (3)$$

$$\begin{aligned} \varepsilon_x &= \frac{\partial u_x}{\partial x} = U_x'(x) - y\Theta_z'(x) \\ \gamma_{xy} &= \frac{\partial u_x}{\partial y} + \frac{\partial u_y}{\partial x} = U_y'(x) - \Theta_z(x) \end{aligned} \quad (4)$$

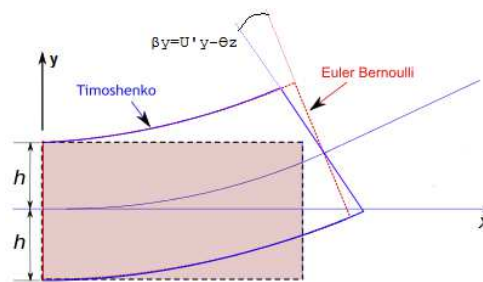


Figure 3: Timoshenko theory (Wikipedia)

We define hereafter

$$\beta_y = U'_y(x) - \Theta_z(x) \quad (5)$$

The variable β_y represents the rotation of the section due to shear. From equation (4) one can notice that shear strains are now constant in the section (and not as in the Euler Bernoulli theory necessarily equal to zero).

2.2 Euler Bernoulli theory: Principal work principle and generalised forces

The virtual work principle is written as (body forces and inertial forces are hereafter neglected. The symbol σ defines stresses):

$$\int_0^L \int_S \delta \varepsilon_x \sigma_x dS dx - w_{exter} = 0 \quad (6)$$

with w_{exter} the work of the external forces.

Replacing (2) in (6) we get:

$$\int_0^L \int_S \delta (U'_x(x) - y \Theta'_z(x)) \sigma_x dS dx - w_{exter} = 0 \quad (7)$$

We define hereafter the *generalised* forces in the section as:

$$\text{Normal force: } F_x = \int_S \sigma_x dS \quad (8)$$

$$\text{Bending moment : } M_z = - \int_S y \sigma_x dS$$

and equation (7) becomes:

$$\int_0^L (F_x \delta U'_x + M_z \delta \Theta'_z) dx - w_{exter} = 0 \quad (9)$$

Within a beam theory $\sigma_y = \sigma_z = \sigma_{yz} = 0$. Furthermore and because of equation (2) $\sigma_{xz} = \sigma_{xy} = 0$. Hooke's law thus becomes (with E the Young's modulus and ν the Poisson's coefficient):

$$\begin{aligned} \sigma_x &= E \varepsilon_x \\ \varepsilon_y &= \varepsilon_z = -\nu \varepsilon_x \end{aligned} \quad (10)$$

Finally, using equations (2), (8) and (10) the generalised forces become:

$$\begin{aligned} F_x &= \int_S E \varepsilon_x dS = \int_S E(U'_x(x) - y\Theta'_z(x))dS = \int_S EU'_x(x)dS = ESU'_x(x) \\ M_z &= - \int_S yE\varepsilon_x dS = - \int_S yE(U'_x(x) - y\Theta'_z(x))dS = \int_S y^2 E\Theta'_z(x)dS = EI_z\Theta'_z(x) \end{aligned} \quad (11)$$

Remarks:

- The axis z is a principal axis and therefore $\int_S y dS = 0$.
- An homogeneous section is considered.

Introducing equation (11) in the virtual work principle (9) we have:

$$\int_0^L (\delta U'_x(x) ESU'_x(x) + \delta \Theta'_z(x) EI\Theta'_z(x))dx - w_{exter} = 0 \quad (12)$$

If $\underline{\mathbf{F}}_s^T = \{F_x, M_z\}$ the generalised force vector and $\underline{\mathbf{D}}_s^T = \{U'_x, \Theta'_z\}$ the generalised displacement vector we define the stiffness matrix of the section $\underline{\mathbf{K}}_s$ as:

$$\underline{\mathbf{F}}_s = \underline{\mathbf{K}}_s \underline{\mathbf{D}}_s = \begin{Bmatrix} F_x \\ M_z \end{Bmatrix} = \begin{bmatrix} ES & 0 \\ 0 & EI_z \end{bmatrix} \begin{Bmatrix} U'_x \\ \Theta'_z \end{Bmatrix} = \begin{bmatrix} ES & 0 \\ 0 & EI_z \end{bmatrix} \begin{Bmatrix} U'_x \\ U'_y \end{Bmatrix} \quad (13)$$

2.3 Timoshenko theory: Principal work principle and generalised forces

The principle work principle now becomes:

$$\int_0^L \int_S (\delta \varepsilon_x \sigma_x + 2\delta \varepsilon_{xy} \sigma_{xy}) dS dx - w_{exter} = 0 \quad (14)$$

Using equation (4) we get:

$$\int_0^L \int_S (\delta(U'_x(x) - y\Theta'_z(x))\sigma_x + (\delta U'_y(x) - \delta\Theta_z(x))\sigma_{xy}) dS dx - w_{exter} = 0 \quad (15)$$

where the generalised forces are:

$$\begin{aligned} \text{Normal force: } F_x &= \int_S \sigma_x dS \\ \text{Shear force: } F_y &= \int_S \sigma_{xy} dS \\ \text{Bending moment: } M_z &= - \int_S y \sigma_x dS \end{aligned} \quad (16)$$

Equation (15) becomes:

$$\int_0^L (F_x \frac{d}{dx} \delta U_x + F_y \frac{d}{dx} \delta \beta_y + M_z \frac{d}{dx} \delta \Theta_z) dx - w_{exter} = 0 \quad (17)$$

Using Hooke's law ($\sigma_x = E\varepsilon_x, \sigma_{xy} = G\gamma_{xy}$, with G the shear coefficient) we obtain:

$$F_x = \int_S \sigma_x dS = \int_S E\varepsilon_x dS = \int_S E \left(\frac{dU_x}{dx} - y \frac{d\Theta_z}{dx} \right) dS = \int_S E U'_x ds = E S U'_x \quad (18)$$

In a similar way we have:

$$\begin{aligned} F_y &= G S \beta_y \\ M_z &= E I_z \Theta'_z \end{aligned} \quad (19)$$

If $\underline{\mathbf{F}}_s^T = \{F_x, F_y, M_z\}$ the generalised force vector and $\underline{\mathbf{D}}_s^T = \{U'_x, \beta_y, \Theta'_z\}$ the generalised strain vector we define the stiffness matrix of the section $\underline{\mathbf{K}}_s$ as:

$$\underline{\mathbf{F}}_s = \underline{\mathbf{K}}_s \underline{\mathbf{D}}_s = \begin{Bmatrix} F_x \\ F_y \\ M_z \end{Bmatrix} = \begin{bmatrix} ES & 0 & 0 \\ 0 & GS & 0 \\ 0 & 0 & EI_z \end{bmatrix} \begin{Bmatrix} U'_x \\ \beta_y \\ \Theta'_z \end{Bmatrix} \quad (20)$$

Remark: The Timoshenko beam theory provides constant shear strains and stresses in the section (see equation (4) and Hooke's law). This result violates the boundary conditions of the beam theory ($\sigma_y = \sigma_z = 0$) and does not agree with the theoretical distribution of stresses which is parabolic for a rectangular cross section. A simplified way to deal with this inconsistency is to change the definition of the shear force by adding a shear corrector factor (or Reissner corrector factor) k that depends on the cross section geometry and the material characteristics [Cow66]. The modified expressions take thus the following form:

$$\text{Shear force: } F_y = \int_S k \sigma_{xy} dS \quad (21)$$

$$\underline{\mathbf{F}}_s = \underline{\mathbf{K}}_s \underline{\mathbf{D}}_s = \begin{Bmatrix} F_x \\ F_y \\ M_z \end{Bmatrix} = \begin{bmatrix} ES & 0 & 0 \\ 0 & kGS & 0 \\ 0 & 0 & EI_z \end{bmatrix} \begin{Bmatrix} U'_x \\ \beta_y \\ \Theta'_z \end{Bmatrix} \quad (22)$$

2.4 A 2 node beam finite element formulation

Consider a 2D beam finite element with two nodes and three degrees of freedom per node (figure 4).

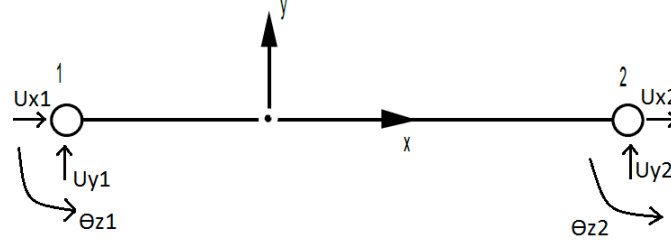


Figure 4: A 2 node finite element beam [Bit13]

Displacements $U_x(x)$, $U_y(x)$ and rotations $\Theta_z(x)$ along the beam are discretized using the nodal displacements as follows:

$$\underline{\mathbf{U}} = \underline{\mathbf{N}} \underline{\Phi} \quad (23)$$

or

$$\begin{Bmatrix} U_x \\ U_y \\ \Theta_z \end{Bmatrix} = \begin{bmatrix} N1 & N2 & N3 & N4 & N5 & N6 \\ N7 & N8 & N9 & N10 & N11 & N12 \\ N13 & N14 & N15 & N16 & N17 & N18 \end{bmatrix} \begin{Bmatrix} U_{x1} \\ U_{y1} \\ \Theta_{z1} \\ U_{x2} \\ U_{y2} \\ \Theta_{z2} \end{Bmatrix} \quad (24)$$

where $N_i(x)$, $i = 1, 18$ the shape functions and $\underline{\Phi}$ the nodal displacements. The equation providing the generalised strain vector $\underline{\mathbf{D}}_s$ becomes (a for axial, s for shear and b for bending):

$$\begin{aligned} \underline{\mathbf{D}}_s &= \begin{Bmatrix} U'_x \\ \beta'_y \\ \Theta'_z \end{Bmatrix} = \begin{bmatrix} B1 & B2 & B3 & B4 & B5 & B6 \\ B7 & B8 & B9 & B10 & B11 & B12 \\ B13 & B14 & B15 & B16 & B17 & B18 \end{bmatrix} \begin{Bmatrix} U_{x1} \\ U_{y1} \\ \Theta_{z1} \\ U_{x2} \\ U_{y2} \\ \Theta_{z2} \end{Bmatrix} \\ &= \begin{bmatrix} B_a \\ B_s \\ B_b \end{bmatrix} \begin{Bmatrix} U_{x1} \\ U_{y1} \\ \Theta_{z1} \\ U_{x2} \\ U_{y2} \\ \Theta_{z2} \end{Bmatrix} \end{aligned} \quad (25)$$

Using the previous equation in the virtual work principle we get a system of linear equations that take the following form (with $\underline{\mathbf{F}}$ the vector of nodal forces at the element level and $\underline{\mathbf{K}}_e$ the element stiffness matrix):

$$\underline{\mathbf{F}} = \underline{\mathbf{K}}_e \underline{\Phi} \quad (26)$$

The element stiffness matrix $\underline{\mathbf{K}}_e$ is given by (where the symbol + means matrix assembly, adding in an adequate way the different degrees of freedom) :

$$\underline{\mathbf{K}}_e = \underline{\mathbf{K}}_a + \underline{\mathbf{K}}_s + \underline{\mathbf{K}}_b \quad (27)$$

$$\begin{aligned} \underline{\mathbf{K}}_a &= \int_0^L B_a^T E S B_a dx \\ \underline{\mathbf{K}}_s &= \int_0^L B_s^T k G S B_s dx \\ \underline{\mathbf{K}}_b &= \int_0^L B_b^T E I B_b dx \end{aligned} \quad (28)$$

2.4.1 An Euler Bernoulli 2 node finite element beam

Consider for example the following classical shape functions for the horizontal, vertical and rotational degrees of freedom [Fre00]:

$$\begin{aligned} N_1 &= 1 - \frac{x}{l} \quad \text{and} \quad N_4 = \frac{x}{l} \\ N_8 &= 1 - 3\left(\frac{x}{l}\right)^2 + 2\left(\frac{x}{l}\right)^3 \quad \text{and} \quad N_9 = x - 2\frac{x^2}{l} + \frac{x^3}{l^2} \\ N_{11} &= 3\left(\frac{x}{l}\right)^2 - 2\left(\frac{x}{l}\right)^3 \quad \text{and} \quad N_{12} = -\frac{x^2}{l} + \frac{x^3}{l^2} \\ N_{14} &= N_8' \quad \text{and} \quad N_{15} = N_9' \\ N_{17} &= N_{11}' \quad \text{and} \quad N_{18} = N_{12}' \end{aligned} \quad (29)$$

In this formulation the rotational and vertical displacements are made interdependent. The other shape functions are considered equal to zero and so equation (24) becomes:

$$\begin{Bmatrix} U_x \\ U_y \\ \theta_z \end{Bmatrix} = \begin{bmatrix} N_1 & 0 & 0 & N_4 & 0 & 0 \\ 0 & N_8 & N_9 & 0 & N_{11} & N_{12} \\ 0 & N_8' & N_9' & 0 & N_{11}' & N_{12}' \end{bmatrix} \begin{Bmatrix} U_{x1} \\ U_{y1} \\ \Theta_{z1} \\ U_{x2} \\ U_{y2} \\ \Theta_{z2} \end{Bmatrix} \quad (30)$$

The different stiffness matrices, for a constant homogeneous section S , take the following form (the matrix due to shear is equal to the zero matrix):

$$\begin{aligned}\underline{\underline{\mathbf{K}_a}} &= \frac{ES}{l} \begin{bmatrix} 1 & -1 \\ -1 & 1 \end{bmatrix} \\ \underline{\underline{\mathbf{K}_b}} &= \frac{EI}{l^3} \begin{bmatrix} 12 & 6l & -12 & 6l \\ 6l & 4l^2 & -6l & 2l^2 \\ -12 & -6l & 12 & -6l \\ 6l & 2l^2 & -6l & 4l^2 \end{bmatrix}\end{aligned}\quad (31)$$

$$\underline{\underline{\mathbf{K}_e}} = \begin{bmatrix} ES/l & 0 & 0 & -ES/l & 0 & 0 \\ 0 & 12EI/l^3 & 6EI/l^2 & 0 & -12EI/l^3 & 6EI/l^2 \\ 0 & 6EI/l^2 & 4EI/l & 0 & -6EI/l^2 & 2EI/l \\ -ES/l & 0 & 0 & ES/l & 0 & 0 \\ 0 & -12EI/l^3 & -6EI/l^2 & 0 & 12EI/l^3 & -6EI/l^2 \\ 0 & 6EI/l^2 & 2EI/l & 0 & -6EI/l^2 & 4EI/l \end{bmatrix}\quad (32)$$

2.4.2 A Timoshenko 2 node finite element beam (1st formulation)

For the case of a Timoshenko beam finite element, the choice of the shape functions is crucial because of the possible shear locking numerical problem [HTK77], [DL87], [ZT05]. If these functions are not appropriately chosen, the finite element beam presents a spurious stiffness for the case of elongated beams. A simple adequate set of shape functions is presented hereafter [Peg94], [GPP94]:

$$\begin{aligned}N_1 = N_8 = N_{15} &= \frac{x_2 - x}{L} \\ N_4 = N_{11} = N_{18} &= \frac{x - x_1}{L}\end{aligned}\quad (33)$$

$$\begin{Bmatrix} U_x \\ U_y \\ \theta_z \end{Bmatrix} = \begin{bmatrix} N_1 & 0 & 0 & N_4 & 0 & 0 \\ 0 & N_8 & 0 & 0 & N_{11} & 0 \\ 0 & 0 & N_{15} & 0 & 0 & N_{18} \end{bmatrix} \begin{Bmatrix} U_{x_1} \\ U_{y_1} \\ \Theta_{z_1} \\ U_{x_2} \\ U_{y_2} \\ \Theta_{z_2} \end{Bmatrix}\quad (34)$$

The generalised strains become:

$$\underline{\underline{\mathbf{D}_s}} = \begin{bmatrix} B_a \\ B_s \\ B_b \end{bmatrix} \underline{\underline{\Phi}} = \begin{bmatrix} -\frac{1}{l} & 0 & 0 & \frac{1}{l} & 0 & 0 \\ 0 & -\frac{1}{l} & -\frac{x_2-x}{l} & 0 & \frac{1}{l} & -\frac{x-x_1}{l} \\ 0 & 0 & -\frac{1}{l} & 0 & 0 & \frac{1}{l} \end{bmatrix} \begin{Bmatrix} U_{x_1} \\ U_{y_1} \\ \Theta_{z_1} \\ U_{x_2} \\ U_{y_2} \\ \Theta_{z_2} \end{Bmatrix}\quad (35)$$

In order to avoid shear locking problems, [DL87] propose to eliminate the linear term in B_s or [HTK77] to sub-integrate the $\underline{\underline{K}}_s$ using only 1 Gauss integration point. According to the solution proposed by [DL87], [GPP94], β_y is now corrected as:

$$\bar{\beta}_y = -\frac{1}{l}U_{y1} - \frac{1}{2}\Theta_{z1} + \frac{1}{l}U_{y2} - \frac{1}{2}\Theta_{z2} = \bar{B}_s \underline{\underline{\Phi}} \quad (36)$$

Finally, the element stiffness matrix, for a constant homogeneous section, takes the following form:

$$\underline{\underline{K}}_e = \begin{bmatrix} \frac{ES}{L} & 0 & 0 & -\frac{ES}{L} & 0 & 0 \\ 0 & \frac{kSG}{L} & \frac{kSG}{2} & 0 & -\frac{kSG}{L} & \frac{kSG}{2} \\ 0 & \frac{kSG}{2} & \frac{EI}{L} + \frac{kSGL}{4} & 0 & -\frac{kSG}{2} & -\frac{EI}{L} + \frac{kSGL}{4} \\ -\frac{ES}{L} & 0 & 0 & \frac{ES}{L} & 0 & 0 \\ 0 & -\frac{kSG}{L} & -\frac{kSG}{2} & 0 & \frac{kSG}{L} & -\frac{kSG}{2} \\ 0 & \frac{kSG}{2} & -\frac{EI}{L} + \frac{kSGL}{4} & 0 & -\frac{kSG}{2} & \frac{EI}{L} + \frac{kSGL}{4} \end{bmatrix} \quad (37)$$

2.4.3 A Timoshenko 2 node finite element beam (2nd formulation)

Another way to avoid shear locking problems is to use higher order functions and to integrate exactly the stiffness matrix. For a 2 node finite element this leads to shape functions that depend on the material properties [DVdG89], [FK93], [KM05], [MKRC06]. For example, according to [FK93] the shape functions become:

$$\underline{\underline{N}} = \begin{bmatrix} N_1 & 0 & 0 & N_4 & 0 & 0 \\ 0 & N_8 & N_9 & 0 & N_{11} & N_{12} \\ 0 & N_{14} & N_{15} & 0 & N_{17} & N_{18} \end{bmatrix} \quad (38)$$

with:

$$\begin{aligned}
N_1 &= 1 - \frac{x}{L} \\
N_4 &= \frac{x}{L} \\
N_8 &= \frac{1}{1+\phi} [2(\frac{x}{L})^3 - 3(\frac{x}{L})^2 - \phi(\frac{x}{L}) + 1 + \phi] \\
N_9 &= \frac{L}{1+\phi} [(\frac{x}{L})^3 - (2 + \frac{\phi}{2})(\frac{x}{L})^2 + (1 + \frac{\phi}{2})(\frac{x}{L})] \\
N_{11} &= \frac{-1}{1+\phi} [2(\frac{x}{L})^3 - 3(\frac{x}{L})^2 - \phi(\frac{x}{L})] \\
N_{12} &= \frac{L}{1+\phi} [(\frac{x}{L})^3 - (1 - \frac{\phi}{2})(\frac{x}{L})^2 - \frac{\phi}{2}(\frac{x}{L})] \\
N_{14} &= \frac{6}{(1+\phi)L} [(\frac{x}{L})^2 - (\frac{x}{L})] \\
N_{15} &= \frac{1}{1+\phi} [3(\frac{x}{L})^2 - (4 + \phi)(\frac{x}{L}) + (1 + \phi)] \\
N_{17} &= \frac{-6}{(1+\phi)L} [(\frac{x}{L})^2 - (\frac{x}{L})] \\
N_{18} &= \frac{L}{1+\phi} [3(\frac{x}{L})^2 - (2 - \phi)(\frac{x}{L})]
\end{aligned} \tag{39}$$

ϕ is the ratio between bending and shear stiffnesses. For an homogeneous section we get:

$$\phi = \frac{12}{L^2} \frac{\int_S Ey^2 dS}{\int_S kG dS} = \frac{12}{L^2} \frac{EI}{kGS} \tag{40}$$

The generalised strains now become:

$$\underline{\mathbf{D}}_{\mathbf{s}} = \begin{bmatrix} N'_1 & 0 & 0 & N'_4 & 0 & 0 \\ 0 & N'_8 - N_{14} & N'_9 - N_{15} & 0 & N'_{11} - N_{17} & N'_{12} - N_{18} \\ 0 & N'_{14} & N'_{15} & 0 & N'_{17} & N'_{18} \end{bmatrix} \begin{Bmatrix} U_{x_1} \\ U_{y_1} \\ \Theta_{z_1} \\ U_{x_2} \\ U_{y_2} \\ \Theta_{z_2} \end{Bmatrix} \tag{41}$$

Finally, the stiffness matrix of the element takes the following form:

$$\underline{\underline{\mathbf{K}_e}} = \begin{bmatrix} \frac{ES}{L} & 0 & 0 & -\frac{ES}{L} & 0 & 0 \\ 0 & \frac{12EI}{(1+\phi)L^3} & \frac{6EI}{(1+\phi)L^2} & 0 & -\frac{12EI}{(1+\phi)L^3} & \frac{6EI}{(1+\phi)L^2} \\ 0 & \frac{6EI}{(1+\phi)L^2} & \frac{(4+\phi)EI}{(1+\phi)L} & 0 & -\frac{6EI}{(1+\phi)L^2} & \frac{(2-\phi)EI}{(1+\phi)L} \\ -\frac{ES}{L} & 0 & 0 & \frac{ES}{L} & 0 & 0 \\ 0 & -\frac{12EI}{(1+\phi)L^3} & -\frac{6EI}{(1+\phi)L^2} & 0 & \frac{12EI}{(1+\phi)L^3} & -\frac{6EI}{(1+\phi)L^2} \\ 0 & \frac{6EI}{(1+\phi)L^2} & \frac{(2-\phi)EI}{(1+\phi)L} & 0 & -\frac{6EI}{(1+\phi)L^2} & \frac{(4+\phi)EI}{(1+\phi)L} \end{bmatrix} \quad (42)$$

For elongated beams, ϕ is almost zero and the matrix reduces to the classical Euler Bernoulli stiffness matrix, see equation (32). The main problem of this finite element formulation is that it is not appropriate for non linear calculations as the shape functions depend on the material properties that evolve with the loading. Nevertheless, some good results were obtained by keeping the initial shape functions (calculated at the first step - elasticity) unchanged, [KM05], [MKRC06].

2.4.4 Timoshenko finite elements with internal degrees of freedom

Another way to avoid shear locking problems is to enrich the displacements field [IW91] and to add internal nodes in the element [IF93], [CKCed]. In that way higher order shape functions are obtained that do not depend on the material properties. The numerical integration is exactly performed and the elements are suitable for non linear calculations.

The finite element presented in [CKCed] (named “FCQ” Timoshenko beam for “Full Cubic Quadratic”) has additional internal degrees of freedom, cubic shape functions for the vertical displacements and quadratic for the rotations. The element is free of shear locking and one element is able to predict the exact tip displacements for any complex distributed loadings and any suitable boundary conditions. One element gives the exact solution for the case of bending of a Timoshenko beam free of distributed loadings. It is also proven that the element presented in [FK93] is a particular case of the more general FCQ Timoshenko beam element. For more information the reader is invited to read the relevant reference.

3 Multifiber beam formulation

The section of the finite element beam (Euler Bernoulli or Timoshenko) is divided in different “fibers” [OH80]. In each fiber a constitutive law is introduced (e.g. concrete,

steel...). Depending on the mesh discretization of the section (e.g. with triangular or rectangular finite elements) one or more Gauss points are associated in each fiber, see figure 5.

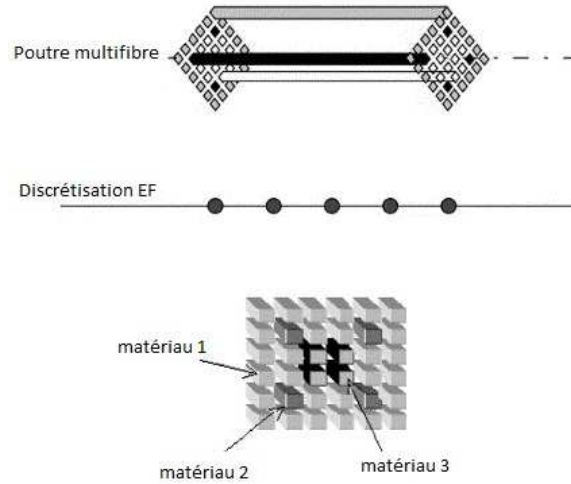


Figure 5: Multifiber beam modelling [GPP94], [MKRC06]

The different formulations of the finite element beams presented in section 2 (expressed now in 3D) can be used for the multifiber element. Consider equations (1) and (3) expressing the kinematic assumptions: the y (and z in 3D) are replaced with y_f (and z_f), the coordinates of the fiber f in the section. The generalised forces take the following forms (where E_f and G_f the Young's and the shear moduli of the fiber respectively):

$$F_x = \int_S E_f \varepsilon_x dS = \int_S E_f \left(\frac{dU_x}{dx} - y_f \frac{d\Theta_z}{dx} \right) dS = \int_S E_f dS U'_x - \int_S E_f y_f dS \Theta'_z \quad (43)$$

and in a similar way:

$$\begin{Bmatrix} F_x \\ F_y \\ M_z \end{Bmatrix} = \begin{bmatrix} \int_S E_f dS & 0 & - \int_S E_f y_f dS \\ 0 & \int_S k G_f dS & 0 \\ - \int_S E_f y_f dS & 0 & \int_S E_f y_f^2 dS \end{bmatrix} \begin{Bmatrix} U'_x \\ \beta_y \\ \Theta_z \end{Bmatrix} \quad (44)$$

By introducing the previous equation of the virtual work principle we obtain:

$$\int_0^L \delta \underline{\mathbf{D}}_s^T \underline{\mathbf{K}}_s \underline{\mathbf{D}}_s dx - w_{exter} = 0 \quad (45)$$

Considering that

$$\underline{\mathbf{D}}_s = \begin{bmatrix} B_a \\ B_s \\ B_b \end{bmatrix} \underline{\Phi} = \underline{\mathbf{B}} \underline{\Phi} \quad (46)$$

the virtual work principle becomes:

$$\int_0^L \delta \underline{\Phi}^T \underline{\mathbf{B}}^T \underline{\mathbf{K}}_s \underline{\mathbf{B}} \underline{\Phi} dx - w_{exter} = 0 \quad (47)$$

The section stiffness matrix presented hereafter is valid for homogeneous and non homogeneous sections even if the chosen axes are not the principal ones [GPP94]:

$$\underline{\mathbf{K}}_e = \int_0^L \underline{\mathbf{B}}^T \underline{\mathbf{K}}_s \underline{\mathbf{B}} dx \quad (48)$$

The numerical implementation of a multifiber beam is similar to a classical beam with the main difference that further loops are needed in the section level (scanning all the fibers) in order to construct the section stiffness matrix $\underline{\mathbf{K}}_s$ [GPP94], [KM05], [MKRC06].

In the following chapter, a case study is presented on a reinforced concrete viaduct considering soil-structure interaction [GBKT11]. For this, a multifiber Timoshenko beam is coupled with macro-elements [GKM09a], [GKM09b], [Gra13]. The reader can find other applications of the multifiber beam concept in the recent literature: non linear shear [CP94], non linear torsion [MKRC06], shaking table tests [KRM05], [INK⁺08], [GKM09c], retrofitting with fiber reinforced polymers [DMKP13]...

4 Case study: A reinforced concrete viaduct

5 Description of the structure

A 1:2.5 scaled viaduct was tested pseudo-dynamically in ELSA laboratory (JRC Ispra) (figure 6, [PVP⁺96]). Inertial forces were calculated numerically and imposed to the model piers through actuators by applying the adequate displacements. Details of the deck and piers are given (scaled) in figures 7(a) and 7(b). Piers are made of reinforced concrete and present hollow rectangular section shapes. The characteristics of the section of the deck are given in Table 1.

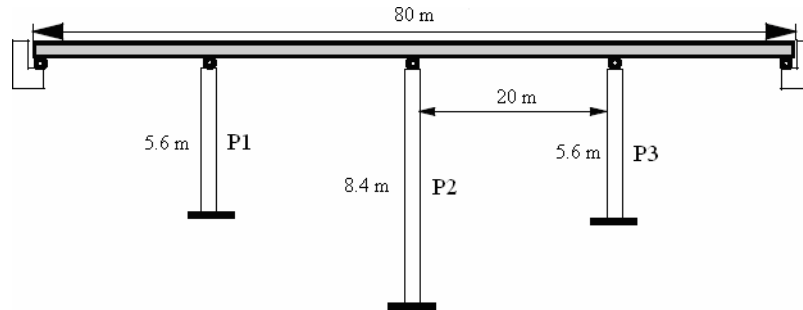


Figure 6: Viaduct: plan view (scale 1:2.5) [PVP+96].

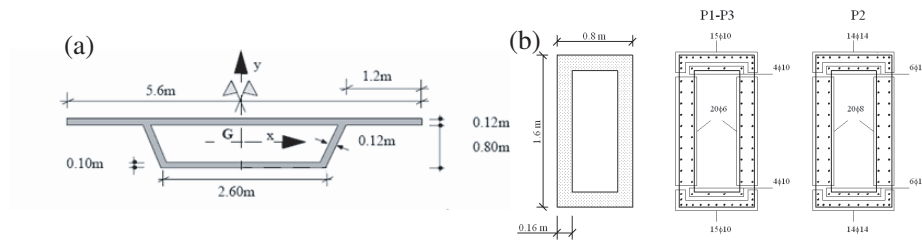


Figure 7: Viaduct: (a) deck, (b) piers (scale 1:2.5) [PVP+96].

Table 1: Viaduct: characteristics of deck cross section.

$A(m^2)$	$I_x(m^4)$	$I_y(m^4)$	$J(m^4)$
1.11	0.13	2.26	2.39

5.1 Finite element mesh

A finite element model using multifiber beams and concentrated masses is chosen to reproduce the structure (figure 8). The piers are at first considered fixed at the base. The mass and rotational inertia details are given in Table 2 [GBKT11].

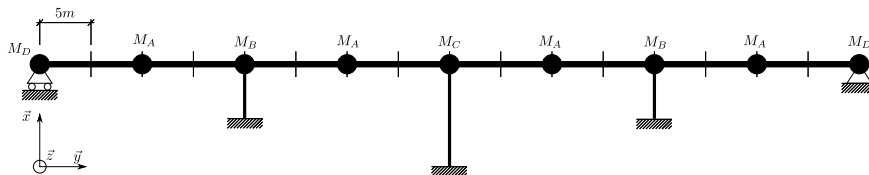


Figure 8: Viaduct: finite element mesh.

Table 2: Viaduct: masses and rotational inertia.

	Mass M (kg)	Rotational inertia I_x (kg.m ²)	Rotat. inertia I_z (kg.m ²)
M_A	27.5	285	234
M_B	32	287	271
M_C	34	288	322
M_D	13.75	143	117

Non linear Timoshenko multifiber beam elements are used to reproduce the behaviour of the piers [KM05], [MKRC06]. Six (6) elements are used for the piers P1 and P3 and nine (9) elements for the pier P2. Forty (40) concrete fibers and eighty (80) steel fibers are assumed in the sections, (figure 9). The deck is simulated using elastic linear beam elements. Calculations are made with FEDEASLab, a finite element MATLAB toolbox [FC04].

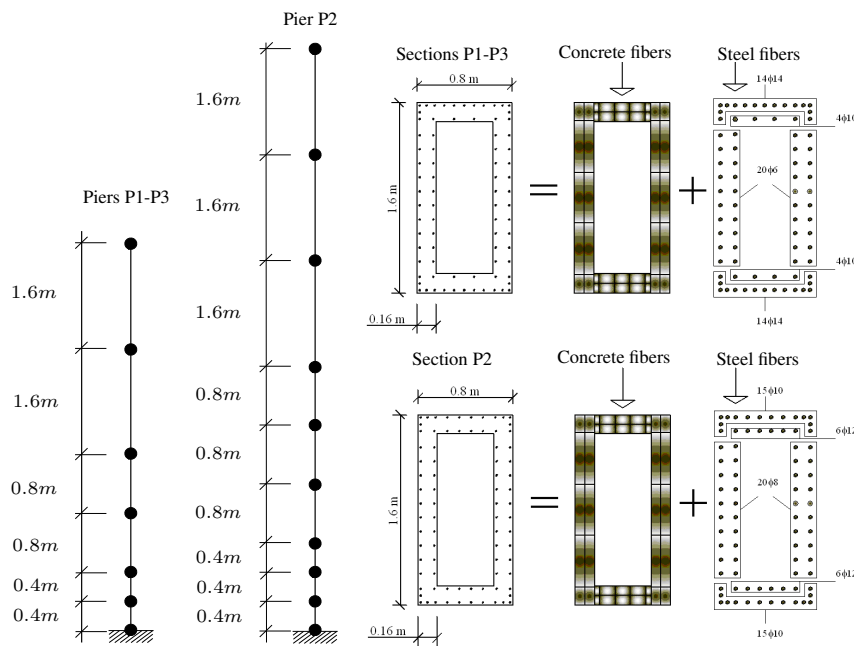


Figure 9: Viaduct: details of the multifiber beam element mesh (piers P1, P2 et P3).

5.2 Material parameters

A damage model with two scalar variables, one in compression and one in tension is adopted for concrete [LB91]. The model is able to reproduce the unilateral effect,

the permanent strains and the stiffness recovery. A modified version of the classical Menegotto-Pinto model [MP73] with an isotropic hardening is used for steel. It is worth noting that as the tests are pseudo-dynamic, the damping coefficient adopted in the numerical simulations has to be small [GBKT11].

5.3 Loading sequence

The accelerations imposed at the base of the structure derive from a synthetic accelerogram consistent with a 5% damping response spectrum selected according to Eurocode 8 for a soil of class B. The peak of accelerations is situated at $0.35g$ (“weak” earthquake). A second similar accelerogram (dilated) is also imposed at the base of the structure. Its peak of acceleration is equal to $0.7g$ (“strong” earthquake) [GBKT11].

5.4 Experimental versus numerical results: dynamic analysis

Figures 10 and 11 show the comparison between the experimental and the numerical results of the dynamic analysis considering the piers fixed at the base. The two earthquakes (weak and strong) are imposed. The figures show the evolution with time of the shear forces at the base and the lateral displacements at the top of the piers P1, P2 and P3 [GBKT11].

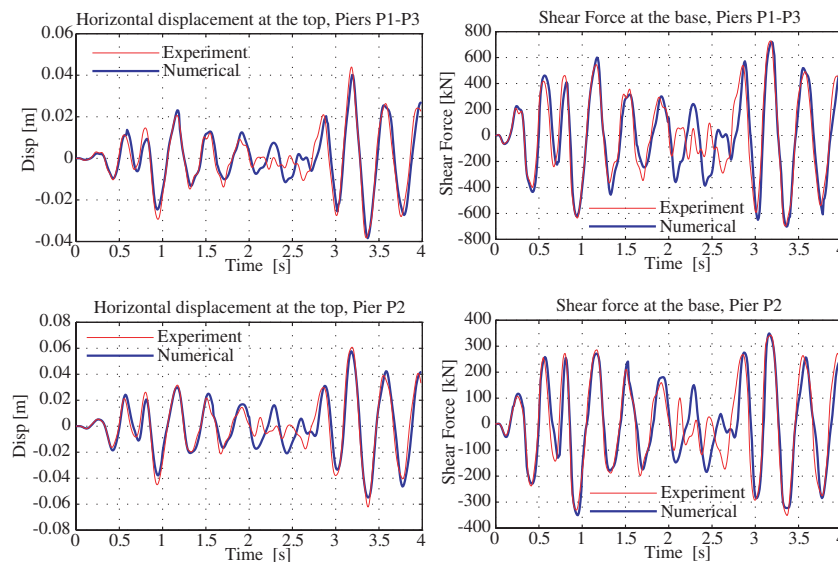


Figure 10: Viaduct - fixed base: comparison between experimental and numerical displacements and shear forces for the weak level earthquake [GBKT11].

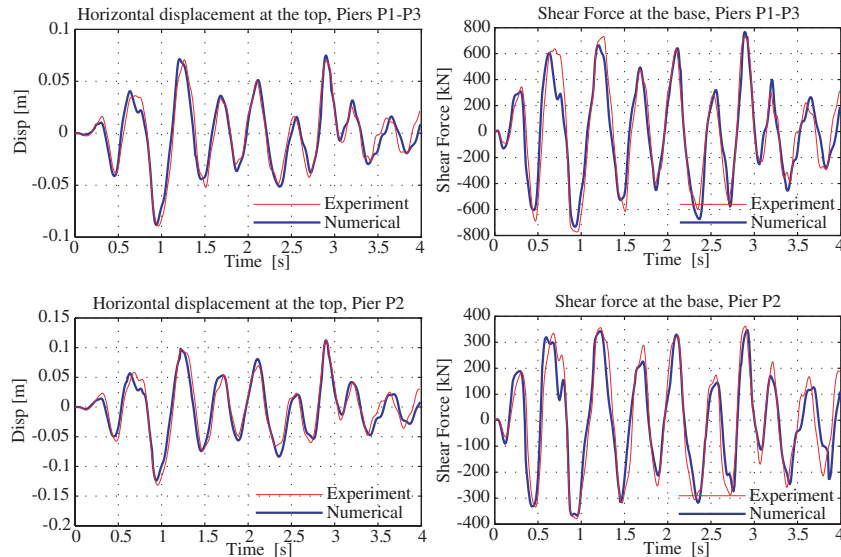


Figure 11: Viaduct - fixed base: comparison between experimental and numerical displacements and shear forces for the strong earthquake [GBKT11].

One can clearly see that despite the small number of degrees of freedom of the finite element model the non linear behaviour of the viaduct is reproduced quite satisfactorily. Not only the peaks in both directions are well reproduced but the frequency content of the response is correctly matched.

5.5 Dynamic analysis considering soil-structure interaction

Two modelling strategies are studied hereafter to take into account soil-structure interaction. The first uses the macro-element approach [GKM09a], [GKM09b], [Gra13] and the second linear elastic springs applied at the base of each pier. The elastic stiffness of the springs is calibrated such as that they accumulate the same energy as the non-linear macro-element [GBKT11]. The three types of boundary conditions are denominated hereafter as follows: linear springs (EL), macro-element (ME) and fixed (Fixed).

The results for the weak earthquake are presented in figure 12 for a class C soil. The predicted numerical behaviour of the viaduct differs depending on the assumed boundary conditions. The displacements are strongly amplified for the case of the structure resting on the macro-element and on the linear elastic springs. The results are more pronounced for the internal forces at the base of the piers (moments and shear forces). Loads on the structure are significantly reduced for the case of the macro-element.

Results obtained with the elastic linear springs are similar to the ones found for the fixed piers [GBKT11].

The limits of the classical engineering approach based on elastic linear springs are thus evident. For the case of the reinforced concrete viaduct internal forces and displacements are higher than the ones obtained using the macro-element, which allows a more appropriate description of the non linear behaviour of the foundation soil system.

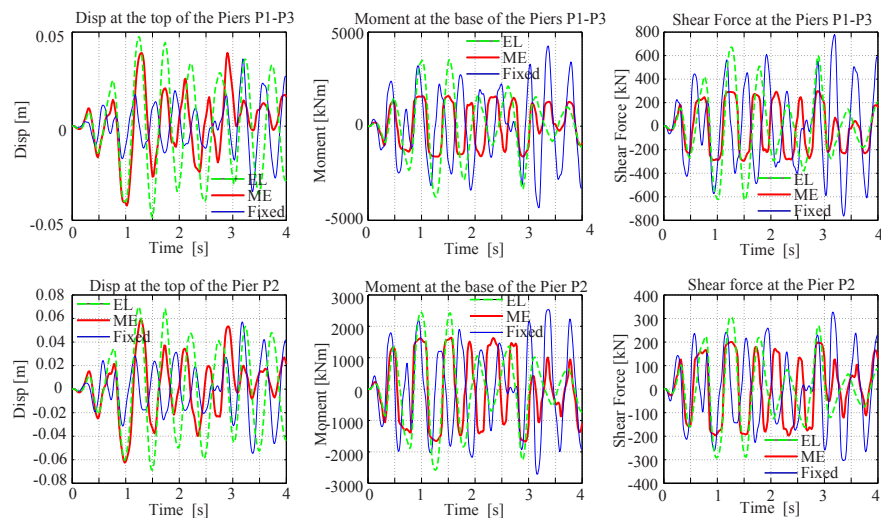


Figure 12: Viaduct - soil-structure interaction: comparison of the displacements, moments and shear forces for the weak motion and for a class C soil [GBKT11].

6 Conclusions

In this course, the formulation of a multifiber beam element was presented in detail. Adopting an Euler Bernoulli or a Timoshenko kinematic assumption, the element is able to reproduce the non linear behaviour of composite structures. A case study on a reinforced concrete viaduct subjected to earthquake loadings showed the performance of the approach. Combined with macro-elements [Gra13], it can take into account in an efficient, fast and robust way soil-structure interaction phenomena.

References

- [Bit13] I. Bitar. Un nouvel élément fini poutre pour la modélisation des structures sous sollicitations complexes. Master thesis, Ecole Centrale de Nantes, 2013.
- [CKCed] D. Caillerie, P. Kotronis, and R. Cybulski. An improved timoshenko finite element beam with internal degrees of freedom. *Finite Elements in Analysis and Design*, 2014 (submitted).
- [Cow66] G.R. Cowper. The shear coefficient in timoshenko’s beam theory. *Journal of Applied Mechanics*, 33(2):335–340, 1966.
- [CP94] D. Combescure and P. Pegon. A fibre model accounting for transverse shear in castem 2000. Technical report, J.R.C., I-21020, Ispra, Italy, 1994. Special publication Nr. I.94.59.
- [DL87] J. Donea and L.G. Lamain. A modified representation of transverse shear in c^0 quadrilateral plate elements. *Computer Methods in Applied Mechanics and Engineering*, 63(2):183 – 207, 1987.
- [DMKP13] C. Desprez, J. Mazars, P. Kotronis, and P. Paultre. Damage model for frp-confined concrete columns under cyclic loading. *Engineering Structures*, 48(0):519 – 531, 2013.
- [DVdG89] V. De Ville de Goyet. *L’analyse statique non linéaire par la méthode des éléments finis des structures spatiales formées de poutres à section non symétrique*. PhD thesis, Université de Liège, 1989.
- [FC04] F.C. Filippou and M. Constantinides. Fedeaslab, getting started guide and simulations examples. Technical report, department of Civil and Environmental Engineering, UC Berkeley, 2004.
- [FK93] Z. Friedman and J.B. Kosmatka. An improved two-node timoshenko beam finite element. *Computers & structures*, 47(3):473–481, 1993.
- [Fre00] F. Frey. *Analyse des structures et milieux continus: mécanique des structures*, volume 2. PPUR, presses polytechniques et universitaires romandes, 2000.
- [GBKT11] S. Grange, L. Botrugno, P. Kotronis, and C. Tamagnini. The effects of soil–structure interaction on a reinforced concrete viaduct. *Earthquake Engineering & Structural Dynamics*, 40(1):93–105, 2011.
- [GKM09a] S. Grange, P. Kotronis, and J. Mazars. A macro-element to simulate 3d soil-structure interaction considering plasticity and uplift. *International Journal of Solids and Structures*, 46(20):3651 – 3663, 2009.

- [GKM09b] S. Grange, P. Kotronis, and J. Mazars. A macro-element to simulate dynamic soil-structure interaction. *Engineering Structures*, 31(12):3034–3046, 2009.
- [GKM09c] S. Grange, P. Kotronis, and J. Mazars. Numerical modelling of the seismic behaviour of a 7-story building: Nees benchmark. *Materials and structures*, 42(10):1433–1442, 2009.
- [GPP94] J. Guedes, P. Pegon, and A. Pinto. A fibre timoshenko beam element in castem 2000. special publication nr. i.94.31. Technical report, J.R.C., I-21020, Ispra, Italy, 1994.
- [Gra13] S. Grange. Simplified modeling strategies for soil-structure interaction problems: The macro-element concept. ALERT (The Alliance of Laboratories in Europe for Research and Technology) doctoral school on "Soil-Structure Interaction", ed. P. Kotronis, C. Tamagnini and S. Grange, 2013.
- [HTK77] T.J.R. Hughes, R.L. Taylor, and W. Kanoknukulchai. A simple and efficient finite element for plate bending. *International Journal for Numerical Methods in Engineering*, 11(10):1529–1543, 1977.
- [IF93] A. Ibrahimbegović and F. Frey. Geometrically non-linear method of incompatible modes in application to finite elasticity with independent rotations. *International journal for numerical methods in engineering*, 36(24):4185–4200, 1993.
- [INK⁺08] N. Ile, X.H. Nguyen, P. Kotronis, J. Mazars, and J.M. Reynouard. Shaking table tests of lightly rc walls: Numerical simulations. *Journal of Earthquake Engineering*, 12(6):849–878, 2008.
- [IW91] A. Ibrahimbegovic and E.L. Wilson. A modified method of incompatible modes. *Communications in Applied Numerical Methods*, 7(3):187–194, 1991.
- [KM05] P. Kotronis and J. Mazars. Simplified modelling strategies to simulate the dynamic behaviour of r/c walls. *Journal of Earthquake Engineering*, 9(02):285–306, 2005.
- [KRM05] P. Kotronis, F. Ragueneau, and J. Mazars. A simplified modelling strategy for r/c walls satisfying ps92 and ec8 design. *Engineering Structures*, 27(8):1197–1208, 2005.
- [LB91] C. La Borderie. *Phénomènes unilatéraux dans un matériau endommageable: modélisation et application l'analyse des structures en béton*. PhD thesis, Université Paris 6, 1991.
- [MKRC06] J. Mazars, P. Kotronis, F. Ragueneau, and G. Casaux. Using multifiber beams to account for shear and torsion: Applications to concrete struc-

- tural elements. *Computer Methods in Applied Mechanics and Engineering*, 195(52):7264–7281, 2006.
- [MP73] M. Menegotto and P. Pinto. Method of analysis of cyclically loaded reinforced concrete plane frames including changes in geometry and non-elastic behaviour of elements under combined normal force and bending. In *IABSE Symposium on resistance and ultimate deformability of structures acted on by well-defined repeated loads, final report, Lisbon*, page 328p, 1973.
- [OH80] D.R.J. Owen and E. Hinton. *Finite elements in plasticity: Theory and practice*. Pineridge Press Ltd, Swansea, England, 1980.
- [Peg94] P. Pegon. A timoshenko simple beam element in castem 2000. Technical report, J.R.C., I-21020, Ispra, Italy, 1994. special publication Nr. I.94.04.
- [PVP⁺96] A.V. Pinto, G. Verzeletti, P. Pegon, G. Magonette, P. Negro, and J. Guedes. Pseudo dynamic testing of large-scale r/c bridges. Technical report, HMC grant holder report EUR 16378 EN, 1996.
- [SFT96a] E. Spacone, F.C. Filippou, and F.F. Taucer. Fiber beam-column model for nonlinear analysis of r/c frames. i: Formulation. *Earthquake Engineering and Structural Dynamics*, 25(7):711–725, 1996.
- [SFT96b] E. Spacone, F.C. Filippou, and F.F. Taucer. Fiber beam-column model for nonlinear analysis of r/c frames. ii: Applications. *Earthquake Engineering and Structural Dynamics*, 25(7):727–742, 1996.
- [ZT05] O.C. Zienkiewicz and R. L. Taylor. *The finite element method for solid and structural mechanics*. Butterworth-Heinemann, 2005.

Simplified modeling strategies for soil-structure interaction problems: The macro-element concept

Stéphane Grange

UJF-Grenoble 1, Grenoble-INP, CNRS UMR 5521, 3SR Lab, Grenoble F-38041, France

In structural and seismic engineering, soil-structure interaction (SSI) can have significant effects in the global and local behavior of a structure compared to case where the same structure is considered completely clamped at the base. This paper presents some key-points to provide a better understanding about why and how the behaviors of the soil and the structure can be affected during dynamic loading through few simple examples. A 3D non-linear interface element able to compute SSI based on the "macro-element" concept is also presented. The particularity of the macro-element lies in the fact that the movement of the foundation is entirely described by a system of generalized variables (forces and displacements) defined at the foundation centre which is consistent with the EC8 recommendations and allowing a very simple and straightforward analysis of SSI problems. The different non-linear behavior at the interface are reproduced in a global way allowing to drastically save computational time. Some examples on different structures and their comparisons with experimental results under cyclic and dynamic loadings using the macro-element can show the effects of SSI.

1 Introduction

Recent developments in the analysis of the seismic response of structures have shown that the proper consideration of soil deformability is of primary importance for an accurate prediction of the deformation and loads experienced by the structure during the earthquake.

In the framework of the "displacement and performance based designs", the main objective of analyzing the SSI phenomena is to get a better estimation of the global

displacement and of the internal forces in the structure in order to have a more accurate design.

The 4 main aspects of soil-structure interaction (SSI) can be summarized in figure 1 and by the following items:

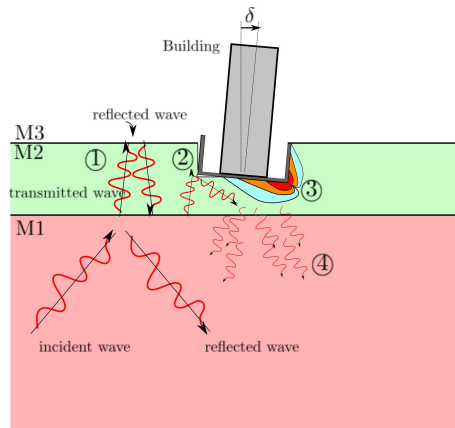


Figure 1: The different soil structure interactions.

- ① wave amplification due to different properties of soil layers (site effect),
- ② inertial and kinematic effects (which have an effect on the solicitations applied to the structure),
- ③ elastic and non-linear effects of the soil-structure interface,
- ④ radiative damping (far field effect).

The effects of items 1 and 2 will be not consider into this chapter which will be focused on items 3 and 4, concerning the effect of the elastic behavior of the soil, the nonlinearities at the soil-foundation interface and radiative damping in the far field to better estimate the behavior of the structure and principally for evaluating its displacements (globally indicated with the symbol δ on figure 1) when subjected to an earthquake. This approach is in total agreement with the methods provided by the EC8-5.

To tackle these issues (and particularly the items 3 and 4), the macro-element concept, a very suitable tool to simulate SSI, is used.

The following sections give a general overview of the effects of the soil-foundation interface on the structure considering elasticity, but also non-linearities and radiative damping. The description of the different phenomena are then introduced in the definition the macro-element. The concept of such modeling is presented and an application to a real structure is provided to show the influence of SSI on the global and local behavior of the structure.

2 The effects of semi-infinite soil media (impedance) and close field non-linearities (plasticity, uplift)

2.1 The elastic linear range: Impedance of the foundation

2.1.1 Effect of the stiffness and damping of the soil

The presence of the soil under the structure does not allow generally to consider the structure completely fixed and clamped at its base. The foundation can affect significantly the behavior of the structure even in its elastic linear range.

For instance, the effects of SSI can be easily illustrated considering the sway-rocking 1-degree of freedom (dof) model in figure 2. This example is briefly summarized in this chapter but is presented in detail in [Wol85].

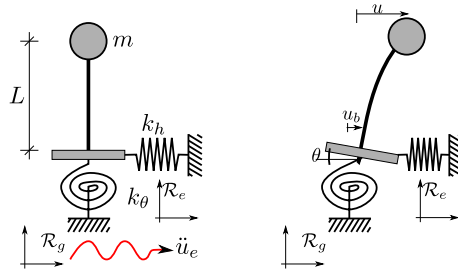


Figure 2: The sway-rocking model.

The structure is composed of an elastic Bernoulli beam of length L , with a lumped mass attached at its top. The beam is fixed on a foundation characterized by an horizontal stiffness (k_h) and a rotational stiffness (k_θ). Two dashpots are considered in parallel with the springs (respectively c_h and c_θ).

The degrees of freedom of the system are the following: u horizontal displacement of the concentrated mass with respect to the base of the foundation; u_b , horizontal displacement of the foundation (with respect to the \mathcal{R}_e reference coordinate axis); θ , rotation of the foundation (with respect to the \mathcal{R}_e reference coordinate axis); u_e , horizontal displacement of the base of the system (with respect to the \mathcal{R}_g galilean reference coordinate axis).

The dynamic equilibrium of this model submitted to an acceleration at the base \ddot{u}_e (with respect to \mathcal{R}_g) can be written easily using the following assumptions: only the harmonic response of the structure, when this latter is submitted to a solicitation of angular frequency ω , is considered; the damping ratios for the structure and for the soil are defined as: $\xi_s = \omega c_s / (2k_s)$, $\xi_h = \omega c_h / (2k_h)$, $\xi_\theta = \omega c_\theta / (2k_\theta)$; the fundamental

angular frequency of structure and the soil are defined as: $m\omega_s^2 = k_s$, $m\omega_h^2 = k_h$, and $mL^2\omega_\theta^2 = k_\theta$.

Then, the dynamic equilibrium equation can be written as follows:

$$\left[1 - \frac{\omega^2}{\omega_s^2} - \frac{\omega^2}{\omega_h^2} \frac{1 + 4\xi_s\xi_h}{1 + 4\xi_h^2} - \frac{\omega^2}{\omega_\theta^2} \frac{1 + 4\xi_s\xi_\theta}{1 + 4\xi_\theta^2} \right] u + 2i \left(\xi_s - \frac{\omega^2}{\omega_h^2} \frac{\xi_s - \xi_h}{1 + 4\xi_h^2} - \frac{\omega^2}{\omega_\theta^2} \frac{\xi_s - \xi_\theta}{1 + 4\xi_\theta^2} \right) u = \frac{\omega^2}{\omega_s^2} u_e \quad (1)$$

If this equations is compared to the dynamic equilibrium of a simple 1-dof system (with a fundamental angular frequency $\tilde{\omega}$; a damping ratio $\tilde{\xi}$, clamped at its base and submitted to an acceleration \tilde{u}_e) given by: $\left[1 - \frac{\tilde{\omega}^2}{\tilde{\omega}^2} + 2i\tilde{\xi} \right] u = \frac{\tilde{\omega}^2}{\tilde{\omega}^2} \tilde{u}_e$, then it follows:

$$\begin{cases} \frac{1}{\tilde{\omega}^2} = \frac{1}{\omega_s^2} + \frac{1}{\omega_h^2} \frac{1 + 4\xi_s\xi_h}{1 + 4\xi_h^2} + \frac{1}{\omega_\theta^2} \frac{1 + 4\xi_s\xi_\theta}{1 + 4\xi_\theta^2} \\ \tilde{\xi} = \xi_s - \frac{\omega^2}{\omega_h^2} \frac{\xi_s - \xi_h}{1 + 4\xi_h^2} - \frac{\omega^2}{\omega_\theta^2} \frac{\xi_s - \xi_\theta}{1 + 4\xi_\theta^2} \\ \tilde{u}_e = \frac{\tilde{\omega}^2}{\omega_s^2} u_e \end{cases} \quad (2)$$

Moreover, if the general expression of the springs and dashpot parameters are assumed as follows (where G is the shear modulus of the soil, ρ its density, V_s the shear wave velocity, and r the characteristic length of the foundation):

$$\begin{cases} k_h = aGr = ar\rho V_s^2 \\ k_\theta = bGr^3 = br^3\rho V_s^2 \\ c_h = c\rho V_s r^2 \\ c_\theta = d\rho V_s r^4 \end{cases} \quad (a, b, c, d) \in \mathbb{R}^4 \quad (3)$$

and by considering the following dimensionless parameters $s = \frac{\omega_s L}{V_s}$, $\bar{m} = \frac{m}{\rho r^3}$ and $\bar{h} = \frac{L}{r}$, writing the equations at the fundamental frequency ($\omega = \tilde{\omega}$) and finally assuming ($\xi_s, \xi_h, \xi_\theta \ll 1$), then we have:

$$\begin{cases} \frac{\tilde{\omega}}{\omega_s} = \frac{1}{\sqrt{1 + s^2\bar{m} \left(\frac{1}{a\bar{h}^2} + \frac{1}{b} \right)}} \\ \tilde{\xi} = \frac{\tilde{\omega}^2}{\omega_s^2} \left(\xi_s + \frac{s^2\bar{m}}{a\bar{h}^2} \frac{\tilde{\omega}}{\omega_s} \frac{c}{2a} \frac{s}{\bar{h}} + \frac{s^2\bar{m}}{b} \frac{\tilde{\omega}}{\omega_s} \frac{d}{2b} \frac{s}{\bar{h}} \right) \end{cases} \quad (4)$$

The representation of these 2 quantities as functions of s is given in figure 3.

The effects of the stiffness of the soil (k_h and k_θ) is to reduce the fundamental period. On the contrary, the material damping of the soil (c_h and c_θ) generates an increase of

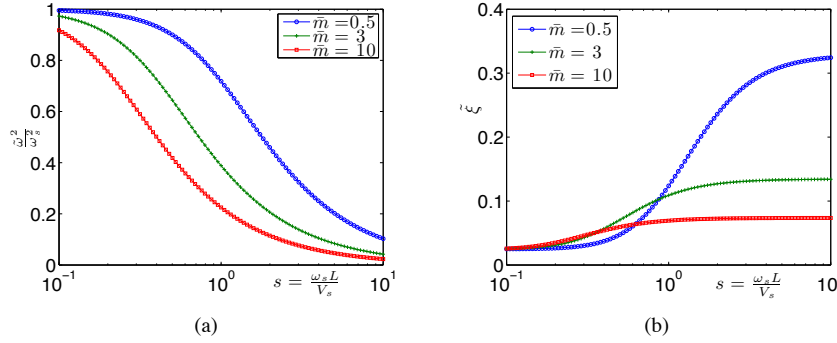


Figure 3: (a) Fundamental frequency evolution $\frac{\tilde{\omega}}{\omega_s}$; (b) Damping ratio evolution $\tilde{\xi}$ compared to the clamped structure with respect to the adimensional fundamental frequency $s = \frac{\omega_s L}{V_s}$ and for different values of $\bar{m} = \frac{m}{\rho r^3}$ and $\bar{h} = 1$.

the global damping. The kinematic loading at the base of the foundation \tilde{u}_e follows the same evolution than $\tilde{\omega}$, i.e a decreasing with s (this last point shows the interaction of the structure with the soil).

This influence of the soil properties on the determination of the fundamental periods is of primary importance for the design of a structure. A shift in the fundamental period can strongly affect the global elastic response of the structure. It is particularly obvious when considering the elastic spectral response of a structure. The maximum spectral acceleration, and thus the force applied to the mass, can be reduced or increased due to this shifting in frequency.

2.1.2 Frequency dependency of the linear properties of the soil

The impedance of the foundation can be seen as the transfer function of the foundation system buried into the soil $H(\omega) = \frac{P(\omega)}{U(\omega)}$ where P is the resisting force generated by the soil $C\dot{U} + KU = P$. Thus, the transfer function H can be characterized by applying a unit harmonic force $P = 1e^{i\omega t}$ to the "massless" foundation and by evaluating the generated displacements U . For multi-degree of freedom foundation system (vertical displacement, horizontal displacement, rotation), the function H is a matrix with components $H_{ij}(\omega) = \frac{P_i(\omega)}{U_j(\omega)}$. Usually it can be proven that in the case of a shallow foundation, H_{ij} is a diagonal matrix without any coupling of the different directions.

Then, the ratio between the force and the displacement gives a complex number where the real and the imaginary parts represent respectively the frequency dependent stiffness and the damping of the soil–foundation system.

The impedance functions are often obtained assuming a rigid foundation on a semi-infinite space and by using Green's functions. The stiffness terms for a circular, rectangular and strip shallow foundation are given in the table 1.

Table 1: Stiffness coefficients for disk (radius r_0), rectangular (a, b) and strip (width b) footings, on homogenous half-space [Wol88], [PH03], [Gaz91]

K^{el}	Circular [Wol88]	Rectangular[PH03]	Strip[Gaz91]
Horizontal	$\frac{8Gr_0}{2-\nu}$	$\frac{G_0}{1-\nu} \beta_{h_x h_x} \sqrt{ab}$	$\frac{2G_0}{2-\nu}$
Vertical	$\frac{4Gr_0}{1-\nu}$	$\frac{G_0}{1-\nu} \beta_{z z} \sqrt{ab}$	$\frac{0.73G_0}{1-\nu}$
Rocking	$\frac{8Gr_0^3}{3(1-\nu)}$	$\frac{G_0}{1-\nu} \beta_{\theta_y \theta_y} b^2 \sqrt{ab}$	$\frac{\pi G_0}{2(1-\nu)} \left(\frac{b}{2}\right)^2$
Torsional	$\frac{16Gr_0^3}{3}$	–	–

Several authors like Wolf [Wol88] have also provided simple models in order to get the dynamic response of foundations using simple analogical models made of combinations of springs, dashpots and additional masses. This family of models is called "Monkey-tail models" and is represented schematically by figure 4. Table 2 gives values of the parameters for a circular foundation.

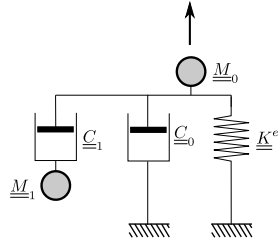


Figure 4: The monkey-tail model, this association of spring, dashpot and additional mass can be done in the 6 directions independently for a shallow foundation.

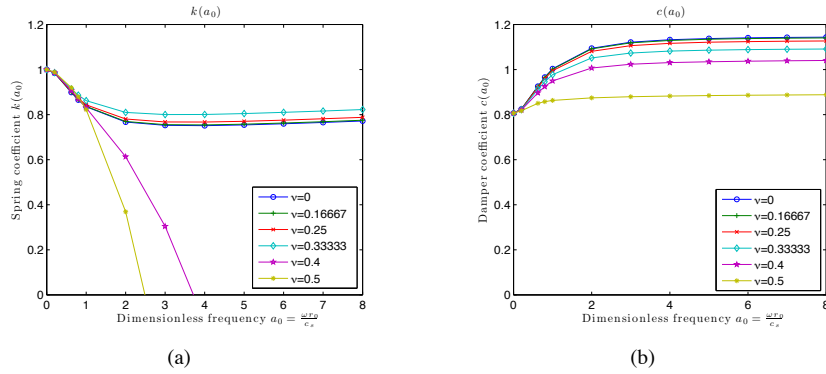
These parameters are associated to the following constants to be introduced into the Monkey-tail model in every directions:

$$\begin{cases} M_0 = \frac{r_0^2}{c_s^2} \mu_0 K^{el} \\ M_1 = \frac{r_0^2}{c_s^2} \mu_1 K^{el} \\ C_0 = \frac{r_0}{c_s} \gamma_0 K^{el} \\ C_1 = \frac{r_0}{c_s} \gamma_1 K^{el} \end{cases} \quad (5)$$

Figure 5 shows the evolution of the real and imaginary part of the transfer function according to the dimensionless frequency $a_0 = \frac{\omega r_0}{V_s}$ in the case of a circular footing. The curves in the figure show that the stiffness and damping parameters depend on the frequency of the applied loading and consequently do not have the same effect for the

Table 2: Parameters used in the Monkey-tail model for a disk on homogenous half-space [Wol88]

	Dimensionless Coefficients for			
	Dashpots		Masses	
	γ_0	γ_1	μ_0	μ_1
Horizontal	$0.78 - 0.4\nu$	–	–	–
Vertical	0.8	$0.34 - 4.3\nu^4$	0 if $\nu \leq \frac{1}{3}$, $0.9(\nu - \frac{1}{3})$ if $\nu \geq \frac{1}{3}$	$0.4 - 4\nu^4$
Rocking	–	$0.42 - 0.3\nu^2$	0 if $\nu \leq \frac{1}{3}$, $0.16(\nu - \frac{1}{3})$ if $\nu \geq \frac{1}{3}$	$0.34 - 0.2\nu^2$
Torsional	–	0.29	–	0.2

Figure 5: (a) stiffness; (b) and damping coefficients for a vertical solicitation on a circular foundation lying on a semi homogenous infinite space for different Poisson's ratio ν

different harmonics present in a real seismic input. For more details about Monkey tail models the reader can see [Wol88].

2.2 The non-linearities effects and loads applied to a structure

Let us assume that the interface between the soil and the foundation does not behave elastically anymore, but develops some non-linearities with residual displacements.

To illustrate the strong effect of non-linearities at the interface between the soil and the foundation on the structure's behavior, the simple Newmark approach can be used.

In the Newmark approach, a rigid body mass of m is moving upon a rigid support. The interface between the mass and the support is considered purely frictional, with a

friction angle φ . Then the relation existing between the normal and shear stresses (or forces) at the interface is illustrated in figure 6. Figure 6 gives also the evolution of the mass displacement with the shear force which behave as a perfect plasticity model without hardening. The limit shear force for a given normal force is indicated with the symbol V_y .

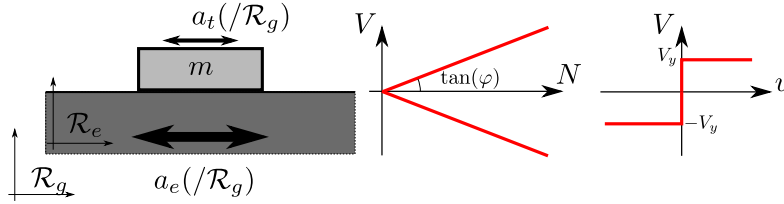


Figure 6: Newmark approach, rigid mass moving on a rigid support, Coulomb criteria characterizing the interface and force-displacement relationship.

The rigid support is then submitted to acceleration $a_e(t)$ (with respect to the Galilean referential axis \mathcal{R}_g). The total acceleration of the mass $a_t(t)$ (here again with respect to the Galilean referential axis \mathcal{R}_g) is then computed assuming its dynamic equilibrium through the equation 6. In this equation u is the relative displacement of the mass on the support and $P(u)$ is the resisting force from the support applied to the mass.

$$\begin{aligned}
 m\ddot{u}(t) - P(u) &= -ma_e(t) \\
 \Rightarrow P(u) &= m(a_e(t) + \ddot{u}(t)) \\
 \Rightarrow a_t(t) &= \frac{P(u)}{m} \quad (6)
 \end{aligned}$$

Since $P(u)$ cannot be higher than the yield force V_y (due to the sliding condition at the interface), the figure 7 and equation 6 simply show that the rigid mass cannot experience a total acceleration $a_t(t)$ higher than $\frac{V_y}{m}$.

This simple example proves 2 things:

- the dynamic loading submitted to the structure depends on the structure but also of the interface behavior. That's why the non-linearities generally generate a decrease in the loading transmitted to the structure (due to the yield stress developed at the base),
- on the contrary the non-linear mechanisms can generate high displacements during the transient loading stage but also at the end with residual displacements.

The non-linear effects that are concentrated at the interface between the structure and the support can be, here again, treated using generalized variable and by condensing the effect in a single point for defining the interface constitutive law. This concept of generalized forces is developed in more details in the following.

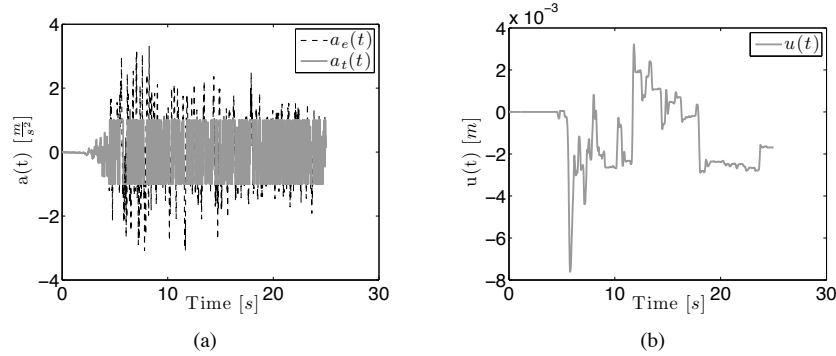


Figure 7: (a) Input acceleration $a_e(t)$ and total acceleration $a_t(t)$ of the mass with respect to the galilean reference coordinate axis \mathcal{R}_g ; (b) Relative displacement $u(t)$ of the mass with respect to the \mathcal{R}_e coordinate axis.

2.3 The concept of generalized forces, EC8 recommendations

The idea of considering generalized forces is motivated by the well known definition of the bearing capacity $N_u = Sq_{max}$ of foundations, where q_{max} is the ultimate compression stress of the soil under a vertical centered load (see [DB73], [MS79], [PH03], and [RJZ04]), and S is the area of the footing.

For shallow foundation under centered vertical loading, the bearing capacity is given by:

$$q_{max} = \frac{a_s}{2} \gamma D_{dm} N_\gamma + q_0 N_q + b_s c N_c \quad (7)$$

where q_0 is the vertical effective stress at the bottom of the foundation, while N_γ , N_q and N_c are bearing capacity factors depending on soil friction angle φ . The relations allowing calculating N_γ , N_q and N_c are given in [CK66] and [RJZ04]. a_s and b_s are shape factors defined in table 3:

Table 3: Shape factors for the bearing capacity of circular, rectangular and strip foundation (note: A , B = length and width of the rectangular footing)

	circular	rectangular	strip ($A \rightarrow \infty$)
a_s	0.6	$(1 - 0.2 \frac{B}{A})$	1
b_s	1.3	$(1 + 0.2 \frac{B}{A})$	1

More recently, some authors have defined the ultimate bearing capacity failure conditions by means of suitable failure criteria defined in the space of generalized forces

applied to the foundation (according to the figure 8, where $V = N_{Ed}$ is the vertical force, $H = V_{Ed}$ is the horizontal force, and $M = M_{Ed}$ the moment applied at the center of the foundation).

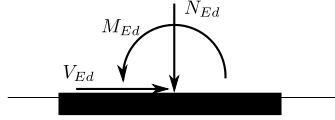


Figure 8: Generalized forces for a shallow foundation.

Nova [NM91] is the first having defined experimentally the shape of such criteria under a combination of generalized forces for cohesive or frictional soils followed by few other authors ([BG94], [CBH02], [CMH04], [Mar94], [GHB99]) and also recently with [Cha07]. The figures 9 give a comparison between these criteria when projected in different planes.

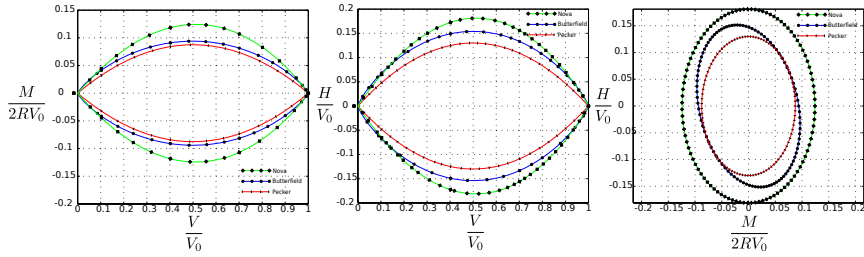


Figure 9: Comparisons between the different failure surfaces given by several authors, plotted with dimensionless variables. Strip foundations for [NM91] and [Pec97], circular footings for [BG94].

Recently, the EC8-5 [EC805] related to SSI problems under seismic loading provide its own criterion for shallow foundations (equation 8).

$$\frac{(1 - e\bar{F})^{c_T} (\beta\bar{V})^{c_T}}{\bar{N}^a \left[(1 - m\bar{F}^k)^{k'} - \bar{N} \right]^b} + \frac{(1 - f\bar{F})^{c_M} (\gamma\bar{M})^{c_M}}{\bar{N}^c \left[(1 - m\bar{F}^k)^{k'} - \bar{N} \right]^d} - 1 \leq 0 \quad (8)$$

with the dimensionless variables: $\bar{N} = \frac{\gamma R_d N_{Ed}}{N_{\max}}$, $\bar{V} = \frac{\gamma R_d V_{Ed}}{N_{\max}}$, $\bar{M} = \frac{\gamma R_d M_{Ed}}{B N_{\max}}$

the different parameters of this equation are provided in appendix F of EC8-5.

In this relationship the parameter \bar{F} represents the horizontal inertial force of the soil and $a, b, c, d, e, f, m, \beta, \gamma, c_M$, and c_T are parameters depending on the cohesive or frictional character of the soil. Figure 10 represents the equation 8 in both cases.

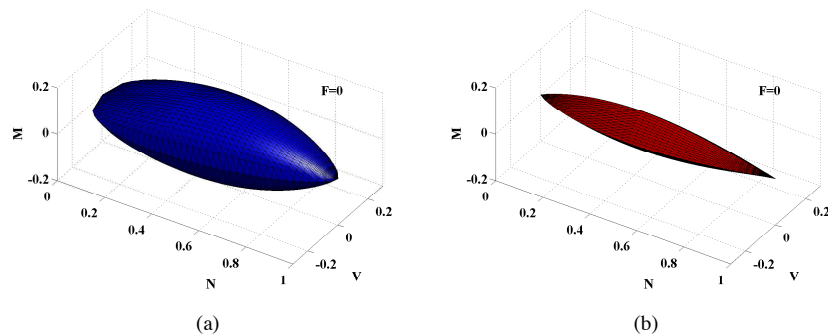


Figure 10: Representation of the bearing capacity for a shallow foundation from EC8 for (a) a purely cohesive soil ; (b) a purely frictional soil.

These failure criteria are needed in order to evaluate the resistance of a foundation under a combination of vertical, horizontal forces or moments. However, if the displacement have to be estimated, the consideration of ultimate failure conditions is not sufficient. That's why, during the last decades, non-linear models based on plasticity mechanisms and on these failure criteria are developed to describe the (reversible and irreversible) load–displacement behavior of the foundation–soil system, under cyclic or dynamic loadings. This family of model is called macro-element.

2.4 The macro-element for soil-structure interactions

A substantial progress towards an efficient and reliable approach to the analysis of soil–structure interaction problems for shallow footings has been recently achieved by the development of the so-called macroelement models for describing the overall behavior of the foundation–soils system (see, e.g, [NM91], [MH01], [CPD01]).

The macro-element approach consists in condensing all non-linearities (as plasticity of the soil and uplift of the foundation) into a finite domain ("close field") and work with generalized variables (forces and displacements) at the centre of the foundation (figure 11, where a superimposed dot $\dot{\cdot}$ denotes a time derivative), allowing thus reducing considerably the necessary degrees of freedom of the numerical model.

In the macro-element approach, the mechanical response of the foundation–soil system is described by means of a constitutive equation relating the generalized load vector, to the generalized displacement vector.

In the framework presented before (considering the impedance and the nonlinearities of the interface) the macro-element approach is very suitable for studying the soil-structure interactions and is completely consistent with the recommendations of the EC8 standards (as shown with equation 8).

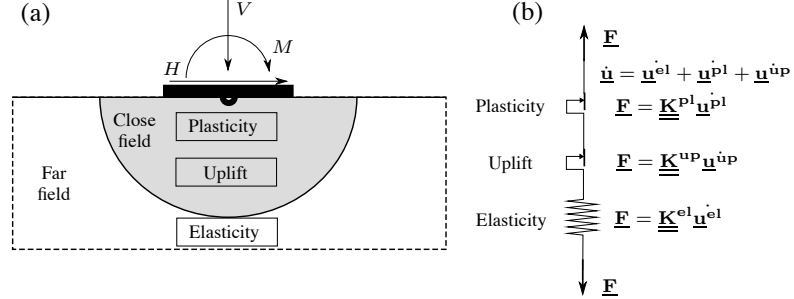


Figure 11: Presentation of the general structure of the macro-element: (a) decomposition in close field and far field (b) analogical system.

For the 3D macro-element presented in [GKM09a], 5 degrees of freedom are considered (torque moment according to the vertical axis is not taken into account). The dimensionless force and displacement vectors are given by equations 9 and 10. The notation is different from the one used in the equation 8 in EC8 because here no safety factors are used.

For a rectangular footing, the generalized force and associated displacement vectors are:

$$\begin{cases} \underline{\mathbf{F}} = {}^t [V', H'_x, M'_y, H'_y, M'_x] = \frac{1}{ABq_{max}} {}^t [V, H_x, M_y/B, H_y, M_x/A] \\ \underline{\mathbf{u}} = {}^t [u'_z, u'_x, \theta'_y, u'_y, \theta'_x] = \frac{\sqrt{A^2+B^2}}{AB} {}^t [u_z, u_x, B\theta_y, u_y, A\theta_x] \end{cases} \quad (9)$$

For a circular footing:

$$\begin{cases} \underline{\mathbf{F}} = {}^t [V', H'_x, M'_y, H'_y, M'_x] = \frac{1}{Sq_{max}} {}^t [V, H_x, M_y/D_{dm}, H_y, M_x/D_{dm}] \\ \underline{\mathbf{u}} = {}^t [u'_z, u'_x, \theta'_y, u'_y, \theta'_x] = \frac{1}{D_{dm}} {}^t [u_z, u_x, D_{dm}\theta_y, u_y, D_{dm}\theta_x] \end{cases} \quad (10)$$

In the above definitions, V , H_x , H_y , M_x and M_y are the resultant forces and moments acting on the foundation; u_z , u_x , u_y , θ_x and θ_y are the displacements and rotations (in the vertical yz and xz planes) of the foundation, and A , B or D_{dm} are a characteristic length (i.e, the foundation widths or diameter), introduced for dimensional consistency (see figure 12).

To reproduce correctly some important features of the experimentally observed behavior of the foundation–soil system such as nonlinearity, irreversibility and dependence from past loading history, the constitutive equation for the macroelement must be formulated in rate–form:

$$\dot{\underline{\mathbf{F}}} = \underline{\mathbf{K}}^{plup} (\underline{\mathbf{F}}, \underline{\mathbf{q}}) \dot{\underline{\mathbf{u}}} \quad (11)$$

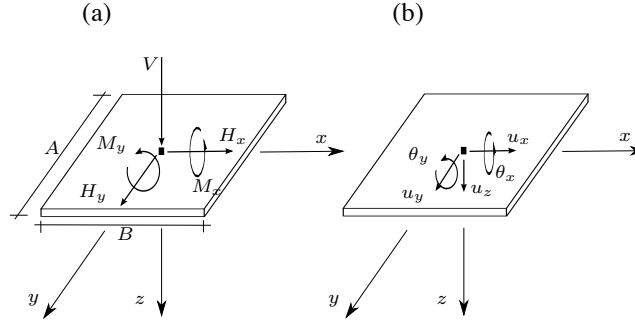


Figure 12: Generalised variables: (a) forces and (b) displacements for a rectangular foundation.

where $\dot{\mathbf{u}}$ is the generalized velocity vector, $\underline{\underline{\mathbf{K}}}^{\text{plup}}$ is the tangent stiffness of the system, depending on the system state and loading direction, and \mathbf{q} is a pseudo-vector of internal variables accounting for the effects of previous loading history.

The properties of the stiffness matrix $\underline{\underline{\mathbf{K}}}^{\text{plup}}$ are selected according to the basic features of observed behavior. To reproduce a rate-independent response, $\underline{\underline{\mathbf{K}}}^{\text{plup}}$ must be positively homogeneous of degree zero with respect to the generalized velocity vector $\dot{\mathbf{u}}$. In order to reproduce an inelastic behavior, $\underline{\underline{\mathbf{K}}}^{\text{plup}}$ must depend on the loading direction $\frac{\dot{\mathbf{u}}}{\|\dot{\mathbf{u}}\|}$ [Kol91].

In the macroelements developed in the framework of the theory of elastoplasticity [NM91, MH01, CPD01, GKM08], the constitutive equation is built starting from the fundamental assumptions of:

- elastic and plastic decomposition of the generalized velocity $\dot{\mathbf{u}} = \dot{\mathbf{u}}^{\text{el}} + \dot{\mathbf{u}}^{\text{pl}} + \dot{\mathbf{u}}^{\text{up}}$
- existence of a yield function $f_i(\mathbf{F}, \mathbf{q}_i)$ for each mechanism i in the generalized load space;
- existence of a plastic potential function $g_i(\mathbf{F}, \mathbf{q}_i)$ for each mechanism i providing the plastic flow direction ($i = pl$ or $i = up$);
- existence of a suitable hardening law for the internal variables,
- enforcement of Prager's consistency condition.

The resulting constitutive equation in rate form then reads (for M coupled mechanisms):

$$\dot{\mathbf{F}} = \underbrace{\left(\underline{\mathbf{K}}^{\text{el}} - \sum_{i=1}^M \sum_{j=1}^M H_{T_{ij}} \left(\underline{\mathbf{K}}^{\text{el}} : \frac{\partial g_i}{\partial \mathbf{F}} \right) \otimes \left(\frac{\partial f_j}{\partial \mathbf{F}} : \underline{\mathbf{K}}^{\text{el}} \right) \right)}_{\underline{\mathbf{K}}^{\text{plup}}} \dot{\mathbf{u}} \quad (12)$$

$$\underline{\mathbf{H}}_{\text{T}} = \left[\underline{\mathbf{H}}^{\text{plup}} + \underline{\mathbf{H}}_0^{\text{plup}} \right]^{-1} \quad (13)$$

where $\underline{\mathbf{K}}^{\text{el}}$ is the elastic stiffness matrix, $\underline{\mathbf{H}}^{\text{plup}}$ is the diagonal matrix of plastic moduli:

$$H_{ij}^{\text{plup}} = \delta_i^j \frac{\partial f_i}{\partial \mathbf{q}_j} \cdot \underline{\mathbf{h}}_j^{\text{plup}} \quad (14)$$

without sum on i ; δ_i^j is the Kronecker symbol and $\underline{\mathbf{H}}_0^{\text{plup}}$ as:

$$H_{0ij}^{\text{plup}} = \frac{\partial f_i}{\partial \mathbf{F}} \cdot \underline{\mathbf{K}}^{\text{el}} \frac{\partial g_j}{\partial \mathbf{F}} \quad (15)$$

The evolution equations for the internal variables are given by:

$$\dot{\mathbf{q}}_i = -\dot{\lambda}_i \underline{\mathbf{h}}_i(\mathbf{F}, \mathbf{q}_i) \quad (16)$$

where:

$$\begin{bmatrix} \dot{\lambda}_1 \\ \dot{\lambda}_2 \\ \vdots \\ \dot{\lambda}_M \end{bmatrix} = \left[\underline{\mathbf{H}}^{\text{plup}} + \underline{\mathbf{H}}_0^{\text{plup}} \right]^{-1} \begin{bmatrix} \frac{\partial f_1}{\partial \mathbf{F}} \cdot \underline{\mathbf{K}}^{\text{el}} \dot{\mathbf{u}} \\ \frac{\partial f_2}{\partial \mathbf{F}} \cdot \underline{\mathbf{K}}^{\text{el}} \dot{\mathbf{u}} \\ \vdots \\ \frac{\partial f_M}{\partial \mathbf{F}} \cdot \underline{\mathbf{K}}^{\text{el}} \dot{\mathbf{u}} \end{bmatrix} \quad (17)$$

The particular elastoplastic mechanism considered in this study has kinematic and isotropic hardening and has been specifically developed for cyclic loading conditions by [Cre01] and adapted by [GKM09a] for 3D problems. The yield function is an adaptation of the criteria provided by EC8 (equation 8) by assuming $\bar{F} = 0$ and coefficient $\beta = \gamma = 1$. Then the adaptation includes the hardening parameters in order to make a consistent evolution of the loading surface according to the experiments [Cre01]. The model is presented in details in [GKM08] and [GKM09a].

The uplift mechanism describes in a phenomenological way uplift using a unique state variable δ as the hardening variable. This variable represents the percentage of the surface of the uplifted footing [Cre01] and [GKM09a],

In the model, the uplift mechanism is described according to the classical plasticity theory. The particularity however is that the loading surface evolves in loading and in

unloading (i.e. unloading is not linear elastic, as it is usually the case in a classical plasticity law) with 2 different hardening rules (one in loading and a different one in unloading). The uplift mechanisms is extensively described into [GKM09a].

Coupling of the plasticity and the uplift mechanisms is finally done following the classical theory of the multi-mechanisms (figure 13, [SH98]). A representation of the failure criteria for both the plasticity and the uplift mechanisms is given in figure 13.

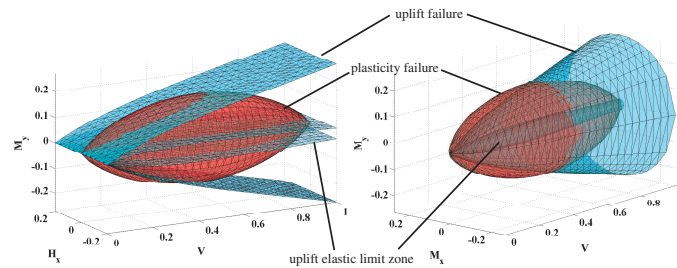


Figure 13: Representation of the failure criterion and of the initial elastic limit zone for the uplift mechanism (blue) and the failure criterion for the plasticity mechanism (red) in the spaces M_y, H_x, V and M_y, M_x, V .

For non linear hardening mechanisms, the resolution of such a problem is done writing the two loading surfaces (f_{pl} and f_{up}) using a first order Taylor development at the converged current point. This development gives two linear equations depending on the increment of the two plastic multipliers $\delta(\Delta\lambda)_{pl}$ and $\delta(\Delta\lambda)_{up}$. The resolution of the two coupled linear equations provides the increments of the plastic multipliers. The force, the plastic displacements and the hardening variables for each mechanism are then calculated (see [SH98]).

The principal difficulty in treating this problem is to evaluate the number ($M = 0,1$ or 2) of activated mechanisms. A numerical test on each mechanism is therefore needed at each step.

3 Numerical simulation of a seven-story RC building

3.1 Main characteristics of the structure

A full-scale vertical slice of a seven-story reinforced concrete (RC) walls building (figure 14) has been subjected to increasing intensity of uniaxial earthquake ground motions on the NEES Large High-Performance Outdoor Shake Table (international benchmark NEES/UCSD [NEE06]). The structure is composed of 2 main perpendic-

ular walls: the web wall and the flange wall linked with the slabs. For the experimental tests, the structure was fixed to the shaking table.

Only the direction Y of loading is considered (parallel to the web wall, see figure 14). Four input motions at different intensities have been used coming from the Sylmar Medical Facility free-field record obtained during the 1994 Northridge Earthquake (EQ1 to EQ4). At the end of the experimental program significant damage (crushing of concrete and buckling of steel bars) was concentrated at the base of the web wall.

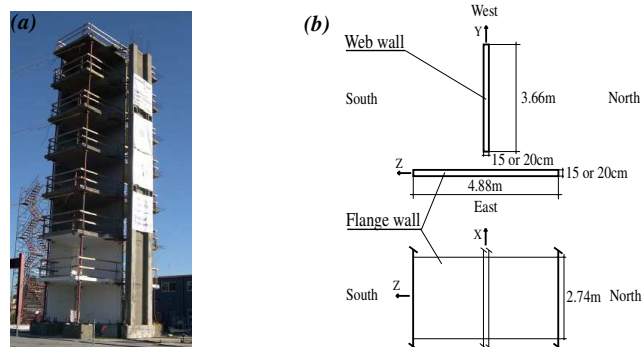


Figure 14: NEES building: (a) North West view of the test specimen and (b) Geometric data of the test specimen, [NEE06].

The capacity of the numerical strategy to reproduce the non linear behavior of the structure considered fixed at the base has been demonstrated in [GKM09b]. The building is modeled using Timoshenko multifiber beam elements [KM05], [MKRC06]. Constitutive laws for the wall materials are based on damage mechanics for concrete [LB91] and plasticity for steel [FPB83], [MP73]. The web wall and the flange wall are decomposed into 19 multifiber Timoshenko beam elements (4 elements for levels 1 and 2, 3 elements for level 3 and 2 elements for levels 5, 6 and 7). The multifiber elements composing the web wall are divided into 20 concrete fibers whereas those of the flange wall are divided into 8 concrete fibers.

In section 3.2 the macro-element has been introduced at the base of the structure. The structure is supposed to rest on a rigid shallow rectangular foundation lying on a soil of given mechanical properties. By changing the parameters of the macro-element 5 different soils and their influence into the non linear behavior of the RC building have been simulated. Comparisons with the behavior of the fixed base building are also presented.

3.2 Numerical simulations of the structure considering Soil-Structure Interaction

The geometric characteristics of the footing are given in figure 15. The center of the foundation is located below the gravity center of the structure (at $2m$ from the edge of the flange wall).

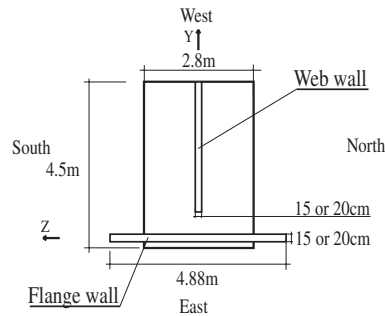


Figure 15: NEES building (SSI numerical model): Geometric characteristics of the foundation.

Various types of soils are considered. Their characteristics are defined in table 4. All soils have a density $\rho = 1900kg.m^{-3}$ and a Poisson coefficient $\nu = 0.4$. The classification used in this table is taken from [Dav99] and [EC805]. The criterion for the classification is the shear wave velocity in the soil (from class A: stiff bed rock to class S1: soil with very poor characteristics). The elastic stiffness is calculated from the dynamic impedances given in [Pec84].

We present hereafter, and this for the last loading sequence EQ4, the numerical results of the 7-story structure considering the 5 different types of soils:

Figure 16(a) shows the maximum overturning moments, story shears, lateral displacements, inter-story drift ratios and floor accelerations for each level. The SSI effect is assessed by comparing the different results with the numerical behavior of the original structure fixed to the shaking table. The internal forces presented here (overturning moments and story shears) are calculated only at the web wall. As expected, numerical results are similar for the fixed structure and for soil 5 (class A: solid bed rock) in terms of forces and displacements. For the other cases, SSI seems to “isolate” the structure in terms of forces. Looking at figures 16(a), (b) one can observe that overturning moments and story shears are reduced. This reduction is more significant for soils with poor characteristics.

Different conclusions are reached as far as displacements are concerned: Figure 16(c) shows that for soil 1, the lateral displacements at the top are lower than for soils 2 and 3. The reason is that not only the first but also the second order mode has a predominant role, modifying thus significantly the global and the local behavior

Table 4: NEES building (SSI numerical model): Characteristics of the soils.

Number	Shear modulus G_0 velocity V_s	Cohesion c friction angle ϕ	Stiffness and damping [Gaz91]	Ultimate bearing stress q_{max}
Soil 1 (S1 class)	$V_s = 70m/s$ $G_0 = 9.31MPa$	$c_u = 35kPa$ $\phi_u = 0$	$K_{\theta\theta} = 295.19MNm/rad$ $K_{zz} = 101.22MN/m$ $K_{hh} = 82.35MN/m$ $C_{\theta\theta} = 7.49MNms/rad$ $C_{zz} = 2.57MNs/m$ $C_{hh} = 2.09MNs/m$	$q_{max} = 0.20MPa$
Soil 2 (D class)	$V_s = 100m/s$ $G_0 = 19MPa$	$c_u = 70kPa$ $\phi_u = 0$	$K_{\theta\theta} = 601.5MNm/rad$ $K_{zz} = 206.18MN/m$ $K_{hh} = 167.8MN/m$ $C_{\theta\theta} = 10.70MNms/rad$ $C_{zz} = 3.67MNs/m$ $C_{hh} = 2.98MNs/m$	$q_{max} = 0.40MPa$
Soil 3 (C class)	$V_s = 180m/s$ $G_0 = 61.5MPa$	$c_u = 250kPa$ $\phi_u = 0$	$K_{\theta\theta} = 1951.4MNm/rad$ $K_{zz} = 668.9MN/m$ $K_{hh} = 544.4MN/m$ $C_{\theta\theta} = 19.50MNms/rad$ $C_{zz} = 6.60MNs/m$ $C_{hh} = 5.40MNs/m$	$q_{max} = 1.43MPa$
Soil 4 (B class)	$V_s = 360m/s$ $G_0 = 246.2MPa$	$c = 115kPa$ $\phi = 30$	$K_{\theta\theta} = 7805.1MNm/rad$ $K_{zz} = 2675.6MN/m$ $K_{hh} = 2177.7MN/m$ $C_{\theta\theta} = 38.24MNms/rad$ $C_{zz} = 13.20MNs/m$ $C_{hh} = 10.67MNs/m$	$q_{max} = 4.013MPa$
Soil 5 (A class)	$V_s > 800m/s$		$K_{\theta\theta} = 18302MNm/rad$ $K_{zz} = infinity$ $K_{hh} = infinity$ $C_{\theta\theta} = 0MNms/rad$ $C_{zz} = 0MNs/m$ $C_{hh} = 0MNs/m$	$q_{max} = infinity$

of the structure. More specifically: (i) in figure 16 it can be observed that the local behavior of the structure changes depending on the characteristics of the soil: for soil 1 numerical predictions provide the location of the maximum moment near the level 2, not at the base of the structure; (ii) both the first and the second mode influence the behavior of the structure on soil 1 in terms of the forces. From [GBKT09], it is obvious that the first two modes contribute to the moments developed in the structure; (iii) Only the first mode influences the behavior of the structure on soils 2 to 5 [GBKT09].

Figure 16(d) shows that the inter-story drift ratio is almost constant for soils 1 and 2, something typical for a structure that remains elastic during the entire loading sequence. This is also verified through the distribution of the damage variable of the concrete constitutive law within the multifiber Timoshenko beam elements representing the structure which is found everywhere equal to 0.

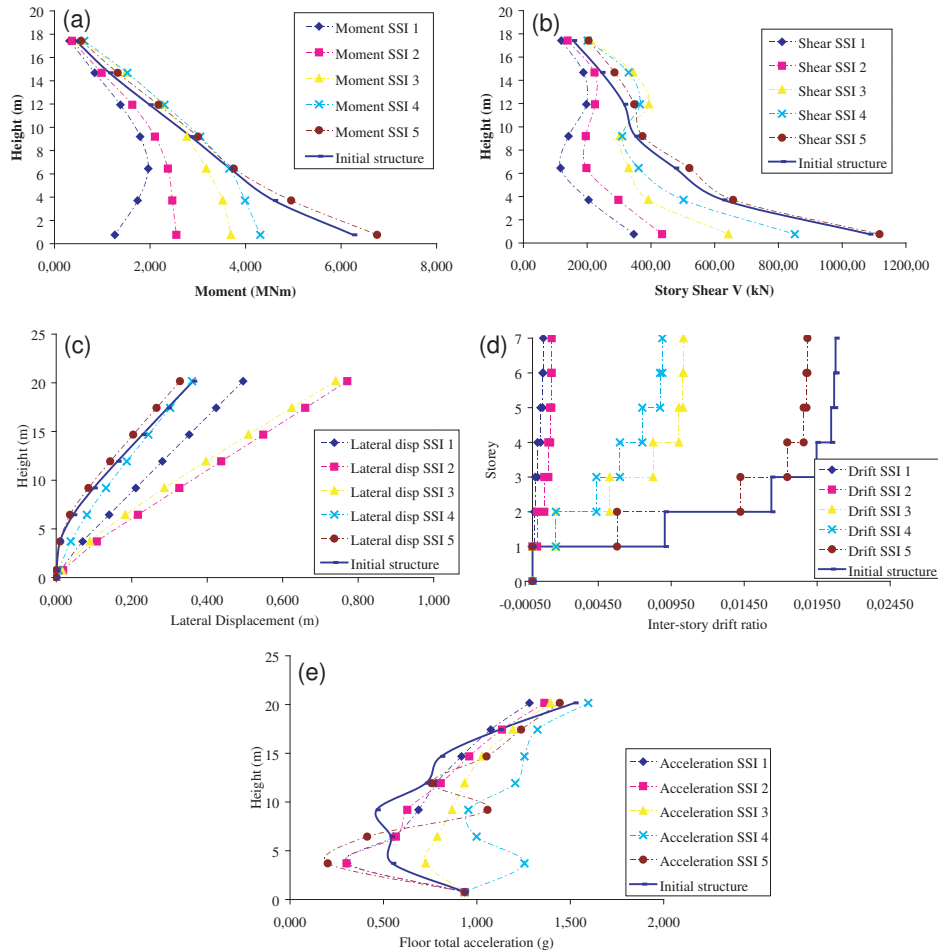


Figure 16: NEES building (SSI numerical model): (a) Maximum overturning moments, (b) story shears, (c) lateral displacements, (d) drifts and (e) floor accelerations for 5 different soils at the web wall and comparison with the structure fixed to the shaking table (EQ4).

Finally, it can be shown that no damage occurs in the structure for soil 1. Non linearities are concentrated at the interface between the foundation and the soil (due to the plasticity and the uplift). For soils 2, 3, 4 and 5, results are different, as the first 3 stories experience some damage.

It is also found that for softer soils damage is not reduced at all levels. For the NEES structure and for the case of soil 2, it may remain high at the second story. The influence of the second mode can explain this phenomenon. Another reason is the fact

that damage in traction grows more rapidly in sections where compression forces - due to the weight of the structure - are smaller (the ultimate moment is lower at the top of the structure than at lower levels).

4 Conclusions

This chapter gives some key points to understand what are the effects of soil-structure interactions and principally the effects in taking into account a stiffness but also non-linearities at the soil level on the behavior of the structure. It has been shown that taking into account the soil into the analysis and the design of the structure can change significantly the results compared to the fixed structure in terms of: fundamental frequency which is generally decreased, global damping which is generally increased, internal forces which can be increased by the fundamental frequency shifting but decreased by non-linearities, displacements of the structures which can be increased or decreased depending of the seismic input. On the example presented in the previous section, it has also been shown that the global behavior of the structure can completely change and can experience different modal shape generating strong damage or internal forces at intermediate level of the structure and not necessary at the base. Finally, no general rules can be deduced. The macro-element concept can give response for designing the structure. Its architecture is also very interesting because it is consistent with the design rules provided by the standards (like EC8) and allow saving computational costs.

References

- [BG94] R. Butterfield and G. Gottardi. A complete three-dimensional failure envelope for shallow footings on sand. *Géotechnique*, 44(1):181–184, 1994.
- [CBH02] MJ. Cassidy, BW. Byrne, and GT. Houlsby. Modelling the behaviour of circular footings under combined loading on loose carbonate sand. *Géotechnique*, 52(10):705–712, 2002.
- [Cha07] CT. Chatzigogos. *Comportement sismique des fondations superficielles: Vers la prise en compte d'un critère de performance dans la conception*. PhD thesis, Ecole Polytechnique, France, 2007.
- [CK66] A. Caquot and J. Kérisel. *Traité de mécanique des sols*. Gautiers-Villars, France., 1966.
- [CMH04] MJ. Cassidy, CM. Martin, and GT. Houlsby. Development and application of force resultant models describing jack-up foundation behaviour. *Marine Structures*, 17:165–193, 2004.

- [CPD01] C. Crémer, A. Pecker, and L. Davenne. Cyclic macro–element for soil–structure interaction: material and geometrical non–linearities. *Int. J. Num. Anal. Meth. Geomech.*, 25:1257–1284, 2001.
- [Cre01] C. Cremer. *Modélisation du comportement non linéaire des fondations superficielles sous séismes*. PhD thesis, LMT Cachan - ENS, Cachan, France, 2001.
- [Dav99] V. Davidovici. *La construction en zone sismique*. Le Moniteur, France., 1999.
- [DB73] EH. Davis and JR. Booker. The effect of increasing strength with depth on the bearing capacity of clays. *Géotechnique*, 23(4):551–563, 1973.
- [EC805] EC8. *NF P 06 030-1, NF EN 1998-1, Eurocode 8 : Calcul des structures pour leur résistance aux séismes*. AFNOR, 2005. Partie 1 : Règles générales, actions sismiques et règles pour les bâtiments, Septembre.
- [FPB83] FC. Filippou, EP. Popov, and VV. Bertero. *Effects of bond deterioration on hysteretic behaviour of reinforced concrete joints*. Earthquake Engrg. Res. Ctr. Univerity of California, Berkeley, 1983. Technical report EERC-83/19.
- [Gaz91] G. Gazetas. *Foundation Engineering Handbook, Chapter 15*. Fang H-Y (ed.), van Nostrand Reinhold: New York., 1991.
- [GBKT09] S. Grange, L. Botrugno, P. Kotronis, and C. Tamagnini. A macro–element to simulate dynamic soil–structure interaction. *Engineering Structures* doi:10.1016/j.engstruct.2009.08.007, 31:3034–3046, 2009.
- [GHB99] G. Gottardi, GT. Houlby, and R. Butterfield. Plastic response of circular footings under general planar loading. *Géotechnique*, 49(4):453–469, 1999.
- [GKM08] S. Grange, P. Kotronis, and J. Mazars. A macro–element for a circular foundation to simulate 3d soil–structure interaction. *Int. J. Num. Anal. Meth. Geomech.*, 32:1205–1227, 2008.
- [GKM09a] S. Grange, P. Kotronis, and J. Mazars. A macro–element to simulate 3d soil–structure interaction considering plasticity and uplift. *Int. Journal of Solids and Structures*, 46:3651–3663, 2009.
- [GKM09b] S. Grange, P. Kotronis, and J. Mazars. Numerical modelling of the seismic behaviour of a 7-story building: Nees benchmark. *Materials and structures, submitted, DOI 10.1617/s11527-008-9462-y*, 42(10):1433–1442, 2009.
- [KM05] P. Kotronis and J. Mazars. Simplified modelling strategies to simulate the dynamic behaviour of r/c walls. *Journal of Earthquake Engineering*, 9(2):285–306, 2005.

- [Kol91] D. Kolymbas. An outline of hypoplasticity. *Archive of Applied Mechanics*, 61:143–151, 1991.
- [LB91] C. La-Borderie. *Phénomènes unilatéraux dans un matériau endommageable: modélisation et application l'analyse des structures en béton*. PhD thesis, Université Paris VI, Paris, France, 1991.
- [Mar94] CM. Martin. Physical and numerical modelling of offshore foundations under combined loads. Master's thesis, DPhil Thesis, University of Oxford, 1994.
- [MH01] C. M. Martin and G. T. Houlsby. Combined loading of spudcan foundations on clay: numerical modelling. *Géotechnique*, 51:687–700, 2001.
- [MKRC06] J. Mazars, P. Kotronis, F. Ragueneau, and G. Casaux. Using multifiber beams to account for shear and torsion. applications to concrete structural elements. *Computer Methods in Applied Mechanics and Engineering*, 195(52):7264–7281, 2006.
- [MP73] M. Menegoto and P. Pinto. Method of analysis of cyclically loaded reinforced concrete plane frames including changes in geometry and non-elastic behaviour of elements under combined normal force and bending. *IABSE Symposium on resistance and ultimate deformability of structures acted on by well-defined repeated loads, final report, Lisbon*, page 328p, 1973.
- [MS79] M. Matar and J. Salençon. Capacité portante des semelles filantes. *Revue française de Géotechnique*, 9:51–76, 1979.
- [NEE06] NEES7story. *NEES/UCSD seven-story building-slice earthquake blind prediction contest*, 2006. <http://nees.ucsd.edu/7Story.html>.
- [NM91] R. Nova and L. Montrasio. Settlements of shallow foundations on sand. *Géotechnique*, 41(2):243–256, 1991.
- [Pec84] A. Pecker. *Dynamique des sols*. Presse, ENPC, Paris, France., 1984.
- [Pec97] A. Pecker. *Seismic Behavior of Ground and Geotechnical Structures*, chapter Analytical formulae for the seismic bearing capacity of shallow strip foundations, pages 261–268. Seco e Pinto (ed.), Balkema: Rotterdam, 1997.
- [PH03] G. Philipponnat and B. Hubert. *Fondations et ouvrages en terre*. Eyrolles, Paris, France., 2003.
- [RJZ04] M.F. Randolph, M.B. Jamiolkowski, and L. Zdravkovi. Load carrying capacity of foundations. *Proc. Skempton Memorial Conf., London*, 1:207–240, 2004.
- [SH98] JC. Simo and TJR. Hughes. *Computational Inelasticity, vol. 7. Mechanics and materials*, Springer Interdisciplinary applied mathematics., 1998.

- [Wol85] JP. Wolf. *Dynamic Soil-Structure-Interaction*. Prentice Hall International Series, Englewood Cliffs, New Jersey, 1985.
- [Wol88] JP. Wolf. *Soil-Structure-Interaction Analysis in time domain*. Prentice Hall International Series, Englewood Cliffs, New Jersey, 1988.

©ALERT Geomaterials
INPG – 3SR
46 avenue Félix Viallet
BP 53
38041 GRENOBLE CEDEX 9
FRANCE

ISBN 978-2-9542517-4-5

Fon: +33 (0) 456 528 621
Fax: +33 (0) 476 827 043
president@alertgeomaterials.eu
<http://alertgeomaterials.eu>

All rights reserved. No part of this book may be reproduced in any form or by any electronic or mechanical means, including information storage and retrieval systems, without written permission from the publisher or author, except in the case of a reviewer, who may quote brief passages embodied in critical articles or in a review.

ALERT Doctoral School 2013

Soil-Structure Interaction

Editors: P. Kotronis, C. Tamagnini, S. Grange

C. G. Lai, M. Martinelli

Soil-structure interaction under earthquake loading: Theoretical framework

L. Thorel

Centrifuge modelling of foundations subjected to cyclic loading

S. Escoffier

Centrifuge modeling of foundations subjected to earthquake loadings

P. Gueguen

Using strong and weak motion to identify the dynamic characteristics and the response of buildings considering soil-structure interaction

R. I. Borja

Discontinuous Deformation

M. Martinelli, C. Tamagnini

Modeling SSI on piled foundations: The effects of kinematic interaction

P. Kotronis

Simplified modeling strategies for soil-structure interaction problems: The multifiber beam concept

S. Grange

Simplified modeling strategies for soil-structure interaction problems: The macro-element concept

ISBN 978-2-9542517-4-5